Fabrication and characterization of SERS active substrates using self-assembly and Langmuir-Blodgett deposition technique

Thesis

Submitted to

Jadavpur University

For the Award of the Degree of

DOCTOR OF PHILOSOPHY (SCIENCE)

By

SOMSUBHRA SAHA, M.Sc., M.Tech

DEPARTMENT OF PHYSICS

JADAVPUR UNIVERSITY

KOLKATA: 700 032

INDIA

2022

CERTIFICATE FROM THE SUPERVISOR(S)

This is to certify that the thesis entitled "**Fabrication and characterization of SERS active substrates using self-assembly and Langmuir-Blodgett deposition technique**" Submitted by Sri Somsubhra Saha who got his name registered on 15th April, 2016 For the award of Ph. D. (Science) degree of Jadavpur University, is absolutely based upon his own work under the supervision of Prof. (Dr.) Joydeep Chowdhury and that neither this thesis nor any part of it has been submitted for either any degree / diploma or any other academic award anywhere before.

Joydeep Chowdhury 3/02/2022

.....

(Signature of the Supervisor(s) date with official seal)

Dr. Joydeep Chowdhury
Professor
Department of Physics
Jadavpur University
Kolkata - 700 032

Dedicated to my

Family

ABSTRACT

The present thesis entitled '**Fabrication and characterization of SERS active substrates using self-assembly and Langmuir-Blodgett deposition technique**' is the fulfillment of the requirements of the Degree of Philosophy (Science) of the Jadavpur University. It embodies the results of investigations which were carried out at the Department of Physics, Jadavpur University under the supervision of Prof. (Dr.) Joydeep Chowdhury. The thesis comprises of eight chapters.

Chapter 1 contains general introduction with a brief review of the existing experimental and theoretical knowledge relevant to the present work and the outline of the purpose and problems studied in the present investigation.

Chapter 2 describes the materials used in the experimental work, sample preparations, synthesis of silver, gold, silver coated gold nanocolloids and discusses various experimental procedures such as Langmuir-Blodgett (LB) deposition technique, Raman, UV-Vis absorption, Field Emission Scanning Electron Microscope (FESEM), High Resolution Tunnelling Electron Microscope (HRTEM), Energy Dispersive X-Ray Analysis (EDX), Atomic Force Microscope (AFM), X-Ray Photoelectron Spectroscopy (XPS) study.

Chapter 3 explains the electrodynamical and quantum chemical calculations and computational details that have been employed in this thesis work.

Chapter 4 deals with the fabrication of a highly sensitive SERS active substrate by self-assembly of silver nanocolloids (Ag NCs) in the bilayer Langmuir- Blodgett (LB) film of stearic acid (SA). Rhodamine 6G (R6G) has been used as the probe molecule to test the efficacy of the as prepared substrate. Gigantic enhancement factors $\sim 10^{12}$ orders of magnitude have been estimated from the surface enhanced resonance Raman scattering [SER(R)S] spectrum of R6G. The optical properties of the as prepared substrates have been envisaged by UV- Vis absorption spectra, while their morphological features are mapped through FESEM and AFM images. A correlation has been drawn between the SER(R)S efficacy and the corresponding FESEM and AFM images of the as prepared substrates. Electric field distributions around the aggregated AgNCs have been estimated with the aid of 3D- FDTD simulation studies.

Chapter 5 discusses the fabrication of SERS active substrate containing silver coated gold (Au@Ag) nanocolloids entrapped in the LB film matrix of SA. The SERS efficacy of the as prepared substrate has been tested with trace concentrations of R6G molecules. Enhancement factors ranging from $\sim 10^4 - 10^{13}$ orders of magnitude have been estimated for the characteristic vibrational signatures of R6G molecule. The optical responses and the morphological features of the substrates are estimated with the aid of UV- Vis absorption spectra and FESEM, AFM images respectively. Correlations between the surface morphologies, fractal dimensions and roughness features of the as prepared substrates are also drawn. The electric field distributions around the aggregated nanocolloids entrapped in the SA matrix have been envisaged with the aid of 3D-FDTD simulations.

Chapter 6 depicts a facile procedure towards the fabrication of highly reproducible, large area SERS active substrates through integration of LB and self-assembly technique. Gold nanoparticles with average particle diameter of ~ 55 nm have been self-assembled on the monolayer LB film matrix of poly (methyl methacrylate). The plasmonic architectures of the substrates have been tuned by lifting the LB film at different surface pressures. The as prepared substrates show their respective efficacies as efficient SERS sensing scaffolds for detecting 4-Mercaptopyridine (4-MPy) molecule at ultrasensitive concentrations. The optical responses and morphological features of the substrates have been envisaged with various characterization techniques. 3D-FDTD simulation studies have been employed to estimate the electric field distributions around the aggregated gold nanoparticles.

Chapter 7 is focused to explore in details the topographical features of SERS active substrates, fabricated through LB and self-assembly techniques, in presence of the probe 4-Mpy molecule. The statistical parameters (ca. lateral correlation length, Hurst exponent, interface width and fractal dimensions) associated with the topographical features of the bare SERS active substrate are also compared with the same substrate in presence of 4-Mpy.

Chapter 8 reports the adsorptive behaviour of probe 4MPy molecule with gold nanoparticles (AuNPs) embedded in the bilayer LB film matrix of SA. The as fabricated AuNps entrapped within the LB film template of SA proved to be a good SERS sensing platform that can sense the analyte 4MPy molecules at trace concentrations ~ 1.0×10^{-9} M. X-ray photoelectron spectroscopy together with SERS spectral analysis signify the adsorption of the analyte 4MPy with AuNPs via

sulfur atom. The experimental observations are supported by Born-Oppenheimer on the fly Molecular Dynamics (BO-OF-MD), time resolved wavelet transform theory (WT) and DFT calculations based on adcluster models. The time resolved vibrational frequency estimations as obtained from WT theory further corroborates experimentally recorded down shifts of the enhanced Raman bands at 711 and 1092 cm^{-1} in comparison to their normal Raman counterparts at 723 and 1114 cm^{-1} respectively. The molecule → metal charge transfer (CT) contribution to the overall enhancement of the SERS spectra of 4MPy molecule has been suggested from electron density difference calculations.

All the results incorporated in the thesis have been published in different journals of international repute. List of publications along with the available reprints are included in the APPENDIX.

Somsubhra Saha

(SOMSUBHRA SAHA)

Acknowledgement

Research work entails an indefatigable effort and loads of patience. The experience of traversing this tortuous academic-course is a puzzling mix of both elation and disappointment, a sporadic feeling of rejoicing and despair. It often brings forth a taste of transient success alongside failure. During this journey I had to secure help from various quarters on numerous occasions.

First of all, I want to mention here that I consider myself abundantly fortunate insomuch as having the able guidance, unbarred support and continuous encouragement from my Supervisor Prof. (Dr.) Joydeep Chowdhury, Professor, Department of Physics, Jadavpur University (JU), Kolkata, throughout the course of my research work. Apart from helping me Academically and Professionally, he has always stood just by me to lift up my sagging spirit whenever I felt downcast. I sincerely heap a copious esteem on him.

Next, I would like to express my sincere gratitude to the University Grants Commission (UGC), Government of India, for providing me financial assistance by way of Junior / Senior Research Fellowship during my entire tenure as a Research Scholar.

I take this opportunity to thank Prof. Sukhen Das, HOD, Department of Physics and all other professors, authorities and office staffs of several academic institutions and organisations apart from JU, for lending me unconditional support during the course of this work.

I owe a debt of thanks to my Seniors Dr. Rina De, Dr. Subhendu Chandra, Dr. Bipan Dutta and my lab mates Dr. Gopa Dutta Pal, Dr. Sannak Dutta Roy, Dr. Snehasish Bhattacharjee, Dr. Soumen Saha, Dr. Sumit Kumar Das, Sunetra Das, Chayan Kumar Mitra, Late Rajdeep Sinha, Swarup Ghosh, Sk. Firoj Haque, Rati Ray Banik and Pritabrata Maity for their constant help, valuable suggestions and moral support during the entire period of my research work. I also like to thank the Department of Physics, JU for recording the FESEM images.

I must pay my profound respect and gratitude to my parents (Mr. Shyamal Saha and Smt. Tapati Saha), parents-in-law (Mr. Ranajit Kumar Basu and Smt. Purabi Basu), and my wife Urmi Basu, for their unstinted cooperation and abiding inspiration which kept me going in high spirits against all odds till the successful completion of my 'Thesis'.

Last but not the least, I am thankful to those also who rendered me all sorts of succour I needed in this mission, but, for some reasons, whose names do not figure here.

Somsubhra Saha

JADAVPUR, KOLKATA – 700032 **SOMSUBHRA SAHA**

Contents

Chapter 1: Introduction

Chapter 2: Experimental Section

Chapter 3: Theoretical and Computational Section

Chapter 1: Introduction

1.1 Introductory Remarks

Raman spectroscopy has enabled the scientists to envisage the structural details and the vibrational signatures of various organic and inorganic molecules [1-5]. The applications of conventional Raman spectroscopy are limited by the extremely small cross section of the Raman scattering process. The discovery and development of **S**urface **E**nhanced **R**aman **S**cattering (SERS) has not only overcome this inherent problem but also has opened up new horizons in the domain of spectroscopy, materials and biological science related research works [6-9]. SERS was first discovered by Fleischmann and his co-workers [10] in the year 1974 at University of Southampton. They have reported an exceptionally million-fold enhancement of Raman signals from pyridine molecules adsorbed (from solution) onto the surface of electrochemically roughened silver electrode. After three years, David Jeanmaire *et al*. and M. G. Albrecht *et al*. have observed similar phenomena and they have reported for the first time that the extraordinary enhancement in the Raman signal depends upon the roughness factor of the nanoparticle surface [11, 12].

The cutting-edge works of Nie and Emory [13], Kneipp *et al*. [14] in the field of SERS research have drawn worldwide attention. It was later further corroborated by the works of Käll [15] and Brus *et al*. [16,17] and their commendable jobs in this field have brought about considerable interest in the area of SERS research [18-20]. According to their reports, enormous SERS enhancement ($\sim 10^4$ orders of magnitude) can be achieved in adequate conditions. These studies also report that the special sites, sometimes recognized as “hot spots” are supposed to play significant role behind this gigantic enhancement. This huge enhancement in the Raman signal can detect molecules at trace concentrations even at single molecular regime.

Based upon these considerations, major part of the modern research efforts in SERS is concentrated in the controlled and reproducible fabrication of metallic nanostructures that create hot geometries where the analyte molecules can appropriately be confined for the colossal Raman enhancement. In order to understand the electromagnetic enhancement mechanism of SERS, the interconnection between the molecular resonance, localized surface plasmon resonance (LSPR) of triangular silver nanoparticles and the Raman excitation profile of the analyte molecules adsorbed on the metallic nanostructures was explored in the collaborative work of Prof. Richard P. Van Duyne and Prof. George C. Schatz *et. al*. [21]. Due to the difficulty in the fabrication of robust and efficient SERS active substrate, the SERS technique is yet to be applied towards the development of vastly accepted, economically feasible diagnostic applications. The major requirements of an

ideal SERS active substrate that can be used in real world diagnostic applications are, the preparation of facile nanostructured substrate with stable shelf life that produce maximum enhancement in the Raman signal with good spectral reproducibility and uniformity.

The current up rise in this field of research is mainly engrossed in the following three directions:

❖ Fabrication of robust and reproducible SERS active substrates of plasmonic and non-plasmonic nanomaterials that can overcome the "SERS uncertainty principle" which predicts the reproducibility of the substrates at the expense of the enhancement factor (EF) of the Raman vibrational signatures.

❖ Understanding the mechanisms involved in the SERS phenomenon as well as to understand the interaction between the far-field SERS spectra of probe molecules with the near-field plasmonic responses of nanoparticles.

❖ Application of this SERS tool in trace detection of drugs, explosives, pesticides, bio molecules, bio imaging, diagnostics and even in cancer cell detection.

1.2 Objective of the Thesis

The specific objectives of this dissertation are:

(i) Fabrication of efficient SERS active substrates by integration of self-assembly and Langmuir-Blodgett (LB) deposition technique with higher order of enhancement and reproducibility.

(ii) Characterization of the as prepared SERS active substrates using various spectroscopic and microscopic techniques.

(iii) To find a correlation between the topographical features of the as fabricated SERS active substrates with their corresponding SERS responses in light of statistical calculations.

(iv) To understand the adsorptive behavior of the molecule-metal complex using Born-Oppenheimer on the fly Molecular Dynamics (BO-OF-MD), Time- Resolved Wavelet Transform Theory and Density Functional Theory (DFT) simulations.

1.3 Raman Spectroscopy

Raman scattering is the inelastic scattering of light by molecules and is named after its discoverer, the Indian Scientist Dr. C. V. Raman. When light is scattered from a molecule, the elastic scattering of the incident photons is pre-dominant such that the scattered photons have the same energy as that of incident photons. This is known as Rayleigh scattering. But some fraction of the incident light (~ 1 in 10^7 photons) is scattered inelastically (i.e., the scattered photons have

the different frequency of the incident photons). The energy of the scattered photons can be higher or lower than the incident photons resulting a shift in the frequency of the scattered photons. This inelastically scattering phenomena of light is known as "Raman Scattering" and the effect is called "The Raman Effect". If the energy of the scattered light is lower than the energy of the incident light, it is called stokes line and if the energy of the scattered light is higher than the energy of the incident light, it is known as anti-stokes line. The overall phenomena of Raman scattering can be explained in light of both the classical and quantum mechanical theories.

1.3.1 Classical Theory of Raman Effect

The interaction of electromagnetic wave with an electric dipole has been taken in consideration to explain the classical theory of the Raman effect. When a molecule is exposed with an electromagnetic wave, since the charge of the nucleus is positive, it experiences a force in the direction of the electric field and are attracted towards the negative pole of the field. Alternatively, the force experienced on the electron cloud by the electric field will be in the opposite direction since the electron charge is negative and the electrons are attracted in the direction towards the positive end of the field. The electron cloud is thus shifted with respect to the nucleus which in turn gives rise to an induced dipole moment in the molecule and this can be expressed as:

$$\vec{\mu} = \alpha . \vec{E} \qquad (1.1)$$

where $\vec{\mu}$, $\vec{E}$ and α stand for the induced dipole moment per unit volume, the incident electric field vector and the polarizability of the molecule respectively. The general expression for a sinusoidal electric field with frequency ω_0 is:

$$\vec{E} = \overrightarrow{E_0} \cos(\omega_0 t) \qquad (1.2)$$

where $\overrightarrow{E_0}$ is the amplitude of the electric field. So, from equations (1.1) and (1.2), the induced dipole moment can be expressed as:

$$\vec{\mu} = \alpha \overrightarrow{E_0} \cos(\omega_0 t) \qquad (1.3)$$

If ω_k is the vibrational frequency of the molecule, the nuclear displacement q has the following expression:

$$q = q_0 \cos(\omega_k t) \qquad (1.4)$$

where q_0 is the vibrational amplitude of the molecule. Using small displacement approximation, the polarizability (α) can be expanded in Taylor series as follows:

$$\alpha = \alpha_0 + \left(\frac{\partial\alpha}{\partial q}\right)_0 q + \cdots \qquad (1.5)$$

where, α_0 and $\left(\frac{\partial\alpha}{\partial q}\right)_0$ are the polarizability and the rate of change of the polarizability of the molecule with the displacement of the molecule respectively when it is in the equilibrium position.

So, from equation (1.3), (1.4) and (1.5) the induced dipole moment can be written as:

$$\vec{\mu} = \alpha_0\vec{E_0}\cos(\omega_0 t) + \left(\frac{\partial\alpha}{\partial q}\right)_0 q_0\vec{E}_0\cos(\omega_0 t)\cos(\omega_k t)$$

$$= \alpha_0\vec{E}_0\cos(\omega_0 t) + \frac{1}{2}\left(\frac{\partial\alpha}{\partial q}\right)_0 q_0\vec{E}_0\left[\cos\left((\omega_0 - \omega_k)t\right) + \cos\left((\omega_0 + \omega_k)t\right)\right] \qquad (1.6)$$

It is clear from equation (1.6) that the induced dipole moment contains three frequencies. The first term of the induced dipole moment contains with frequency ω_0, which is similar with the frequency of the incident electric field and this term represents the "Rayleigh line". In the second and third term of the frequency, $(\omega_0 - \omega_k)$ and $(\omega_0 + \omega_k)$ represent the stokes and anti-stokes line respectively.

Numerous experimental findings indicate that the stokes shifted Raman lines are more intense than the anti-stokes lines. However, the classical theory of Raman effect can describe the origin of stokes and anti-stokes lines but it fails to give an explanation regarding their relative intensities which can be overcome by the quantum mechanical theory of Raman effect.

1.3.2 Quantum Theory of Raman Effect:

The quantum theory of Raman effect helps to comprehend the occurrence of Raman scattering. According to the particle nature of electromagnetic radiation, an electromagnetic wave of frequency ν is related to the energy (E) of each quantum as:

$$E = h\nu \qquad (1.7)$$

where, h is known as Planck's constant. When an electromagnetic wave is incident on the molecule, then the photon can be experienced collisions with the molecule. If this collision is elastic then the energy and the frequency of the molecule will be same as that of the incident photon and the molecule is scattered without any change of frequency and energy. This phenomenon is called "Rayleigh scattering". On the other hand, if the collisions are inelastic, then an exchange of energy is occurred between the photon and the molecule. In that case the scattered molecule can gain or loss energy and this change in energy ΔE depends upon two of its allowed energy states. If the molecule gains energy from the incident photon, it goes from a lower energy state towards a

higher energy state and ΔE becomes positive. In that case the photon is scattered with energy ($h\nu - \Delta E$) which corresponds to the frequency ($\nu - \Delta E/h$) or ($\nu - \Delta\nu$). This is known as stokes line. Alternatively, if the molecule losses energy (releasing its energy to the incident photon during collision), then the photon is scattered with energy ($h\nu + \Delta E$) corresponding to the frequency ($\nu + \Delta E/h$) or ($\nu + \Delta\nu$). This is called anti-stokes line. Figure 1.1 shows the schematic representation of the Rayleigh, stokes and anti-stokes lines. As the energy of the stokes line is higher than the energy of the anti-stokes line, it may conclude that the intensity of the stokes line is higher than the intensity of the anti-stokes line. If the incident photon wavelength matches with the electronic transition of the molecule, the resonance Raman (RR) effect is occurred.

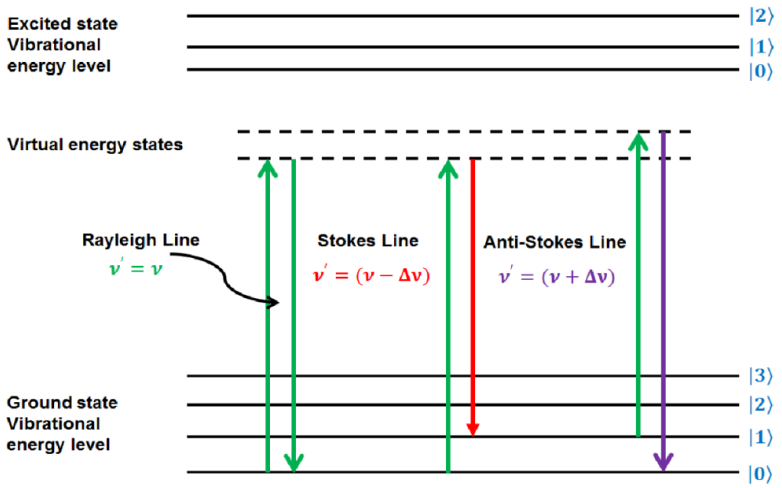

Figure 1.1: Schematic representation of the Rayleigh, stokes and anti-stokes lines

The Maxwell-Boltzmann (MB) statistics can explain the intensity variation of the strokes and anti-stokes lines in the Raman spectra. If n_0 is the number of molecules in the ground state, then the number of molecules n per unit volume in an energy state E at temperature T K is expressed by:

$$\frac{n}{n_0} = \exp\left(-\frac{E}{k_B T}\right) \qquad (1.8)$$

where, k_B represents the Boltzmann constant. Normally, due to thermal equilibrium, the ground states are much populated than the higher energy states, the probability of transition from ground state to the higher energy state is always greater than the opposite transition. Thus, the stokes lines are more intense than the anti-stokes lines.

1.4 Surface Enhanced Raman Scattering (SERS)

Since the accidental discovery of SERS [10], it has left tremendous impact on both fundamental and applied sciences. It not only boosts up the research on the enhanced optical scattering from interfaces, but also provides an ultra-sensitive *in situ* diagnostic tool towards the interpretation of the specific structure and orientation of analyte molecules adsorbed on the nanoparticle surface [13,14,22-25]. The SERS spectroscopy has produced significant consequences in various fields such as surface chemistry, forensic science, condensed matter physics, inorganic chemistry of metals, pharmaceuticals, classical electrostatics, electrochemistry, plasmonics and electromagnetic theory as applicable in small metal particles, optics of small particles, problems of radiating multipoles near metal surfaces, surface-photon interaction, generation of the surface plasmons and second harmonic from molecules and surfaces. Single molecule sensing using SERS technique has got significant attentiveness in the field of biochemistry, biophysics, genetic engineering and also in molecular biology [26-33].

1.4.1 SERS Enhancement Mechanism

The major theoretical investigations on SERS are mostly related to elucidate the mechanism involved behind this enhancement phenomenon, whose exact nature is yet to be cleared. However, it is consensually accepted that both the long-range electromagnetic (EM) effect and short-range chemical (CHEM) effect are concurrently effective.

(A) Electromagnetic Enhancement Mechanism

The increase in intensity of the Raman signal for analyte molecules adsorbed on particular surfaces (rough surface) occurs because of the enhancement in electric field provided by the localized surface plasmon (LSP) of the metallic surface. When metallic particles of a small size are excited by an electric field of light having wavelength λ, the electric field shifts the electron cloud of the metal surface with respect to the nucleus. As, they are dragged apart, a coulomb restoring force seems between them which tries to put back the electron cloud to its original position. Under quasistatic approximation $2d \ll \lambda$, where d is the radius of the nanoparticle, a coherent oscillation occurs between the exciting electric field and the coulombic restoring force. The communal oscillation of the electron cloud is referred as LSP. If the frequency of the incident light wave is in harmony with the frequency of the LSP, the localized surface plasmon resonance (LSPR) occurs which in turn generates an enormous electric field on the surface of the metallic

nano particle. In case of metallic nanoparticles, the plasmon resonance is confined near the surface of the particle, which results higher order of enhancement from the aggregated nanostructure. Figure 1.2 demonstrates a schematic representation of the generation of enhanced electric field owed to localized surface plasmon resonance (LSPR).

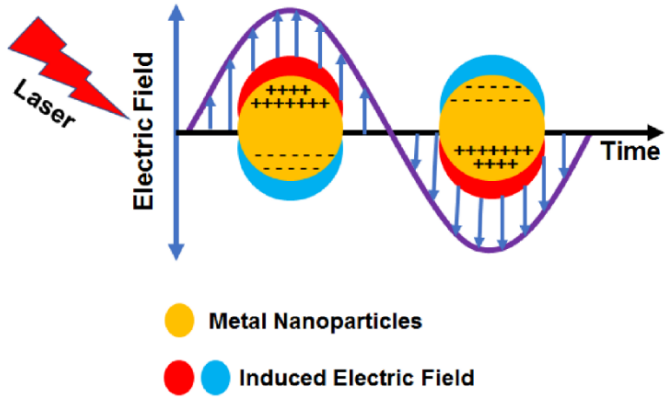

Figure 1.2: Schematic representation of the generation of enhanced electric field owed to localized surface plasmon resonance (LSPR).

The EM enhancement mechanism of SERS can be enlightened on the basis of the following models.

(a) Isolated Metal Particles

The isolated metal particles model is based on the quasistatic approximation i.e., size of the metal sphere that is illuminated by a laser field is small compared to the wavelength of the incident light. In this case, the Raman scattering originates from the molecules adsorbed near the surface of the metallic sphere. It is supposed that the metallic particle having dielectric constant ε_1 is surrounded by a medium with dielectric constant ε_0. If the electric field of the incident electromagnetic wave is $\overrightarrow{E_0}$, then the resulting electric field outside of the sphere $\overrightarrow{E_{out}}$ can be written by approximating the Maxwell's equation to Laplace's equation. Thus, $\overrightarrow{E_{out}}$ has the following expression,

$$\vec{E}_{out} = \vec{E}_0 z - \alpha \vec{E}_0 \left[\frac{\vec{z}}{r^3} - \frac{3z}{r^5}(z\hat{z} + x\hat{x} + y\hat{y}) \right] \qquad (1.9)$$

where, the first and second term represent the applied electric field and the induced dipole that originates from the polarization of the electron density of the sphere. The polarizability of the sphere is α and r signifies the radial distance from the metallic sphere. x, y, z and $\hat{x}, \hat{y}, \hat{z}$ are the

usual cartesian coordinates and their cartesian unite vectors respectively. The metallic polarizability α and the radius of the sphere "a" is related as

$$\alpha = ga^3 \qquad (1.10)$$

where, the expression for g is,

$$g = \frac{\varepsilon_i - \varepsilon_0}{\varepsilon_i + 2\varepsilon_0} \qquad (1.11)$$

When the imaginary part of ε_i is small, the real part is equal to $-2\varepsilon_0$, in that case α becomes very large which results a large induced field that guides the electromagnetic enhancement. This is known as plasmon resonance. In plasmon resonance condition, the real part of ε_i should be negative and very large in magnitude. Again equation (1.11) reveals that if there is a change in the dielectric constant of the surrounding medium, the plasmon resonance wavelength will also change. The Raman intensity E_{out}^2 at the surface of the sphere ($r = a$) is represented as:

$$E_{out}^2 = E_o^2[|1 - g|^2 + 3\cos^2\theta(2Re(g) + |g|^2)] \qquad (1.12)$$

where the angle between the direction incident field and the vector $\vec{r}$ is denoted by θ. Considering a large value of |g|, equation (1.12) have the following expression,

$$E_{out}^2 = E_0^2|g|^2(1 + 3\cos^2\theta) \qquad (1.13)$$

Equation (1.13) reveals that the largest field intensities is attained for θ = 0° and 180°. In Raman scattering, an oscillating dipole in the adsorbed molecule is induced by the incident field. The components of this dipole radiation that are shifted by the vibrational frequencies of the molecule directs the Raman scattering intensities. Assuming the location of the molecule is at maximum enhancement position, considering $|g| \gg 1$ the overall enhancement owed to the incident and scattered field can be represented as:

$$G_R = \frac{E_{out}^2 E_{out}'^2}{E_0} = 16|g|^2|g'|^2 \qquad (1.14)$$

The primed symbols denote the field assessed at scattered frequency. Applying the Drude model of free-electron theory, the metal dielectric constant will be:

$$\varepsilon_i = 1 - \frac{\omega_p^2}{\omega(\omega + i\gamma)} \qquad (1.15)$$

where, ω_p and γ represent the plasmon frequency and plasmon width respectively. If the ratio between ω_p and γ is ~ 10, the peak value of g will also be ~ 10. For spherical particles, the electromagnetic enhancements are small as the surface plasmons for most materials are far enough

i.e., γ is large (typically due to inter band transitions). In case of spheroid objects, the enhancement is greater since the plasmon resonances for such objects arise at frequencies that are red-shifted with respect to spherical particles to the frequencies where the plasmon width is adequately insignificant to compel $g \geq 10$. The results as attained in the case of isolated metal particle model are closely linked to the optical efficiencies, such as absorption, scattering and extinction cross section of the spherical particles as estimated by classical Mie theory for longer wavelength limit $a \ll \lambda$.

If $x = 2\pi a(\varepsilon_0)^{\frac{1}{2}}/\lambda$ then the extinction cross-section Q_{ext} can be expressed as:

$$Q_{ext} = 4x\mathrm{Im}(g) \qquad (1.16a)$$

and the scattering cross-section Q_{sca} is:

$$Q_{sca} = \frac{8}{3}x^4|g|^2 \qquad (1.16b)$$

As $x^4 \propto \frac{1}{\lambda^4}$, that the wavelength dependence of Eq. (1.16b) is similar to the larger limit of $|g|$ in Eq. (1.13). As far as the plasmon width is lesser than the plasmon energy, the extinction cross-section has the equal wavelength dependence as the larger limit of $|g|$ in Eq. (1.13). Therefore, in the small particle limit, SERS excitation and extinction plasmon peaks and widths should be the same.

(b) Isolated Spheroids Model

As the precise analytical solutions of spheroid particles in electrodynamics is very complex, the theoretical work done based upon spheroid particles has been estimated by numerical solutions of Maxwell's equations [34,35] and analytical electrostatic solutions [36,37] which are valid only for small particles. Similar outcomes have been observed from both these theories with particle size < 100 nm. Assuming a spheroid with major and minor axis of length 2b and 2a respectively and a constant electric field $\vec{E}_0$ applied along the major axis, Zeman and Schatz gave a precise expression of the Raman enhancement factor (EF) for the molecule distributed randomly on the spheroid surface as given below:

$$G_R = R(\omega)R(\omega - \Delta) \qquad (1.17)$$

where,

$$R(\omega) = |1-g|^2 + \left[\frac{2\mathrm{Re}(1-g)g^*}{Q_1(\xi_0)} + \frac{|g|^2}{Q_1^2(\xi_0)(\xi_0^2-1)}\right] \times \left[\frac{-(\xi_0^2-)^{1/2} + \xi_0^2 \sin^{-1}(1/\xi_0)}{(\xi_0^2-1)^{1/2} + \xi_0^2 \sin^{-1}(1/\xi_0)}\right] \qquad (1.18)$$

$$\xi_0 = \left(1 - \frac{a^2}{b^2}\right)^{-\frac{1}{2}} \qquad (1.19)$$

$$Q_1(\xi_0) = \frac{1}{2}\xi_0 \ln\left(\frac{\xi_0 + 1}{\xi_0 - 1}\right) - 1 \qquad (1.20)$$

and g have the following expression

$$g = \frac{\varepsilon_i - \varepsilon_0}{\varepsilon_i + \chi\varepsilon_0} \qquad (1.21)$$

where χ in equation 1.21 is represented as,

$$\chi = -1 + \frac{1}{(\xi_0^2 - 1)\left[\frac{\xi_0}{2}\ln\left(\frac{\xi_0+1}{\xi_0-1}\right) - 1\right]} \qquad (1.22)$$

The expression of g in equation (1.21) is the generalization of the expression as given in equation (1.11). Actually, the value of the parameter χ is equal to 2, larger than 2 and smaller than 2 for sphere, prolate and oblate spheroids respectively. In case of prolate spheroids, when χ is > 2, the plasmon resonance condition $\mathrm{Re}(\varepsilon_i + \chi\varepsilon_0) = 0$ is satisfied for a wavelength that is red shifted plasmon resonance for a sphere and alternatively it is blue shifted for oblate sphere. However, the resonance defined here is due to the excitation of electric field along the major axis of the spheroids. On the other hand, the plasmon resonance related to the minor axis is found to be blue and red shifted compared to the wavelength of a spherical particle in case of prolate and oblate sphere respectively. As most SERS active metals exhibit free electron like behaviour at longer wavelength, the maximum contribution to SERS owes from the red shifted plasmon resonance. Thus, larger SERS intensities is gained from non-spherical (prolate or oblate) particles over the spherical one.

(c) Collective Resonances

The classical surface plasmon enhancement calculations are precisely associated with the collective interactions between the resonating structures. The weak and strong coupling between the resonances may arise depending upon the interparticle distances. If the interparticle distance is very small, then coupling and the appearance of new resonance frequency is taken into place. Relatively weak coupling and shifts in resonance frequency arises due to large interparticle separations. Moskovits [38] reported that the collective resonances are bumps on the metallic surface and the resonance frequency is dependent upon the bump density. According to the Maxwell-Garnett theory, the bumpy surface is assumed as a transition layer of metal spheres

having dielectric constant $\bar{\varepsilon}(\omega)$ in a dielectric matrix whose dielectric constant is ε_0. The effective dielectric constant $\bar{\varepsilon}(\omega)$ is estimated by evaluating the following equation,

$$\frac{\bar{\varepsilon}(\omega)-\varepsilon_0}{\bar{\varepsilon}(\omega)+2\varepsilon_0}=q\frac{\varepsilon(\omega)-\varepsilon_0}{\varepsilon(\omega)+2\varepsilon_0} \qquad (1.23)$$

where, q is the volume fraction of the composite material filled with metal spheres. According to Marton and Lemon, the singularity in $\bar{\varepsilon}(\omega)$ is known as "conduction resonance" [39]. In case of coupled dipole mode of all spheres having resonant frequency ω_R, where ω_R satisfies the equation,

$$\varepsilon(\omega_R)=-\epsilon_0\frac{2+q}{1-q} \qquad (1.24)$$

As $q \to 0$, equation (1.24) becomes,

$$\varepsilon(\omega_R)+2\epsilon_0=0 \qquad (1.25)$$

Considering $\varepsilon(\omega)=\varepsilon_b-\frac{\omega_p^2}{\omega^2}$, where ε_b and $-\frac{\omega_p^2}{\omega^2}$ stands for the inter band and the free-electron contribution respectively, the expression for the resonance wavelength λ_R, as obtained by Moskovits is [38]

$$\lambda_R=\lambda_P\left(1+\varepsilon_b+\frac{2+q}{1-q}\right)^{\frac{1}{2}} \qquad (1.26)$$

where, $\lambda_p=\frac{2\pi c}{\omega_p}$.

With the increase of q, λ_R moves towards infinity. The expression for the intensity "I" of pre-resonantly enhanced Raman scattering in terms of the stokes frequency (ω), resonance frequency (ω_R) and excitation frequency (ω_L) can be written as,

$$I\sim\left[\frac{\omega^2(\omega_L^2+\omega_R^2)}{(\omega_R^2-\omega_L^2)}\right]^2 \qquad (1.27)$$

Di Lella *et. al*. [40] have reported the frequency dependence of the imaginary part of $\bar{\varepsilon}(\omega)$ for q = 0.5 and ε = 1 in order to measure the possible classical enhancement of bumpy films. Considering the induced dipole moments in the metal islands as point dipoles, Burstein and Chen *et. al*. [41] reported the collective resonances in metal island films on a substrate. They also allowed the contribution from the image dipoles in a dielectric substrate and from the dipoles of neighbouring islands towards the local field of a given island.

Weitz et. al. proposed a different approximation regarding the electromagnetic enhancement G for adsorbates on island films. If $A(\omega)$ is the absorption of the island film, then $A(\omega)$ have the following representation,

$$A(\omega) = qd\varepsilon_2(\omega)\frac{\omega}{c}\frac{\left|\overline{E}_{in}\right|^2}{|E_0|^2} \qquad (1.28)$$

where, q is the volume fraction of silver in the film having effective thickness d. E_0 represents the incident field strength and $\left|\overline{E_{in}}\right|^2$ denotes the effective average field intensity inside the islands. If $\varepsilon\overline{E}_{in}$ be the local field at the surface of the island outside the metal, then neglecting the field components that is parallel to the surface, the expression for G will be,

$$G \approx \frac{c^2}{q^2d^2}A(\omega_L)A(\omega)F \qquad (1.29)$$

where,

$$F = \frac{|\varepsilon(\omega_L)|^2|\varepsilon(\omega)|^2}{\varepsilon_2(\omega_L)\varepsilon_2(\omega)\hbar\omega_L\hbar\omega} \qquad (1.30)$$

(d) Quadrupole Polarizability Mechanism

In case of SERS enhancement, it is well known that the enhancement of the electromagnetic fields that arises due to the LSPR is dominant. Though there are several calculations regarding this EM mechanism applying electrodynamics methods and considering bulk dielectric constant, the EM mechanism can be well described by the dipole polarization concept. However, there are some experimental results which endorse the involvement of other factors. According to Moskovits *et. al*. [42], The existence of the enhanced field derivatives could have the potency to direct the enhanced SERS through the quadrupole-dipole term from the expression of the induced dipole moment. The kth component of the induced moment μ_k is related to the multipole polarizabilities as,

$$\mu_k = \alpha_{km}E_m + \frac{1}{3}A_{kmn}\frac{\partial E_n}{\partial x_m} + \frac{1}{\omega}G_{km}H_m + \cdots \qquad (1.31)$$

where α_{km}, A_{kmn} and G_{km} are the elements of the dipole-dipole polarizability tensor, dipole-quadrupole polarizability tensor and dipole-magnetic-dipole polarizability respectively and the corresponding expressions are given below,

$$\alpha_{km} = \sum_j \frac{H(\omega)(\langle i|\mu_k|j\rangle\langle j|\mu_m|f\rangle)}{\hbar} \qquad (1.32)$$

$$A_{kmn} = \sum_j \frac{H(\omega)(\langle i|\mu_k|j\rangle\langle j|\theta_m|f\rangle)}{\hbar} \qquad (1.33)$$

$$G_{km} = \sum_{j} \frac{H(\omega)(\langle i|\mu_k|j\rangle\langle j|M_m|f\rangle)}{\hbar} \qquad (1.34)$$

In the above expressions, $H(\omega) = \omega_{ij}/(\omega_{ij}^2 - \omega^2)$. μ and θ are molecular electric dipole and quadrupole respectively and M is the magnetic dipole operator. Here i and j represent the initial and final states of the system. According to the report of Campion *et. al*. [43], the ratio of the forbidden a_{2g} to allowed a_{1g} modes of benzene was independent of excitation wavelength when benzene was adsorbed on the flat silver surface. They observed that, near the silver surface, the field derivative should be large while the non-existence of field derivative implies that the molecules are not localized at the desired position at where the field derivative will be large.

Since, Campion's experiment deals with flat surface, so the field derivative effect will absent in case of the typical SERS experiments which are performed with the surfaces that exhibit significant curvature. In that condition, there should be the existence of another mechanism where the field gradient term can contribute. Tian *et. al*. [44] suggested that the strongest enhancement is found for molecules placed at the top of a cone and a rapid decrease of the enhancement factor is experienced with the increasing distance from the surface of the metallic nanoparticles. The SERS EF is strongly dependent on the type of roughness that is subject to the curvature of the surface. Thus, the quadrupole interaction is stronger than the dipole interaction in case of very sharp roughness.

(e) Multipolar Enhancement Mechanism

When a SERS active substrate is excited at the resonance frequency, the field is enhanced which in turn produces an enhanced Raman signal from the molecule. When a molecule is trapped within the narrow intermediate space of two curved metallic surfaces, it would produce an enhanced Raman signals in the visible optical region. The dipolar approximation fails in the case of edge-to-edge separations between two spheres of same size smaller than their radius. In that situation the excitation of higher order multipoles should be considered [45].

Let's assume that a molecule is labelled with index i = 2 at z = 0 placed in between two spheres centered at z = -D and z = D. The two spheres are labelled as i = 1 and i = 3 respectively. If a system of two identical spheres are excited by an external electric field E_0 parallel to the z axis at frequency ω, the local electric field at the site of the molecule is expressed in terms of the multipolar moments as,

$$E_L(\omega) = E_0 + \sum_{l=1}^{\infty} \sqrt{\frac{4\pi}{2l+1}}(l+1)\left[\frac{q_{l,1} + (-1)^{l+1} q_{1,3}}{D^{l+2}}\right] \qquad (1.35)$$

where, $q_{l,i}$ is the multipolar moments and has the following representation,

$$q_{l,i} = F_{l.i} + \sum_{l',i'} B_{l,i}^{l',i'} q_{l',i'} \qquad (1.36)$$

where i, i' label the particles, and l, l' are indices labelling the pole order that extends over all positive integers. The coupling coefficients are expressed by the following relation,

$$B_{l,i}^{l',i'} = (-1)^{k+l'+1} \sqrt{\frac{2l+1}{2l'+1}} \frac{(l+l')!}{l!\, l'!} \frac{\alpha_{i,i}(1-\delta_{ii'})}{|z_i - z_{i'}|^{l+l'+1}} \qquad (1.37)$$

$$k = \begin{cases} 0 & \text{if } z_i < z_{i'} \\ l & \text{if } z_i > z_{i'} \end{cases} \qquad (1.38)$$

where, δ and $\alpha_{l,i}$ represent the Kronecker delta and the l- polar polarizability of particle i respectively. $F_{l.i}$ is the external electric field and is represented as,

$$F_{l,i} = \sqrt{\frac{3}{4\pi}} a_{l,i} E_0 \delta_{l.1} \qquad (1.39)$$

In comparison with the dipolar contribution, if $E_L(\omega)$ represents the local field, then, $E_L(\omega) = g_1(\omega)E_0$. where, where $g_1(\omega)$ is given by,

$$g_1(\omega) = 1 + \sum_{l=1}^{\infty} \sum_{i=1}^{3} \frac{(l+1)a^l \alpha_{1,i}}{D^{l+2} a_i} \left[(T^{-1})_{l,1}^{1,i} + (-1)^{l+1} (T^{-1})_{l,3}^{1,i}\right] \qquad (1.40)$$

Here T^{-1} is the inverse of the matrix T defined as:

$$T_{l,i}^{l',i'} = \delta_{l,l'}\delta_{i,i'} - \tilde{B}_{l,i}^{l',i'} \qquad (1.41)$$

Here $\alpha_{l,i}$ is the dipole polarizability and a_i is the radius of the particle i. The inelastic dipole polarizability $\alpha_m^I(\omega_R, \omega)$ is related to the dipole moment $p_m(\omega_R)$ as,

$$p_m(\omega_R) = \alpha_m^I(\omega_R, \omega) g_1(\omega) E_0 \qquad (1.42)$$

where, $g_1(\omega)$ denotes the fully multipolar field factor for the three particles. The total dipole moment for the Raman signal is the sum of the dipole moments included in the three particles at frequency ω_R. Thus, the total dipole moment can be written as,

$$p(\omega, \omega_v) = g_1(\omega) g_2(\omega_R) \alpha_m^I(\omega_R, \omega) E_0 \qquad (1.43)$$

where, $g_2(\omega_R)$ has the following expression,

$$g_2(\omega_R) = 1 + \sum_{l=1}^{\infty}\sum_{i=1}^{3}\sum_{l'=1}^{3}\frac{a_1}{a_2}\left(S^{-1}\right)_{l,i}^{l,i'}\ \tilde{B}_{l,i'}^{1,2} \qquad (1.44)$$

where, the inverse S matrix $\left(S^{-1}\right)_{l,i}^{l,i'}$ is defined as,

$$\tilde{S}_{l,i}^{l',i'} = \delta_{l,l'}\ \delta_{i,i'}\ - \tilde{D}_{l,i}^{l',i'} \qquad (1.45)$$

$$\tilde{D}_{l,i}^{l',i'} = \tilde{B}_{l,i}^{l',i'} + \sum_{k=2}^{L}\tilde{B}_{l,i}^{k,2}\tilde{B}_{k,2}^{l',i'} \quad (1.46)$$

Thus, the expression of overall EF of Raman intensity now includes the contribution of multipoles of all order and the representation of this overall enhancement is,

$$G = |g_1(\omega)g_2(\omega_R)|^2 \qquad (1.47)$$

(f) Radiation Enhancement Mechanism: Dipole Re-Radiation Theory

In SERS, radiation due to an oscillating dipole $\vec{p}_m(\omega_R, \vec{r}_m)$ are remarkably affected by the dielectric properties of its surroundings [46,47]. The overall SERS enhancement is approximately, the product of the incident and Raman enhancement processes. For plasmonic nanostructures, the total power P_{Total} radiated by the oscillating dipole $\vec{p}_m(\omega_R, \vec{r}_m)$ is represented by [48],

$$P_{Total}(\omega_R, \vec{r}_m) = \frac{1}{2}\omega_R \mathrm{Im}\left[\vec{p}_m^{*}(\omega_R, \vec{r}_m)\cdot\vec{E}_m(\omega_R, \vec{r}_m)\right] \qquad (1.48)$$

where, $\vec{E}_m(\omega_R, \vec{r}_m)$ denotes the local field generated by the oscillating dipole $\vec{p}_m(\omega_R, \vec{r}_m)$ in presence of a plasmonic nanostructure. The total power P_{Total} at Raman scattered frequency ω_R is dissipated as radiative power (P_{Rad}) and non-radiative power (P_{NR}). Thus,

$$P_{Total}(\omega_R, \vec{r}_m) = P_{Rad} + P_{NR} \qquad (1.49)$$

The Raman radiation field $\vec{E}_R(\omega_R, \vec{R})$ at the observer coordinate R in the far field is consisted with $\vec{E}_m(\omega_R, \vec{R})$ and $\vec{E}_{DR}(\omega_R, \vec{R})$ such that,

$$\vec{E}_R(\omega_R, \vec{R}) = \vec{E}_m(\omega_R, \vec{R}) + \vec{E}_{DR}(\omega_R, \vec{R}) \qquad (1.50)$$

where, $\vec{E}_m(\omega_R, \vec{R})$ represents the field emitted from the molecular oscillating dipole $\vec{p}_m(\omega_R, \vec{r}_m)$ and $\vec{E}_{DR}(\omega_R, \vec{R})$ is the secondary field or the dipole re-radiation field scattered from the nanostructure which is excited by $\vec{p}_m(\omega_R, \vec{r}_m)$.

The measured Raman intensity integrated all over the solid angle is given by,

$$P_{Rad} = \oiint \frac{1}{2}\,\mathrm{Re}\{\overrightarrow{E_R}(\omega_R, \vec{R}) \times \overrightarrow{H_R^{*}}(\omega_R, \vec{R})\}\,.\,\vec{n}\,ds \qquad (1.51)$$

The Joule heat dissipated in the plasmonic structures of volume V and conductivity σ is known as non-radiative power and is given by,

$$P_{NR} = \iiint \frac{1}{2} \mathrm{Re}\{\sigma \vec{E}(\omega_R, \vec{r}) \cdot \vec{E}^*(\omega_R, \vec{r})\} dv \qquad (1.52)$$

So, the power of the total Raman-scattered radiation (P_{Rad}) over all the solid angles is represented by,

$$P_{Rad} = \frac{1}{2}\omega_R \mathrm{Im}[\vec{p}_m^*(\omega_R, \vec{r}_m) \cdot \vec{E}_m(\omega_R, \vec{r}_m)] - \frac{1}{2}\iiint \mathrm{Re}\{\sigma \vec{E}(\omega_R, \vec{r}) \cdot \vec{E}^*(\omega_R, \vec{r}_m)\} dv \qquad (1.53)$$

The radiant power from the oscillating dipole $\vec{p}_m(\omega_R, \vec{r}_m)$ in the absence of plasmonic nanostructure is given by,

$$P_0 = \frac{1}{2}\omega_R \mathrm{Im}[\vec{p}_m^*(\omega_R, \vec{r}_m) \cdot \vec{E}_m'(\omega_R, \vec{r}_m)] \qquad (1.54)$$

where, $\vec{E}_m'(\omega_R, \vec{r}_m)$ is the virtual local field at $\vec{r}_m$ and arises due to the isolated oscillating dipole $\vec{p}_m(\omega_R, \vec{r}_m)$ in the absence of any plasmonic nanostructure.

The exact expression for the radiation enhancement is,

$$M_{Rad}(\omega_0, \vec{r}_m) = \frac{P_{Rad}}{P_0} \qquad (1.55)$$

If $\vec{E}_{local}(\omega_R, \vec{r}_m)$ is the local field produced by a plane wave-light field $\vec{E}_0(\omega_R, \vec{r}_m)$ at frequency ω_R, then using the optical reciprocity theorem, M_{Rad} is denoted as,

$$M_{Rad}(\omega_0, \vec{r}_m) \approx \left| \frac{\vec{E}_{local}(\omega_R, \vec{r}_m)}{\vec{E}_0(\omega_R, \vec{r}_m)} \right|^2 \qquad (1.56)$$

The SERS EF at $\vec{r}_m$ can be represented by,

$$EF(\omega_0, \omega_R, \vec{r}_m) = M_{loc}(\omega_0, \vec{r}_m) M_{Rad}(\omega_R, \vec{r}_m) \qquad (1.57)$$

Assuming, the frequency of the Raman scattered light is very close to that of the incident light, the above equation is simplified as,

$$EF(\omega_0, \omega_R, \vec{r}_m) \approx \left| \frac{\vec{E}_{local}(\omega_0, \vec{r}_m)}{\vec{E}_0(\omega_0, \vec{r}_m)} \right|^4 \cdot \left| \frac{\vec{E}_{local}(\omega_R, \vec{r}_m)}{\vec{E}_0(\omega_R, \vec{r}_m)} \right|^4$$

$$\approx \left| \frac{\vec{E}_{local}(\omega_0, \vec{r}_m)}{\vec{E}_0(\omega_0, \vec{r}_m)} \right|^4 \qquad (1.58)$$

The above equation represents the well known $|E|^4$ approximation that is usually obeyed to evaluate the SERS EF.

(g) Recent Developments on the EM Mechanism of SERS

In case of closely packed metallic or plasmonic nanoparticles, coupling between the individual plasmon oscillations can occur via near-field interactions. As a result, the LSPs are generated that can control the electric field distributions around the plasmonic nano particles. SERS is a near-field phenomena which is recorded in the far-field region. To find an interrelation between the near-field LSPR generated within the individual plasmonic nanostructures with the enhancement of the far-field, a new optical technique has been introduced. Unfortunately, there are only few numbers of exiting literatures on this area of research work. In 2016, Prof. G. C. Schatz and Prof. R. P. Van Duyne collaboratively encountered the high-resolution distance dependent investigation of SERS by atomic layer deposition [49]. In a separate report, they have investigated the relationships between the near-field and far-field phenomena for three dimensional SERS active substrates through the integration of experimental and theoretical approaches [50,51]. Moreover, Prof. R. P. Van Duyne *et. al*. reported the SERS spectra of analyte molecules from periodically ordered substrates fabricated by nanosphere lithography technique [52,53]. Furthermore, Van Duyne *et. al*. also showed that the best SERS enhancement can be attained with the excitation wavelength lying on the blue edge of the LSPR band, roughly separated by one half from the wavelength of the vibrational energy mode [54,55]. Also, there are few more available investigations reporting the generation of maximum SERS enhancement from the analyte-nanoparticle system with the irradiation of low excitation energy [56-59].

The spatial distributions of electric field around the nano aggregated domains have been further utilized to estimate the SERS EF following the dipole reradiation (DR) theory and Plane Wave (PW) approximation method. Furthermore, the T- matrix formalism has been incorporated in the Lorentz-Mie theory for the estimation of the EF from both the PW and DR approximation [60]. The PW approximation expresses the SERS EF $G(\bar{\upsilon}, \bar{\upsilon}')$ as the product of electric field intensities incident at wavenumber "$\bar{\upsilon}$" [$\left|\vec{E}_{loc}(\vec{r}_0, \bar{\upsilon})\right|^2$] and the other at Stokes shifted wavenumber "$\bar{\upsilon}'$" [$\left|\vec{E}_{loc}(\vec{r}_0, \bar{\upsilon}')\right|^2$] for the location of the molecule fixed at $\vec{r}_0$ as [61,62]

$$G(\bar{\upsilon}, \bar{\upsilon}') = \left|\vec{E}_{loc}(\vec{r}_0, \bar{\upsilon})\right|^2 \left|\vec{E}_{loc}(\vec{r}_0, \bar{\upsilon}')\right|^2 \qquad (1.59)$$

For zero Stokes shift approximation the expression (1.59) is further reduced to

$$G(\bar{\upsilon}, \bar{\upsilon}') = \left|\vec{E}_{loc}(\bar{\upsilon})\right|^4 \qquad (1.60)$$

Thus, the SERS EF approximately scales as fourth power of the local electric field intensity incident at wavenumber "$\bar{\upsilon}$". It is often considered that the PW deals with both the incident and Stokes shifted photons. Albeit, $\left|\vec{E}_{loc}(\omega)\right|^2$ denotes the EF of the incident photon, the EF due to the emitted photon is associated with the emission of radiation by an induced dipole in the molecular location at the Stokes shifted frequency. The plasmon enhancement in the far-field arises due to the interaction of the emitted radiation with the nanoparticles. This is called the dipole reradiation (DR) theory and under quasistatic approximation the EFs that are obtained using the DR and PW approximation are similar in case of spherical particles.

According to the DR theory, the EF in the far-field region can be estimated by,

$$G(\theta_s, \varphi_s) = \frac{\left|\vec{F}_R(\theta_s, \varphi_s)\right|^2}{\left|\vec{F}_{R,0}(\theta_s, \varphi_s)\right|^2} \qquad (1.61)$$

where, the far-field amplitude of the molecule/ particle system is represented by $\vec{F}_R(\theta_s, \varphi_s)$ while $\vec{F}_{R,0}(\theta_s, \varphi_s)$ denotes the corresponding far-field amplitude of the scattered radiation from an isolated molecule.

Mueller *et. al*. reported the plasmonic enhancement of SERS by encapsulating the sexithiophene (6T) molecule into the carbon nanotubes (CNTs) deposited on gold nanodimers. The as fabricated substrate provides $\sim 10^6 - 10^7$ orders of EM enhancement when it was excited in resonance with the LSPR of the as prepared gold nanodimer [63].

Gupta *et. al*. reported a simple technique to generate electromagnetic hotspot by so called "plasmonic patch" that was fabricated by adsorbing a transparent elastomeric film (say PDMS) with gold/ silver nanostructures. They have transferred the as fabricated plasmonic patch on a normal SERS substrates and SERS-inactive gold mirror. This technique provides a higher SERS enhancement with 100-fold increase in the limit of detection from the regular SERS substrates and even from the SERS-inactive gold mirror. The investigation of the EM hotspots using finite-difference time domain (FDTD) simulations is in harmony with the experimental outcomes [64].

Ameer *et. al*. reported a cost effective, rapid and reproducible non-lithographic technique to modify the shape of silver nanoparticles which results a red-shift in the LSPR spectrum and opens new surface area due to which the Raman probe molecules could attach with the silver nanoparticles. The SERS experiment was performed using 2 Mercapto benzimidazole as Raman

probe and the 632.8 nm laser line was used as excitation source. The enhancement of the Raman signal was estimated of the order $\sim 10^5 - 10^8$ from the as-prepared substrates [65].

Shaikh *et. al*. reported the fabrication of robust SERS active substrate using Ag nanoparticles (AgNPs) with various size and surface coverage. The nanoparticles are grown on large area glass substrate using cost effective successive ionic layer adsorption and reduction (SILAR) method. By changing the reduction time and deposition cycle, the size and coverage of the AgNPs can be altered. At higher growth cycles, the AgNPs became non-spherical which in turn generates an intense quadrupole plasmon resonance. The efficacy of the SERS active substrates is tested with Rhodamine 6G (R6G) and Methylene Blue molecules. The substrates provide an EM enhancement $\sim 10^7$ orders of magnitude towards the total SERS EF of $\sim 10^9$ [66].

Nam *et. al*. reported SERS enhancement of R6G and Crystal Violet (CV) molecule by adding SiO_2 nanoparticles (SiO_2NPs) with Au nanorods (AuNRs) in liquid state. Using FDTD simulation studies they have showed that the SiO_2NPs can produce an increased dipolar electric resonance due the interaction of the surface plasmon of the AuNRs. For both the Raman analytes the AuNRs/ SiO_2NPs system exhibits the detection limit upto $\sim 10^{-10}$ M [67].

Fularz *et al*. reported a composite of ZnO nanowire and AgNPs that can deliver higher SERS enhancement due to the LSPR excitation. Introduction of point defect in the ZnO lattice of the nanocomposites by the heat treatment method in oxygen surroundings also allows the effective charge transfer enhancement. They have reported a considerable amount of enhancement (up to 5-fold) in the relative peak intensity from the heat treated ZnO NW/ Ag NPs composite [68].

Recently, Rastogi *et. al*. used the nanopatterned lithographic technique for the development of a robust SERS active substrate containing gold nano pillar arrays (Au-NPA). Also, the interpillar distances between the Au-NPAs (called hotspots) were tuned down to < 10 nm regime. The 3D-FDTD simulation studies have been used to envisage the electric field distributions around the as fabricated Au-NPAs which shows good agreement with the experimentally observed data. [69].

Wang *et. al*. reported a facile fabrication of an efficient SERS active substrate containing polymethyl methacrylate (PMMA) film attached with plasmonic AgNPs. The close arrangement of AgNPs in the as-fabricated PMMA/ AgNP substrate can generate a large amount of plasmonic hot spots which produces an excellent SERS performance that can detect parathion (PT) and

fenitrothion (FNT) at minimum detection limit of 10^{-9} M and 10^{-10} M with enormous enhancement factor of 10^8 and 10^9 orders of magnitude respectively [70].

(B) Chemical Enhancement Mechanism

However, the magnitude of the EM enhancement has the dominant contribution to SERS compared to the chemical (CHEM) enhancement, the role of the CHEM enhancement is quite important as it can explain the selective enhancement, broadening and / or significant shift of Raman bands in the SERS spectra of the analyte molecules in comparison to their NRS counterpart that can't be determined from the EM enhancement mechanism. The presence of this CHEM mechanism was first proposed by Gersten *et. al*. [71] in 1979. They have suggested an electron tunnelling phenomenon between the metal and the molecular surface that produces a resonance at a point in the proximity of the Fermi surface. Later they have called this mechanism as "chemical" or charge transfer (CT) mechanism. The CHEM mechanism owes to the transfer of an electron from the Fermi level (E_F) of the nanostructured substrate to the HOMO or LUMO of the adsorbed analyte or vice versa.

(a) Charge Transfer (CT) Theory of SERS

The Raman transition term belonging to the components of the polarizability tensor is quite important to understand the selective enhancement of the various vibrational modes of the adsorbed Raman probe molecules associated to various irreducible representations.

The intensity of Raman transition is expressed as:

$$I = \left[8\pi(\omega \pm \omega_{I'I})^4 \frac{I_L}{9c^4}\right] \sum \alpha_{\sigma\rho}^2 \qquad (1.62)$$

where, I_L is the incident laser intensity. ω and $\omega_{I'I}$ denote the frequency of the incident laser and the molecular transition frequency between the states I and I′ respectively. $\alpha_{\sigma\rho}$ represents the polarizability tensor element and the subscripts σ and ρ signify the three directions (x, y, z) in the Euclidean space. In case of surface plasmon resonance, if $g(\epsilon)$ is a function of the complex dielectric function $\epsilon(\omega)$ of the corresponding medium, then

$$g(\epsilon) = \frac{[\epsilon(\omega) - \epsilon_0]}{[\epsilon(\omega) + 2\epsilon_0]} \qquad (1.63)$$

Using the 2nd order perturbation theory, the $\alpha_{\sigma\rho}$ can be expressed as,

$$\alpha_{\sigma\rho} = \sum_{S \neq I,I'} \left\{ \frac{\langle I|\mu_\sigma|S\rangle\langle S|\mu_\rho|I'\rangle}{E_S - E_I - \hbar\omega} + \frac{\langle I|\mu_\rho|S\rangle\langle S|\mu_\sigma|I'\rangle}{E_S - E_I + \hbar\omega} \right\} \qquad (1.64)$$

Here μ represents the dipole moments operator, S denotes all the excited states of the system and σ, ρ are the direction of the scattered and incident polarization. The equation (1.64) is known as the Kramer, Heisenberg and Dirac (KHD) expression of the polarizability tensor for molecule-metal system [72,73]. All the vibronic states (I, I' and S) can be signified as:

$$|I\rangle = |I_e\rangle|i\rangle \qquad (1.65\ a)$$

$$|I'\rangle = |I_e\rangle|f\rangle \qquad (1.65\ b)$$

$$|S\rangle = |S_e\rangle|k\rangle \qquad (1.65\ c)$$

where, the subscript e in the above representations indicate purely electronic state and $|i\rangle$, $|f\rangle$ and $|k\rangle$ denotes the vibrational wave functions. According to Albrecht [74], the polarization tensor components ($\alpha_{\sigma\rho}$) is a sum of three terms called A, B and C and to obtain the expression of $\alpha_{\sigma\rho}$ he used the Herzberg- Teller (HT) mixing of vibronic functions that can be written as:

$$|S\rangle = |S_e, 0\rangle + \sum \lambda_{SR} Q |R_e, 0\rangle \qquad (1.66)$$

In the above expression, λ_{SR} have the following representation,

$$\lambda_{SR} = \frac{h_{SR}}{(E_R^0 - E_S^0)} \qquad (1.67)$$

where,

$$h_{SR} = \left\langle S_e, 0 \left| \left(\frac{\partial V_{eN}}{\partial Q}\right)_0 \right| R_e, 0 \right\rangle \qquad (1.68)$$

In equation (1.68), V_{eN} denoted the electron- nuclear attraction term within the Hamiltonian which is estimated at the equilibrium nuclear positions. For, truly electronic transition moment between states,

$$\mu_{SI}^{\sigma} = \langle S_e|\mu^{\sigma}|I_e\rangle \qquad (1.69\ a)$$

$$\mu_{RI}^{\sigma} = \langle R_e|\mu^{\sigma}|I_e\rangle \qquad (1.69\ b)$$

$$\mu_{SR}^{\sigma} = \langle S_e|\mu^{\sigma}|R_e\rangle \qquad (1.69\ c)$$

Moreover, according to Albrecht [74], the polarization tensor elements ($\alpha_{\sigma\rho}$) can be represented under RR conditions as follows:

$$\alpha_{\sigma\rho} = A + B + C \qquad (1.70)$$

where, the term A represents the Franck-Condon (FC) contribution, whereas the terms B and C together signify the HT contributions and are known to be responsible for the selective enhancement of the Raman bands through molecule to metal CT and metal to molecule CT respectively [75-77]. The term A, B, C have the following expressions,

$$A = \sum_{S=F,K\neq I} \sum_{k} \left[\frac{\mu_{SI}^{\sigma}\mu_{SI}^{\rho}}{\hbar(\omega_{SI} - \omega)} + \frac{\mu_{SI}^{\rho}\mu_{SI}^{\sigma}}{\hbar(\omega_{SI} + \omega)} \right] \langle i|k\rangle\langle k|f\rangle \qquad (1.71)$$

$$B = \sum_{R=F,K} \sum_{S=F,K} \sum_{k} \left[\frac{\mu_{IR}^{\sigma} h_{RS} \mu_{SI}^{\rho}}{\hbar(\omega_{RI} - \omega)} + \frac{\mu_{IR}^{\rho} h_{RS} \mu_{SI}^{\sigma}}{\hbar(\omega_{RI} + \omega)} \right] \frac{\langle i|k\rangle\langle k|Q_k|f\rangle}{\hbar\omega_{RS}}$$
$$+ \sum_{R=F,K} \sum_{S=F,K} \sum_{k} \left[\frac{\mu_{IS}^{\sigma} h_{SR} \mu_{RI}^{\rho}}{\hbar(\omega_{RI} - \omega)} + \frac{\mu_{IS}^{\rho} h_{SR} \mu_{RI}^{\sigma}}{\hbar(\omega_{RI} + \omega)} \right] \frac{\langle i|Q_k|k\rangle\langle k|f\rangle}{\hbar\omega_{RS}} \qquad (1.72)$$

$$C = \sum_{R=F,K} \sum_{S=F,K} \sum_{k} \left[\frac{\mu_{IR}^{\sigma} h_{IS} \mu_{SR}^{\rho}}{\hbar(\omega_{RI} - \omega)} + \frac{\mu_{IR}^{\rho} h_{IS} \mu_{SR}^{\sigma}}{\hbar(\omega_{RI} + \omega)} \right] \frac{\langle i|k\rangle\langle k|Q_k|f\rangle}{\hbar\omega_{RS}}$$
$$+ \sum_{R=F,K} \sum_{S=F,K} \sum_{k} \left[\frac{\mu_{SR}^{\sigma} h_{IS} \mu_{IR}^{\rho}}{\hbar(\omega_{RI} - \omega)} + \frac{\mu_{SR}^{\rho} h_{IS} \mu_{IR}^{\sigma}}{\hbar(\omega_{RI} + \omega)} \right] \frac{\langle i|Q_k|k\rangle\langle k|f\rangle}{\hbar\omega_{RS}} \qquad (1.73)$$

where, the transition dipole moment between states $|I\rangle$ and states $|S\rangle$ are represented by μ_{SI}^{σ} and μ_{SI}^{ρ} respectively. ω and ω_{RI} denote the incident laser frequency and the frequency of the molecular transition between state $|I\rangle$ and $|R\rangle$ respectively. h is the HT matrix element and Q_k represent the normal mode of vibration. The term A is usually related to the RR spectroscopy. So, if the excitation is far away from the resonance, the numerator of the term A vanishes and if the excitation is on resonance, the enhancement confines for the totally symmetric normal modes of vibration of the molecule.

If the incident light wave is not only in resonance with the surface plasmon but also for a charge-transfer transition in the molecule-metal system, the A term splits into two terms, A_f and A_k. In that case the corresponding expressions are as follows:

$$A_f = \left(\frac{2}{\hbar}\right) \mu_{FI}^{\sigma}\mu_{FI}^{\rho} \langle i|k\rangle\langle k|f\rangle \frac{\omega_{FI} + \omega_f}{(\omega_{FI} + \omega_f)^2 - \omega^2} \qquad (1.74\ a)$$

$$A_k = \left(\frac{2}{\hbar}\right) \mu_{FK}^{\sigma}\mu_{FK}^{\rho} \langle i|k\rangle\langle k|f\rangle \frac{\omega_{FK} + \omega_f}{(\omega_{FK} + \omega_f)^2 - \omega^2} \qquad (1.74\ b)$$

$$B = -\left(\frac{2}{\hbar^2}\right)\sum_{K\neq I}\frac{\left[\mu_{KI}^{\sigma}\mu_{FI}^{\rho}+\mu_{KI}^{\rho}\mu_{FI}^{\sigma}\right](\omega_{KI}\omega_{FI}+\omega^2)h_{KF}\langle i|Q|f\rangle}{(\omega_{KI}^2-\omega^2)(\omega_{FI}^2-\omega^2)} \qquad (1.75)$$

$$C = -\left(\frac{2}{\hbar^2}\right)\sum_{K\neq I}\frac{\left[\mu_{KI}^{\sigma}\mu_{FK}^{\rho}+\mu_{KI}^{\rho}\mu_{FK}^{\sigma}\right](\omega_{KI}\omega_{FK}+\omega^2)h_{IF}\langle i|Q|f\rangle}{(\omega_{KI}^2-\omega^2)(\omega_{FK}^2-\omega^2)} \qquad (1.76)$$

The terms A_f and B are responsible for the molecule-to-metal transition whereas the term A_k and C correspond to the metal-to-molecule transition. But both the totally and non-totally symmetric modes are present in many SERS spectra. The term A corresponds to the totally symmetric modes in the spectra, while, the B and C terms are responsible for the enhancement of both totally and nontotally symmetric vibrations. Thus, both the terms B and C should be included in the expression of the polarization tensor element. If the metal-to-molecule CT (C) is considered then the corresponding representations regarding the molecule-to-metal CT (B) can also be found by interchanging the I and K. Figure 1.3 shows the state diagram of the molecule-metal system. Transitions from the molecular ground state $|I\rangle$ to some of the excited state $|K\rangle$ via μ_{IK} are allowed.

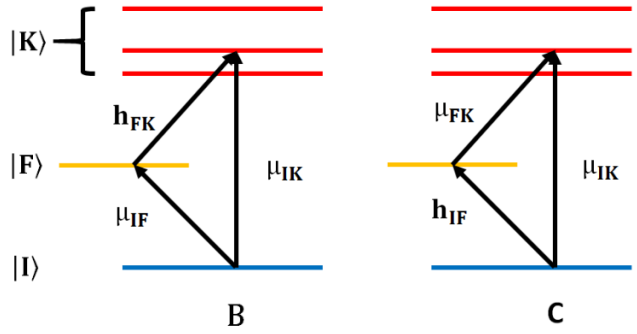

Figure 1.3: Schematic representation of the energy state-diagram of a molecule -metal system showing CT mechanism. $|I\rangle$ and $|K\rangle$ signify the molecular states, while $|F\rangle$ denotes the charge-transfer state.

In case of term B, a molecule to metal CT transition to the Fermi state $|F\rangle$ is allowed through μ_{IF}. The $|F\rangle$ and $|K\rangle$ states are linked via the HT vibronic coupling term h_{FK}. Similarly, for the C term, the metal to molecule CT transition from the Fermi state $|F\rangle$ is allowed through μ_{FK}. The $|F\rangle$ and $|I\rangle$ states are connected via the HT vibronic coupling term h_{IF}.

From equation (1.62), (1.63) and (1.76) the following expression can be attained:

$$R_{IFK}(\omega) = \frac{\mu_{KI}\mu_{FK}h_{IF}\langle i|Q_k|f\rangle}{[(\epsilon_1(\omega)+2\epsilon_0)^2+\epsilon_2^2][(\omega_{FK}^2-\omega^2)+\gamma_{FK}^2][(\omega_{IK}^2-\omega^2)+\gamma_{IK}^2]} \qquad (1.77)$$

where, ϵ_2, γ_{FK}, and γ_{IK} are the damping parameters. The CT enhancement factor of SERS is given by $|R_{IFK}(\omega)|^2$. The three different terms in the denominator have different resonance contributions

towards the SERS enhancement. The first term denotes the plasmon resonance at $\epsilon_1(\omega) = -2\epsilon_0$. The second term defines charge-transfer resonance arises at frequency $\omega = \omega_{FK}$. The third term signifies the molecular resonance at frequency $\omega = \omega_{IK}$. In the third case, the surface enhanced resonance Raman scattering [SE(R)RS] phenomena emerge only if the resonance condition is attained. The SERS EF is highly sensitive to the values of these three damping parameters. The numerator of the A, B and C term is quite important in order to estimate the CT contribution of SERS. In non-resonant condition the Albrecht's A term is non-vanishing if the dipole transition moments μ_{FK}^{σ}, μ_{FK}^{ρ} and the vibrational overlap integral (FC factors) $\langle i|k\rangle\langle k|f\rangle$ are simultaneously non-zero. At least any one of the following two conditions should be fulfilled for the non-vanishing FC factors:

(i) There must exist a displacement of the minima in the potential energy surfaces (PESs) of the two states involved in the transition $(\Delta Q_k \neq 0)$ along a given normal coordinate Q.

(ii) There must be an alteration in the curvature of the potential energy surface (PES) $[\Delta\nu_k \neq 0]$.

It is considered that the CT enhancement mechanism of SERS is similar to the RR process. Though, in SERS-CT, the transient exited state is a CT level of the metal-adsorbate (M-A) complex. From the exclusive point of view of the adsorbed molecule, the resonant process occurs between the ground state of the neutral molecule (singlet S_0 electronic ground state of the adsorbate) and the conforming anion (doublet D_0 electronic ground state of the adsorbate). If Q is the normal coordinate of the ground state, then the displacement (ΔR) between the PES minima of the S_0 and the D_0 states are expressed as:

$$\Delta Q = L^{-1}\Delta R \qquad (1.78)$$

where L^{-1} is the inverse of the normal mode matrix of the S_0 state. The as obtained values of ΔQ are used to estimate the relative intensities of Raman lines (I_i) under resonance conditions by employing the Peticolas equation [78]:

$$I_i = P\Delta Q_i^2 \nu_i^3 \qquad (1.79)$$

where, P is a constant and and ν_i signifies the vibrational frequency of the "*i*th" normal mode in the S_0 state. For the C term to be non-disappearing, the terms $\langle i|Q|f\rangle$, h_{IF}, μ_{KI} and μ_{FK} must be subsequently non-zero which is the major requirement for the HT surface selection rule. The simplified representation of this surface selection rule is:

$$\Gamma(Q_K) = \sum_K \Gamma\left(\mu_{CT}^{\perp}\right) \otimes \Gamma_K \qquad (1.80)$$

where $\Gamma(Q_K)$ denotes the irreducible representation of the vibrational signature corresponding to the SERS bands, $\Gamma\left(\mu_{CT}^{\perp}\right)$ represents the irreducible representation to which the element of the CT dipole moment perpendicular to the surface belongs in combined metal-molecule system, and Γ_K is the irreducible representation of the molecular excited state to which an optical transition $|I\rangle \rightarrow |K\rangle$ is allowed. The summation represents all the allowed, presumably lower-lying optical transitions.

(b) Recent Reports on Charge Transfer Mechanism of SERS

Aranda *et. al*. reported the selective enhancement of the SERS spectra of Pyridazine (PdZ) molecule adsorbed on a silver electrode and this selective enhancement corresponds to the metal-to-molecule CT mechanism from the metal-molecule system. A simultaneous enhancement of both the in-plane A_1 mode and out-of-plane B_1 modes is reported which suggests that both types of vibrations are operative via the Franck-Condon factors (i.e., the A term in the expression of the Raman polarizability tensor) [79].

Jafari *et. al*. reported the theoretical simulation of the SERS-CT spectra of different analyte molecules (such as, Pyrazinine, Para-Methylpyridine and Pyrimidine) adsorbed onto the silver clusters. The simulations have been done with the aid of density functional theory (DFT) using the excited state gradient approximation. With the change of the field, the selective enhancement and de enhancement of both the totally and non-totally symmetric vibrational modes were noticed which was in harmony with the experimental results. The nature of the SERS-CT spectra may be helpful to comprehend the character of the selective enhancements and to envisage the surface selection rules [80].

Fan *et. al*. proposed the fabrication of a highly sensitive semiconducting SERS active substrate with WO_{3-x} thin films. The amorphous and non-stoichiometric properties of WO_{3-x} stimulate the photo induced CT resonance between the substrates and the adsorbate molecules which results higher SERS activity. The efficacy of the substrate is tested with R6G molecule and the detection limit as estimated was below 10^{-9} M [81].

Guo *et. al*. reported the fabrication of two structures such as, TiO_2/ MBA/ CdS and CdS/ MBA/ TiO_2 in order to investigate the SERS-CT process at the interface between CdS and TiO_2 nanoparticles (NPs). 4-Mercaptobenzoic acid (4-MBA) is used as both the linker and the Raman

analyte. The CT direction of the two systems is from CdS to TiO_2 when the system is excited using 633 and 785 nm laser line. Introduction of CdS to the TiO_2/ MBA system and TiO_2 to the CdS/ MBA system results peak shift as well as change in intensities in the SERS spectra. The change in peak intensities in the two systems reveal different CT process. Moreover, the CT process between the CdS and TiO_2 is highly affected by the direction of the dipole moment of MBA molecule [82].

Jiang *et. al*. proposed the fabrication of SERS active substrate by photo catalytic reduction of Chloroauric acid ($HAuCl_4$) on TiO_2 NPs. 4-MBA was used as Raman probe molecule and a higher order of SERS enhancement is recorded from the Au-TiO_2 substrate due to the CT induced enhancement effect. This higher order of enhancement stems from the TiO_2-to-4MBA CT along with the additional contribution of CT by the LSPR of Au. The EF as estimated was $\sim 0.7 \times 10^4$ with the lowest detectable concentration of the 4-MBA molecule $\sim 1.0 \times 10^{-8}$ M [83].

Su *et. al*. reported fabrication of SERS active substrates using the organic-inorganic hybrid perovskites ($CH_3NH_3PbBr_3$) material. The potency of the as prepared SERS active substrates was tested with 4- Mercapto pyridine (4-MPy) and 6-Mercapto purine (6-MP) molecule and the EF from these two molecules of interest was estimated to be $\sim 2.1 \times 10^4$ and $\sim 1.4 \times 10^4$ respectively that corresponds to the CT mechanism [84].

Recently, Dao *et. al*. has been applied the SERS technique to understand the CT mechanism of the 2,4,5- trichlorophenoxyacetic acid (2,4,5-T) when it was adsorbed on silver substrate surface. Also, the DFT simulation has been employed simultaneously to envisage the metal-adsorbate interaction. Further, the CT mechanism has been encountered with the aid of frontier-orbital theory and the charge density difference mapping [85].

Zhang *et. al*. reported the fabrication of a novel SERS active substrate with In- doped CdO(ICO)NPs using different amount of In^{3+} doping elements. 4-MPy was used as SERS probe molecule and the SERS enhancement was dominated by the CT effect where the direction of the CT was from the ICO NPs towards the analyte 4-MPy molecule [86].

1.4.2 SERS active substrates

SERS active substrate is basically a metal surface with nanoscale characteristics. The overall enhancement of the SERS signal mainly depends upon the nature of the metal and the nanoscale characteristics of the substrate. An efficient SERS active substrate should have higher order of enhancement with good spectral reproducibility and uniformity. Though there are various

successful methods of preparing efficient SERS active substrates, the most popular and widely used methods are mentioned below.

(a) Electrochemically Roughened Electrodes

The fabrication of SERS active substrate on electrochemically roughened electrode is very simple and straightforward. Several methods are available in the literature to make the Au and Ag surface electrochemically rough in order to use as SERS active substrate [87,88]. The SERS enhancement and the surface roughness depend upon the rate and number of the oxidation-reduction cycle [87]. Also, the roughening procedure plays a significant role towards the generation of variable roughness features on the substrate surface which in turn affects the SERS signal [89].

(b) Colloidal nanoparticle substrates

This is the most popular method towards the fabrication of SERS active substrates for decades [90]. Chemical reduction and laser ablation are the most common procedure for the fabrication of colloidal nanoparticle substrates. The chemical reduction is relatively easier method, where metallic nanoparticles are formed by the reduction of metallic salt solution using a reducing agent. There are plenty of chemistries available in order to control the size, shape and aggregation of the nanoparticles. In this connection it is worth to mention that, the single molecule SERS [14] and the surface enhanced resonance Raman scattering [SE(R)RS] [13] were first reported using Ag nanoparticles. Albeit, this is a very simple method, but surface contamination and lack of reproducibility is the major drawback for this type of substrate.

(c) Non-Lithographic substrates

Several non-lithographic techniques are available for the fabrication of SERS active substrates. The basic phenomenon of non-lithographic template is to deposit a SERS active metal on an existing non-SERS active nanopatterned template. There are many processes for the coating of SERS active metals like self-assembly, plating, thermal deposition, electrochemical deposition etc. For the fabrication of SERS active substrate using non-lithographic method, the coating of metal films over polysterene (PS) [91,92] and silica [93] nanospheres have been established as a simple and effective method. Also, the use of various nanoporous substrates like porous gallium nitride (GaN) [94], porous Si [95,96], porous anodic aluminium oxide (AAO) [97,98] etc have been reported in non-lithographic technique. The fabrication of various nanospheres [99],

nanopillars [100,101], nanorods [102,103], nanodots [104] have been reported using the AAO templates.

(d) Lithographic substrates

There are numerous lithography-based methods among which the Electron beam lithography (EBL) [105-107] is a well-known technique for the fabrication of SERS active substrates due to its high level of control, remarkable spectral reproducibility and high enhancement. Now a days the EBL is a very useful technique as the size, shape and the interparticle spacing of various nanopatterns can be readily tuned in this technique. But for the large-scale production, the EBL technique may not be suitable for its low yield and high cost. The nanosphere lithography (NSL) technique [52,108,109] is relatively cost effective and Van Duyne and his co-workers are the pioneer to use this technique for the fabrication of SERS active substrate [110]. NSL is a bottom-up approach and it can produce various nanopatterns without any need of energy beam.

(e) Langmuir-Blodgett Film substrates

The Langmuir- Blodgett (LB) technique is a sophisticated and popular technique that can deposit single layer ultrathin nanostructured films with controlled layer structure. Since, the lithographic techniques are confined by the diffraction limit, the top-down formation of metallic nanoparticles towards the fabrication of robust SERS active substrates with controlled optical properties in the visible spectral region remains a matter of challenge. On the contrary, self-assembly of the molecules at the air water interface in the LB technique delivers a bottom-up fabrication process without these limitations. In the LB technique, a monolayer/ multilayer of amphiphilic molecules (e.g., Stearic acid, Poly(methyl) methacrylate, Arachidic acid) are deposited on a solid substrate by spreading them at the air-water interfaces.

LB technique was successfully applied by Prof. Ricardo Aroca *et al*. in their pioneering works where they have used the LB technique as an essential part of molecular architectures to design various SERS active substrates [111-118]. After that, Prof. Peidong Yang [119], and Surovtsev *et al*. [120] has been effectively utilized the LB technique for the monolayer assembly of aligned silver nanowires and nanomaterials.

Wang *et. al*. reported the fabrication of a SERS active substrate through the combination of nanosphere lithography and reactive ion etching techniques using Ag semi shell arrays with controlled diameter and tuneable interparticle spacing [121]. First, the LB technique was used to

deposit an ordered monolayer of polystyrene (PS) nanospheres with different sizes on glass substrates. Second, the size and the interparticle distances of the as deposited monolayers of PS nanospheres were altered using reactive ion etching method. Finally, a Ag layer with 30 nm thickness was evaporated onto the etched PS mask to obtain a SERS active substrate containing Ag films with periodic nanostructures.

Prof. M. A. El-Sayed *et. al*. successfully used the LB technique to assemble monolayers of gold nanocages with different percent of surface coverage [122]. Furthermore, they have also applied the LB technique to deposit the poly (p-phenylene ethynylene) [PPE] molecule onto the monolayers of gold nanocages. They have reported that the SPR band of the gold nanocages undergo significant red-shifts as the surface coverage of the gold nanocages increases. An explanation has been given regarding the red-shift of the surface plasmon band considering the existence of two plasmon fields (inside and outside of the gold nanocages) and is further substantiated with the aid of discrete dipole approximation (DDA) theory. Also, a plenty of recent reports are available where the LB technique has been successfully applied for the fabrication of SERS active substrate. [123-130].

(f) Recent Reports on SERS active substrates

Since the accidental discovery of SERS, fabrication of robust and reproducible SERS active substrates that can be readily used for trace analysis and ultrasensitive detection is one of the recent up-thirst on this exciting field of research. Recently, a plenty of research works are published concerning the fabrications of efficient SERS active substrates.

S. K. Das *et. al*. reported a simple procedure to fabricate a SERS active substrate by the coherent integration of Langmuir- Blodgett (LB) and self-assembly techniques. They have deposited 4-Cyano-4'Pentylbiphenyl (5-CB) nematic liquid crystal (LC) molecule by Langmuir-Reverse Schaefer (L-*R*Sh) method followed by the incubation of this as-deposited L-*R*Sh films into the gold nanocolloids for two different times. Self-assembly of the gold nanoparticles (Au NPs) onto the ordered 5-CB L-*R*Sh films creates segregated clusters and dendrimeric patterns of AuNPs which in turn may result the generation of hot spots correspond to the SERS enhancement. The SERS efficacy of the as prepared substrates was tested with 4-MPy molecule and the estimated relative standard deviation (RSD) $\leq$ 10% for the SERS bands 4-MPy signifies good spectral reproducibility of the substrates. The hidden parameters behind the enormous enhancement were

investigated using the Height-Height Correlation Factor (HHCF) and the phase trajectories. The chaotic pattern of the as prepared substrates was also estimated from the Lyapunov exponent [123].

Xu *et. al*. reported the fabrication of SERS active substrate by electrostatic assembly of silk nanoribbons (SNRs) and AuNPs to generate sandwich hot spot structures which can be developed by the alternation of SNRs and AuNPs ratio. 4- Aminothiophenol (4-ATP) was used as probe molecule to record the SERS spectra from the as prepared substrate. The estimated EF ~ 5.8×10^6 with sensitivity of 10^{-3} M and the RSD ~ 11.2 % proves the superiority of the substrate [131].

Mei *et. al*. designed an uniform 3D topography of AuNR- bridged silver coated gold (Au@Ag) SERS tags by using waxberry-like AuNPs as core and capping it by vertically oriented AuNR arrays. The surface of the AuNRs were blocked by thiol- ligands and the AgNPs were allowed to grow anisotropically on the tips of the AuNRs. This tends to form Ag-Ag and Au-Ag hotspots in a single NP which contributes to the higher SERS enhancement with analytical enhancement factor (AEF) of ~ 3.4×10^6. The ultrasensitive SERS tag was also used for thiram detection [132].

Barveen. *et. al*. reported the fabrication of a flexible and efficient SERS active substrate containing gld nanostars (AuNSs) and PMMA using photo reduction method. The SERS efficacy of the substrate was tested using R6G molecule. Moreover, the superiority of the as fabricated AuNSs/ PMMA SERS active substrate had been established through the detection of two antibiotics such as ciprofloxacin (CPX) and chloramphenicol (CAP) with high sensitivity, enormous enhancement factor ($\sim 2.03 \times 10^9$), lower detection limit ($\sim 3.41 \times 10^{-11}$ M), excellent reproducibility (< 7.32 %) and uniformity [133].

Yang *et. al*. reported the development of a novel SERS active substrate by using hydrogen reduced H-Ta_2O_5 nanosheets (H-Ta_2O_5 NSs) and high valance Mo-doped Ta_2O_5 nanorods (Mo-Ta_2O_5 NRs). The Mo-Ta_2O_5 NR substrates provide a higher SERS signal with ~ 2.2×10^7 and detection limit of ~ 9×10^{-9} M when Methyl Violet (MV) was used as Raman adsorbate molecule under the laser excitation source of 532 nm [134].

Lafuente *et. al*. reported a reproducible and cost-effective technique to fabricate a homogeneous SERS active substrate using Langmuir- Schaefer (LS) technique. They have lifted Octadecylthilate capped AuNPs on a quartz slide by LS technique using a LB trough. To optimize the SERS efficacy, the thiol capped AuNPs have been dispersed in a solution with various hexane:

chloroform ratios that has been used as spreading solution during the LS deposition technique. The SERS efficacy of the as prepared substrates is evaluated using R6G as adsorbate molecule. The order of AEF was estimated to be ~ 10^8 and the lowest detection concentration of R6G is found to be 10^{-11} M with RSD < 10% establishes the potency of the as prepared substrates [135].

Bhunia *et. al*. proposed the development of a flexible SERS active films by containing Polydimethylsiloxane (PDMS) implanting Carbon dots (C-dots) and surface attached AgNPs. 4-ATP was used as SERS probe molecule and the AEF ~10^6 was calculated for the as prepared SERS active films. Additionally, this substrate is proved to be a promising SERS active substrate for detecting bacterial cells. The detection limits of 4-ATP and P. *aeruginosa* bacteria as obtained from the as prepared SERS films are ~ 10^{-9} M and 10^4 cells/ mL respectively validates the efficacy of the as prepared substrate [136].

Tahghighi *et. al*. proposed a simple procedure for the preparation of tunable SERS active substrate by depositing monolayer AuNPs by LB deposition technique on APTES functionalized glass and fused silica slides. The surface plasmons are altered by tuning the packing density of the AuNPs applying electroless plating. 4-MBA was used as probe molecule to investigate the SERS efficacy of the as prepared substrate [137].

Recently, Zhang *et. al*. reported the fabrication of three-dimensional low-cost SERS active substrate using ordered micro pyramid array and silver nanoparticles (MPA/ AgNPs). The SERS efficacy of the substrate was tested using R6G molecule. The enhancement factor and the limit of detection of R6G molecule was estimated to be 8.8×10^9 and 1.0×10^{-12} M respectively. Finally, the as prepared substrate was used for the detection of thiram with LOD ~ 10^{-7} M. [138].

A solid SERS active was developed by Li *et. al*. using AgNPs with different particle size (59, 41 and 29 nm) and anodized aluminium oxide (AAO) template. Using liquid-liquid interface self-assembly method, the AgNPs were self-assembled into the AAO holes. 4-MBA was used as Raman probe molecule and the analytical enhancement factor (AEF) was estimated to be ~ 1.17×10^6. The substrate shows good spectral reproducibility with relative standard deviation 6.45%. Additionally, this as fabricated substrate was used for the detection of levofloxacin in milk with LOD ~ 1.88×10^{-6} M. [139].

1.4.3 Applications of SERS

Over the past decades SERS has been proven as an interesting field of current research in different branches of physics, chemistry, biology and material sciences. This non-destructive

technique is capable to determine the orientations of the molecules along with the detection of single molecule at trace concentrations [140-143]. Now a days SERS technique is easily applied in many diagnostic applications, real world detection, art and archaeology, pharmaceutical engineering, environmental sciences, biological sciences etc.

(a) SERS in Sensing and Bioimaging

S. K. Das *et. al*. reported the template-based fabrication of a SERS active substrate by the self-assembly of the gold nanocolloids (AuNCs) in the bilayer LB film of stearic acid (SA). 4-MPy was used as SERS analyte in order to test the SERS efficacy of the as prepared substrate. The as prepared substrate was utilized for the detection of normal and cancerous cell lines related to the prostate and breast cancers. The principal component analysis (PCA) and loading spectra was applied to distinguish and recognize the cancerous cells from the corresponding normal cells at molecular range [129].

Beffara *et. al*. proposed the fabrication of a SERS sensors based on suspended core photonic crystal fiber (PCF) along with a small triangular silica core enclosed by three large holes. The as estimated RSD values of 1.5% and 4.6% proves the reproducibility and repeatability of the substrates. The as prepared substrates were employed to detect the levels of haptoglobin (Hp) in clinical ovarian cyst fluid (OCF) to segregate the stages of cancers for numerous patients which was in accordance with the usual clinical technique to detect the ovarian cancer [144].

Adams *et. al*. synthesized gold and poly(vinylpyrrolidone) (PVP) functionalized $Fe_3O_4@SiO_2$ nanoparticles composites with 200 nm in size. The presence of roughened gold modules leads to enhance the EM field intensity by generating hot spots which in turn makes the as prepared composite material as an excellent SERS substrate. The as prepared substrates have been used to detect glucagon-like peptide 1 (GLP-1) which is known as a large gastrointestinal hormone that helps to stimulate the release of insulin form the pancreas β cells. The fast and prompt separation (~ 30 s) of the desired molecule from the solution upon binding with the particles and the estimated LOD of ~ 10^{-7} M evidences the superiority of the as synthesized composite over the SERS bio sensing [145].

Cabello *et. al*. reported the synthesis of Cu@Au bimetallic nanoparticles which can be utilized as a useful tool to detect an extensive range of molecules at trace concentrations. The SERS efficiency of the as prepared substrate has been verified by Rhodamine B (RhB) and Methylene Blue (MB) molecule under the excitation of 785 nm and 514 nm laser source

respectively. The LOD ~ 10^{-12} M and 10^{-9} M as estimated for the RhB and MB molecule respectively along with the EF ~ 3×10^5 orders of magnitude that arises from the LSPR due to the generation of hotspots proves the efficiency of the as prepared substrate. The as prepared substrates have been used for the detection of Cholesterol, Propanil, Adamantane, Acetaminophen, 4- Mercaptobenzoic acid and Dopamine at trace concentration level [146].

Lin *et. al*. proposed an acousto-aided liquid marble-based SERS platform for highly sensitive SERS sensing. The potency of the as fabricated SERS platform was established with the detection of alkaline phosphate (ALP) which is known as an important diagnostic indicator for some specified human diseases like osteoporosis, leukaemia, lymphoma and hepatitis. The as developed SERS platform is capable to detect the ALP activity from human serum samples with detection limit 0.33 UL^{-1} [147].

S. K. Das *et. al*. reported the fabrication of an efficient SERS active substrate through the self-assembly of the AuNPs in reverse Schaeffer film template of 5-CB liquid crystal molecule that can detect the "normal", "moderately high" and "very high" diabetic conditions from the corresponding blood plasma samples using the SERS technique. The experimental outcomes were analysed from the principal component analysis (PCA) and linear discriminant analysis (LDA) tools. [125]

The fabrication of a SERS based sensor using a combination of deoxyribonucleic acid (DNA) and Au nano popcorn have been reported by Chen *et. al*. that can detect the SERS-CoV2 virus just in 15 minutes with an LOD ~ 10 PFU/ml. [148].

Karunakaran *et. al*. reported the simultaneous detection of dual P16/ Ki-67 biomarker during the progression of cervical cancer in 20 minutes using SERS nano-tag fabricated by the combination of Au nanostar and Ag nanoflower (AuNS@AgNF) [149].

(b) SERS in Environmental Analysis

Liu *et. al*. reported the preparation of a multifunctional SERS active substrate using CuO@Ag nanowires on Cu mesh capable of detecting R6G up to femtomolar concentration with estimated EF ~ 10^{11} orders of magnitude. The as prepared substrate can detect up to 10^{-5} M thiram dissolved in toluene from the mixture of water- toluene which proves that the substrate can be used as an efficient tool to detect environmental pollutants [150].

Hu *et. al*. developed a SERS active substrate using self-assembly of large area and high density AuNRs arrays synthesized by seed mediated method that can detect the mixed pesticides from contaminated fruits surface. By the self-modelling mixture analysis method, the Raman spectral feature of each composition can be extracted from the Raman spectra recorded from the mixture of various pesticides. The as prepared substrates can act as a sensitive tool for the detection of thiram and thiabendazole (TBZ) from different fruits surface. The LOD from the surface of apple, pear and tomato estimated to be 0.041, 0.047 and 0.029 ng/cm^2 for thiram and 0.79, 0.80 and 0.76 ng/cm^2 respectively along with the acceptable recoveries establishes the efficiency of the as prepared substrate over the sensing of various fruit pesticides [151].

Subramaniam *et. al*. reported a SERS active hybrid nanostructure containing Ag/TiO_2 nanoplates and nanorods that can detect pesticides at ultrasensitive concentration. The as fabricated Ag/TiO_2 modified SERS sensor is capable to detect the chlorpyrifos pesticide on the surface of grapes and tomatoes with LOD 2 ng/cm^2 and 5 ng/cm^2 respectively [152].

Lee *et. al*. proposed a simple, cost effective and easier way for the development of a filter paper-based SERS sensor with high sensitivity and reproducibility using AgNPs. In order to check the SERS efficacy, 4-ATP was used as SERS probe and the estimated RSD and the LOD values of 6.19 % and 0.60 nM respectively for the 4-ATP molecule demonstrates the reproducibility and sensitivity of the as prepared SERS sensor. Moreover, the SERS sensor has the ability to detect the thiram and ferbam pesticides with LOD ~ 0.46 nM and 0.49 nM respectively [153].

Xu *et. al*. reported the fabrication of 3D SERS active substrates using polycaprolactone (PCL) fibrous mat and silver coated gold nanorods (Au@AgNRs) modified with a layer of poly (sodium 4-styrenesulfonate) (PSS). The as prepared substrates can sense 4-MPy with a range of concentrations from 10^{-4} M – 10^{-8} M. The as prepared substrate can detect both organic and inorganic arsenic, arsenate, p-arsanilic acid and roxarsone at trace concentrations suggesting the potency of the as prepared substrates as an environmental sensor [154].

Zhao *et. al*. proposed the fabrication of a SERS sensor developed by modifying the inner wall of the capillary with AgNps. The 4,4'-dipyridyl (Dpy) molecule has been used as Raman probe and the detection of the Hg^{2+} has been performed indirectly by observing the variation in SERS spectral profile of the analyte Dpy molecule. The LOD of the as prepared sensor for detecting $Hg^{2+}$was estimated to be 0.1 ppb, which was much lower than the concentration of Hg^{2+}as set by the United States Environmental Agency (USEPA) for drinking water. The real-

world sensing has been performed using this sensor and the estimated recovery ranges were 96.10% – 102.06 % [155].

By the combination of the SERS and Resonance Rayleigh Scattering (RRS) spectra Wen *et. al*. reported the development of a highly sensitive SERS/ RRS dual mode assay platform that can detect several organic pollutants at trace concentrations. They have reported the LODs of the different organic pollutants like oxytetracycline (OTC), tetracycline (TEC), glyphosate (GLY) and bisphenol A (BPA) are estimated to be 0.64, 6.2×10^{-3}, 0.03 and 0.53×10^{-3} ng/ml respectively. [156].

Recently, Fan *et. al*. reported the fabrication of a SERS active sensor using bovine-serum-albumin (BSA) assisted gold- silicon nanowire arrays (Au@SiNWAs) that can detect mercury ion (Hg^{2+}) in water with LOD of 1 pM. This sensor can detect the Hg^{2+} ion present in water at a reliable and accurate way with relative standard deviation ~ 9.21% [157].

(c) SERS in Diagnostic Applications

Bindesri *et. al*. presented a fabric based conductive electrochemical sensor modified with AgNPs that can act as an efficient SERS active substrate where *p*-ATP has been used as a SERS sensing probe to investigate the SERS efficacy of the as prepared sensor. Furthermore, this electrochemical SERS sensor has been used to detect a generally prescribed antibiotic "levofloxacin" which is used for the treatment of different bacterial infections in respiratory and urinary tract [158].

Muhammad *et. al*. proposed the fabrication of a SERS active substrate using AuNPs array constructed on a canonical anodic aluminium oxide (AAO) template. R6G with different concentrations ranging from 10^{-6} M to 10^{-9} M has been used as SERS analyte to check the SERS activity of the substrate. An estimated EF ~ 4.6×10^{7} with the lowest detection concentration of R6G ~ 10^{-9} M has been reported. The as prepared SERS active substrates were used to investigate the serum samples collected from the mice with total body irradiation treatment. Moreover, the blood and urine samples of various cancer patients under radiotherapy treatment has also been tested using the substrate. So, this technique is served as an efficient technique for the diagnostics of severe radiation injury at the initial time for both animals and human beings [159].

Chen *et. al*. developed a dual mode SERS based aptasensor using DNA aptamers immobilized with Au nanopopcorn substrate that can precisely distinguish and diagnose the SARS-CoV-2 and Influenza A/ H1N1 viruses simultaneously with high sensitivity [160].

Su *et. al*. reported the fabrication of a microfluidic SERS chip for the sensing of blood samples. The SERS capability of the chip was investigated using the serum and creatinine samples. The LOD for creatinine was estimated to be ~ 4.42×10^{-3} µmol/ mL in water which proves the efficiency of the SERS chip. The blood samples as collected from the patients with chronic renal failure and from the healthy people were tested by this as prepared SERS chip and the obtained results were found to be in harmony with the results attained by enzymatic technique [161].

Khlebtsov *et. al*. developed a lateral flow immunoassay (LFIA) tool, based on SERS by using AuNR as core and Au as shell. The 1,4-nitrobenzenthiole (NBT) molecule has been used as Raman analyte molecule that has been placed between the core and the shell. The potency of the SERS labels has been tested with the precise detection of the cardiac troponin I (cTnI) which is known as a biomarker of heart disease. The LOD of cTnI detected with the as prepared SERS tags is evaluated to be ~ 0.1 ng/mL which was within the diagnostic range of cTnI present in the blood serum for the heart infarcted patients [162].

Pramanik *et. al*. developed an efficient anti-spike antibody attached with AuNPs which can specifically detect the COVID-19 viral antigen or the SARS-CoV2 virus in naked eye by a simple colorimetric change within 5 minutes. For fast and sensitive detection, the SERS technique was applied using 4-ATP as a Raman probe molecule. The as reported SERS probe that was developed via the combination of antibody and AuNPs attached with 4-ATP can detect the COVID-19 antigen and virus at a lowest concentration of 4 pg/ ml and 18 virus particles/ ml respectively [163].

Recently, Wang *et. al*. reported the fabrication of a low cost plasmonic SERS active substrate with colloidal AgNPs that can be used for the quantification of bacterial growth and diagnosis of viral infection. With the aid of multivariate data analysis, the as prepared substrate can diagnose viral infection with 93% prediction accuracy. [164].

Fabrication of a magnetically assisted sandwich type SERS based biosensor has been reported by Wu *et. al*. that can simultaneously detect three cancer related micro RNAs (e.g. miRNA-122, miRNA-223 and miRNA-21) at atto molar concentration level. The as fabricated biosensor has been developed using fractal AuNPs and silver coated magnetic nanoparticles. The

LOD of the miRNA-122, miRNA-223 and miRNA-21 in human serum are 349 aM, 374 aM and 311 aM respectively. [165].

(d) SERS in Forensic Science

Fikiet *et. al*. in a review article represented a variety of forensic applications using some new SERS surfaces. In that review article, the various uses of SERS in forensics applications and the corresponding relevant advancements are also discussed [166].

Hakonen *et. al*. reported the femtograms detection of some common forensic elements such as Cyclosarin, Amphetamine, RDX and Picric acid using commercially available SERS substrates portable spectrometers. Moreover, the nature of the huge enhancement was investigated with the aid of 3D FEM and DFT studies [167].

Gao *et. al*. reported the fabrication of a novel SERS active substrate using AgNps and flexible, colourless and transparent polyethyleneterephthalate (PET) that delivers uniform hot spots with high sensitivity and reproducibility. The SERS efficacy of the substrate is exemplified with R6G molecule with concentration range $10^{-5} - 10^{-10}$ M. Furthermore, the as prepared substrate is used for the detection of 2, 4, 6-Trinitrotoluene (TNT) with detection limit ~ 10^{-13} mol/ L using 4-ATP modified AgNPs [168].

Byram *et. al*. proposed the fabrication of a SERS active substrate using gold nano structures (NSs) and nano particles (NPs) by laser ablation in liquid (LAL) method that can sense multiple analytes from a mixture of dyes/ explosives. The as prepared SERS active substrate can detect various explosive molecules (such as, picric acid (PA), 3-nitro-1,2,4- triazol-5-one (NTO) and 2,4- dinitro-toluene (DNT)) from the mixtures of explosive + dye (R6G, MB and CV) and explosive + explosive with good reproducibility and low detection limits [169].

Liyanage *et. al*. reported the fabrication procedure of a SERS nano sensor by the self-assembly of triangular gold nano prisms on a flexible adhesive film. Due to the sharp tips and edges, the as synthesized nano prisms produce strong EM field enhancements which in turn generates an enhanced Raman signal. Moreover, the SERS feasibility of the as prepared SERS nano sensor has been tested by the detection of three different explosives (TNT, RDX and PETN) at ppq (parts-per-quadrillion) scale. An estimated EF ~ 10^6 orders of magnitude with 100% accuracy level in the sensing of different explosive materials further corroborates the efficiency of the as prepared sensors [170].

Wang *et. al*. developed a portable SERS module using AgNPs for rapid and quantitative detection of fentanyl. Using this portable SERS platform, they have detected fentanyl spiked in urine at a minimum detection limit ~ 5 ng/ ml. This as fabricated SERS module can detect fentanyl from various reactional drugs such as heroin or tetrahydrocannabinol (THC) at 0.1 mass percent [171].

Velicka *et. al*. reported the detection of caffeine and paraxanthine from human saliva using Electrochemical Surface Enhanced Raman Scattering spectroscopy (EC-SERS). They have developed a SERS active layer using colloidal AgNPs which can detect the presence of paraxanthine in saliva with LOD ~ 15 μM [172].

Recently, Hassanain *et. al*. proposed the fabrication of a lectin-functionalized extractor chip that can distinguish two types of human Erythropoietin (EPO) isoforms (e.g., recombinant EPO [rhuEPO] and endogenous EPO [enEPO]) within 15 minutes from blood plasma using SERS technique. They have applied the SERS tool for the picomolar detection of rhuEPO which has been misused by the athletes in order to improve their oxygen level and boost up their performance [173].

1.4.4 Limitations of the SERS technique

Despite the immense advantages of SERS technique for its excellent selectivity and sensitivity, there exist a number of significant limitations/ disadvantages to this technique. These are

- Intense SERS signals can only be attained from a particular set of metal surfaces, but the surface enhanced infrared spectroscopy can be observed in any kind of surfaces.
- The relative contribution of the different enhancement process of SERS is still unclear. The enhancement of SERS signal can vary with the surface morphology, applied potential and the laser excitation source.
- At present, the general surface selection rule is still unavailable that can properly envisage the surface orientation of the adsorbate molecule from the respective SERS spectrum. On the contrary, a well-established surface selection rules are available for other surface sensitive tools such as surface enhanced infrared spectroscopy and electron energy loss spectroscopy (EELS).

- ❖ Occurrence of in situ photodecomposition on the SERS active substrate surface leading to the generation of amorphous carbon bands in the SERS spectra is a major problem with this technique.
- ❖ There are still some difficulties in the fabrication of cost effective, homogeneous, highly efficient and reproducible SERS active substrate.
- ❖ The choice of substrate for a given SERS probe molecule is limited.
- ❖ Limited re-usability of SERS active substrate.
- ❖ Decrease in the SERS signal due to the degradation of the SERS active substrate with time.

References

1. B. Dutta, T. Tanaka, A. Banerjee, J. Chowdhury, *J. Phys. Chem. A*, 2013, **117**, 4838.
2. Z. Movasaghi, S. Rehman, I. U. Rehman, *Appl. Spectrosc. Rev*., 2007, **42**, 493.
3. R. J. Clark, T. J. Dines, *Angew. Chem. Inr. Ed. Egl*., 1986, **25**, 131.
4. B. Dutta, R. De, C. Pal, J. Chowdhury, *Spectrochem. Acta part A*, 2012, **96**, 837.
5. L. A. Lyon, C. D. Keating, A. P. Fox, B. E. Baker, L. He, S. R. Nicewarner, S. P. Mulvaney, M. J. Natan, *Anal. Chem*., 1998, **70**, 341.
6. R. P. Van Duyne, *Chemical and Biological Applications of Lasers,* C.B. Moore (Ed.), Vol. 4, Chap. 1. (Academic Press), New York, 1979.
7. R. K. Chang, T. E. Furtak (Eds.), *Surface Enhanced Raman Scattering*, Plenum Press, New York, 1982.
8. R. Aroca, *Surface enhanced Vibrational Spectroscopy*, John Wiley and Sons Ltd, United Kingdom, 2006.
9. J. H. Granger, N. E. Schlotter, A. C. Crawford, M. D. Porter, *Chem. Soc. Rev*., 2016, **45**, 3865.
10. M. Fleischmann, P. J. Hendra, A. J. McQuillan, *Chem. Phys. Lett*., 1974, **26**, 123.
11. D. L. Jeanmaire, R. P. Van Duyne, *J. Electroanal. Chem. and Interfacial Electrochem.*, 1977, **84**, 1.
12. M. G. Albrecht, J. A. Creighton, *J. Am. Chem. Soc.*, 1977, **99**, 5215.
13. S. Nie, S. R. Emory, *Science*, 1997, **275,** 1102.
14. K. Kneipp, Y Wang, H. Kneipp, L. T. Perelman, I. Itzkan, R. R. Dasari, M. S. Field, *Phys. Rev. Lett.*, 1997, **78,** 1667.

15. H. Xu, E. J. Bjerneld, M. Kall, L. Börjesson, *Phys. Rev. Lett.*, 1999, **83,** 4357.
16. A. M. Michaels, M. Nirmal, L. E. Brus, *J. Am. Chem. Soc.*, 1999, **121,** 9932.
17. A. M. Michaels, J. J. Jiang, L. E. Brus, *J. Phys, Chem.* B, 2000, **104,** 11965.
18. P. G. Etchegoin, M. Meyer, E. C. Le Ru, *Phys. Chem. Chem. Phys.*, 2007, **9**, 3006.
19. P. G. Etchegoin, E. C. Le Ru, *Phys. Chem. Chem. Phys.*, 2008, **10**, 6079.
20. G. Haran, *Acc. Chem. Res.*, 2010, **43,** 1135.
21. J. Zhao, J. A. Dieringer, X. Zhang, G. C. Schatz, R. P. Van Duyne, *J. Phys. Chem. C*, 2008, **112**, 19302.
22. L. A, Austin, S. Osseiran, C. L. Evans, *Analyst*, 2016, **141**, 476.
23. S. K. Gahlaut, D. Savargaonkar, C. Sharan, S. Yadav, P. Mishra, J. P. Singh, *Anal. Chem.*, 2020, **92**, 2527.
24. M. M. Joseph, N. Narayanan, J. B. Nair, V. Karunakaran, A. N. Ramya, P. T. Sujai, G. Saranya, J. S. Arya, V. M. Vijayan, K. K. Maity, *Biomater*. 2018, **181**, 140.
25. D. G. de Oliveira, L. P. F. Peixoto, S. Sánchez-Cortes, G. F. S. Andrade, *Vib. Spectrosc.*, 2016, **87**, 8.
26. M. Muniz-Miranda, M. Puggelli, R. Ricceri, G. Gabrielli, *Langmuir*., 1996**, 12**, 4417.
27. S. D. Roy, M. Ghosh, J. Chowdhury, *J. Raman Spectrosc*., 2015, **46**, 451.
28. M. Muniz- Miranda, F. Muniz- Miranda, A. Pedone, *Phys. Chem. Chem. Phys*., 2016, **18**, 5974.
29. Y. Ran, P. Strobbia, V. Cupil-Garcia, T. Vo-Dinh, *Sens. Actuators* B, 2019, **287**, 95.
30. C. Muehlethaler, M. Leona, J. R. Lombardi, *Anal. Chem.*, 2016, **88**, 152.
31. A. Hakonen, K. Wu, M. S. Schimidt, P. O. Andersson, A. Boisen, T. Rindzevicius, *Talanta*, 2018, **189**, 649.
32. Y. Yu, T.-H. Xiao, Y. Wu, W. Li, Q.-G. Zeng, L. Long, Z.-Y. Li, *Adv. Photonics*, 2020, **2**, 014002.
33. D. Sun, F. Cao, Y. Tian, A. Li, W. Xu, Q. Chen, W. Shi, S. Xu, *Anal. Chem.*, 2019, **91**, 15484.
34. P.W. Barber, R.K. Chang, H. Massoudi, *Phys. Rev. B*, 1983, **27**, 7251.
35. W.-H. Yang, G.C. Schatz, R.P. Van Duyne, *J. Chem. Phys*., 1995, **103**, 869.
36. D.-S. Wang, M. Kerker, *Phys. Rev. B*, 1981, **24**, 1777.
37. M. Kerker, D.-S. Wang, H. Chew, *Appl. Opt*., 1980, **19**, 4159.
38. M. Moskovits, *J. Chem. Phys*., 1978, **69**, 4159.
39. J. P. Marton, J. R. Lemon, *Phys. Rev*., 1971, **84**, 271.

40. D. P. DiLella, A. Gohin, R. H. Lipson, P. McBreen, M. Moskovits, *J. Chcm. Phys*., 1980, **73**, 4282.
41. C. Y. Chen, E. Burstein, *Phys. Rev. Lett*., 1980, **45**, 1287.
42. J. K. Sass, H. Neff, M. Moskovits, S. Holloway, *J. Phys. Chem*., 1981, **85**, 621.
43. S. S. Perry, S. R. Hatch, A. Campion, *J. Chem. Phys*., 1996, **104**, 6856.
44. J. L. Yao, G. P. Pan, K. H. Xue, D. Y. Wu, B. Ren, D. M. Sun, J. Tang, X. Xu, Z. Q. Tian, *Pure Appl. Chem*., 2000, **72**, 221.
45. F. Claro, *Phys. Rev. B*, 1982, **25**, 7875.
46. E. C. Le Ru, P. G. Etchegoin, *Principles of surface-enhanced Raman spectroscopy and related plasmonic effects*, Elsevier, Amsterdam, 2009.
47. R. Rojas, F. Claro, *J. Chem. Phys*., 1993, **98**, 998.
48. L. Novotny, B. Hecht, *Principles of Nano-Optics*, Cambridge Univ. Press, New York, 2012.
49. S. S. Masango, R. A. Hackler, N. Large, A.-I. Henry, M. O. McAnally, G. C. Schatz, P. C. Stair, R. P. Van Duyne, *Nano Lett*., 2016, **16**, 3898.
50. B. Sharma, M. F. Cardinal, M. B. Ross, A. B. Zrimesk, S. V. Bykov, D. Punihaole, S. A. Asher, G. C. Schatz, R. P. Van Duyne, *Nano Lett*., 2016, **16**, 7968.
51. B. Sharma, P. Bugga, L. R. Madison, A.-I. Henry, M. G. Blaber, N. G. Greeneltch, N. Chiang, M. Mrksich, G. C. Schatz, R. P. Van Duyne, *J. Am. Chem. Soc*., 2016, **138**, 13952.
52. A. J. Haes, C. L. Haynes, A. D. McFarland, G. C. Schatz, R. P. Van Duyne, S. Zou, *MRS Bull*., 2005, **30**, 368.
53. X. Zhang, C. R. Yonzon, M. A. Young, D. A. Stuart, R. P. Van Duyne, *IEE Proc. Nanobiotechnol*., 2005, **152**, 195.
54. A. D. McFarland, M. A. Young, J. A. Dieringer, R. P. Van Duyne, *J. Phys. Chem. B*, 2005, **109**, 11279.
55. P. L. Stiles, J. A. Dieringer, N. C. Shah, R. P. Van Duyne, *Annu. Rev. Anal. Chem*., 2008, **1**, 601.
56. D. Kurouski, N. Large, N. Chiang, N. Greeneltch, K. T. Carron, T. Seiderman, G. C. Schatz, R. P. Van Duyne, *Analyst*, 2016, **141**, 1779.
57. M. D. Doherty, A. Murphy, J. McPhillips, R. J. Pollard, P. Dawson, *J. Phys. Chem. C*, 2010, **114**, 19913.
58. J. P. Litz, J. P. Camden, D. J. Masiello, *J. Phys. Chem. Lett*., 2011, **2**, 1695.

59. S. L. Kleinman, B. Sharma, M. G. Blaber, A.-I. Henry, N. Valley, R. G. Freeman, M. J. Natan, G. C. Schatz, R. P. Van Duyne, *J. Am. Chem. Soc*., 2013, **135**, 301.
60. R. Boyack, E. C. Le Ru, *Phys. Chem. Chem. Phys*., 2009, **11**, 7398.
61. L. K. Ausman, G. C. Schatz, *J. Chem. Phys*., 2009, **131**, 084708.
62. L. K. Ausman, G. C. Schatz, *J. Phys. Chem. C*, 2012, **116**, 17318.
63. N. S. Mueller, S. Hegg, P. Kusch, E. Gaufres, N. Y.-W. Tang, U. Hubner, R. Martel, A. Vijayaraghavan, S. Reich, *Faraday Discuss*, 2017, **205**, 85.
64. P. Gupta, J. Luan, Z. Wang, S. Cao, S. H. bae, R. R. Naik, S. Singamaneni, *ACS Appl. Mater. Interfaces*, 2019, **11**, 37939.
65. E. S. Ameer, S. Varahagiri, D. W. Benza, D. R. Willet, Y. Wen, F. Wang, G. Chumanov, J. N. Anker, *J. Phys. Chem. C*, 2016, **120**, 20886.
66. I. M. Shaikh, S. D. Sartale, *J. Raman Spectrosc*., 2018, **49**, 1274.
67. J. Nam, P. K. Duy, C. Seo, S. Eom, D. N. Minh, J. Lee, J. H. Sim, H. Chung, Y. Kang, *J. Raman Spectrosc*., 2019, **50**, 1485.
68. A. Fularz, S. Almohammed, J. H. Rice, *ACS Appl. Nano Mater*., 2020, **3**, 1666.
69. R. Rastogi, H. Arianfard, D. Moss, S. Juodkazis, P.-M. Adam, S. Krishnamoorthy, *ACS Appl. Mater. Interfaces*, 2021, **13**, 9113.
70. T.-J. Wang, N. R. Barveen, Z.- Y. Liu, C.- H. Chen, M.- H. Chou, *ACS Appl. Mater. Inter*., 2021, **13**, 34910.
71. J. I. Gersten, R. L. Birke, J. R. Lombardi, *Phys. Rev. Lett*., 1979, **43**, 147.
72. H. A. Kramers, W. Heisenberg, *Z. Phys*., 1925, **31**, 681.
73. P. A. M. Dirac, *Proc. R. Soc. London*, 1927, **114**, 710.
74. A. C. Albrecht, *J. Chem. Phys*., 1961, **34**, 1476.
75. R. L. Birke, J. R. Lombardi, *J. Chem. Phys*., 1986, **84**, 4174.
76. M. Osawa, N. Matsuda, K. Yoshii, I. Uchida, *J. Phys. Chem*., 1994, **98**, 12702.
77. J. R. Lombardi, Z. Sun, C. Wang, J. Yang, B. Zhao, *J. Phys. Chem. C*, 2008, **112**, 5605.
78. W. L. Peticolas, D. P. Strommen, V. Lakshminarayanan, *J. Chem. Phys*., 1980, **73**, 4185.
79. D. Aranda, S. Valdiva, F. I. Avila, I. Soto, J. C. Otero, I. L. Tocon, *Phys. Chem. Chem. Phys*., 2018, **20**, 29430.
80. S. A. Jafari, M. H. Khodabandeh, Z. Jamshidi, *Phys. Chem. Chem. Phys*., 2019, **21**, 23996.

81. X. Fan, M. Li, Q. Hao, M. Zhu, X. Hou, H. Huang, L. Ma, O. G. Schmidt, T. Qiu, *Adv. Mater. Interfaces*, 2019, **6**, 1901133.
82. L. Guo, X. Zhang, P. Li, R. Han, Y. Liu, X. Han, B. Zhao, *N. J. Chem*., 2019, **43**, 120.
83. X. Jiang, X. Sun, D. Yin, X. Li, M. Yanmg, X. Han, L. Yang, B. Zhao, *Phys. Chem. Chem. Phys*., 2017, **19**, 11212.
84. X. Su, H. Ma, H. Wang, X. Li, X. X. Han, B. Zhao, *Chem. Commun*. 2018, **54**, 2134.
85. D. Q. Dao. T. C. Ngo, T. T. H. Le, Q. T. Trinh, T. L. A. Nguyen, B. T. Huy, N. N. Tri, N. T. Trung, M. T. Nguyen, *J. Phys. Chem. A*, 2021, **125**, 8529.
86. M. Zhang, Y. Wang, X. Wang, B. Zhao, R. Ruan, *J. Phys. Chem. C*, 2021, **125**, 17125.
87. D. D. Tuschel, J. E. Pemberton, J. E. Cook, *Langmuir*, 1986, **2**, 380.
88. M. E. Abdelsalam, P. N. Barlett, J. J. Bamberg, S. Cintra, T. A. Kelf, A. E. Russell, *Electrochem. Commun*., 2005, **7**, 740.
89. G. Sauer, U. Nickel, S. Schneider, *J. Raman Spectrosc*., 2000, **31**, 359.
90. P. C. Lee, D. Meisel, *J. Phys. Chem*., 1982, **86**, 3391.
91. L.A. Dick, A. D. McFarland, C. L. Haynes, R. P. Van Duyne, *J. Phys. Chem. C*, 2010, **114**, 11717.
92. L. Baia, M. Bais, J. Popp, S. Astilean, *J. Phys. Chem. B*, 2006, **110**, 23982.
93. X. Liu, C. H. Sun, N. C. Linn, B. Jiang, P. Jiang, *J. Phys. Chem. C*, 2009, **113**, 14804.
94. T. L. Williamson, X. Gou, A. Zukoski, A. Sood, D. J. Diaz, P. W. Bohn, *J. Phys. Chem. B*, 2005, **109**, 20186.
95. S. Chan, S. Kwan, T. W. Koo, L, P, Lee, A. A. Berlin, *Adv. Mater*, 2003, **15**, 1595.
96. A. Y. Panarin, S. N. Terekhov, K. I. Kholostov, V. P. Bondarenko, *Appl. Surf. Sci*., 2010, **256**, 6969.
97. B. Mondal, S. K Saha, *Chem. Phys. Lett*., 2010, **497**, 89.
98. R. J. Walsh, G. Chumanov, *Appl. Spectrosc*., 2001, **55**, 1695.
99. H. H. Wang, C. Y. Liu, S. B. Wu, N. W. Liu, C. Y. Peng, T. H. Chan, C. F. Hsu, J. K. Wang, Y.L. Wang, *Adv. Mater*., 2006, **18**, 491.
100. C. Ruan, G. Eres, W. Wang, Z. Zhang, B. Gu, *Langmuir*, 2007, **23**, 5757.
101. A. J. Chung, Y. S. Huh, D. Erickson, *Nanoscale*, 2011, **3**, 2903.
102. M. Schierhorn, S. J. Lee, S. W. Boettcher, G. D. Stucky, M. Moskovits, *Adv. Mater*., 2006, **18**, 2829.

103. Z. Huang, G. Meng, Q. Huang, B. Chen, C. Zhu, Z. Zhang. *J. Raman Spectrosc*., 2013, **44**, 240.

104. G. Kartopu, M. Es-Saini, A. V. Sapelkin, D. Dunstan, *Phys. Status Solidi*, 2006, **203**, R82.

105. D. P. Fromm, A, Sundaramurthy, A. Kinkhabwala, P. J. Schuck, G. S. Kino, W. E. Moerner, *J. Chem. Phys*., 2006, **124**, 061101.

106. T. Wu, Y.-W. Lin, *Appl. Surf. Sci*., 2018, **435**, 1143.

107. K. Sivashanmugan, J. D. Liao, J. W. You, C. L. Wu, *Sens. Actuators B*, 2013, **181**, 361.

108. X. Zhao, J. Wen, M. Zhang, D. Wang, Y. Wang, L. Chen, Y. Zhang, J. Yang, Y. Du, *ACS Appl. Mater & Interface*, 2017, **9**, 7710.

109. X. Fang, C. Zheng, Z. Yin, Z. Wang, J. Wang, J. Liu, D. Luo, Y. J. Liu, *ACS Appl. Mater & Interface*, 2020, **12**, 12345.

110. J. A. Dieringer, A. D. McFarland, N. C. Shah, D. A. Stuart, A. V. Whitney, C. R. Yonzon, M. A. Young, X. Zhang, R. P. Van Duyne, *Faraday Discuss*., 2006, **9**, 132.

111. R. Aroca, C. Jennings, G. J. Kovacs, R. O. Loutfy, P. S. Vincett, *J. Phys. Chem*., 1985, **89**, 4051.

112. G. J. Kovacs, R. O. Loutfy, P. S. Vincett, C. Jennings, R. Aroca, *Langmuir*, 1986, **2**, 689.

113. R. Aroca, D. Battisti, *Langmuir*, 1990, **6**, 250 and references cited therein.

114. G. Moula, R. F. Aroca, *Anal. Chem*., 2011, **83**, 284 and references cited therein.

115. N. P. W. Pieczonka, R. F. Aroca, *Chem. Soc. Rev*., 2008, **37**, 946.

116. C. J. L. Constantino, R. F. Aroca, C. R. Mendonca, S. V. Mello, D. T. Balogh, O. N. Oliveira Jr, *Spectrochemica Acta Part A*, 2001, **57**, 281 and references cited therein.

117. P. Alessio, C. J. L. Constantino, R. F. Aroca, O. N. Oliveira Jr, *J. Chil. Chem. Soc*., 2010, **55**, 469 and references cited therein.

118. A. R. Guerrero, Y. Zhang, R. F. Aroca, *Small*, 2012, **8**, 2964 and references cited therein.

119. A. Tao, F. Kim, C. Hess, J. Goldberger, R. He, Y. Sun, Y. Xia, P. Yang, *Nano Lett*., 2003, **3**, 1229.

120. N. V. Surovtsev, S. V. Adichtchev, T. A. Duda, L. D. Pokrovsky, L. L. Sveshnikova, *J. Phys. Chem. C*, 2010, **114**, 4803.

121. C. Wang, W. Ruan, N. Ji, W. Ji, S. Lv, C. Zhao, B. Zhao, *J. Phys. Chem. C*, 2010, **114**. 2886.

122. M. A. Mahmoud, M. A. El-Sayed, *J. Phys. Chem. C*, 2011, **115**, 12726.

123. S. K. Das, M. Ghosh, S. Ghosh, J. Chowdhury, *Appl. Surf. Sci*., 2019, **484**, 1263.

124. M. Tahghighi, D. Janner, J. Ignes-Mullal, *Nanomaterials*, 2020, **10**, 2264.

125. S. K. Das, T. S. Bhattacharya, M. Ghosh, J. Chowdhury, *New. J. Chem*., 2021, **45**, 2670.

126. W. L. Chen, Y.-H. Huang, H.-Y. Cheng, T.-R. Kuo, Y.-M. Chang, *J. Raman Spectrosc*., 2018, **4**, 792.

127. M. L. Hupfer, R. Meyer, T. Deckert-Gaudig, S. Ghosh, A. Skabeev, K. Peneva, V. Deckert, B. Dietzek, M. Presselt, *Langmuir*, 2021, **37**, 11018.

128. R. Wang, N. Li, C. Wang, J. Gao, L. Guo, Z. Qin, J. Gu, M. Wang, Z. Liu, T. Jiao, *Langmuir*, 2021, **37**, 8616.

129. S. K. Das, K. Pal, T. S. Bhattacharya, P. Karmakar, J. Chowdhury, *Sens. Actuators B*, 2019, **299**, 126962.

130. R. Wang, M. Li, J. Zhou, L. Zhang, J. Gu, M. Wang, T. Jiao, *ACS Omega*, 2021, **6**, 4430.

131. F. Xu, F. Ma, Z. Ding, L. Xiao, X. Zhang, Q. Lu, G. Lu, D. L. Kaplan, *ACS Appl. Mater. Interfaces*, 2019, **11**, 42896.

132. R. Mei, Y. Wang, Q. Yu, Y. Yin, R. Zhao, L. Chen, *ACS Appl. Mater*., 2020, **12**, 2059.

133. N. R. Barveen, T.- J. Wang, Y.- H. Chang, *Chem Eng. J*., 2022, **431**, 134240.

134. L. Yang, Y. Peng, Y. Yang, J. Liu, H. Huang, B. Yu, J. Zhao, Y. Lu, Z. Huang, Z. Li, J. R. Lombardi, *Adv. Sci*., 2019, **6**, 1900310.

135. M. Lafuente, S. Ruiz-Rincon, R. Mellada, P. Cea, M. P. Puna, *Appl. Surf. Sci*., 2020, **506**, 144663.

136. S. K. Bhunia, L. Zeiri, J. Manna, S. Nandi, R. Jelinek, *ACS Appl. Mater. Interfaces*, 2016, **8**, 25637.

137. M. Tahghighi, I. Mannelli, D. Janner, J. Ignes- Mullol, *Appl. Surf. Sci*., 2018, **447**, 416.

138. C. Zhang, S. Chen, Z. Jiang, Z. Shi, J. Wang, L. Du, *ACS Appl. Mater. Interfaces*, 2021, **13**, 29222.

139. N. Li, S. Han, S. Lin, X.-Y. Sha, W. Hasi, *New. J. Chem*., 2021, **45**, 7571.

140. J. P. Camden, J. A. Dieringer, Y. Wang, D. J. Masiello, L. D. Marks, G. C. Schatz, R. P. Van Duyne, *J. Am. Chem. Soc*., 2008, **130**, 12616.

141. H. Liang, Z. Li, W. Wang, Y. Wu, H. Xu, *Adv Mater*., 2009, **21**, 1.

142. T. Vo- Dinh, M. V. K. Hiromoto, G. M. Begun, R. L. Moody, *Anal. Chem*., 1984, **56**, 1667.

143. E. C. Le. Ru, M. Meyer, P. G. Etchehoin, *J. Phys. Chem. B*, 2006, **110**, 1944.

144. F. Beffara, J. Perumal, A. P. Mahyuddin, M. Choolani, S. A. Khan, J. L. Auguste, S. Vedraine, G. Humbert, U. S. Dinish, M. Olivo, *J. Biophotonics*., 2020, **13**, e201960120.
145. S. A. Adams, J. L. Hauser, A. C. Allen, K. P. Lindquist, A. P. Ramirez, S. Oliver, J. Z. Zhang, *ACS Appl. Nano Mater*., 2018, **1**, 1406.
146. G. Cabello, K. C. Nwoko, J. F. Marco, M. Sanchez-Arenillas, A. M. Mendez-Torres, J. Feldmann, C. Yanez, T. A. D. Smith., *J. Alloys and Compounds*, 2019, **791**, 184.
147. W. Lin, S. Lai, D. Lu, Q. Zhang, X. Lin, J. Lin, J. Wang, Z. Huang, *Sens. Actuators B*, 2022, **356**, 131361.
148. H. Chen, S.-G. Park, N. Choi, H.-J. Kwan, T. Kang, M.-K. Lee, J. Choo, *ACS Sens*., 2021, **6**, 2378.
149. V. Karunakaran, V. N. Saritha, A. N. Ramya, V. P. Murali, K. G. Raghu, K. Sujathan, K. K. Maiti, *Anal. Chem*., 2021, **93**, 11140.
150. C. Liu, M. Yang, J. Yu, F. Lei, Y. Wei, Q. Peng, C. Li, Z. Li, C. Zhang, B. Man, *Sens. Actuators B*., 2020, **307**, 127663.
151. B. Hu, D. W. Sun, H. Pu, Q. Wei, *Talanta*, 2020, **217**, 120998.
152. T. Subramaniam, K. Girija, *J. Food. Compos. Anal*., 2022, **106**, 104330.
153. M. Lee, K. Oh, H. K. Choi, S. G. Lee, H. J. Youn, H. L. Lee, D. H. Jeong, *ACS Sens*., 2018, **3**, 151.
154. S. Xu, W. Tang, D. B. Chase, D. L. Sparks, J. F. Rabolt, *ACS Appl. Nano. Mater*., 2018, **1**, 1257.
155. Y. Zhao, Y. Yamaguchi, Y. Ni, M. Li, X. Dou, *Spectrochimica Acta Part A*, 2020, **233**, 118193.
156. G. Wen, S. Pan, M. Gan, A. Liang, Z. Jiang, *ACS Appl. Bio. Mater*., 2021, **4**, 4582.
157. C. Fan, X. Zhang, J. M. Lv, J. Bai, Z. Qiu, Y. M. Zhao, Z. L. Wu, H. J. Xu, *Anal. Methods*, 2021, **13**, 3274.
158. S. D. Bindesri, D. S. Alhatab, C. L. Brosseau, *Analyst*, 2018, **143**, 4128.
159. M. Muhammad, C. Shao, Q. Huang, *Spectrochem. Acta Part A*, 2019, **223**, 117282.
160. H. Chen, S.- K. Park, Y. Joung, T. Kang, M.- K. Lee, J. Choo, *Sens. Actuators B*, 2022, **355**, 131324.
161. X. Su, Y. Xu, H. Zhao, S. Li, L. Chen, *Talanta*, 2019, **194**, 903.

162. B. N. Khlebtsov, D. N. Bratashov, N. A. Byzova, B. B. Dzantiev, N. G. Khlebtsov, *Nano Res*., 2019, **2**, 413.

163. A. Pramanik, Y. Gao, S. Patibandla, D. Mitra, M. G. McCandless, L. A. Fassero, K. Gates, R. Tandon, P. C. Ray, *Nanoscale Adv*., 2021, **3**, 1588.

164. W. Wang, S. Kang, P. J. Vikesland, *Environ. Sci. Technol*., 2021, **55**, 9119.

165. J. Wu, X. Zhou, P. Li, X. Lin, J. Wang, Z. Hu, P. Zhang, D. Chen, H. Cai, R. Niessner, C. Haisch, P. Sun, Y. Zheng, Z. Jiang, H. Zhou, *Anal. Chem*., 2021, **93**, 8799.

166. M.A. Fikiet, S. R. Khandasammy, E. Mistek, Y. Ahmed, L. Halamkova, J. Bueno, I. K. Lednev, *Spectrochem. Acta Part A*, 2018, **197**, 255.

167. A. Hakonen, K. Wu, M. S. Schmidt, P. O. Andersson, A. Boisen, T. Rindzevicius, *Talanta*, 2018, **189**, 649.

168. R. Gao, X. Song, C. Zhan, C. Weng, S. Cheng, K. Guo, N. Ma, H. Chang, Z. Guo, L. B. Luo, L. Yu, *Sens. Actuators B*, 2020, **314**, 128081.

169. C. Byram, S. S. B. Moram, V. R. Soma, *Analyst*, 2019, **144**, 2327.

170. T. Liyanage, A. Rael, S. Shaffer, S. Zaidi, J. V. Goodpaster, R. Sardar, *Analyst*, 2018, **143**, 2012.

171. H. Wang, Z. Xue, Y. Wu, J. Gilmore, L. Wang, L. Fabris, *Anal. Chem*., 2021, **93**, 9373.

172. M. Velicka, E. Zacharovas, S. Adomaviciute, V. Sablinskas, *Spectrochem. Acta Part A*, 2021, **246**, 118956.

173.W. A. Hassanain, F. L. Theiss, E. L. Izake, *Talanta*, 2022, **236**, 122879.

Chapter 2: Experimental Section

2.1 Introductory Remarks

This chapter represents the detail discussions regarding the preparation of samples/ substrates and their characterizations using various characterization techniques like Normal Raman, SERS, UV- Vis absorption, Field Emission Scanning Electron Microscope (FESEM), High Resolution Tunnelling Electron Microscope (HRTEM), Energy Dispersive X-ray Analysis (EDX), Atomic Force Microscope (AFM), X-ray Photoelectron Spectroscope (XPS) etc.

2.2 Materials

Spectral grade Rhodamine 6G (R6G; ~ 95% dye content), 4-Mercaptopyridine (4-MPy; ~ 95% purity), Stearic acid (SA; > 99% purity), poly (methyl methacrylate) [PMMA, average molecular weight (M_w) ~ 1,20,000] and chloroauric acid ($HAuCl_4$) were purchased from Sigma-Aldrich and were used without further purification. Silver nitrate ($AgNO_3$), sodium borohydride ($NaBH_4$), ascorbic acid (AS), trisodium citrate, ethanol and acetone of spectral grade were purchased from E- Merck (Germany) and were used as received. Spectral grade Chloroform was purchased from SRL, India and no further purification was done before using it. Prior to the experiment, all the glass wares used in the experimental synthesis were cleaned with freshly prepared aqua- regia followed by thorough rinsing with distilled water. The solutions required for the experimental purposes were prepared by triple distilled water subsequently deionized using Milli- Q- plus system of Millipore Corporation, USA. The resistivity and the pH of the deionized water were 18.2 MΩ cm and 6.8 cm respectively.

2.3 Synthesis of Silver Nanocolloid (AgNC)

Silver nanocolloids (AgNCs) were synthesized according to the method as proposed by Creighton *et. al.* [1]. At first, an aqueous solution of 1.0×10^{-3} M $AgNO_3$ and 2.0×10^{-3} M $NaBH_4$ were prepared. The $NaBH_4$ was ice cooled by keeping it in a refrigerator for further use. The $AgNO_3$ solution was kept in a dark place as it is very photo sensitive in visible light. Then, 5 ml of as prepared aqueous solution of $AgNO_3$ was added rapidly to 15 ml ice- cooled aqueous solution of $NaBH_4$ with constant stirring. After the addition of aqueous $AgNO_3$ solution, a stable yellowish solution was generated that represents the formation of AgNCs and the as prepared AgNC was kept in a refrigerator at ~5°C temperature for two weeks for stability prior to the use in experimental purposes.

2.4 Synthesis of Gold Nanocolloid (AuNC)

Spherical gold nanocolloids (AuNCs) of average particle diameter ~ 55 nm were prepared by citrate reduction method as described by Frens and S. Basu *et al.* [2,3]. Typically, 50 ml aqueous solution of 0.25 M $HAuCl_4$ was taken in a flask and the solution was used as a precursor salt. After that the aqueous $HAuCl_4$ solution was heated up to boiling and 400 µl of 1% trisodium citrate was added to it followed by continuous stirring. Firstly, the colour of the solution became deep blue which finally changed to pink by the reduction process indicating the formation of quasi spherical gold nano colloidal particles with average particle diameter ~ 55 nm.

2.5 Synthesis of Silver coated Gold Nanocolloid (Au@AgNC)

The silver coated gold nano colloids (Au@AgNCs) were prepared by a two-step process. At first, AuNC with average particle diameter ~ 25 nm was prepared by the citrate reduction method as reported by Frens and S. Basu *et al.* [2,3]. The as prepared AuNCs were used as core and was coated with silver nanoparticles applying the procedure as described by N. R Jana *et. al*. to synthesize the Au@AgNCs. Briefly, to the as synthesized AuNCs, 50 µL aqueous solution of AS (0.1 M) was added followed by the subsequent addition of 250 µL aqueous solution of $AgNO_3$ (0.01 M) with vigorous stirring. The red coloured AuNCs solution finally turned to greenish yellow that confirms the formation of Au@AgNC.

2.6 Langmuir- Blodgett (LB) Deposition Technique

Langmuir- Blodgett (LB) technique is a very simple, sophisticated and well-known technique capable of depositing a single monolayer of amphiphilic molecules at the air- water interface. It also allows to produce multilayer structures with varying layer composition. During the LB film deposition, the surface pressure and surface tension plays a significant role. The instrument that can deposit the LB film is known as LB trough which contains a pair of computer-controlled Teflon barriers that are used to compress the monolayer, a Langmuir trough on which the molecule is spread and the monolayer is fabricated, a surface pressure sensor for measuring the surface pressure and a dipping equipment to dip the substrates onto which the films is to be deposited. The LB film deposition can be made by upstroke and downstroke. There are three techniques by which the LB films can be deposited and these are,

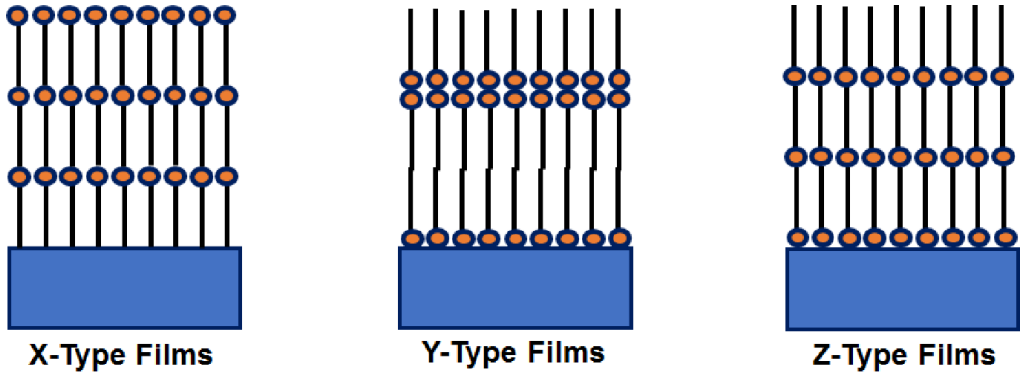

Figure 2.1: Different types of LB film deposition

(1) X-Type Deposition: In this type of deposition, when the substrate enters into the liquid only then the molecules can be deposited. The molecules are organized in head to tail arrangement.

(2) Y-Type Deposition: In this type of deposition, the molecules are deposited by down stroke only and it is the most common technique to deposit multilayer films.

(3) Z-Type Deposition: In this type of deposition, the film can be deposited only by the up stroke. The schematic diagram of various types of LB film deposition has been presented in Figure 2.1.

Before performing the LB film deposition, the quartz glass slides were cleaned vigorously with ethanol, deionized water and acetone. The monolayer and bilayer LB films of PMMA and SA respectively were lifted by Y- type deposition technique using an alternate layer computer-controlled Langmuir-Blodgett (LB) trough (Model No. D2007, Apex Instruments). Chloroform was used as solvent in the spreading solution and triple distilled deionized water of pH ~ 6.8 and 18.2 MΩ cm resistivity were used as sub phase. The room temperature surface pressure- area ($\pi - A$) compression isotherm was measured by the Wilhelmy method using a filter paper. The spreading solutions in the chloroform solvent were dispensed drop wise by a micro syringe on the air- water interface of the LB trough sustained at room temperature. After waiting for 20 minutes, such that all the chloroform solvent gets evaporated, the spreading molecules form floating monolayer at the air- water interface. Then the monolayer films were compressed quasistatically by moving the Teflon barrier of the dual LB trough at a constant speed of 2 mm/ min till the desired surface pressure attains. Due to the barriers compression, the surface pressure increases proportionally with the decrease of the area/ molecule of the system. The variation of surface pressure as a function of area/ molecule is represented as π- A isotherm plot. The room temperature $\pi - A$ compression isotherm was recorded during the compression steps by a film balance. After

reaching the desired surface pressure, the LB films of the SA and PMMA molecules were lifted on pre-cleaned quartz slides (Tedpella, Inc).

2.7 Preparation of the samples for SERS measurements

The as prepared LB films were incubated into the Ag, Au@Ag and Au nanocolloids for a desired time such that the nanocolloids are self-assembled onto the various LB film matrices. After that the films were removed from the nano colloids, washed repeatedly with deionized water and dried in a hot air oven under vacuum to eliminate the excess metallic ions presented on the LB films surfaces. Then the as prepared substrates were dipped into various concentrations of aqueous solutions of Raman probe molecules (such as, R6G, 4-MPy) for appropriate dipping times (DTs) to record the SERS signal.

2.8 Measurement of Normal Raman (NR) and SERS Spectra

The normal Raman (NR) and surface enhanced Raman scattering (SERS) spectra were recorded by J- Y Horiba Confocal Triple Raman Spectrometer (Model: T 64000) attached with

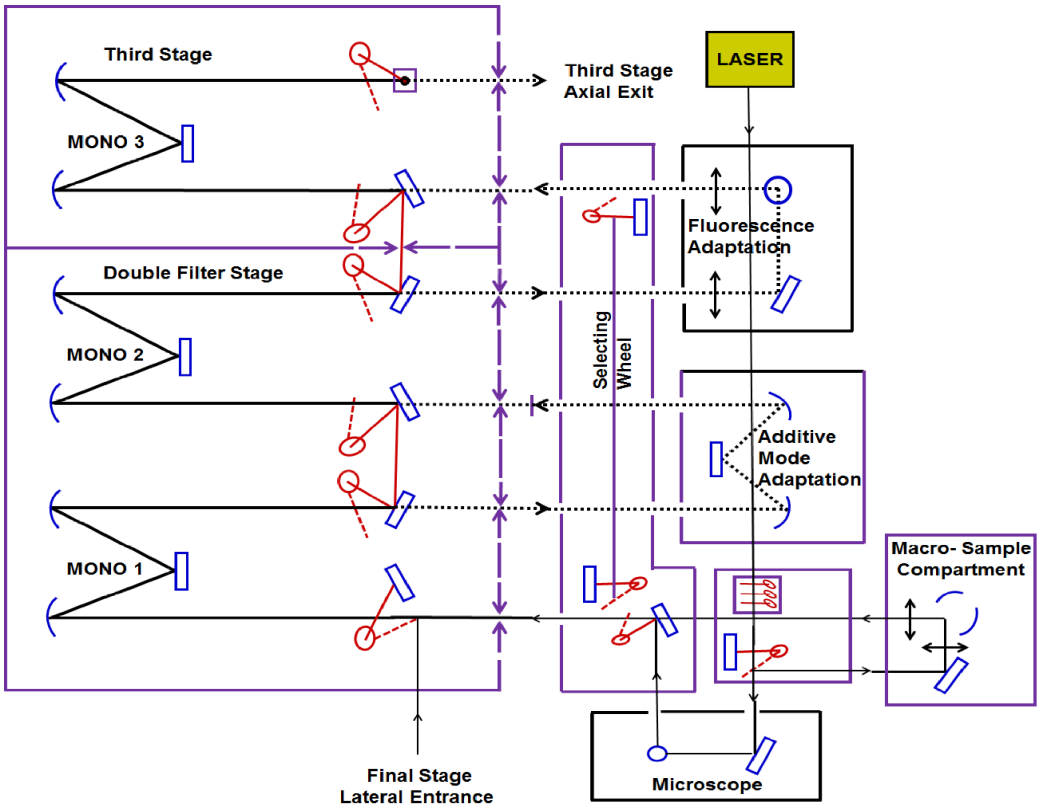

Figure 2.2: Schematic diagram of J–Y Horiba Confocal Triple Raman Spectrometer (Model: T64000)

holographic gratings of 1800 groove/ mm and a TE cooled synapse CCD detector from J- Y Horiba. The samples were excited using 514.5 [Spectra Physics, USA (Model.Stabilite2017)] and 632.8 nm [Melles Griot] excitation lights of $Ar^{+}$and He-Ne laser respectively. The laser was focused with an Olympus open stage microscope of 50x objective (Numerical Aperture = 0.75) lens and the scattered signals were collected at 180^{0} scattering angle to the excitations. The data acquisition times for both the NR and SERS spectra were 20 seconds. The detector and the data acquisition were controlled by Lab Spec 5 software as provided by Horiba. Figure 2.2 represents the schematic representation of the J–Y Horiba Confocal Triple Raman Spectrometer (Model: T64000).

2.9 Measurement of UV-Vis Absorption Spectra

Molecules are excited to a higher energy state when it absorbs light of a certain wavelength. The value of absorbance (A), extinction coefficient (ε), path length (l) and concentration of the solution is related as,

$$A = \varepsilon . c . l \qquad (2.1)$$

For various molecules, the absorbed radiations are in various wavelengths. In the UV-Vis absorption spectrometer, the emitted light from the source is passed through a diffraction grating and are followed by a rotating disc. Then the light spreads in two individual routes and proceeds through the sample and reference cell and are collected to a detector. Thus, the absorption spectrum of the sample can be acquired from the monitor.

The UV-Vis absorption spectra of both the synthesized nano colloids and the as prepared substrates had been recorded using JASCO UV–Vis absorption spectrometer (Model: V–630). For recording the UV- Vis absorption spectra of the nano colloids, the nano colloids were taken in a

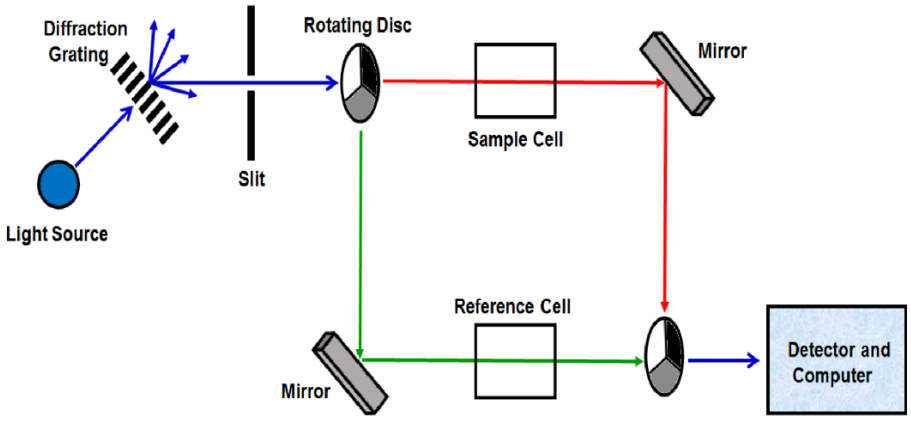

Figure 2.3: Schematic representation of JASCO UV–Vis V–630 spectrometer

quartz cuvette with 1 cm optical path length and the absorption spectra of the substrates were recorded by putting the slides in to the slide holder of the UV-Vis absorption spectrometer. The schematic representation of JASCO UV–Vis V–630 spectrometer is depicted in Figure 2.3.

2.10 Field Emission Scanning Electron Microscope (FESEM)

The Field Emission Scanning Electron Microscope (FESEM) is a robust and widely used instrument that is used to study the surface topography, composition, crystallographic properties

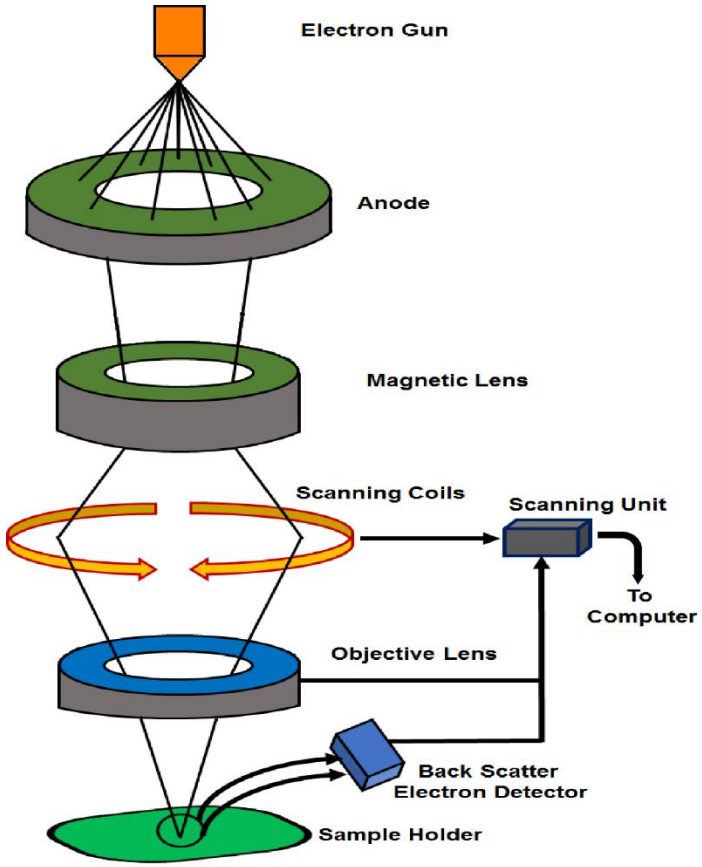

Figure 2.4: Schematic diagram of FESEM

etc of a sample. The elemental composition of a material, formation of magnetic domains can also be determined using the FESEM. The extremely large focal depth of the FESEM is suitable for topographic imaging. The FESEM consists of an optical system that generates electron probe, a sample holder to place the sample, a secondary electron detector that collects the secondary electrons, an image display unit and an operating system that performs various operations. The electron optical system is kept in vacuum and it consists with an electron gun, a condenser lens and an objective lens and some other components. Under vacuum condition, the Field Emission

source produces electrons that are accelerated in a field gradient. The beam focusses onto the specimen after passing through electromagnetic lenses which results the emission of different types of electrons from the impingement area of the specimen. The secondary electrons are collected by a detector and by correlating the intensity of these secondary electrons with the scanning primary electron beam, the image of the sample surface is generated which is displayed on the computer screen. The schematic diagram of a FESEM system is shown in Figure 2.4. The FESEM topography images of the as prepared substrates were recorded with INSPECT F50 FESEM with 10KV excitation energy.

2.11 High Resolution Tunnelling Electron Microscope (HRTEM)

Transmission Electron Microscope (TEM) is a very powerful microscopic technique that is used in material sciences and is consisted with three crucial systems as follows,

(1) An electron gun to generate the electron beam and a condenser system to focus the electron beams to the object.

(2) An image processing system which consists of objective lens, a movable stage for holding the sample and projector lenses that focus the electrons streaming through the specimen stage that is placed between the condenser lens and the objective lens in order to construct a magnified real image.

(3) An image recording system that converts the electron image into a digital image.

The schematic diagram of a HRTEM is given in Figure 2.5. The electron beam that is produced by the electron gun is incident onto the specimen after passing through the magnetic conducting lens. The beam may be partially diffracted and transmitted depending upon the incident angle and both the beams are coupled to generate an image which is known as phase contrast image. The diffracted beam is eliminated by passing the resultant beam through the magnetic objective lens and aperture for obtaining an image with higher intensity and contrast. Thus, only the transmitted beam is proceeded through the projector lens for additional magnification to obtain the final image which is recorded in the fluorescent screen or CCD. The high contrast image is also known as Bright Field Image that is produced due to the elastic scattering originated exclusively from the transmitted beam. The HRTEM images of the as synthesized nanocolloids were recorded with Tecnai TF20 ST Transmission Electron Microscope with 200 KV accelerating voltage.

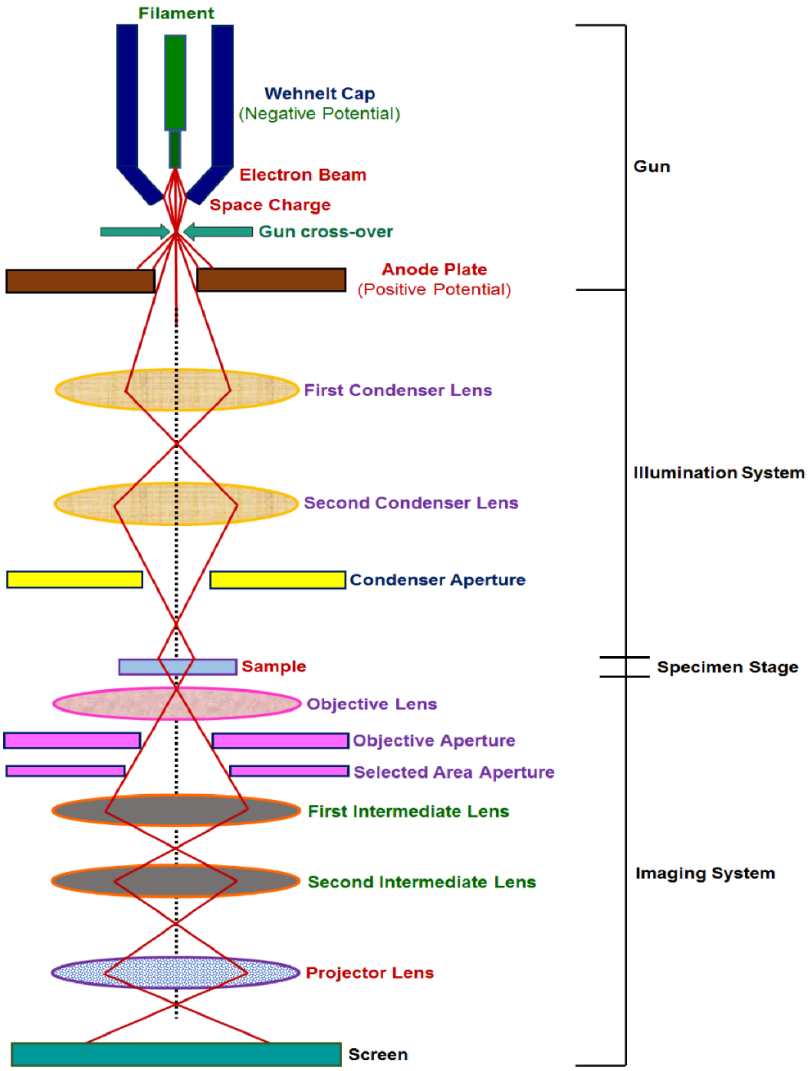

Figure 2.5: Schematic representation of HRTEM

2.12 Energy Dispersive X-ray Analysis (EDX)

Energy Dispersive X-ray Analysis (EDX) is a well-known analytical technique that is used for the chemical characterization and full quantitative elemental analysis of a sample exists in the sample composition. When a beam of charged particles with higher energy is incident onto the specimen then the electrons in the ground state are excited from lower energy state towards the higher energy state. The energy difference between the two states can be released as X- ray. The energy dispersive spectrometer can calculate the number and energy of the emitted X-rays from the sample. The EDX spectrum is represented as a histogram of the number of X-rays calculated at individual energy. The schematic diagram of an EDX is shown in Figure 2.6. The EDX analysis was carried out using an EDAX made Si (Li) type EDX detector.

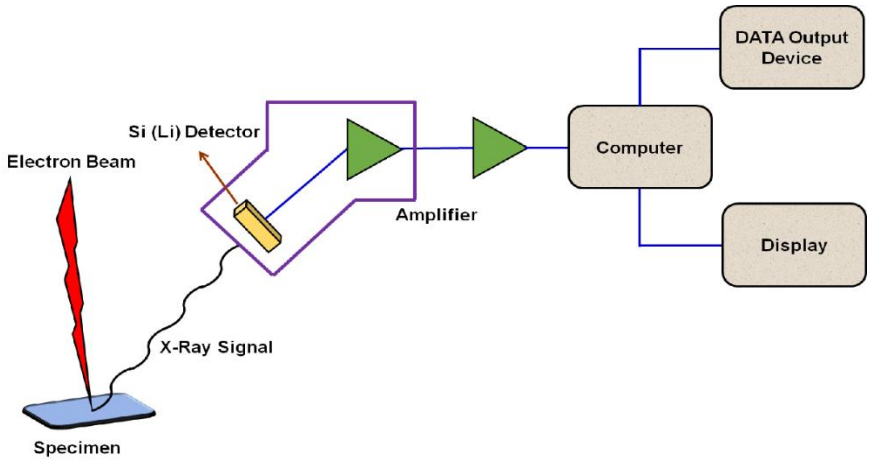

Figure 2.6: Schematic diagram of EDX

2.13 Atomic Force Microscope (AFM)

The Atomic Force Microscope (AFM) is high resolution scanning probe microscope and has appeared as a useful technique for analysing the surface interactions. The schematic diagram of an AFM is represented in Figure 2.7.

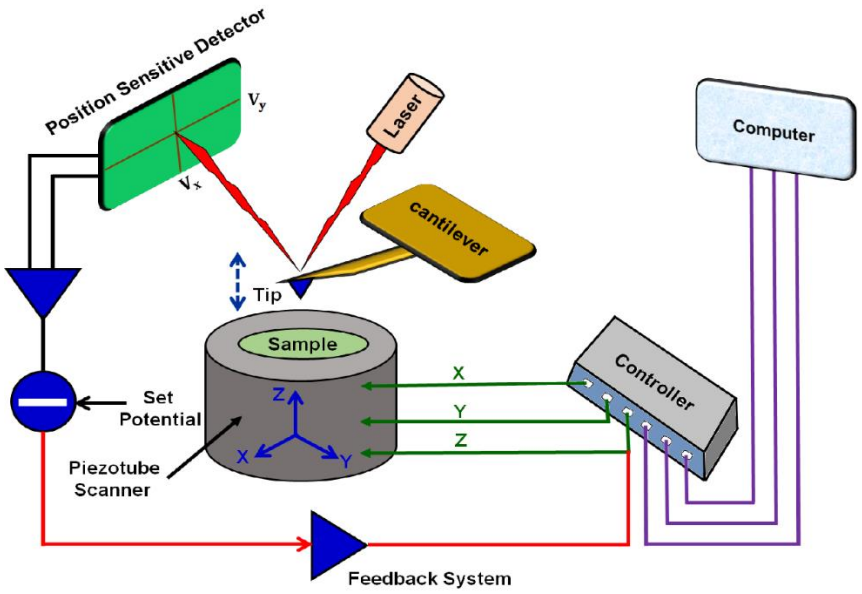

Figure 2.7: Schematic diagram of AFM

The major components of AFM are,

(1) The AFM probe that is supported on a soft cantilever.

(2) An optical lever to measure the deflections of the cantilever.

(3) The feedback loop to record the interaction forces between the molecules on the tip with the sample surface.

(4) A piezo-tube scanner to move the tip in a three-dimensional direction with respect to the sample.

(5) A conversion system to convert the instrumental raw data into a useful display.

Using the AFM, a nano scale three-dimensional profile of the specimen surface is obtained by monitoring the local forces between the tip molecule and the specimen surface at very small separation between the sample and probe. Three basic imaging modes are operative in AFM and these are.

❖ **Contact Mode:** In this AFM imaging mode the separation between the probe and sample surface is < 0.5 nm.

❖ **Intermittent contact mode or tapping mode:** In this AFM imaging mode the separation between the probe and sample surface is $0.5 - 2$ nm.

❖ **Non-contact Mode:** In this AFM imaging mode the separation between the probe and sample surface is $0.1 - 10$ nm.

The AFM morphologies of the as prepared substrates were carried out with Asylum Research (Model No. MFP-3D) Atomic Force Microscope (AFM) procured from Oxford Instruments operated in the tapping mode.

2.14 X-ray Photoelectron Spectroscopy (XPS)

The X-ray Photoelectron Spectroscopy (XPS) is a powerful technique that is widely used in surface analysis. The XPS can reveal the quantitative analysis of elemental compositions of a sample as well as the chemical and electronic state and also the binding states of an element in a sample. The main components of an XPS are,

(1) An Ultra High Vacuum (UHV) system (Pressure $< 10^{-8}$ Torr) to attain a prolonged photoelectron path length. The UHV system can also maintains a clean surface along with the prevention of contaminations.

(2) An X-ray source to irradiate the sample.

(3) An electron analyser to collect the photo electrons and a detector to count the electrons.

(4) Ion gun that is used for sample cleaning and also for depth profiling.

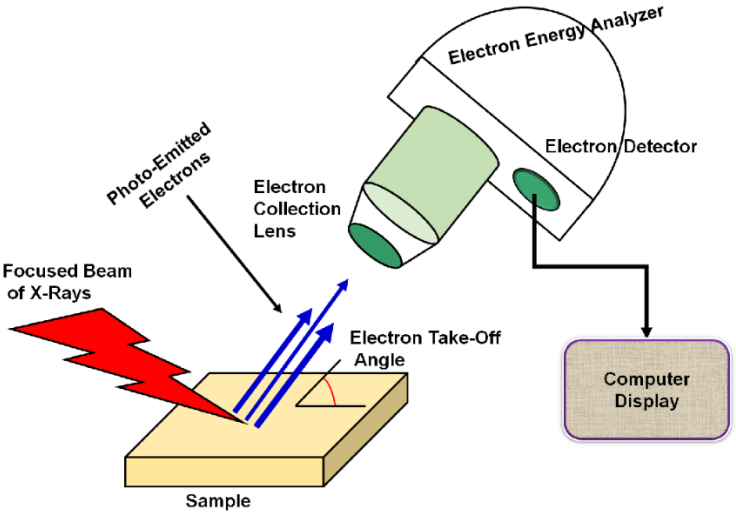

Figure 2.8: Schematic diagram of XPS

The schematic diagram of an XPS system is shown in Figure 2.8. When a sample is irradiated with monochromatic X-rays, the electrons are emitted from the sample surface. The emitted electrons are known as photoelectrons with energies characteristics to the elements present in the sample. The distribution of energy of the emitted photoelectrons can be estimated using an electron energy analyser. An XPS spectra is obtained by plotting the number of emitted electrons with their corresponding binding energies. The XPS analysis of the as prepared substrates was carried out using ULVAC PHI 5000 Versa Probe- II, operating at pressure ~ 1.6×10^{-6} Pascal. To irradiate the substrates the Al Kα (hυ = 1486.6 eV) X-ray source with a fixed operating power at 25 Watt and X-ray focus area 100 μm in diameter were applied. An analyser pass energy ~ 58.7 eV in 0.125 eV steps were employed to record the high resolution XPS spectra. The C1s peak at 284.5 eV was used as a reference of the binding energy scale.

References

1. J. A. Creighton, C. G. Blatchford, M. G. Albrecht, *J. Chem. Soc. Faraday Trans*. 2, 1979, **75**, 790.
2. G. Frens, *Nat. Phys. Sci*., 1973, **241**, 20.
3. S. Basu, S. K. Ghosh, S. Kundu, S. Panigrahi, S. Praharaj, S. Pande, S. Jana, T. Pal, *J. Colloid Inter. Sci*., 2007, **313**, 724.

Chapter 3: Theoretical and Computational Section

3.1 Introductory Remarks

The experimental results reported in this dissertation are further corroborated by theoretical calculations. The EM enhancements of the Raman spectra from the aggregated nanoparticles are estimated with the aid of Three-Dimensional Finite Difference Time domain (3D-FDTD) simulation studies. Moreover, the topographical features of the SERS active substrates have been envisaged from statistical considerations in terms of height-height correlation function (HHCF), auto correlation function (ACF), Hurst exponent, Lyapunov exponent etc. In the field of molecular spectroscopy, successful utilization of computational quantum chemistry has been made in order to elucidate the structure and properties of the molecule. The adsorptive behaviour of analyte 4-Mercaptopyridine (4MPy) molecule with gold nanoparticles (AuNPs) embedded in the bilayer Langmuir-Blodgett (LB) film matrix of stearic acid (SA) have been investigated by Born-Oppenheimer on the fly Molecular Dynamics (BO-OF-MD), time resolved wavelet transform theory (WT) and Density Functional Theory (DFT) calculations based on adcluster models. This present chapter deals with the discussions on the several theoretical and computational methods that has been effectively applied in our studies.

3.2 Finite Difference Time Domain (FDTD) Method

The Finite Difference Time Domain method is a widely accepted and well-known method to solve the EM problems using Maxwell's equations. The FDTD method can be used to solve varieties of EM problems including the estimation of the EM enhancement in SERS spectra. Though this method is little bit expensive but it is so simple method such that one can easily compute this program in three-dimensional code also. This technique was first addressed by Kane Yee in 1966 [1] and in the early 70s, this technique has been advanced by many other scientists. Under difference approximations of spatial and temporal derivatives of the Maxwell's curl equations (more precisely, Ampere's and faraday's laws), Yee suggested a distinct solution to the Maxwell's equations.

3.2.1 The Yee Algorithm

The Yee algorithm was first addressed by K. Yee in the year 1966 and can be recapitulated as below,

(1) All the derivatives present in the Ampere's and Faraday's laws are replaced by finite differences. The space and time have been discretized in a way such that the electric $(\vec{E})$ and magnetic $(\vec{H})$ fields begin to stagger in both space and time.

(2) The "update equations" which can unveil the future fields in terms of past fields can be obtained by solving the subsequent difference equations.

(3) The $\vec{H}$ and $\vec{E}$ fields are estimated as one time-step into the future such that they become the past fields and this step has been repeated till the desired duration.

The schematic representation of a typical 3D Yee cell is shown in Figure 3.1.

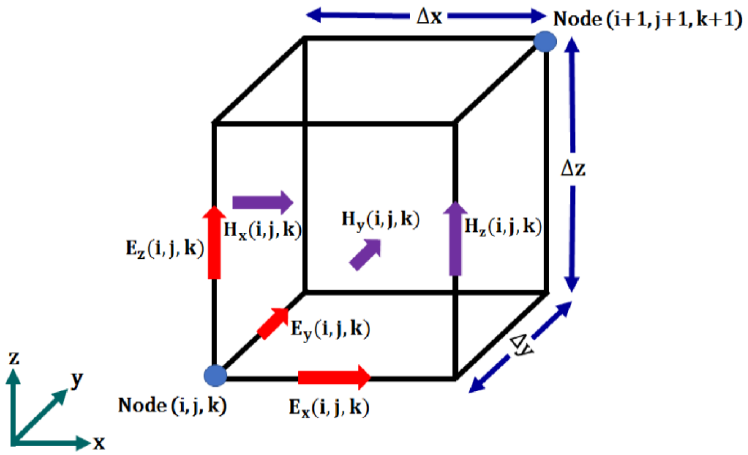

Figure 3.1: Schematic representation of a typical 3D Yee cell

3.2.2 Update Equations

The Faraday's and Ampere's law in a medium is represented as,

$$(\vec{\nabla} \times \vec{E}) = -\mu \frac{\partial \vec{H}}{\partial t} \qquad (3.1)$$

$$(\vec{\nabla} \times \vec{H}) = \varepsilon \frac{\partial \vec{E}}{\partial t} \qquad (3.2)$$

where, μ and ε signify the magnetic permeability and electrical permittivity of the medium respectively. Equation (3.1) represents the temporal derivative of the $\vec{H}$ field in connection with the spatial derivative of the $\vec{E}$ field that may be used to develop the $\vec{H}$ field. Alternatively, the equation (3.2) indicates the temporal derivative of the $\vec{E}$ field in connection with the spatial

derivative of the $\vec{H}$ field which may be employed to develop the $\vec{E}$ field. This repetitive process of developing one field after another is called as the "leap-frog" method.

The spatial and temporal derivatives of the Maxwell's electromagnetic equations [equation (3.1) and (3.2)] is replaced by finite difference equation discretized in Yee cells with the aid of the FDTD simulations based on Yee's algorithm. The temporal derivatives appear in the equation (3.1) and (3.2) are replaced by a finite difference incorporating the electric/ magnetic field at a fixed point at two different times. The spatial derivative appears in the equation (3.1) and (3.2) are replaced by a finite difference through the incorporation of the electric/ magnetic field at two different points but one time. The modified equations in terms of finite differences are known as "update equations". The electric and magnetic fields are estimated by solving the update equations iteratively until two consecutive iterations have significantly close value.

3.2.3 Perfectly Matched Layer (PML) Boundary Condition

Perfectly Matched Layer (PML) is an extensively accepted non-reflecting numerical technique used for wave simulations. The PML is an artificial layer that is developed to create no reflection irrespective of the frequency, polarization and the incidence angle of a plane wave upon its interface. The PML was first introduced by Jeanne-Pierre Berenger [2] in 1994. Berenger's PML is based on the splitting of each field component of Maxwell's equation into two separate parts due to which a non-physical absorbing medium is created in the neighbourhood of the outer FDTD mesh boundary having a wave impedance independent of the frequency and the incidence angle of the outgoing scattered waves. Due to the PML absorbing media boundary, the FDTD method has grown to be an efficient simulation technique for a versatile scope of applications.

3.2.4 Total-Field/ Scattered-Field (TF/SF) Formalism

As the FDTD is finite in size whereas, the plane wave is extended infinitely along the perpendicular direction to its propagation, there was a difficulty in evaluating the interaction of an incident wave with objects or structures placed within the computational domain. In order to compute such type of problems it is considered that in most situations, the incident wave is a plane wave which have to be originated within the FDTD region. By calculating the scattered field in spite of the total field this problem was overcome before 1980. In this method the incident wave has to be replaced by the current sources but in that case, the FDTD noise restricted the dynamic

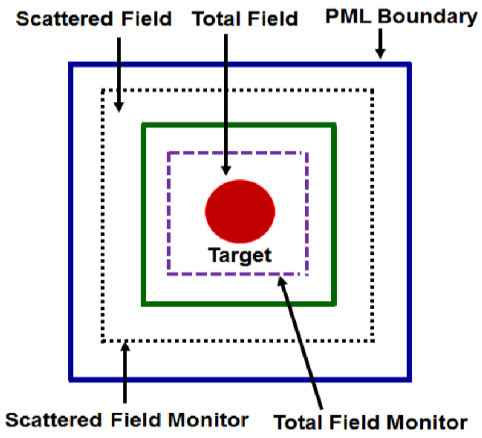

Figure 3.2: Schematic representation of the FDTD simulation domain consisting TF/SF source

range of the FDTD domain. To solve this problem, a finer method was proposed by D. E. Merewether *et. al*. [3] which is known as the Total-Field/ Scattered- Field (TF/SF) method or the Huygens surface method. The concerned zone is surrounded by an imaginary surface at which the sources replaces the incident wave. Inside the closed region, the total field is present that consists with the incident and the scattered field while the outer region is known as the scattered field region that contains with the scattered field only. The schematic representation of the FDTD simulation domain consisting TF/SF source is shown in Figure 3.2.

Let, $\vec{E}_{inc}$ and $\vec{H}_{inc}$ denote the incident $\vec{E}$ and $\vec{H}$ field respectively. Similarly, if the total field and the scattered field are denoted by ($\vec{E}_{tot}$ and $\vec{H}_{tot}$) and ($\vec{E}_{scat}$ and $\vec{H}_{scat}$) respectively, then from the TF/SF definition it can be expressed that,

$$\vec{E}_{scat} = \vec{E}_{tot} - \vec{E}_{inc} \qquad (3.3\ a)$$

$$\vec{H}_{scat} = \vec{H}_{tot} - \vec{H}_{inc} \qquad (3.3\ b)$$

According to the TF/ SF formalism, the field in the internal region of the FDTD domain is ($\vec{E}_{tot}, \vec{H}_{tot}$) and the external region contains with fields ($\vec{E}_{scat}, \vec{H}_{scat}$). The absorption coefficient (Q_{abs}), scattering coefficient (Q_{scat}) and extinction coefficients (Q_{ext}) can also be estimated from the TF/ SF formalism. For an arbitrary shaped nanoparticle, the Q_{abs}, Q_{scat} and Q_{ext} can be written as [4]

$$Q_{abs} = \frac{U_{abs}(\omega)}{\pi a^2 I_i} \qquad (3.4)$$

$$Q_{scat} = \frac{U_{scat}(\omega)}{\pi a^2 I_i} \qquad (3.5)$$

$$Q_{ext} = Q_{abs} + Q_{scat} \qquad (3.6)$$

where, U_{abs} and U_{scat} are the amount of power absorbed and scattered per unit area respectively. The radius of the nanoparticle is denoted by "a" and I_i signifies the intensity of the incident radiation.

3.3 FDTD Computational Details

The spatial distributions of the $\vec{E}$ field along the aggregated nanostructures had been estimated using 3D-FDTD simulation studies. The FDTD calculations were carried out with the aid of 3D- FDTD Lumerical Solutions, Inc [5]. The dimension of the Yee cell was selected as (1 x 1 x 1) nm^3 for the simulations. The Johnson- Christy dielectric data for gold [6] and water, with real refractive index 1.33, were introduced as the background medium. In the simulation run, a plane polarized light wave was incident on the nano particles with the excitation at desired wavelengths. The perfectly matched layer (PML) boundary condition was introduced to eliminate the unwanted reflections and back scattering of the $\vec{E}$ fields. The $\vec{E}$ field distributions within the aggregated nanoparticles were recorded using a frequency domain field monitor. The extinction spectra were estimated employing the TF/SF method. To ensure the total concurrence of the $\vec{E}$ field the simulation time was set at 500 fs.

3.4 Statistical Analysis of Rough Surfaces

Mathematically, a random rough surface can be represented as $h = h(\vec{q})$, where h denotes the mean surface height and $\vec{q}$ signifies the position vector on the surface. The height h of any rough surface is a single valued function of $\vec{q}$. For a randomly rough surface it is considered that the variation of height is a random field with reference to the position. As the random rough surface of interest is homogeneous and isotropic, a brief idea regarding the random field in connection with some roughness parameters associated with a random rough surface is given below.

3.4.1 First Order Statistics

The probability of being the height of the surface within h and $h + dh$ at any point on the surface is $p(h)dh$, where $p(h)$ is a non-negative function of h and is known as the height distribution function which upon normalization can be written as,

$$\int_{-\infty}^{+\infty} p(h)dh = 1 \qquad (3.7)$$

As the height distribution varies with the roughness of the surface, the most common representation of the height distribution is the Gaussian height distribution which can be expressed as,

$$p(h) = \frac{1}{\omega\sqrt{2\pi}} \exp\left(-\frac{h^2}{2\omega^2}\right) \qquad (3.8)$$

where, ω denotes the root-mean-square (RMS) roughness or the interface width. In this connection it is worth to mention that considering the other roughness parameters are unchanged, the surface become rougher with the increase of the value ω. To measure the symmetry of the distribution for a mean surface level, the "skewness" (γ_3) parameter is introduced which is a dimensionless parameter and is defined by,

$$\gamma_3 = \frac{1}{\omega^3} \int_{-\infty}^{+\infty} h^3 p(h)dh \qquad (3.9)$$

The skewness of a surface can be positive or negative in sign which denotes that the farther points are proportionally higher or lower than the average surface height respectively. "Kurtosis" (γ_4) is also a dimensionless parameter which can be used to estimate the sharpness of the height distribution function and it can be defined as,

$$\gamma_4 = \frac{1}{\omega^4} \int_{-\infty}^{+\infty} h^4 p(h)dh \qquad (3.10)$$

For a perfectly random surface i.e., for Gaussian distribution of the surface height profile, the value of γ_4 is equal to 3.0. Moreover, if the value of γ_4 is less than 3, then it is called platykurtic which corresponds to a mild peak. Similarly, if the value of γ_4 is greater than 3, it is called leptokurtic that signifies sharp peak.

3.4.2 Second Order Statistics

With the help of first order statistics, the properties of random variables at a distinct site from the statistical point of view can be explained easily whether it fails to elucidate the correlation between the random variables at different positions. Considering $\vec{q}_1$ and $\vec{q}_2$ as two different positions, a joint distribution probability density function has been proposed to understand the correlation of a random field $h(\vec{q})$ at $\vec{q}_1$ and $\vec{q}_2$ which fulfils,

$$\int_{-\infty}^{+\infty}\int_{-\infty}^{+\infty} p_j(h_1, h_2; \vec{q}_1, \vec{q}_2)dh_1dh_2 = 1 \qquad (3.11)$$

$$\int_{-\infty}^{+\infty} p_j(h_1, h_2; \vec{q}_1, \vec{q}_2)dh_1 = p(h_2) \qquad (3.12)$$

$$\int_{-\infty}^{+\infty} p_j(h_1, h_2; \vec{q}_1, \vec{q}_2)dh_2 = p(h_1) \qquad (3.13)$$

where, the minimal distributions of $p_j(h_1, h_2; \vec{q}_1, \vec{q}_2)$ are denoted by $p(h_1)$ and $p(h_2)$ and generally, the term $p_j(h_1, h_2; \vec{q}_1, \vec{q}_2)$ represents the connection of the height profile at two different positions. For a homogeneous arbitrary field $p(h_1) = p(h_2) = p(h)$ where h_1 and h_2 does not depend on one another. The auto-relation function $[R(\vec{q}_1, \vec{q}_2)]$ for a joint distribution can be defined as,

$$R(\vec{q}_1, \vec{q}_2) = \frac{G(\vec{q}_1, \vec{q}_2)}{A^2} \qquad (3.14)$$

where, $G(\vec{q}_1, \vec{q}_2)$ is known as the auto-covariance function which can be represented as,

$$G(\vec{q}_1, \vec{q}_2) = E\{h(\vec{q}_1)h(\vec{q}_2)\} = \int_{-\infty}^{+\infty}\int_{-\infty}^{+\infty} h_1h_2p_j(h_1, h_2; \vec{q}_1, \vec{q}_2)dh_1dh_2 \qquad (3.15)$$

If the two positions $\vec{q}_1$ and $\vec{q}_2$ are overlapped i.e., $|\vec{q}_1 - \vec{q}_2| = \lambda = 0$, where λ is the distance between the two positions $\vec{q}_1$ and $\vec{q}_2$ and in that case the difference between the functions $G(\vec{q}_1, \vec{q}_2)$ and $R(\vec{q}_1, \vec{q}_2)$ depends upon only the term A^2. For a homogeneous and isotropic rough surface both the $G(\vec{q}_1, \vec{q}_2)$ and $R(\vec{q}_1, \vec{q}_2)$ depend on λ, i.e.,

$$G(\vec{q}_1, \vec{q}_2) = G|\vec{q}_1 - \vec{q}_2| = G(\lambda) \qquad (3.16)$$

$$R(\vec{q}_1, \vec{q}_2) = R(\lambda) \qquad (3.17)$$

The lateral correlation length (ζ) is a measure of the distance between any two points on the surface at which the heights of the two points are correlated and can be estimated from the value of $R(\lambda)$ at which it drops to $1/e$ of its value at zero lag (i.e., at $\lambda = |\vec{q}_1 - \vec{q}_2|$), such as,

$$R(\zeta) = 1/e \qquad (3.18)$$

In this connection it is plausible to mention that if the distance between two points on the surface is less than the value of ζ, then the surface heights of those two points are supposed to be correlated. Similarly, if the two points are beyond the value of ζ, then the surface heights of those two points are independent of each other.

Let us consider, two different samples with different correlation functional form but with same RMS roughness (ω) and lateral correlation length (ζ). In that case, a new parameter, roughness exponent or Hurst exponent (α) is need to be introduced for the full illustration of surface roughness. The value of α is equal to 1 for a Gaussian correlation and for an exponential correlation, the value of α is equal to 0.5. Similar to the correlation function $R(\vec{\lambda})$, the height-height correlation function (HHCF) $H(\vec{\lambda})$, can be represented as,

$$H(\vec{\lambda}) = E\left\{\left[h(\vec{q}) - h(\vec{q} + \vec{\lambda})\right]^2\right\} \qquad (3.19)$$

The interrelation between the $H(\vec{\lambda})$ and $R(\vec{\lambda})$ can be defined as,

$$H(\vec{\lambda}) = 2\omega^2\left[1 - R(\vec{\lambda})\right] \qquad (3.20)$$

For a homogeneous, isotropic random surface, $H(\vec{\lambda})$ is an even function in respect of λ i.e., $H(\vec{\lambda}) = H(\lambda)$. In that situation, the equation (3.20) will have the following representations,

$$\text{for } \lambda = 0, H(0) = 0$$
$$\text{and for } \lambda \to \infty, H(\lambda \to \infty) = 2\omega^2 \qquad (3.21)$$

In the reciprocal space, one more statistical parameter is introduced known as Power spectrum which have the following expression,

$$P(\vec{k}) = \frac{1}{2\pi}\int_{-\infty}^{+\infty} G(\lambda)e^{-i\vec{k}.\vec{\lambda}}d\lambda \qquad (3.22)$$

where, $\vec{k}$ is the wave vector in the Fourier space. The power spectrum does not depend on the direction for a homogeneous, isotropic and random rough surface.

3.4.3 Self-Affine Surfaces

An object is called self-affine if it remains unchanged after the transformation of the object by different proportion in all directions. A self-affine surface is a type of fractal entity which can be defined by the fractal dimension of the surface. The HHCF of a self-affine rough surface can be written as,

$$H(q) = 2\omega^2\left[1 - e^{\left(-\frac{q}{\zeta}\right)^{2\alpha}}\right]$$
$$= 2\omega^2 f\left(\frac{q}{\zeta}\right) \qquad (3.23)$$

where, $\vec{q}$ is the displacement vector, ω^2 denotes the RMS roughness, α represents the Hurst exponent $(0 \leq \alpha \leq 1)$ and ζ signifies the lateral correlation length. The scaling function $f(x)$ can be defined as, $f(x) = f\left(\frac{q}{\zeta}\right)$ which have the following characteristics,

$$f(x) = x^{2\alpha}, \text{for } x \ll 1$$
$$f(x) = 1, \text{for } x \gg 1 \qquad (3.24)$$

The value of α helps to determine whether it is anticorrelations $(0 < \alpha < 0.5; \text{sub diffusion})$, long-range correlations $(0.5 < \alpha < 1; \text{super diffusion})$ or an uncorrelated series $(\alpha = 0.5; \text{diffusion})$. Within the lateral correlation length $(q \ll \zeta)$, the value of α corresponds to the short-range roughness characteristics and the power law is obeyed. On the other hand, away from the lateral correlation length $(q \gg \zeta)$, the HHCF acquires the asymptotic value $(\sim 2\omega^2)$ signifying the long-range roughness characteristics [7]. The fractal dimension (D_s) is related to the value of α as,

$$\alpha = d + 1 - D_s \qquad (3.25)$$

where, the dimension of the embedded space is denoted by $(d + 1)$. The feature of a self-affine system also can be represented by the power spectrum in the reciprocal space and can be defined as,

$$P(k) = \frac{4\pi\alpha\omega^2\zeta^2}{(1 + k^2\zeta^2)^{1+\alpha}} \qquad (3.26)$$

From the power spectrum it can be shown that the FWHM of $P \propto \frac{1}{\zeta}$.

3.4.4 Chaos and Lyapunov Exponent

Chaos is a non-periodic characteristic in a system with noiseless parameters or inputs that depends sensitively upon the initial conditions. To be chaotic, a system should reveal sensitive dependence on initial conditions which means that the neighbouring trajectories that start very close together will diverge exponentially fast.

Let, x_0 is an initial point and $(x_0 + \delta_0)$ be a nearby point, where δ_0 denotes an exceedingly small initial separation. If δ_n satisfies the separation after l steps, then the relation between δ_l and δ_0 can be explained as,

$$|\delta_l| \approx |\delta_0| e^{\lambda l} \qquad (3.27)$$

where, λ is known as the Lyapunov exponent. The Lyapunov exponent (λ) divulges the information about the rate of exponential convergence or divergence of trajectories in phase space with time. For a system to be chaotic, the value of λ should be positive. Moreover, if the value of λ is negative, then the system is called periodic orbit and for a stable orbit, the value of λ is zero [8].

3.5 Computational Details for Statistical Analysis of the Substrate Surfaces

The various statistical parameters like the lateral correlation length, RMS roughness or the interface width, Hurst exponents etc had been evaluated from the Gwyddion 2.49 software [9]. The estimation of Lyapunov exponents of the chaotic substrates had been made from TISEAN software applying Rosenstein's method [10,11].

3.6 Density Functional Theory (DFT)

The density functional theory (DFT) has been established as a well-known technique to enumerate the electronic structure of several types of molecules in the condense phase [12-14]. It is a quantum mechanical approach and is based upon the principles of many body quantum mechanics. This technique can produce highly satisfactory results with lower computational resources.

In 1927, the way of calculating the approximate wavefunctions and energies for atoms and ions was introduced by Hartree which is called the Hartree function. After few years, the Hartree-Fock model was introduced considering the Pauli principles and the multielectron wave function. Also, in 1927, a statistical model was proposed by Thomas and Fermi that can conclude the energy of atoms from the electron distribution in an atom. Primarily in that statistical model, only the nuclear-electron and electron-electron interaction terms were considered but in 1928, an exchange energy functional term was added by Dirac. The applications of the Thomas- Fermi model is inadequate due to some major drawbacks and complete disregard of the electron correlation effect. To overcome this problem, P. Hohenberg and W. Kohn (H- K) introduced the DFT method in 1964.

The basic concept of DFT is to replace the complicated wavefunctions containing 3N variables with the function of electron density that comprises only 3 variables. In the first H-K theorem, Hohenberg and Kohn established that the ground state properties of a many-electron system are uniquely dependent on the electron density. In the second H-K theorem, they proved that the ground state energy can be attained by the energy minimization of the system according

to the electron density. The 1st and 2nd H- K theorem only furnish the existence of the one-to-one mapping relations between the electron density function and system properties of a many electrons system without giving any exact relation between them.

In 1965, Kohn and Sham (K- S) published a paper where the multielectron problem has been simplified into a non- interacting electrons problem in an effective potential. The basic concepts of the K- S approach are as follows: **(1)** Representation of the molecular energy as a sum of terms, within which, only one comparatively small term, involves the "unknown functional". So, the moderately large errors in this energy term will not bring up any big errors into the total energy. **(2)** To calculate an initial guess of the K- S orbitals and energy levels by using an initial guess of the electron density in the K- S equations. These orbitals and energy levels are then iteratively refined using this initial guess in a way as it has been done in the Hartree- Fock self-consistent field (HF SCF) method. The energy of the system is obtained from the electron density which is calculated using the final K- S orbitals.

The ground state electron energy (E_0) of a molecule can be expressed as a sum of the electron kinetic energies $\langle T[\rho_0]\rangle$, the nucleus- electron attraction potential energies $\langle V_{Ne}[\rho_0]\rangle$ and the electron- electron repulsive potential energies $\langle V_{ee}[\rho_0]\rangle$ as,

$$E_0 = \langle T[\rho_0]\rangle + \langle V_{Ne}[\rho_0]\rangle + \langle V_{ee}[\rho_0]\rangle \qquad (3.28)$$

The potential corresponding to the nucleus- electron interaction for all the nuclei can be represented as,

$$\langle V_{Ne}\rangle = \sum_{i=1}^{2n} \sum_{\text{nuclei A}} -\frac{Z_A}{\vec{r}_{iA}} = \sum_{i=1}^{2n} v(\vec{r}_i) \qquad (3.29)$$

where, $Z_A/\vec{r}_{iA}$ represents the potential energy that arises from the interaction between electron i and nucleus A at various distance $\vec{r}$. 2n is the total number of electrons in a closed shell molecule and $v(\vec{r}_i)$ is the external potential for the attraction of electron i to all the nuclei. If $f(\vec{r})$ represents a spatial function of electron i of the system and ψ be the total wave function of the system, then, taking ρ as density function, the following expression can be written [15],

$$\int \psi \sum_{i=1}^{2n} f(\vec{r}_i)\, \psi d\tau = \int \rho(\vec{r})\, f(\vec{r}) d\vec{r} \qquad (3.30)$$

The integration on the left-hand side of the above equation contains the spatial and spin coordinate while the right-hand side integration contains only the spatial coordinate of the system. From equation (3.29) and (3.30), the expectation value $\langle V_{Ne} \rangle$ can be written in terms of the ground state density function ρ_0 as,

$$\langle V_{Ne} \rangle = \int \rho_0(\vec{r}) v(\vec{r})\, d\vec{r} \qquad (3.31)$$

Thus, equation (3.28) can be written as,

$$E_0 = \langle T[\rho_0] \rangle + \int \rho_0(\vec{r})\, v(\vec{r}) d\vec{r} + \langle V_{ee}[\rho_0] \rangle \qquad (3.32)$$

The middle term of equation (3.32) is the expression of the classical electrostatic attractive potential energy. As the proper functionals of the terms $\langle T[\rho_0] \rangle$ and $\langle V_{ee}[\rho_0] \rangle$ is unknown, an idea of a fictitious reference system of non-interacting electrons has been introduced by Kohn and Sham in order to get exactly the same distribution of electron density of the real system.

The deviation of the real electrostatic kinetic $[\Delta\langle T[\rho_0] \rangle]$ and potential energy $[\Delta\langle V_{ee}[\rho_0] \rangle]$ from that of the reference system can be expressed as,

$$\Delta\langle T[\rho_0] \rangle = \langle T[\rho_0] \rangle_{real} - \langle T[\rho_0] \rangle_{ref} \qquad (3.33)$$

and

$$\Delta\langle V_{ee}[\rho_0] \rangle = \langle V_{ee}[\rho_0] \rangle_{real} - \frac{1}{2} \int \int \frac{\rho_0(\vec{r}_1)\rho_0(\vec{r}_2)}{\vec{r}_{12}} d\vec{r}_1 d\vec{r}_2 \qquad (3.34)$$

The 1st term of equation (3.34) represents the electron-electron repulsion energy of a real system and the 2nd term denotes the repulsion energy of a pair of classical charge cloud separated at a distance $\vec{r}_{12}$. Using equation (3.33) and (3.34), the equation (3.32) can be written as,

$$E_0 = \int \rho_0(\vec{r}) v(\vec{r}) d\vec{r} + \langle T[\rho_0] \rangle_{ref} + \frac{1}{2} \int \int \frac{\rho_0(\vec{r}_1)\rho_0(\vec{r}_2)}{\vec{r}_{12}} d\vec{r}_1 d\vec{r}_2 + \Delta\langle T[\rho_0] \rangle + \Delta\langle V_{ee}[\rho_0] \rangle \qquad (3.35)$$

The sum of the last two term of equation (3.35) designates the deviation of kinetic energy from the reference system and the deviation of electron- electron repulsive energy from the classical system and is known as the exchange- correlation energy $E_{xc}[\rho_0]$,

$$E_{xc}[\rho_0] = +\Delta\langle T[\rho_0] \rangle + \Delta\langle V_{ee}[\rho_0] \rangle \qquad (3.36)$$

So, using equation (3.36), the equation (3.35) becomes,

$$E_0 = \int \rho_0(\vec{r}) v(\vec{r}) d\vec{r} + \langle T[\rho_0] \rangle_{ref} + \frac{1}{2} \int \int \frac{\rho_0(\vec{r}_1)\rho_0(\vec{r}_2)}{\vec{r}_{12}} d\vec{r}_1 d\vec{r}_2 + E_{XC}[\rho_0] \qquad (3.37)$$

The 1st term of the equation (3.37) is the integral of the product of density and the external potential and can be written as,

$$\int \rho_0(\vec{r})v(\vec{r})d\vec{r} = \int \left[\rho_0(\vec{r}_1) \sum_{\text{nuclei A}} -\frac{Z_A}{\vec{r}_{iA}}\right] \overrightarrow{dr}_1 = -\sum_{\text{nuclei A}} Z_A \int \frac{\rho_0(\vec{r}_1)}{\vec{r}_{iA}} d\vec{r}_1 \qquad (3.38)$$

The expectation value of the kinetic energy of the non-interacting electrons in the reference system can be denoted by,

$$\langle T[\rho_0]\rangle_{ref} = \left\langle \psi_r \middle| \sum_{i=1}^{2n} -\frac{1}{2}\nabla_i^2 \middle| \psi_r \right\rangle \qquad (3.39)$$

For the non- interacting electrons, ψ_r can be represented as a single Slater determinant related to the occupied spin molecular orbitals and for a four-electron system ψ_r can be written as,

$$\psi_r = \frac{1}{\sqrt{4}} \begin{vmatrix} \psi_1^{KS}(1)\alpha(1) & \psi_1^{KS}(1)\beta(1) & \psi_2^{KS}(1)\alpha(1) & \psi_2^{KS}(1)\beta(1) \\ \psi_1^{KS}(2)\alpha(2) & \psi_1^{KS}(2)\beta(2) & \psi_2^{KS}(2)\alpha(2) & \psi_2^{KS}(1)\beta(1) \\ \psi_1^{KS}(3)\alpha(3) & \psi_1^{KS}(3)\beta(3) & \psi_2^{KS}(3)\alpha(3) & \psi_2^{KS}(1)\beta(1) \\ \psi_1^{KS}(4)\alpha(4) & \psi_1^{KS}(4)\beta(4) & \psi_2^{KS}(4)\alpha(4) & \psi_2^{KS}(1)\beta(1) \end{vmatrix} \qquad (3.40)$$

In the above determinant, ψ_i^{KS} denotes the Kohn- Sham spatial orbitals and α, β represents the spin functions.

Involving the Slater determinants, equation (3.39) can be expressed in terms of spatial KS orbitals as,

$$\langle T[\rho_0]\rangle_{ref} = -\frac{1}{2}\sum_{i=1}^{2n} \left\langle \psi_1^{KS}(1) \middle| \nabla_1^2 \middle| \psi_1^{KS}(1) \right\rangle \qquad (3.41)$$

Thus, equation (3.41) can be written as,

$$E_0 = -\sum_{\text{nuclei A}} Z_A \int \frac{\rho_0(\vec{r}_1)}{\vec{r}_{iA}} d\vec{r}_1 + -\frac{1}{2}\sum_{i=1}^{2n} \left\langle \psi_1^{KS}(1) \middle| \nabla_1^2 \middle| \psi_1^{KS}(1) \right\rangle + \frac{1}{2}\int\int \frac{\rho_0(\vec{r}_1)\rho_0(\vec{r}_2)}{\vec{r}_{12}} d\vec{r}_1 d\vec{r}_2 + E_{XC}[\rho_0] \qquad (3.42)$$

Moreover, in order to deal with the exchange correlation $E_{XC}[\rho_0]$ and to find the effective approximations for $E_{XC}[\rho_0]$, the local density approximation (LDA) and the gradient corrected (GC) approximation have been introduced in the DFT method. Recently, the Becke three (B3) parameter hybrid functional method which is a combination of the Hartree- Fock exchange with DFT exchange has been widely used in density functional theory. This functional can be represented as,

$$AE_X^{Slater} + (1-A)^* E_X^{HF} + B^* \Delta E_X^{Becke} + E_C^{VWN} + C^* \Delta E_C^{non-local} \qquad (3.43)$$

where, A, B, and C are the constants determined by Becke [16]. The correctional functional LYP includes both local and non-local terms proposed by Lee- Yang- Parr (LYP) [17] and has the following representation,

$$C^{*}E_{C}^{LYP} + (1 - C)^{*}E_{C}^{VWN} \qquad (3.44)$$

where, VWN is used to add excess correlation along with LYP.

3.6.1 Basis Sets in DFT Calculation

A basis set is a set of mathematical functions that is used to represent the electronic wavefunction in the DFT method towards the calculation of different molecular properties. The linear combinations of basis set yield molecular orbitals (MO).

The method in which the molecular orbitals can be approximated as linear combinations of basis functions is generally called the linear combination of atomic orbitals (LCAO). The atomic orbitals (AO) of an atom are basically known as basis function. In case of polyatomic molecules, the individual identity of the atoms has been lost due to the electron density distribution in the valence shell of the individual atoms. For isolated atom, due to the accumulation of electron densities in the bond region, the distribution of charge in a molecule is anisotropic. For the estimations of electronic structures, standard basis sets are used as a linear combination of Gaussian Type Orbitals (GTOs). The corresponding Gaussian function can be represented as,

$$g(\alpha, \vec{r}) = Cx^{m}y^{n}z^{l}e^{-\alpha r^{2}} \qquad (3.45)$$

where, the constant α determines the size of the function to form the orbital and $\vec{r} = \sqrt{m^2 + n^2 + l^2}$ is the distance between the electron and nucleus.

A minimal basis set, that contains only three Gaussian primitives per basis function used for each atom. The size of the basis set has been enlarged in order to incorporate large number of basis functions for each atom. For example, Pople and co-workers [18] proposed a large basis set 6-311++G (d,p) which is also known as triple- split- valence basis function. In this basis set, the core orbitals are characterized in terms of six Gaussians and the valence orbitals split into three shells containing three, one and one Gaussian components. The ++ sign represents the addition of diffuse function to the basis set for heavy ions, or hydrogen atoms.

3.7 Molecular Dynamics

Molecular Dynamics (MD) simulation is able to furnish a complete explanation of atomic and molecular interactions characteristics to microscopic and macroscopic properties of numerous systems [19]. In the ab-initio MD [20], where the forces are estimated on-the-fly from specific electronic structure calculation is a very famous and well-known method. But, the computational cost for this ab-initio MD method is high. Moreover, one of the major drawbacks of ab-initio method is that a very small energy scale lies below the value of k_BT. In this present thesis, the Born- Oppenheimer molecular dynamics (BOMD) method is successfully applied along with the DFT method.

3.7.1 Born-Oppenheimer Molecular Dynamics (BOMD)

In Born-Oppenheimer molecular dynamics (BOMD), at each MD step the potential energy $E\left[\{\psi_i\};\vec{R}\right]$ is reduced with respect to the single particle wavefunctions or the Kohn-Sham (K-S) orbital $\{\psi_i(\vec{r})\}$ under the holonomic orthonormality constraint $\langle\psi_i(\vec{r})|\psi_j(\vec{r})\rangle = \delta_{ij}$. Thus, the corresponding Lagrangian has the following expression,

$$\mathcal{L}_{BO}\left(\{\psi_i\};\vec{R},\dot{\vec{R}}\right) = \frac{1}{2}\sum_{I=1}^{N} M_I\dot{\vec{R}}_I^{\,2} - \min_{\{\psi_i\}} E\left[\{\psi_i\};\vec{R}\right] + \sum_{i,j}\vec{\Lambda}_{ij}\left(\langle\psi_i|\psi_j\rangle - \delta_{ij}\right) \tag{3.46}$$

where, $\vec{\Lambda}$ denotes the Hamiltinian Lagrangian multiplier matrix. The corresponding Eular-Lagrange equation as obtained from the proposed Lagrangian $\mathcal{L}_{BO}$, considering the two degrees of freedom $\vec{R}_I$ and ψ_i can be expressed as,

$$\frac{d}{dt}\frac{\partial\mathcal{L}_{BO}}{\partial\dot{\vec{R}}_I} = \frac{\partial\mathcal{L}_{BO}}{\partial R_I} \tag{3.47a}$$

$$\frac{d}{dt}\frac{\partial\mathcal{L}_{BO}}{\partial\langle\dot{\psi}_i|} = \frac{\partial\mathcal{L}_{BO}}{\partial\langle\psi_i|} \tag{3.47b}$$

Solving the equation (3.47a) and (3.47b), the generic Born-Oppenheimer equations of motion (EOM) can be represented as,

$$M_I\ddot{\vec{R}}_I = -\vec{\nabla}_{\vec{R}_I}\left[\min_{\{\psi_i\}} E\left[\{\psi_i\};\vec{R}\right]_{\{\langle\psi_i|\psi_j\rangle=\delta_{ij}\}}\right]$$

$$= -\frac{\partial E}{\partial \vec{R}_I} + \sum_{i,j} \vec{\Lambda}_{ij} \frac{\partial}{\partial \vec{R}_I} \langle \psi_i | \psi_j \rangle - 2 \sum_i \frac{\partial \langle \psi_i |}{\partial \vec{R}_I} \left[\frac{\partial E}{\partial \langle \psi_i |} - \sum_j \Lambda_{ij} | \psi_j \rangle \right] \qquad (3.48a)$$

$$0 \leq -\frac{\partial E}{\partial \langle \psi_i |} + \sum_j \vec{\Lambda}_{ij} | \psi_j \rangle$$

$$= -\hat{H}_e \langle \psi_i | + \sum_j \vec{\Lambda}_{ij} | \psi_j \rangle \qquad (3.48b)$$

The first and second term on the right-hand side of equation (3.48a) is denoted as Hellmann-Feynman force F_{HF} [21,22] and Pulay or wavefunction force F_{WF} [23] respectively. The F_{WF} is known as a constraint force which arises from the holonomic orthonormality constraint and exists only when the basis functions $\emptyset_j$ depend explicitly on $\vec{R}$. The third term on the right-hand side of equation (3.48a) arises due to the inherent dependence on the atomic positions via the expansion coefficient $C_{ij}(\vec{R})$ with the linear combination of atomic orbitals $\emptyset_j$ such as,

$$\psi_i(\vec{R}) = \sum_j C_{ij}(\vec{R})\, \emptyset_j \qquad (3.49)$$

The factor 2 in the equation (3.48a) arises due to the assumption of the real KS orbitals. The last term of equation (3.48a) disappears if $\psi_i(\vec{R})$ be an eigenfunction of the Hamiltonian within the subspace spanned by the unnecessarily complete basis set. [24,25]. Also, the last term of equation (3.48a) is known as non-self-consistent force F_{NSC} because due to the non-linear KS function, the eigenfunctions of the Hamiltonian $\hat{H}_e$ can be attained only at accurate self-consistency.

Ignoring either F_{WF} or F_{NSC} and employing the Hellmann-Feynman theorem to a non-eigenfunction will give a perturbative estimation of the generalized forces [26] such as,

$$F = F_{HF} + F_{WF} + F_{NSC} \qquad (3.50)$$

As the generalized force is linearly dependent upon the error in the electronic charge density, the more accurate way is to estimate the exact forces rather than the total energies.

However, as a consequence of the Born-Oppenheimer (BO) approximation, the nuclear and electronic subsystems are fully separated from each other. Considering adiabatic separation, the maximum acceptable integration time step can be allowed up to the nuclear resonance limit.

3.8 Time Resolved Wavelet Transform Theory

Fourier Transform is performed in order to envisage the vibrational properties of the molecule from the molecular dynamics trajectories [27-29]. It has also been reported in the literature [30-32] that the wavelet analysis [33] approach is able to provide the similar results. The wavelet transform $W_n(s)$ for an input function $f(t)$ can be represented as,

$$W_n(s) = \int_{-\infty}^{+\infty} dt' f(t') \psi^* \left(\frac{t' - n}{s} \right) \qquad (3.51)$$

and the corresponding discrete expression is,

$$W_n(s) = \sum_{n'=0}^{N-1} f(n'.\delta t) \psi^* \left(\frac{(n' - n).\delta t}{s} \right) \qquad (3.52)$$

Where, s and n denote the wavelet scale and the time variation respectively. n' represents the time step index and δt defines the time-step. According to the formalism of Torrence and Compo [34], the function ψ is called the "mother wavelet" which is given by the Morlet function,

$$\psi(t) = \pi^{-1/4} e^{i\omega_0 t - t^2/2\sigma^2} \qquad (3.53)$$

where, the parameter ω_0 has been set at 2π and according to this assumption, the Fourier frequency is given as, $\omega \simeq 1.01/s$ [34]. The parameter σ affects the time- frequency resolution that is dominated by an uncertainty principle [33].

3.9 Computational Details for the DFT and BOMD Calculations

The Born-Oppenheimer on the fly (BO-OF-MD) molecular dynamics, time resolved wavelet transform theory and the DFT have been performed to understand the adsorptive behaviour of analyte 4MPy molecule with AuNPs entrapped in the bilayer LB film matrix of stearic acid (SA). The BO-OF-MD simulations had been carried out using CPMD program operated in linux environment [35]. The 4Mpy molecule and bulk gold (Au) atoms with $\rho_{Au} \sim 19.32\ g/cm^3$ [36] were placed in the simple cubic cell of dimension 10.0 Å. Periodic boundary conditions were applied on the cell with 10 Å edges to ensure no appreciable interactions between the periodic images. The BO-OF-MD simulations were then executed in the NVT ensemble at room temperature over an equilibrium time of 30 picoseconds. The time step was set to 4.0 a.u. The temperature of the ensemble was controlled through Nose-Hoover thermostat [37,38]. The gradient corrected Perdew, Burke and Ernzerhof (PBE) functional [39] had been

utilized to model the electronic exchange and correlation factors. Core electrons were treated with pseudopotentials of Troullier and Martins [40], while valance electrons were represented by plane-wave basis set truncated at an extended energy cutoff of 80 Ry. The simulated data and the respective snap shots were visualized using the VMD [41] visualization software.

The DFT calculations were accomplished from Gaussion-09 suite of software [42] using B3LYP [16,17] exchange correlation functional. For structural optimizations and calculations of vibrational frequencies 6-31++g(d,p) basis was used for the light elements (C, H, N and S) of 4MPy molecule. For gold cluster models, the valence and the core electrons of Au atoms were defined by the pseudopotential LANL2DZ basis set. The vibrational frequencies of the respective molecule-metal cluster models, so attained from B3LYP/ 6-31++g(d,p) [for C, H, N and S] / LANL2DZ (for Au atoms) level of theory had been scaled with the scaling factor 0.98. In the process of geometry optimization for the fully relaxed method with very tight criteria, convergence of all the calculations without any imaginary values in the vibrational frequencies presage the accomplishment of local minima on the potential energy surfaces. The electron densities of the 4Mpy molecule and the Au atoms have been calculated using B3LYP / 6-31++g(d,p) [for C, H, N and S] and B3LYP / LANL2DZ level of theory respectively. However, for the molecule-metal cluster models, the electron density differences (EDD) have been estimated using B3LYP / 6-31++g(d,p) [for C, H, N and S] / LANL2DZ (for Au atoms) level of theory.

The differential Raman scattering cross section (DRSC) $\left(\frac{d\sigma}{d\Omega}\right)$ values had been estimated from the scattering activities using the general expression in harmonic approximation represented by [43,44]

$$I_{Raman} = \left(\frac{d\sigma}{d\Omega}\right)_i = \frac{(2\pi)^4}{45}\frac{h}{8\pi^2 c\omega_i}\frac{(\omega_0-\omega_i)^4}{1-\exp(-hc\omega_i/k_B T)}S_i \qquad (3.54)$$

where, h, c, k_B and T represents the Planck constant, speed of light, Boltzman constant and Kelvin temperature respectively. The frequencies (in cm^{-1}) of the incident light and the "*i*th" vibrational mode are depicted by ω_0 and ω_i respectively. The Raman scattering factor ($Å^4/amu$) for the "*i*th" normal mode of vibration is expressed as $S_i = 45\left(\frac{d\alpha}{dQ_i}\right)^2 + 7\left(\frac{d\gamma}{dQ_i}\right)^2$ where $\left(\frac{d\alpha}{dQ_i}\right)$ and $\left(\frac{d\gamma}{dQ_i}\right)$ are the derivatives of the isotropic and anisotropic polarizabilities α and γ with respect to the "Q_ith" normal moderespectively.

The wavelet transform (WT) theory had been applied to estimate the time resolved vibrational spectra for both the 4MPyH and 4MPyD forms of 4MPy molecule in presence of Au cluster system using BO-OF-MD calculations. The vibrational signatures of 4MPyH and 4MPyD in the vicinity of Au cluster were obtained from the Fourier transform of the trajectories so generated from the BO-OF-MD calculations [45]. The stretching distances of atoms as a function of time linked with the vibrational modes of the molecule were elicited from the BO-OF-MD trajectories. The VDOS of the corresponding normal modes were then attained with the aid of Fourier transformation. Thereafter the wavelet transform was applied for the estimation of frequency as a function of time for individual vibrational modes of molecule.

The wavelet transform $W_n(S)$ in the reciprocal space is expressed as [46],

$$W_n(s) = \sum_{k=1}^{n-1} \hat{F}_k \hat{\psi}(s\omega_k) e^{i\omega_k n\delta t} \qquad (3.55)$$

where ω_k represent the angular frequency for the k_{th} normal mode and F_k and $\hat{\psi}$ are the Fourier transformations of the time series F_n and the mother wavelet $\psi(t)$, respectively. The mother wavelet $\psi(t)$ is represented as

$$\psi(t) = \pi^{-1/4} e^{i\omega_0 t - t^2/2\sigma^2} \qquad (3.56)$$

Here the parameters ω_0 and σ are considered from previous literatures [45,47]. Successful applications of the above functional form of the mother wavelet $\psi(t)$ as reported elsewhere and are known to reproduce the Fourier power spectrum accurately [45-48].

References

1. K. S. Yee, *IEEE Trans. on Antennas and Propagation*, 1966, **14**, 302.
2. J.-P. Berenger, *J. Computational Physics*, 1994, **114**, 195.
3. D. E. Merewether, R. Fisher, F.W. Smith, *IEEE Trans. Nucl. Sci.*, 1980, **27**, 1829.
4. C.F. Bohren, D.R. Huffman, *Absorption and Scattering of Light by Small Particles*, Wiley, New York, 1983.
5. Lumerical FDTD Solutions 8.5, Lumerical Inc.: Vancouver, Canada, 2013.
6. P. B. Johnson, R. W. Christy, *Phys. Rev. B*, 1972, **6**, 4370.
7. T. Gredig, E. A. Silverstein, M. P. Byrne, J. *Phys. Conf. Ser*., 2013, **417**, 012069.
8. A. Wolf, J. B. Swift, H. L. Swinney, J. A. Vastano, *Physica D*, 1985, **16**, 285.
9. http://gwyddion.net/download/2.49/

10. R. Hegger, H. Kantza, *Chaos*, 1999, **9**, 413.
11. M. T. Rosenstein, J. J. Collins, C. J. De Luca, *Physica D*, 1993, **65**, 117.
12. R. Dreizler, E. Gross, *Density Functional Theory*, Plenum Press, New York, 1995.
13. W. Koch, M. C. Holthausen, *A Chemist's Guide to Density Functional Theory*, Wiley- VCH, Weinheim Ed. 2, 2002.
14. R. G. Parr, W. Yang, *Density Functional Theory of Atoms and Molecules*, Oxford University Press, New York, 1989.
15. Jensen F, *Introduction to computational chemistry*, 2nd edn. Wiley, New York, 2007.
16. A. D. Becke, *J. Chem. Phys*., 1993, **98**, 5648.
17. C. Lee, W. Yang, R. G. Parr, *Phys. Rev. B*, 1988, **37**, 785.
18. W. J. Hehre, L. Radom, P. V. R. Schleyer, J. A. Pople, *Ab-initio molecular orbital theory*, Wiley, New York, 1986.
19. S. Gupta, P. K. Varadwaj, *Int. J. Pharma. Sci. Res*., 2018, **9**, 1333.
20. D. Marx, J. Huver, *Ab Initio Molecular Dynamics: Basic Theory and Advance Methods*, Cambridge University Press, Chambridge, 2009.
21. H. Hellmamm, *Einfuhrung in die Quantenchemie, Deuticke*, Leipzig, Germany, 1937.
22. R. P. Feynman, *Phys. Rev*., 1939, **56**, 340.
23. P. Pulay, *Mol. Phys*., 1969, **17**, 197.
24. J. Almlof, T. Helgaker, *Chem. Phys. Lett*., 1981, **83**, 125.
25. M. Scheffler, J. P. Vigneron, G. B. Bachelet, *Phys. Rev. B*, 1985, **31**, 6541.
26. P. Bendt, A. Zunger, *Phys. Rev. Lett*., 1983, **50**, 1684.
27. M. E. Tuckerman, *Statistical Mechanics: Theory and Molecular Simulation*, Oxford University Press Inc., 2010.
28. B. J. Berre, R. J. Pecora, *Dynamic Light Scattering, John Wiley and Sons Ltd*., 1976
29. D. A. McQuarrie, *Statistical Mechanics*, University Science Books, 2nd edn, 2000.
30. B. S. Mallik, A. Semparithi, A. Chandra, *J. Chem. Phys*., 2008, **129**, 194512.
31. B. S. Mallik, A. Semparithi, A. Chandra, *J. Phys. Chem. A*, 2008, **112**, 5104.
32. A. Rahaman, R. Wheeler, *J. Chem. Theory Comput*., 2005, **1**, 769.
33. C. K. Chui, *An Introduction to Wavelet, Academic Press Inc*., San Diego, California (USA), 1992.
34. C. Torrence, G. P. Compo, *Bull. Amer. Metor. Soc*., 1998, **79**, 61.

35. http://www.cpmd.org/,Copyright IBM Corp 1990-2008, Copyright MPI fur Festkorperforschung Stuttgart 1997-2001.
36. B. J. Kim, J. Bang, C. J. Hawker, E. J. Kramer, *Macromol*., 2006, **39**, 4108.
37. S. Nose, *J. Chem. Phys*., 1984, **81**, 511.
38. W. G. Hoover, *Phys. Rev. A*, 1985, **31**, 1695.
39. J. P. Perdew, K. Burke, M. Ernzerhof, *Phys. Rev. Lett*., 1997, **77**, 3865.
40. N. Troullier, J. L. Martins, *Phys. Rev. B*, 1991, **43**, 1993.
41. W. Humphrey, A. Dalke, K. Schulten, *J. Mol. Graphics*, 1996, **14**, 33.
42. M. J. Frisch, G. W. Trucks, H. B. Schiegel, G. E. Scuseria, M. A. Robb, J. R. Cheeseman, J. A. Montgomery Jr., T. Vreven, K. N. Kudin, J. C. Burant, Gaussian 09, Gaussian, Inc., Pittsburgh, PA, 2009.
43. P. L. Polavarapu, *J. Phys. Chem*., 1990, **94**, 8106.
44. M. Dekker. The Raman Effect, vol. 1(chap. 2) New York, 1971.
45. B. Dutta, B. Bhattacharjee, J. Chowdhury, *ACS Omega*, 2018, **3**, 6794.
46. M. Pagliai, F. Muniz-Miranda, G. Cardini, R. Righini, V. Schettino, *J. Phys. Chem. Lett*., 2010, **1**, 2951.
47. M. Muniz-Miranda, M. Pagliai, F. Muniz-Miranda, V. Schettino, *Chem. Commun*., 2011, **47**, 3138.
48. J. F. Kirby, C. J. Swain, *Geo phys. J. Int*., 2013, **194**, 78.

Chapter 4: Self-assembly of silver nanocolloids in the Langmuir- Blodgett Film of Stearic acid: Evidence of an efficient SERS sensing platform

---

4.1 Introductory Remarks

SERS is a powerful and surface sensitive tool that enhances Raman signals of probe molecules adsorbed on the rough nanostructured surfaces**.** It enables one to determine the molecular orientations as well as to detect trace concentrations of molecules down to single molecule detection limit. Noble metallic nanoparticles of different geometries [1-9] have been used for the fabrication of SERS active substrates due to their interesting tunable plasmonic behaviours and prospective applications. Among many different noble metals, silver nanoparticles (AgNPs) have been established as an efficient SERS active substrate since decades [10,11]. There has been an incessant wave in this area of research aiming towards the fabrication of novel and efficient SERS active substrates which can be readily used for trace analysis and ultrasensitive detection.

This present chapter reports a different technique to fabricate a novel SERS active substrate through self-assembly of silver nanocolloids (AgNCs) in the bilayer LB film of stearic acid (SA). The electrostatic interaction between the negatively charged acid group of SA and the positively charged AgNC allows the entrapment of the aggregated nanocolloids in the SA matrix. The SERS efficacy of the as prepared substrate has been tested with Rhodamine 6G (R6G) molecules. Gigantic enhancement factors ranging from $\sim 10^7 - 10^{12}$ orders of magnitude have been estimated. The electric field distributions around the nanoaggregated colloids have been envisaged from three- dimensional finite difference time domain (3D-FDTD) simulation studies.

4.2 Results and Discussions

4.2.1 Pressure (π) – area (A) isotherm of Langmuir monolayer

Room temperature surface pressure (π) – area (A) compression isotherm of a Langmuir monolayer of SA in pure water sub phase has been recorded and is shown in Figure 4.1. The nature of the isotherm is in accordance with that reported elsewhere [12]. The area / SA molecule is estimated to be ~ 0.22 (nm^2)/ molecule. Bilayer LB film of SA molecule is then lifted on the pre-cleaned quartz substrate at a constant surface pressure of 25 mN/ m by Y-type deposition technique. This preferred technique allows tail-tail architecture there by favouring the polar COO^- group of SA molecule in the second layer to point outwards. The bilayer LB films of SA were subsequently dipped in the as synthesized nanocolloidal silver solutions at various dipping times (DTs) ranging from 45 minutes to 48 hours. The bilayer LB films were then repeatedly washed

with deionized water to remove the excess silver ions that may get adsorbed on the surface of the SA films and are allowed to dry in a vacuum chamber.

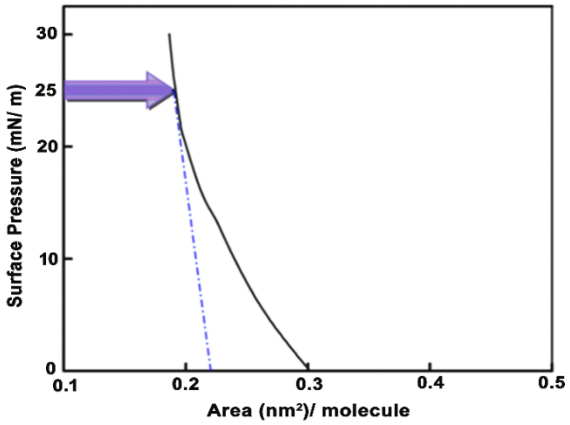

Figure 4.1: Room temperature surface pressure (π)– area (A) compression isotherm of a Langmuir monolayer of SA in pure water sub phase.

4.2.2 Absorption spectrum of the as prepared substrates

Figure 4.2 shows the room temperature UV- Vis electronic absorption spectrum of Ag nanocolloids (AgNCs). The yellowish AgNC shows a single absorption maximum centered at ~ 397 nm, characteristic of LSPR [13]. However, the absorption spectra of AgNC self-assembled in the bilayer LB film of SA at various DTs (also shown in the same Figure) exhibit broad and structureless features. The LSPR band of AgNC self-assembled in the bilayer LB film of SA undergoes progressive bathochromic shift with the change in the DTs from 45 minutes to 36 hours. The general broadening of the absorption spectra may signify the possibility of silver nano colloidal aggregates to get entrap in the bilayer LB film of SA. The rationale towards the formation of these hot aggregated geometries may be due to the neutrality of surface charges from the carboxylic ($COOH^-$) head group of SA with the unneutralized positive charges of AgNCs [14]. Strong dipole dipole coupling between the aggregated nanoparticles may be the reason for the featured red shift. However, after 48 hours of DT, the LSPR band undergoes hypsochromic shift and absorption maximum is shifted at ~ 421 nm. This down shift is exhibited by the films may be due to the decrease in dielectric constant for metal nanoparticles surrounded by the neighbouring nanoparticles [15].

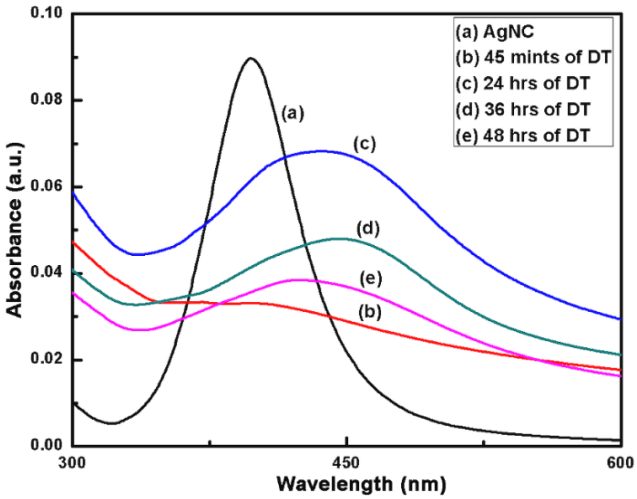

Figure 4.2: Room temperature UV- Vis electronic absorption spectra of (a) Ag NC and [(b) - (e)] Ag NC self-assembled in the bilayer LB film of SA at various DTs.

4.2.3 SER(R)S study and enhancement factor of Raman bands

The concentration dependent SER(R)S spectra of R6G molecule adsorbed on AgNC dipped in bilayer LB film of SA for 24 hours are shown in Figure 4.3. The optical absorption maximum of R6G ~ 525 nm in concurrence with the availability of the laser excitation source at ~ 514.5 nm allow us to record the SER(R)S spectra of the molecule. The SERS spectra of R6G molecule at varied concentrations of the adsorbate under off resonant condition are also recorded with 632.8 nm red laser excitation source. The representative SERS spectra of R6G molecule at three different concentrations of the adsorbate with 632.8 nm laser excitation source are shown in Figure 4.4. The spectra exhibit background noise with considerable low signal to noise ratio in comparison with that recorded with 514.5 nm excitation source.

Figure 4.5 shows the variations in intensities of 614, 773, 1363, 1509, 1575 and 1650 cm^{-1} SER(R)S bands with the logarithm of adsorbate concentrations. The SER(R)S spectra at trace concentrations of the adsorbate exhibit enhanced Raman bands characteristic of R6G molecule. The spectra are marked by enhanced Raman bands centered at ~ 614; 1363, 1509, 1575, 1650 and 773 cm^{-1} ascribed to in- plane α (C-C-C) bending; ν (C-C) stretching and out-of- plane γ (C-H) bending vibrations associated with the xanthenes ring moiety of the R6G molecule respectively [16]. The adsorbate concentration dependence of SERS bands of R6G molecule, in general, arises from the surface coverage. It is now well established on silver island films and on nanocolloids

[17-20] that at extremely low concentrations, the metal surface coverage by the adsorbates is sub monolayer. In the absence of sufficient scattering molecules, the SER signals in this range of concentrations are weak. With increase in concentration of the adsorbate, the SERS signal increases and attains a maximum intensity at monolayer coverage, where both electromagnetic and charge transfer contributions to SERS maximize. On further increase in concentration of the adsorbates, multilayers are formed and the SERS signal decreases in intensity. It therefore seems plausible that the monolayer coverage of the adsorbed R6G molecule may have formed on the as prepared substrate at a concentration ~ 1.0 x 10^{-10} M which shows maximum enhancement of the SER(R)S signals. The analytical enhancement factors (AEFs) of the Raman bands of R6G molecule adsorbed on the as prepared substrates have been calculated using the relation [21]

$$\mathrm{AEF} = \sigma_{\mathrm{SER(R)S}}[\mathrm{C_{RR}}]/\sigma_{\mathrm{RR}}[\mathrm{C_{SER(R)S}}] \qquad (4.1)$$

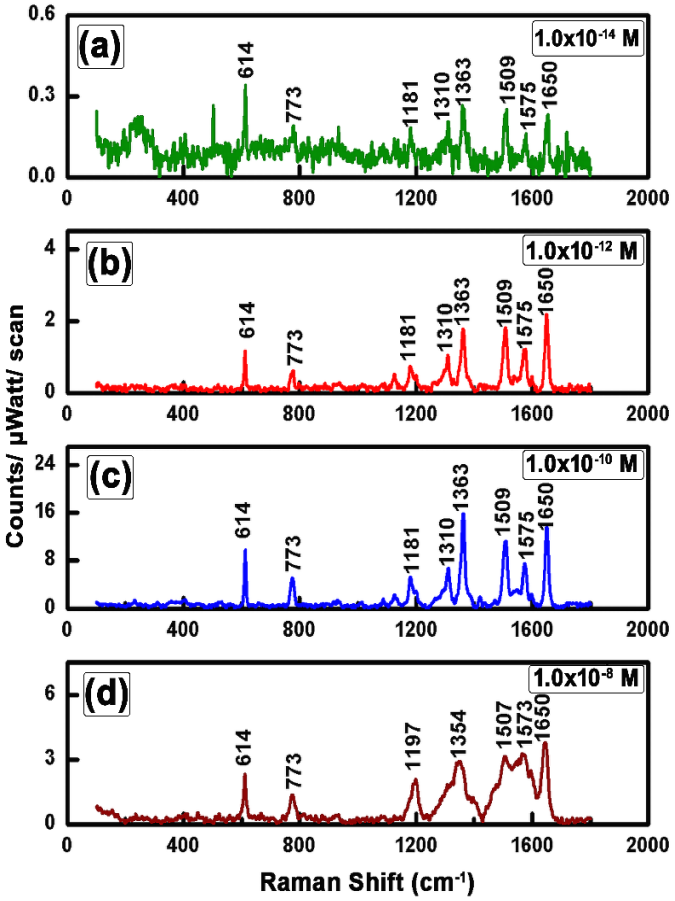

Figure 4.3: SER(R)S spectra of R6G molecule at varied concentrations of the adsorbate (λ_{ex}= 514.5 nm).

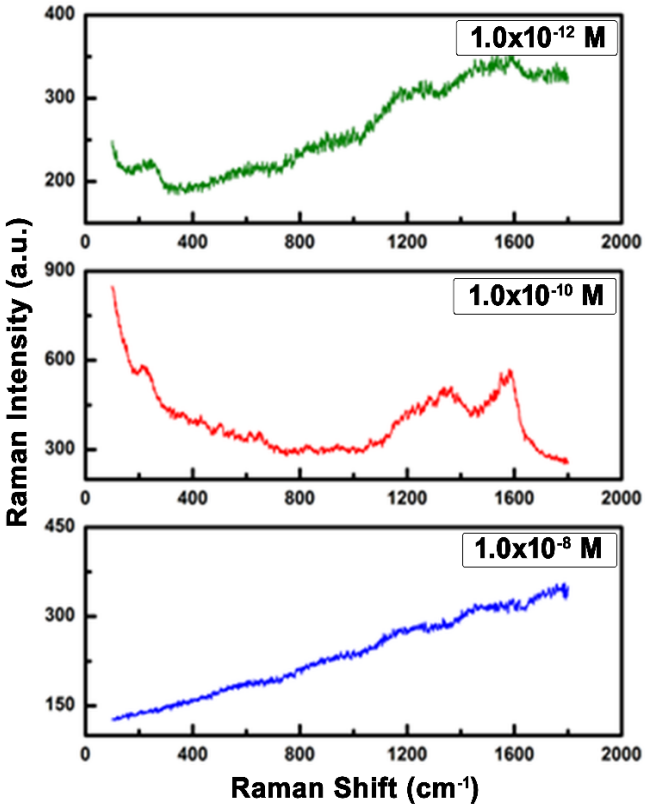

Figure 4.4: SERS spectra of R6G molecule at varied concentrations of the adsorbate (λ_{ex}= 632.8 nm).

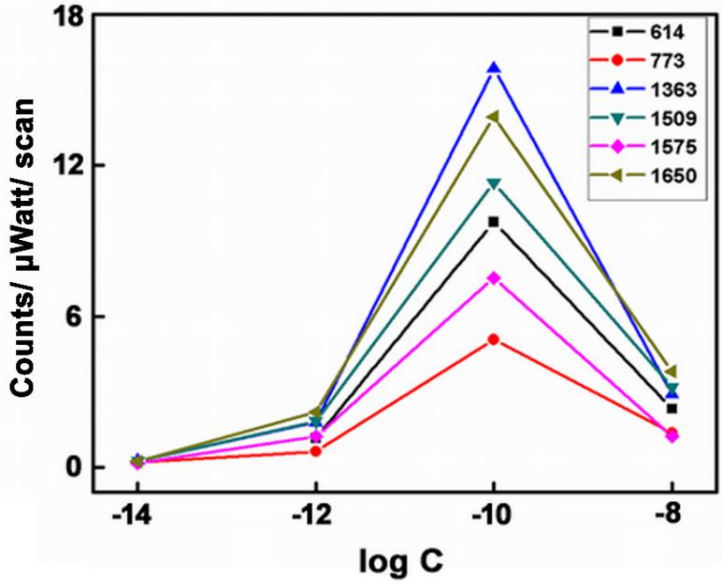

Figure 4.5: The variations in SER(R)S intensities of 614, 773, 1363, 1509, 1575 and 1650 cm^{-1} bands of R6G molecule with the change in concentrations of the adsorbate.

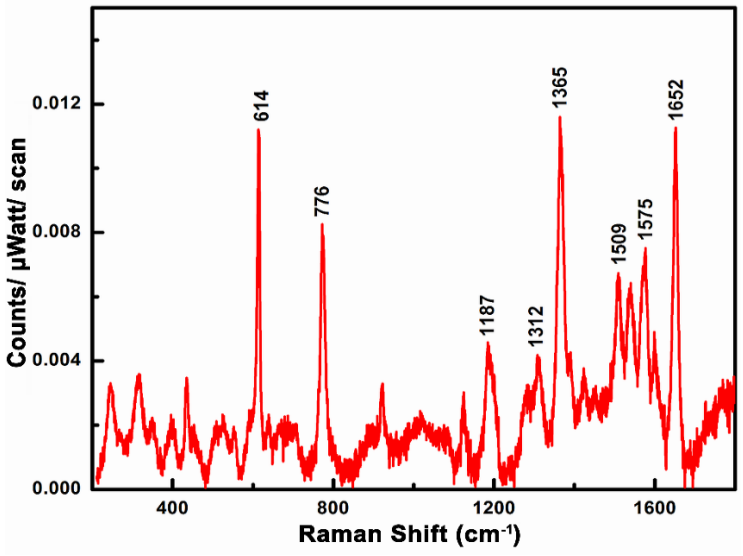

Figure 4.6: Background corrected resonance Raman (RR) spectrum of 1.0 x 10^{-3} M R6G in aqueous solution (λ_{ex}= 514.5 nm).

where, C and σ represent the concentration and the integrated peak area of the Raman bands respectively measured from baseline. The background corrected RR spectrum of 1.0×10^{-3} M R6G in aqueous solution is shown in Figure 4.6. The AEFs for 614, 773, 1363, 1575 and 1650 cm^{-1} bands of R6G are tabulated in Table 4.1. Gigantic enhancement factors ranging from $\sim 10^{7} - 10^{12}$ orders of magnitude have been estimated for the above-mentioned bands.

Figure 4.7 shows the SER(R)S spectra of 1.0×10^{-10} M R6G adsorbed on bilayer LB film of SA dipped in AgNC at various DTs ranging from 45 minutes to 48 hours. Strong enhancements of 614, 773, 1181, 1310, 1363, 1509 and 1650 cm^{-1} bands, all representing the vibrational signatures of R6G molecule, further substantiate the competence of the as prepared substrates as an efficient SERS sensing platform. In this connection, it is worth to mention that the vibrational signatures of R6G molecule exhibit enhancement factors $\sim 3.0 \times 10^{5}$ orders of magnitude and the limit of detection (LOD) ~ 1.0×10^{-5} M, when silver nanocolloids (AgNCs) are adsorbed on silanized glass substrate [22]. Interestingly, self- assembled silver nanoparticle (AgNP) monolayer on glassy carbon exhibit significant SER(R) enhancement of R6G molecule with LOD ~ 10^{-9} M [23]. Highly efficient SERS active substrate has been reported by immersing mica modified cetyltrimethyl ammonium bromide (CTAB) into AgNC. The LOD of the substrate for R6G is estimated to be 1.0×10^{-14} M [24]. SERS substrates based on the silicon- hydrogen bond

Table 4.1: Analytical Enhancement factors (AEF) of SER bands of R6G molecule adsorbed on the as prepared substrates.

NRS (cm^{-1})	Adsorbate Concentrations								Assignment[a]
	10^{-8} M		10^{-10} M		10^{-12} M		10^{-14} M		
	SERS	AEF	SERS	AEF	SERS	AEF	SERS	AEF	
614	614	2.01 x10^{7}	614	6.69 x10^{9}	614	6.05 x10^{10}	614	1.99 x10^{12}	α (C-C-C)
776	773	1.95 x10^{7}	773	6.79 x10^{9}	773	7.31 x10^{10}	773	1.07 x10^{12}	γ (C-H)
1187	1197	2.12 x10^{8}	1181	3.40 x10^{10}	1181	1.51 x10^{11}	1181	6.52 x10^{12}	β (C-H)
1312	--	---	1310	5.78 x10^{10}	1310	1.42 x10^{11}	1310	8.81 x10^{12}	
1365	1354	1.04 x10^{8}	1363	1.16 x10^{10}	1363	9.10 x10^{10}	1363	4.57 x10^{11}	ν (C-C)
1509	1507	5.73 x10^{7}	1509	8.77 x10^{10}	1509	1.49 x10^{12}	1509	6.02 x10^{12}	ν(C-C)
1575	1573	6.59 x10^{7}	1575	1.98 x10^{10}	1575	4.20 x10^{11}	1575	2.44 x10^{12}	ν(C-C)
1652	1650	3.68 x10^{7}	1650	1.17 x10^{10}	1650	1.92 x10^{11}	1650	8.08 x10^{11}	ν (C-C)

Note: NRS: normal Raman spectrum; SERS: surface-enhanced Raman spectroscopy.

[a]α, β: in- plane bending; γ: out- of-plane bending; ν: stretching.

assembly of AgNPs on Si- wafer is reported to exhibit vibrational signatures of R6G molecule at 1.0×10^{-12} M concentration of the adsorbate [25]. The AEFs $\sim 10^{7} - 10^{12}$ orders of magnitude, estimated for the as prepared substrate (vide supra), suggest that it is superior or comparable to AgNP as dried AgNC solutions on microscopic slides. The LOD of R6G molecule has been estimated to be 1.0×10^{-14} M which is reduced by five orders from its practical LOD [26]. AgNPs

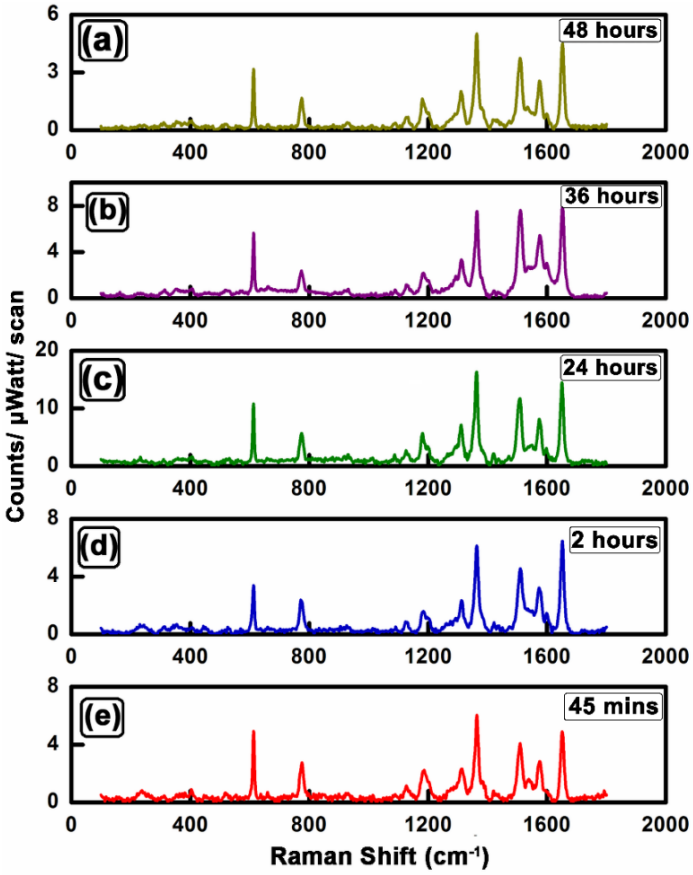

Figure 4.7: SER(R)S spectra of R6G molecule at various DTs (λ_{ex}= 514.5 nm).

films, as obtained after drying ethanol induced AgNCs, are reported to behave as an efficient SERS active substrate that can detect R6G in the concentration range 1.0×10^{-10} M - 1.0×10^{-14} M [27]. The LOD of the probe molecule on the as prepared substrate is also reduced by nine and five orders of magnitude in comparison to R6G on AgNC adsorbed on silanized glass and on AgNP in glassy carbon substrates respectively [22,23].

4.2.4 Surface morphology of the as prepared substrates

To estimate a correlation between SER(R)S efficacy and the corresponding morphological features, the FESEM and AFM images of the as prepared SERS active substrates have been captured. Figure 4.8 shows the FESEM images of the bare quartz slide, bilayer LB film of SA and FESEM images of the bilayer LB films of SA dipped in AgNCs at various DTs [Figure 4.8 (C)-(F)] smear distinctive entrapment of silver nanocolloidal particles within the SA matrix of the bilayer LB film. From the FESEM images (as shown in Figure 4.8), it is seen that the silver clusters

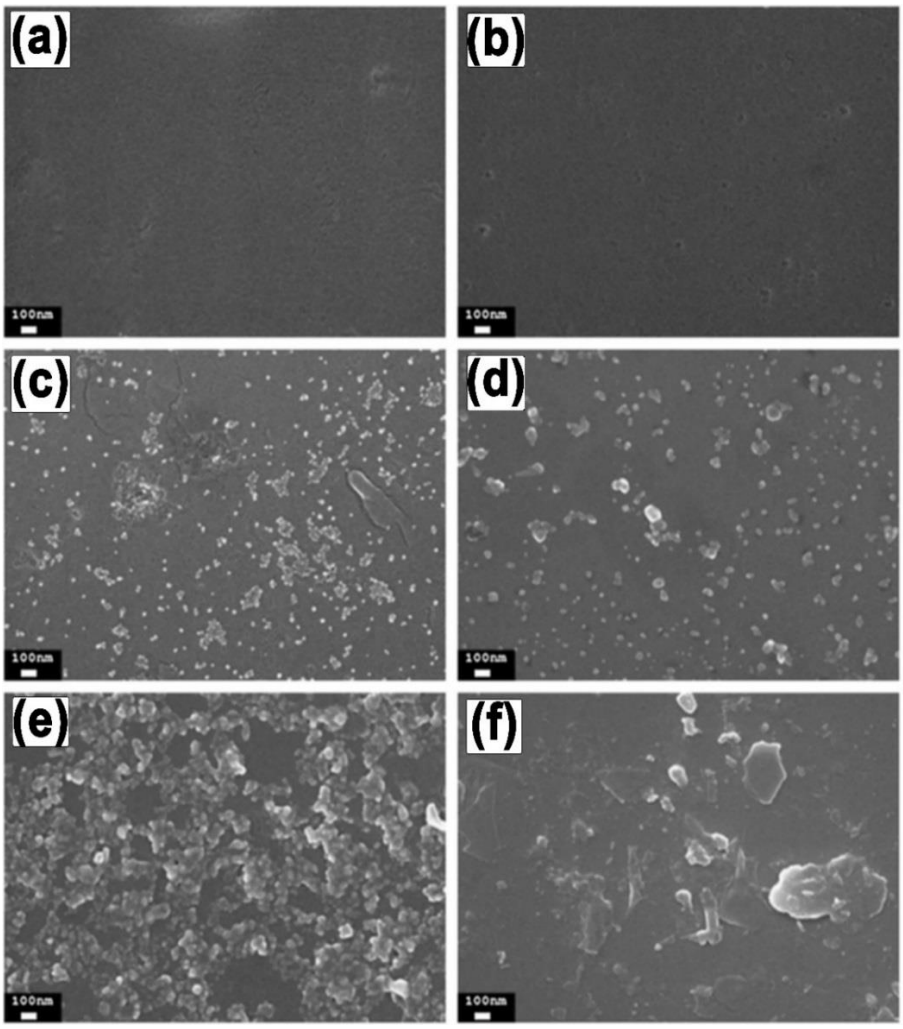

Figure 4.8: Nanometer scale FESEM images of the as prepared samples. (a) Bare quartz slide, (b) Bilayer LB film of SA lifted at 25 mN/m surface pressure, Bilayer LB film of SAincubated in Ag NC at (c) 45 mints (d) 24 hrs (e) 36 hrs (f) 48 hrs of DTs.

entrapped in the bilayer LB film of SA dipped in the colloidal solutions for 45 minutes and 24 hours appear as small fractal aggregates. However, at 36 hours of DT, larger aggregates of Ag nanoclusters are recorded which with further increase in DT (~ 48 hours) twirl to discrete lumps. These changes in the morphological features may be due to the aerial oxidation of silver clusters on the bilayer LB film of SA [14]. The optical responses to these changes in the morphological features of the as prepared substrates may result in the broadening of spectral signatures together with the bathochromic and hypsochromic shifts of the LSPR band in the electronic absorption spectra (Figure 4.2) as reported earlier (vide supra).

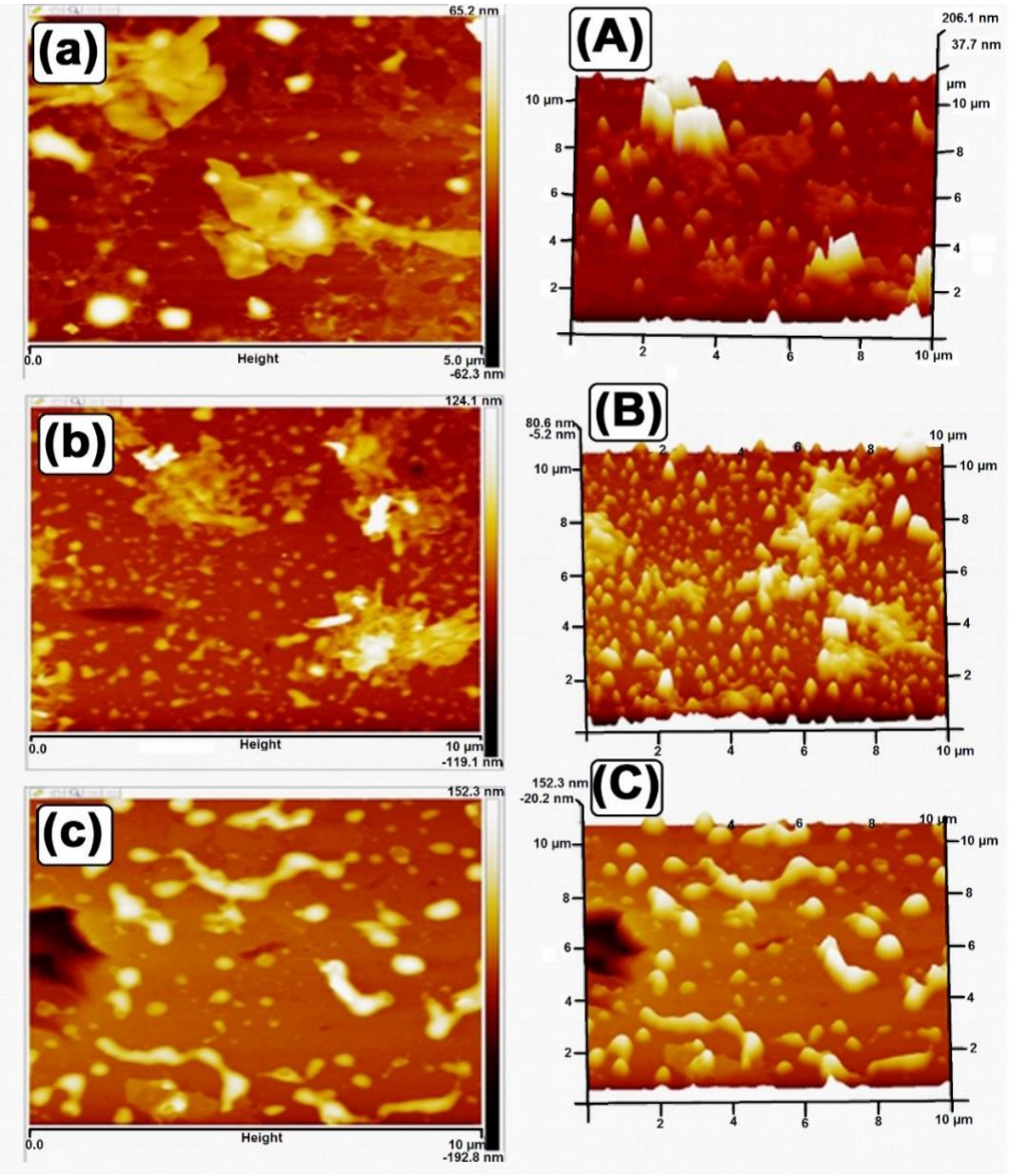

Figure 4.9: Nanometer scale AFM images of the as prepared substrates. The left column contains topographic 2D AFM images at (a) 45 mints, (b) 24 hrs and (c) 48 hrs of DTs. The right column shows the 3D AFM images of the same samples at (A) 45 mints, (B) 24 hrs and (C) 48 hrs of DTs.

Figure 4.9 shows the 2D and 3D AFM images of the as prepared bilayer LB film of SA incubated in silver nanocolloidal solution at various DTs. The AFM topography images reveal that with the increase in DTs, the initial fractal like features of the nanoparticles transform towards lumpy structures. The SER(R)S spectrum of 1.0×10^{-10} M R6G, adsorbed on the LB film of SA

dipped in AgNCs for 24 hours, exhibits the most enhanced Raman bands with high signal to noise ratio (Figure 4.7). The corresponding 3D AFM image exhibits the entrapment of the aggregated Ag nanoparticles in the SA matrix as sharp tips and definite interparticle spacing. These precise interstitials spacing between the plasmonic nanoparticles may be the probable host for generation of hot spots responsible for gigantic SER(R)S enhancements. The root mean square (RMS) roughnesses of the bilayer LB films of SA incubated in AgNCs at various DTs are estimated using the following relation:

$$R_q = \sqrt{\frac{\Sigma(Z_i)^2}{N}} \qquad (4.2)$$

where, Z_i is the current value of peak-to-valley difference in height within the analyzed region and N is the number of points within the box cursor. The variations in the RMS values of surface roughness's of the as prepared substrates with various DTs on AgNCs are shown in Figure 4.10. The plot indicates increase in the roughness features of the as prepared substrates with the increase in DTs. The RMS roughness of the bilayer LB film of SA dipped for 24 hours in AgNC is estimated to be 23.93 nm. This nanometer ranged RMS roughness may be considered as the benchmark roughness feature for the as prepared substrate to generate the most intense vibrational signatures of R6G molecule in the SER(R)S spectrum [Figure 4.9 (b) and 4.9 (B)].

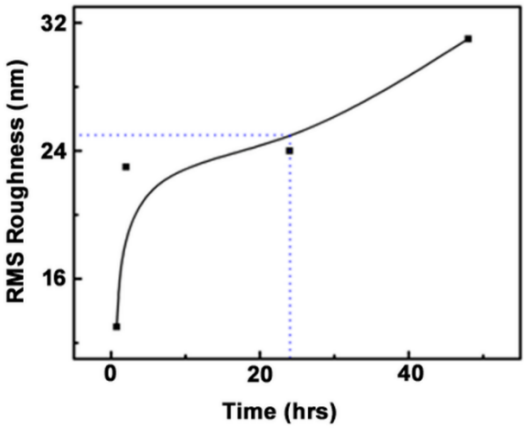

Figure 4.10: Variation in the RMS values of surface roughness's of the as prepared substrates with various DTs in AgNCs.

The fractal dimensions of the as prepared substrates have also been estimated using the following relation,

$$S \propto R^D \qquad (4.3)$$

where, S is the area of each structure and R exhibits the average distance from the centre of mass of each structure to its perimeter and D is the Hausdroff dimension [28]. Figure 4.11 shows ln R vs ln S plots of the as prepared substrates with various DTs in AgNCs. The slopes of ln R vs ln S plot allow one to estimate the desired fractal dimension of the nano aggregated assembles. The

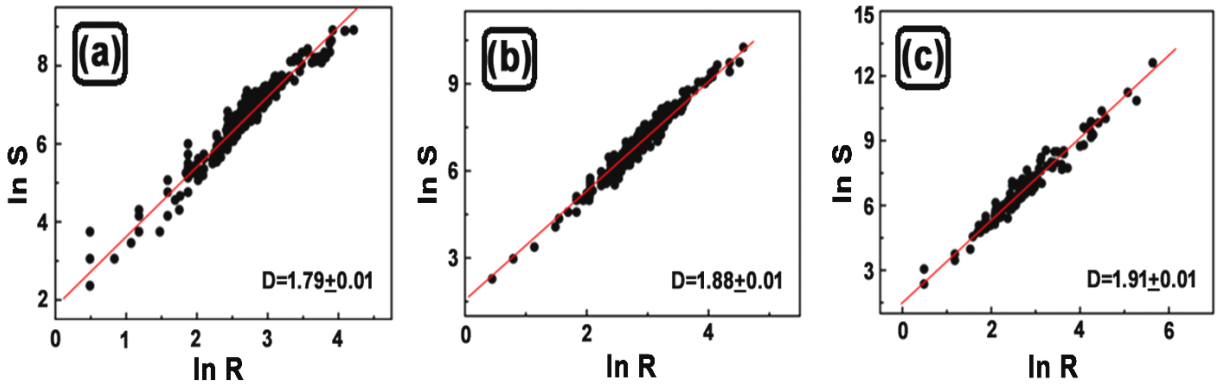

Figure 4.11: ln R vs ln S plot of the as prepared substrates incubated in AgNC at (a) 45 mints (b) 24 hours (c) 48 hours of DTs. The error in the slope determination is coming from the line fitting.

fractal dimensions of the bilayer LB films of SA dipped in AgNC solution for 45 mints, 24 hours and 48 hours of DTs are estimated to be 1.79 ± 0.01, 1.88 ± 0.01and 1.91 ± 0.01 respectively. These results are in accordance with the morphological features of the self-assembled AgNCs on the bilayer LB film of SA as discussed earlier from the FESEM and AFM images.

4.2.5 Estimation of EM enhancement around the aggregated AgNCs

To envisage a correlation between the hot aggregated geometries of the plasmonic nanoparticles and the huge enhancement factors of the SER(R)S bands, the electric field distributions around the plasmonic nano particles have been estimated. LSPRs of metallic nanostructures can spawn evanescent waves containing high spatial frequency information of the interacting object. These near field waves are the standing waves leading to the confinement of large EM field responsible for the generation of hot spots. The electric fields are estimated directly from the FESEM topography of the as prepared bilayer LB film of SA dipped in AgNCs for 24 hours. The as prepared films are not uniformly hot, it may have cold spots characteristic of the fractal nature of the aggregated nanocolloids [29]. The FESEM image, as shown separately in Figure 4.12, however exhibits large number of aggregated structures favourable for the generation

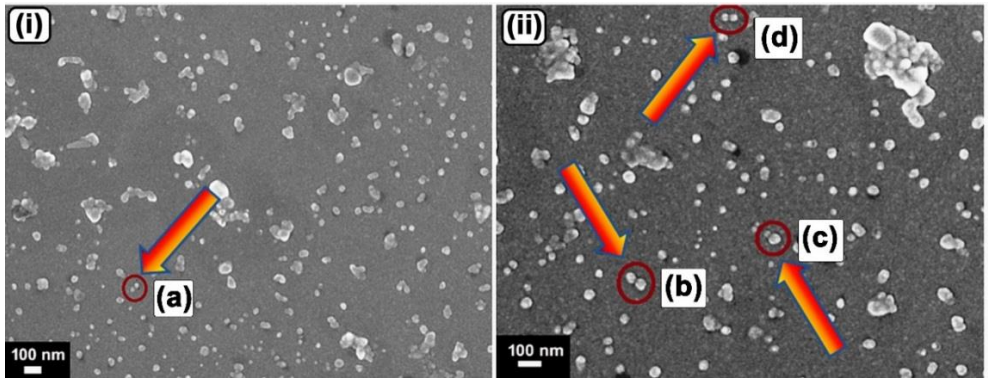

Figure 4.12: Selected Ag nano aggregated geometries of the as prepared substrates captured from the FESEM images used for the 3D-FDTD simulations.

of hot geometries. The hottest among the hotspots have been identified for the inter particle gap ~ 1.7 nm where the spatial distribution of electric field $|\vec{E}|$~32 Volt /m is extended over an approximate length of ~ 20 nm. The localization of strong $|\vec{E}|$ field corresponds to $\sim 10^6$ orders of magnitude enhancement of SER(R)S bands according to the plane wave (PW) approximation (Figure 4.13). From Figure 4.12, it is clearly seen that the simple hetero

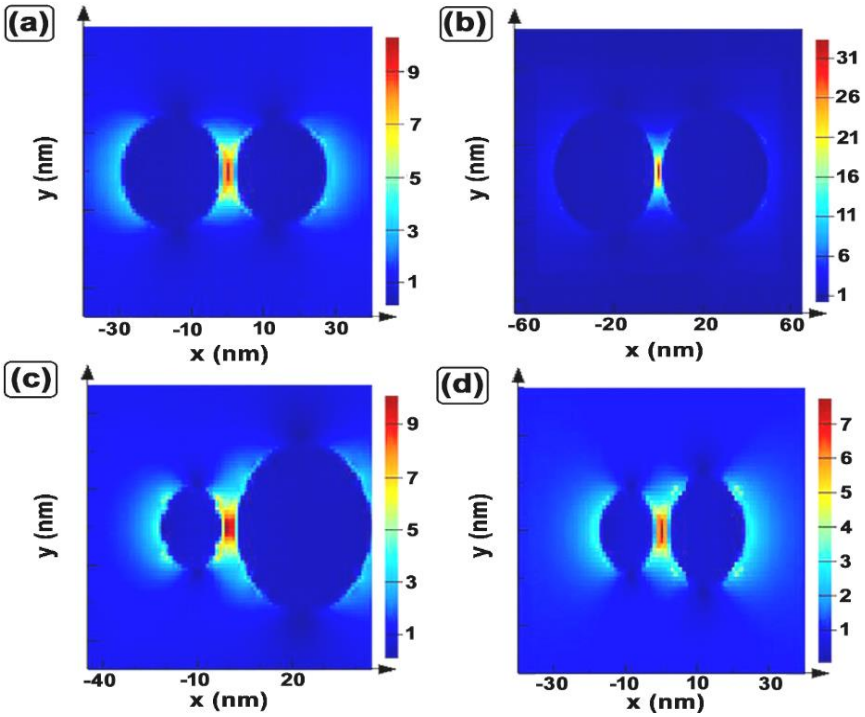

Figure 4.13: Electric field distribution around the hot-spots as estimated from 3D- FDTD simulations ($\lambda_{ex} = 514.5$ nm, the polarization of the incident light wave is along x- axis).

dimeric spherical aggregates are more evident to generate the hottest spots in comparison to other homo / hetero dimeric or higher order nano aggregated structures. However, $\sim 10^7 - 10^{12}$ orders of magnitude enhancements (Table 4.1) for almost all the Raman bands may also signify moderate involvement of Resonant and CT mechanism (in addition to the EM contribution) towards the overall enhancement of the SER(R)S bands of the molecule at 1.0×10^{-10} M concentration of the adsorbate.

4.3 Conclusion

Ag nanocolloids self-assembled in the bilayer LB film of SA have been established as a promising SERS active substrate. The efficacy of the as prepared substrate has been tested with R6G as probe molecule. Gigantic enhancement factors ranging from $\sim 10^7 - 10^{12}$ orders of magnitude have been reported for the characteristic vibrational signatures of R6G molecule. The optical responses, surface morphologies and the fractal dimensions of the as prepared substrates have been estimated. Correlation between the hot aggregated geometries of the plasmonic nanoparticles and the huge enhancement factors of the SER(R) bands have been drawn from 3D-FDTD simulations. The interparticle coupling of the surface plasmons in the nanoaggregated domains may be tuned by lifting the LB film of SA at different surface pressures.

References

1. N. R. Jana, T. Pal, *Adv. Mater*., 2007, **19**, 1761.
2. C. L. Nehl, H. Liao, J. H. Hafner, *Nano Lett*., 2006, **6**, 683.
3. X. Dong, X. Ji, J. Jing, M. Li, W. Yang, *J. Phys. Chem. C*, 2010, **114**, 2070.
4. M. Y. Tsvetkov, B. N. Khlebtsov, V. A. Khanadeev, V. N. Bagratashvili, P. S. Timashev, M. I. Samoylovich, N. G. Khlebtsov, *Nanoscale Research Lett*., 2013, **8**, 250.
5. P. Rajapandiyan, J. Yang, *J. Raman Spectrosc*., 2014, **45**, 574.
6. K. Malek, A. Brzozka, A. Rygula, G. D. Sulka, *J. Raman Spectrosc*., 2014, **45**, 281.
7. Z. Hu, Z. Liu, L. Li, B. Quan, Y. Li, J. Li, C. Gu, *Small*, 2014, **10**, 3933.
8. Y. H. Kwon, R. Ossig, F. Hubenthal, H. D. Kronfeldt, *J. Raman Spectrosc*., 2012, **43**, 1385.
9. D. Jana, A. Mandal, G. De, *ACS Appl. Mater. Inter*., 2012, **4**, 3330.
10. J. Chowdhury, P. Pal, M. Ghosh, T. N. Misra, *J. Colloid. Interface Sci*., 2001, **235**, 317.
11. J. Chowdhury, M. Ghosh, *J. Raman Spectrosc*., 2004, **35**, 1023.

12. M. J. Hwang, K. Kim, *Langmuir*, 1999, **15**, 3563.
13. J. A. Creighton, C. G. Blatchford, M. G. Albrecht, *J. Chem. Soc., Faraday Trans. 2*, 1979, **75**, 790.
14. J. Sarkar, P. Pal, G. B. Talapatra, *Chem. Phys. Lett*., 2005, **401**, 400.
15. M. A. Mahmoud, C. E. Tabor, M. A. El- Sayed, *J. Phys. Chem. C*, 2009, **113**, 5493.
16. P. Hildebrant, M. Stockburger, *J. Phys. Chem*., 1984, **88**, 5935.
17. J. Chowdhury, M. Ghosh, *J. Colloid Interface Sci*., 2004, **277**, 121.
18. J. Chowdhury, M. Ghosh, P. Pal, T. N. Misra, *J. Colloid Interface Sci*., 2003, **263**, 318.
19. M. Moskovits, J. S. Suh, *J. Phys. Chem*., 1988, **92**, 6327.
20. U. K. Sarkar, A. J. Pal, S. Chakraborti, T. N. Misra, *Chem. Phys. Lett*., 1992, **190**, 59.
21. S. Chandra, J. Chowdhury, M. Ghosh, G. B. Talapatra, *J. Phys. Chem. A*, 2012, **116**, 10934.
22. M. Culha, M. Kahraman, N. Tokman, G. Turkoglu, *J. Phys. Chem. C*, 2008, **112**, 10338.
23. H. Chen, Y. Wang, J. Qu, S. Dang, *J. Raman Spectrosc*., 2007, **38**, 1444.
24. G. Wei, H. Zhou, Z. Liu, Z. Li, *Appl. Surf. Sci*., 2005, **240**, 260.
25. Q. Shao, R. Que, L. Cheng, M. Shao, *RSC Adv*., 2012, **2**, 1762.
26. Y. C. Liu, C. C. Yu, S. F. Sheu, *J. Mater. Chem*., 2006, **16**, 3546.
27. L. Sun, Y. Song, L. Wang, C. Guo, Y. Sun, Z. Liu, Z. Li, *J. Phys. Chem. C*, 2008, **112**, 1415.
28. C. Haley, J. H. Weaver, *Surf. Sci*., 2002, **518**, 243.
29. M. Moskovits, L. L. Tay, J. Yang, T. Haslett, *Proc. SPIE, Nanoparticles and Nanostructured Surfaces: Novel Reporters with Biological Applications*, 2001, **4258**, 43.

Chapter 5: Silver coated gold nanocolloids entrapped in organized Langmuir-Blodgett Film of Stearic acid: Potential evidence of a new SERS active substrate

---

5.1 Introductory Remarks

Fabrication of metallic nanostructured SERS active substrates are crucial to gain highly reproducible and uniform SERS spectra augmented with enormous enhancement factors. As the SERS intensity depends upon the excitation of the LSPR around the SERS active nanoparticles, it is found significant to tune the factors (i.e., size, shape, inter particle spacing and the dielectric environment around the nanoparticles) that affects the LSPR in order to obtain maximum signal strength and good reproducibility [1-6]. The nanometer sized silver coated gold nano colloids (Au@AgNCs) have been established as an efficient SERS active material with higher order of enhancement and sensitivity [7]. However, the recent trends of research in this area, albeit scarce, are focused towards the fabrication of new SERS sensitive substrates using LB technique, which are reproducible, facile to prepare and favour interparticle LSP couplings [8-10].

This chapter is primarily focused on the fabrication of a novel SERS active substrate of Au@AgNCs self-assembled in the bilayer Langmuir- Blodgett (LB) film matrix of stearic acid (SA). The efficacy of the SERS activity has been tested with Rhodamine 6G (R6G) molecule. Enhancements of the Raman bands have been discussed in the light of EM mechanism. The spatial distribution of electric fields around the self-assembled Au@Ag nanoparticles are also estimated with the aid of three-dimensional finite difference time domain (3D- FDTD) simulation studies.

5.2 Results and Discussions

5.2.1 Pressure- area isotherm of Langmuir monolayer of SA

Room temperature pressure (π) - area (A) isotherm of a Langmuir monolayer of SA at the air- water interface is shown in Figure 5.1. The nature of the isotherm is in concordance with the earlier reports [11] and the area/ SA molecule is estimated to be ~ 0.22 (nm^2)/ molecule. The bilayer LB film of SA is lifted on the pre- cleaned quartz substrate at a constant surface pressure of 25 mN/ m. The film is lifted by Y- type deposition technique so that the polar COO^- group of the SA molecules point outwards in the periphery of the bilayer.

5.2.2 Optical and SER(R)S properties of the as prepared substrates

The room- temperature UV- Vis electronic absorption spectra of the as synthesized Au and Au@Ag nanocolloidal particles are shown in Figure 5.2. Pure Au and Au@AgNCs exhibit single

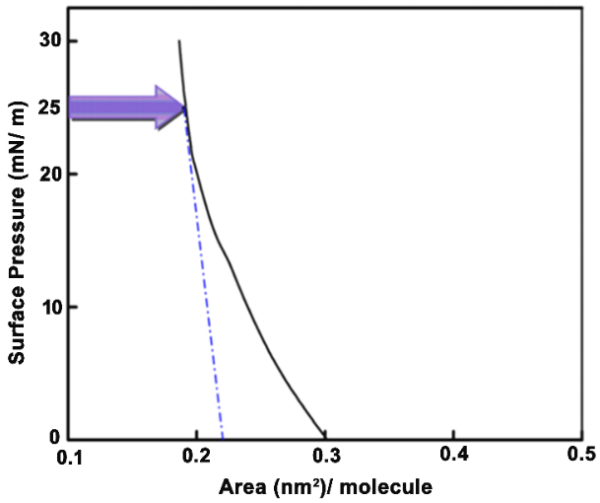

Figure 5.1: Room temperature surface pressure (π)– area (A) compression isotherm of a Langmuir monolayer of SA in pure water sub phase.

absorption maximum centered at ~ 526 nm and 417 nm respectively, characteristic of their respective surface plasmon (SP) electronic transitions [12,13]. The HRTEM image and EDX spectra of the Au@AgNC having ~ 25 nm core diameter and ~ 13 nm shell thickness are shown

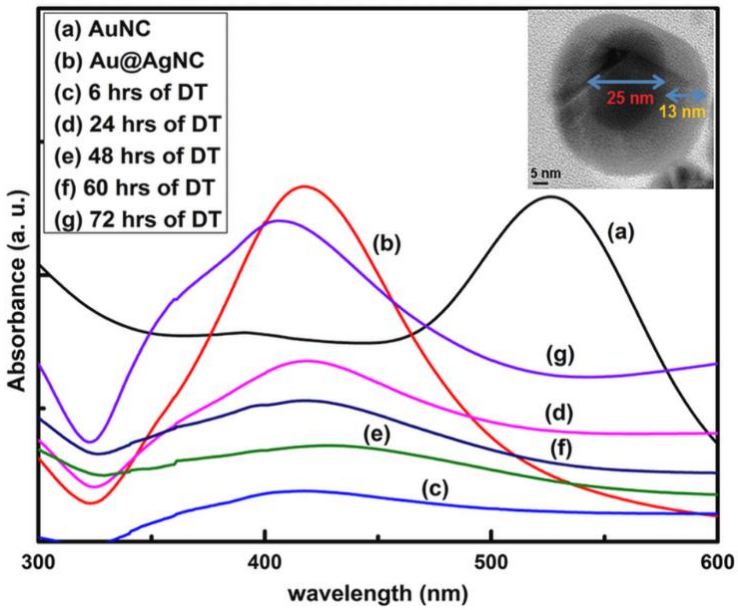

Figure 5.2: Room temperature UV- Vis electronic absorption spectra of (a) AuNC, (b) Au@ AgNC and [(c) – (g)] Au@ AgNC self-assembled in the bilayer LB film of SA at various DTs. Inset shows the HRTEM image of the as synthesized Au@AgNC.

in the inset of Figure 5.2 and Figure 5.3 respectively. Figure 5.2 also shows the absorption spectra of Au@AgNCs self-assembled in the organized bilayer LB film of SA at various dipping times (DTs) ranging from 6 hours to 72 hours.

Interestingly, the spectrum of the bilayer LB film of SA, incubated for 24 hours in Au@Ag NCs (Figure 5.2 (d)), is marked by broad structureless feature with no remarkable shift of the SP band. The broadening of the absorption spectra, in general, presages spontaneous aggregation of the Au@AgNCs on the bilayer LB film matrix of SA [14]. In Au@AgNC, there are residual surface charges which subsist due to incomplete reduction of metal ions in presence of reducing agent. The polar COO^- group of the bilayer LB film of SA may attract the unneutralized positively charged Au@Ag nanoparticles by virtue of charge neutrality consideration. This may lower the population of residual surface charges on the nano colloidal surface, which in turn results in the reduction of repulsive interactions between the charged nanocolloidal particles and favours the formation of distinct aggregates in the LB film matrix of SA. The schematic representation showing the interaction between SA in the bilayer LB film and the Au@Ag NC is shown in Figure 5.4. The coupling of the electrostatic fields among the neighbouring aggregated nanoparticles also contributes to the broadening of the electronic absorption spectra [15,16]. After 48 hours of DT [Figure 5.2 (e)], the SP band is remarkably red shifted and appears as distinct maximum centered at ~ 434 nm. This red shift may be owed to the strong dipole dipole coupling between the neighboring Au@Ag nanoparticles. Interestingly, with further increase in DT (ca. ~ 60 hours), this

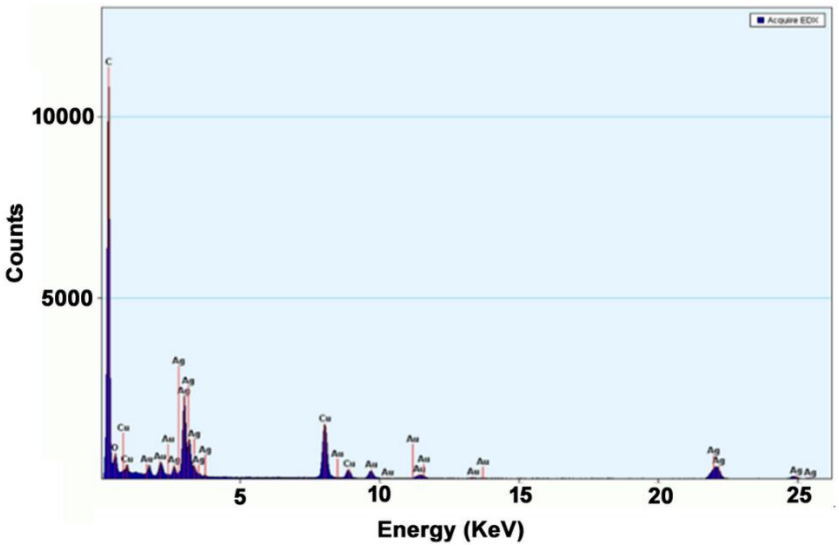

Figure 5.3: EDX analysis of the as synthesized Au@AgNC.

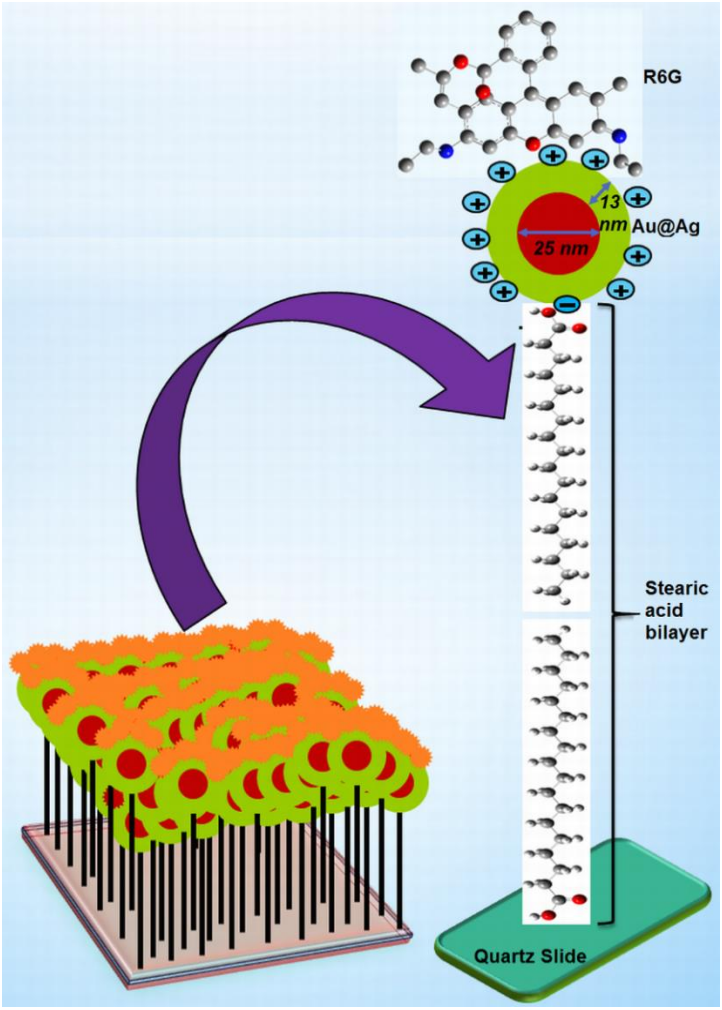

Figure 5.4: Schematic representation showing the interaction between SA in the bilayer LB film and the Au@Ag nanocolloid.

band undergoes considerable down shift and centered at ~ 423 nm. The blue shift is attributed to the alteration in the dielectric constant for metal nanoparticles surrounded by other metal nanoparticles [9,17]. However, at 72 hours of DT, the SP band undergoes further hyposchromic shift and exhibits distinct structureless band maximum centered at ~ 407 nm with the appearance of a prominent hump at ~ 354 nm. This hump in the absorption spectrum is attributed to quadrapolar resonance which is mostly reported to appear for spherical and nearly spherical nanoparticles [15]. The optical responses of the UV- Vis absorption spectra may provide an index to understand the variations in surface morphology of the aggregated nanocolloids self-assembled on the LB film of SA at various DTs.

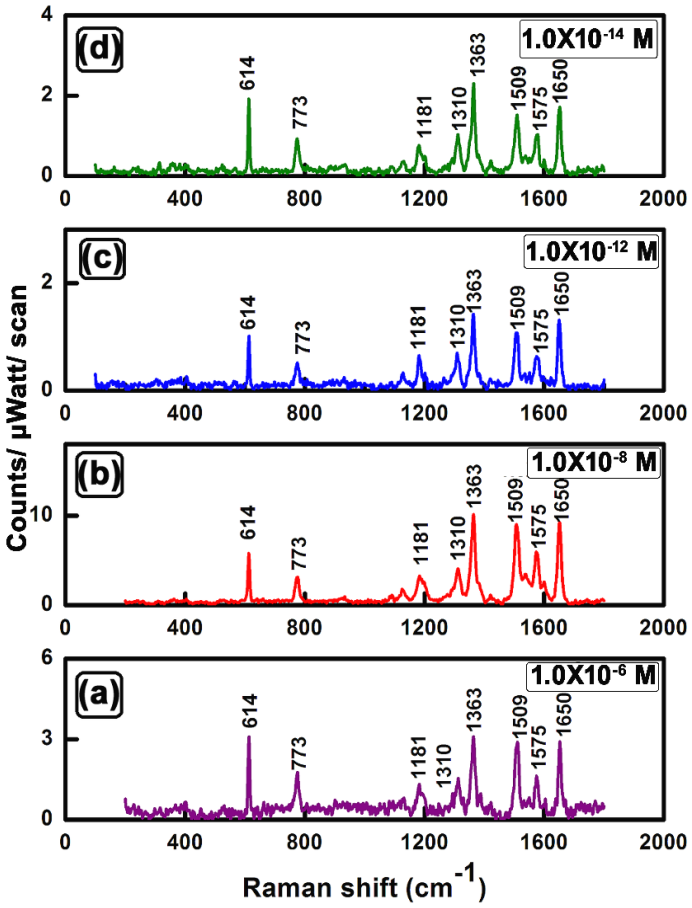

Figure 5.5: SER(R)S spectra of R6G molecule at varied concentrations of the adsorbate (λ_{ex}= 514.5 nm).

Figure 5.5 shows the concentration dependent SER(R)S spectra of R6G molecule adsorbed on the as prepared bilayer LB film of SA dipped in Au@AgNCs for 24 hours. The electronic absorption maximum of the probe R6G at ~ 525 nm together with the green laser excitation source allow us to record the surface enhanced resonance Raman scattering [SER(R)S] spectra of the molecule. The spectra are marked by enhanced Raman bands centered at ~ 614, 773, 1181, 1363, 1509, 1575 and 1650 cm^{-1} characteristic of R6G molecule [18]. The enhanced bands at ~ 614, 773, 1181, 1310, 1363, 1509, 1575 and 1650 cm^{-1} have been ascribed to in- plane vibrations, while 773 cm^{-1} band has been assigned to C – H out of plane mode associated with the xanthene ring plane of the R6G molecule. Figure 5.6 shows the variations in intensities of 614, 773, 1363, 1509, 1575 and 1650 cm^{-1} SER(R)S bands of R6G molecule with logarithm of the adsorbate concentrations. The concentration dependent variations in intensities of SER(R)S bands, in general, arises from

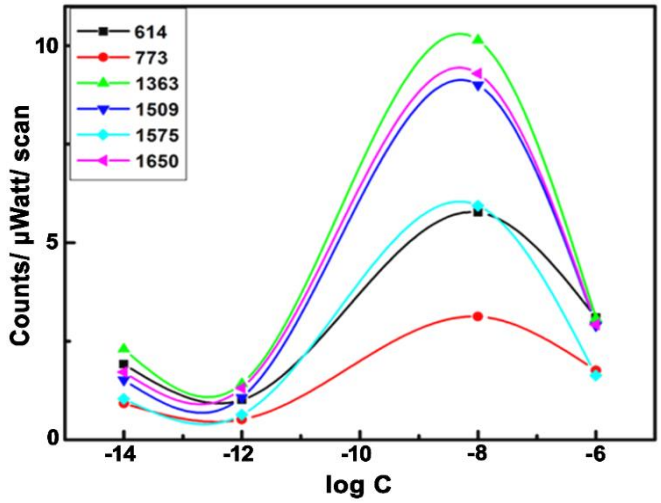

Figure 5.6: The variations in SER(R)S intensities of 614, 773, 1363, 1509, 1575 and 1650 cm^{-1} bands of R6G molecule with the change in concentrations of the adsorbate.

surface coverage [19,20]. At extremely low concentrations, the metal surface coverage by the adsorbates is sub monolayer. The SERS signal increases with increase in concentration of the adsorbate, attains a maximum intensity at monolayer coverage, where both the contributions from the EM and charge transfer (CT) effect to SERS maximize. With further increase in concentration of the adsorbates, multilayers are formed, resulting in the overall decrement of SERS signal. It therefore seems plausible that the monolayer coverage of the adsorbed R6G molecule on the as prepared substrate may have formed at a concentration $\sim 1.0 \times 10^{-8}$ M which exhibits maximum enhancement of the SER(R)S signals.

The SER(R)S and the RR spectra have been normalized with respect to 1363 cm^{-1} band. The relative intensity of this band does not change significantly in RR and in the SER(R)S spectra. In order to envisage the enhancements of SER(R)S bands, the apparent enhancement factors (AEF) have been estimated using the following relation [21].

$$\mathrm{AEF} = \sigma_{\mathrm{SER(R)S}}[\mathrm{C_{RR}}]/\sigma_{\mathrm{RR}}[\mathrm{C_{SER(R)S}}] \qquad (5.1)$$

where $[\mathrm{C_{RR/SER(R)S}}]$ and $\sigma_{\mathrm{RR/SER(R)S}}$ represent the concentrations and the integrated peak areas of the RR/ SER(R)S bands respectively normalized with respect to 1363 cm^{-1} band. The integrated areas of the RR, SER(R)S bands are measured from the baseline. The background corrected normalized RR spectrum of 0.1 M R6G in aqueous solution and the normalized SER(R)S spectra

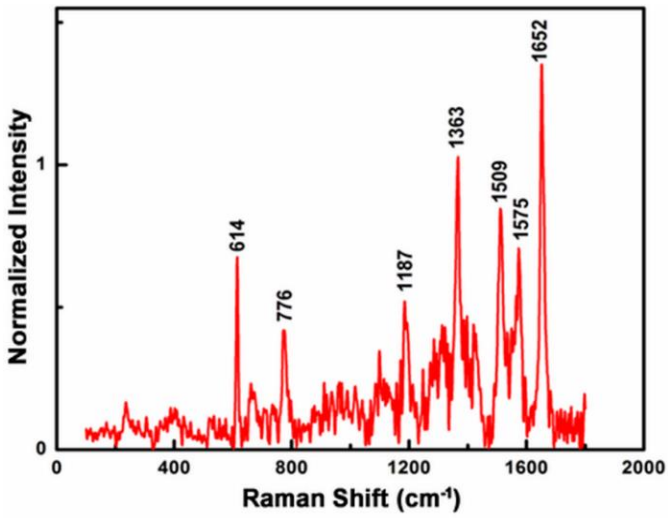

Figure 5.7: Normalized resonance Raman (RR) spectrum of 0.1 M R6G in aqueous solution (λ_{ex}= 514.5 nm) [Normalization has been done with respect to 1363 cm^{-1} band].

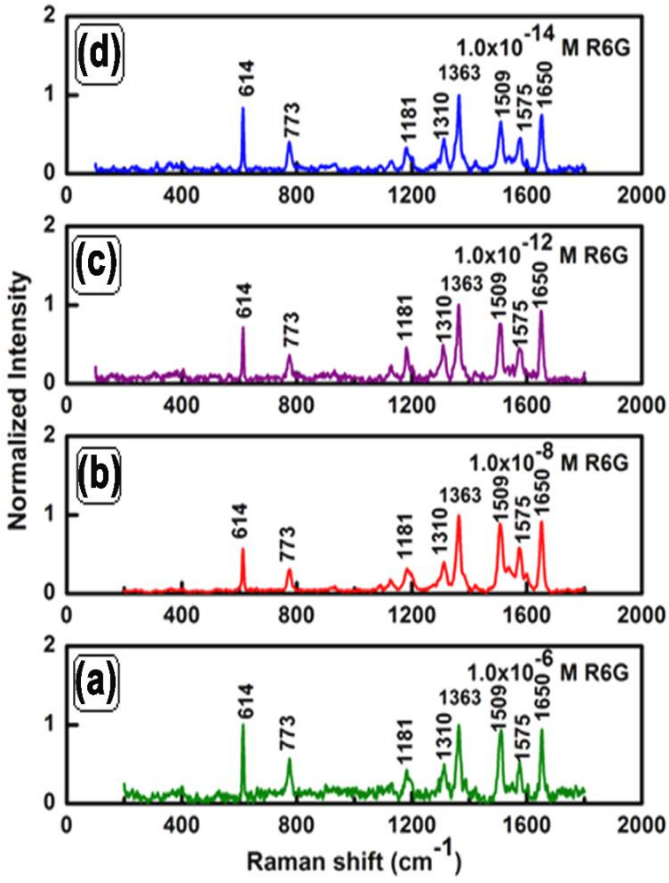

Figure 5.8: Normalized SER(R)S spectrum of R6G at various concentration of the adsorbate (λ_{ex}= 514.5 nm) [Normalization has been done with respect to 1363 cm^{-1} band].

of R6G at various concentrations of the adsorbate are shown in Figure 5.7 and 5.8 respectively. The apparent enhancement factors (AEFs) for 614, 773, 1181, 1363, 1509, 1575 and 1650 cm^{-1} bands have been given in Table 5.1. Enhancement factors ranging from $\sim 10^4 - 10^{13}$ orders of magnitude have been estimated for the above-mentioned bands. The normalized SER(R)S spectra

Table 5.1: Apparent enhancement factors (AEF) of SER(R)S bands of R6G molecules adsorbed on the as prepared substrate surface at various concentrations of the adsorbate

NRS (cm^{-1})	**Adsorbate Concentrations**								**Assignment[a]**
	10^{-6} M		**10^{-8} M**		**10^{-12} M**		**10^{-14} M**		
	SERS	**AEF**	**SERS**	**AEF**	**SERS**	**AEF**	**SERS**	**AEF**	
614	614	1.32 x10^5	614	8.72 x10^6	614	1.03 x10^{11}	614	1.08 x10^{13}	α (C-C-C)
776	773	1.25 x10^5	773	8.74 x10^6	773	7.83 x10^{10}	773	1.04 x10^{13}	γ (C-H)
1187	1181	8.96 x10^4	1181	2.30 x10^6	1181	5.92 x10^{10}	1181	3.38 x10^{12}	β (C- H)
1363	1363	9.26 x10^4	1363	9.98 x10^6	1363	9.23 x10^{10}	1363	8.96 x10^{12}	ν (C-C)
1509	1509	1.05 x10^5	1509	9.79 x10^6	1509	8.13 x10^{10}	1509	7.42 x10^{12}	ν (C-C)
1575	1575	6.46 x10^4	1575	9.43 x10^6	1575	8.05 x10^{10}	1575	7.26 x10^{12}	ν (C-C)
1652	1650	5.81 x10^4	1650	7.18 x10^6	1650	6.58 x10^{10}	1650	5.88 x10^{12}	ν (C-C)

Note: NRS: normal Raman spectrum; SERS: surface-enhanced Raman spectroscopy.

[a]α, β: in- plane bending; γ: out- of- plane bending; ν: streatching.

of 1.0×10^{-14} M R6G, recorded from 5 distinct spots each from three different as prepared substrates incubated in Au@Ag nanocolloidal solutions for 24 hours of DT, are shown in Figure

5.9. The spectral profiles are highly reproducible and exhibit distinct vibrational signatures of R6G molecule. The AEFs of the enhanced Raman bands, as obtained from the triplicate experiments after striking at five distinct spots on the as prepared substrates, are shown in Table 5.2. The estimated AEFs also support the reproducibility of the SER(R)S spectra of R6G molecule adsorbed on the as prepared substrates. These results suggest that the as prepared bilayer LB film of SA. dipped in Au@AgNCs for 24 hours behave as an efficient SERS active substrate for sensing R6G molecules at trace concentrations.

Kneipp et al. reported SERS enhancement factor (EF) $\sim 10^{14}$ orders of magnitude for NaCl activated nanocolloidal aggregates or clusters [22-25]. The EF was reported to be independent on the size of the nanoclusters. However, the huge EF ($\sim 10^{14}$) was questioned by Etchegoin *et. al.*

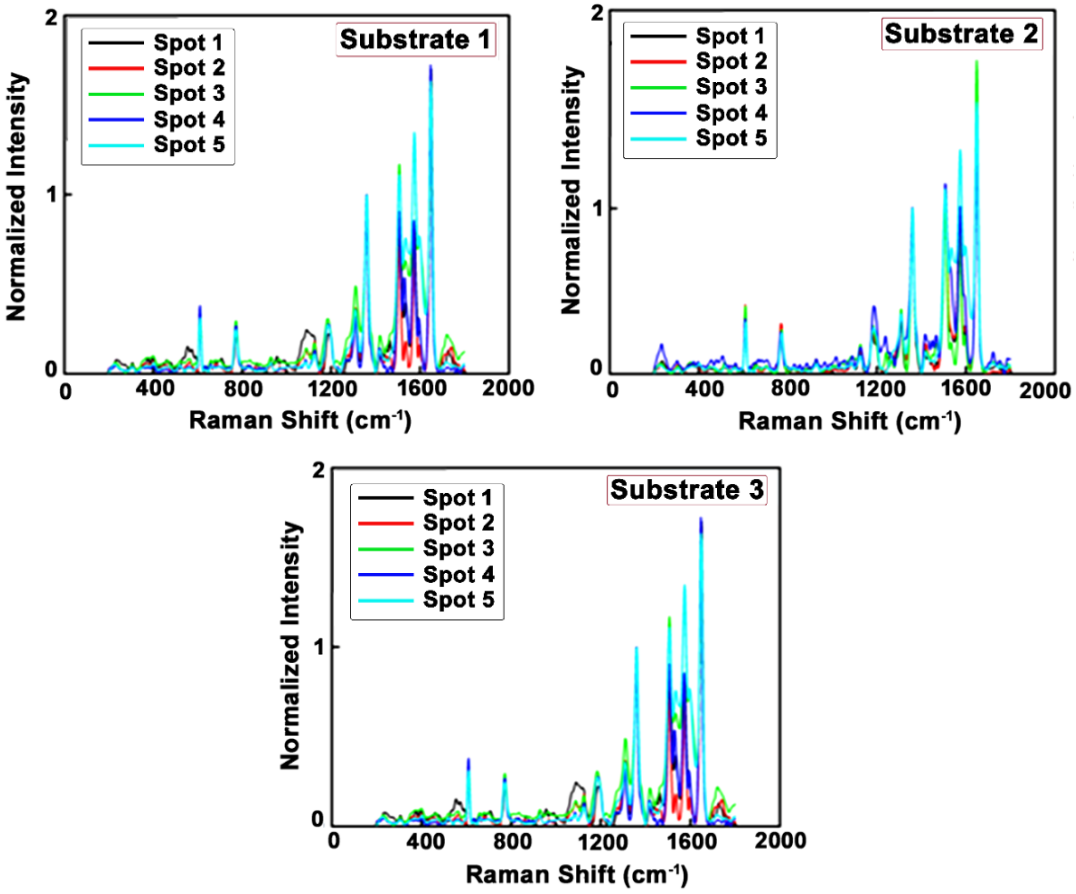

Figure 5.9: Normalized SER(R)S spectra of 1.0×10^{-14} M R6G, recorded from 5 distinct spots each from three different as prepared substrates (1, 2, 3) dipped in Au@Ag nanocolloid for 24 hours of DT (λ_{ex}= 514.5 nm) [Normalization has been done with respect to 1363 cm^{-1} band].

Table 5.2: Apparent enhancement factors (AEFs) of SER(R)S bands of 1.0×10^{-14} M R6G molecules as obtained from the triplicated experiments after striking at five distinct spots each from the three different *as- prepared* substrates at 24 hrs of DT

SERS bands (cm^{-1})	**AEF (Substrate 1)**					**AEF (Substrate 2)**					**AEF (Substrate 3)**				
	Spot 1	**Spot 2**	**Spot 3**	**Spot 4**	**Spot 5**	**Spot 1**	**Spot 2**	**Spot 3**	**Spot 4**	**Spot 5**	**Spot 1**	**Spot 2**	**Spot 3**	**Spot 4**	**Spot 5**
614	6.38 $\times 10^{12}$	8.02 $\times 10^{12}$	6.57 $\times 10^{12}$	1.15 $\times 10^{13}$	7.58 $\times 10^{12}$	8.16 $\times 10^{12}$	8.85 $\times 10^{12}$	8.80 $\times 10^{12}$	7.25 $\times 10^{12}$	6.83 $\times 10^{12}$	6.72 $\times 10^{12}$	5.87 $\times 10^{12}$	8.28 $\times 10^{12}$	6.92 $\times 10^{12}$	6.79 $\times 10^{12}$
773	6.22 $\times 10^{12}$	9.46 $\times 10^{12}$	7.51 $\times 10^{12}$	7.40 $\times 10^{12}$	7.33 $\times 10^{12}$	7.03 $\times 10^{12}$	8.82 $\times 10^{12}$	7.19 $\times 10^{12}$	6.87 $\times 10^{12}$	7.43 $\times 10^{12}$	6.05 $\times 10^{12}$	6.85 $\times 10^{12}$	8.04 $\times 10^{12}$	7.10 $\times 10^{12}$	7.57 $\times 10^{12}$
1181	7.78 $\times 10^{12}$	5.66 $\times 10^{12}$	1.07 $\times 10^{13}$	1.11 $\times 10^{13}$	4.85 $\times 10^{12}$	3.24 $\times 10^{12}$	4.20 $\times 10^{12}$	8.54 $\times 10^{12}$	1.16 $\times 10^{13}$	8.62 $\times 10^{12}$	6.68 $\times 10^{12}$	7.62 $\times 10^{12}$	1.08 $\times 10^{13}$	8.70 $\times 10^{12}$	8.48 $\times 10^{12}$
1363	1.26 $\times 10^{13}$	1.23 $\times 10^{13}$	1.28 $\times 10^{13}$	1.38 $\times 10^{13}$	1.13 $\times 10^{13}$	1.09 $\times 10^{13}$	1.25 $\times 10^{13}$	1.14 $\times 10^{13}$	1.34 $\times 10^{12}$	1.14 $\times 10^{13}$	1.12 $\times 10^{13}$	1.22 $\times 10^{13}$	1.22 $\times 10^{13}$	1.04 $\times 10^{13}$	1.23 $\times 10^{13}$
1509	6.86 $\times 10^{12}$	8.53 $\times 10^{12}$	7.71 $\times 10^{12}$	1.49 $\times 10^{13}$	1.62 $\times 10^{13}$	1.26 $\times 10^{13}$	1.26 $\times 10^{13}$	1.22 $\times 10^{13}$	1.27 $\times 10^{13}$	1.22 $\times 10^{13}$	1.00 $\times 10^{13}$	7.52 $\times 10^{12}$	1.31 $\times 10^{13}$	9.64 $\times 10^{12}$	1.29 $\times 10^{13}$
1575	2.33 $\times 10^{13}$	1.80 $\times 10^{13}$	1.03 $\times 10^{13}$	2.52 $\times 10^{13}$	1.29 $\times 10^{13}$	1.55 $\times 10^{13}$	1.48 $\times 10^{13}$	1.13 $\times 10^{13}$	1.49 $\times 10^{13}$	2.48 $\times 10^{13}$	1.27 $\times 10^{13}$	9.05 $\times 10^{12}$	2.26 $\times 10^{13}$	1.22 $\times 10^{13}$	2.57 $\times 10^{13}$
1650	1.47 $\times 10^{13}$	1.07 $\times 10^{13}$	1.15 $\times 10^{13}$	1.47 $\times 10^{13}$	1.87 $\times 10^{13}$	1.57 $\times 10^{13}$	1.52 $\times 10^{13}$	1.64 $\times 10^{13}$	1.16 $\times 10^{13}$	1.42 $\times 10^{13}$	1.45 $\times 10^{13}$	1.34 $\times 10^{13}$	1.36 $\times 10^{13}$	1.38 $\times 10^{13}$	1.48 $\times 10^{13}$

They suggested that the improper way of normalization may be the genesis of the enormous claims of SERS EF $\sim 10^{14}$ orders of magnitude. Moreover, AEF as estimated from equation (5.1) [vide supra] is best suited for SERS in colloidal solutions. The intrinsic problem in the AEF definition rests in the fact that it does not recognize SERS to be a type of surface spectroscopy. The crucial step from transferring 3D solutions to 2D SERS active substrates may markedly affect the estimated AEF values by several orders of magnitude [26]. However, precise estimation of the EF may be obtained from SERS substrate EF (SSEF), defined as [26]

$$SSEF = [I_{SERS}/N_{SURF}]/[I_{RS}/N_{VOL}] \qquad (5.2)$$

where, I_{SERS} and I_{RS} are the intensities of the SER bands and the normal Raman spectrum respectively, N_{SURF} is the number of molecules adsorbed on the SERS active substrate at respective adsorbate concentrations and N_{VOL} is the number of molecules sampled in the bulk solution.

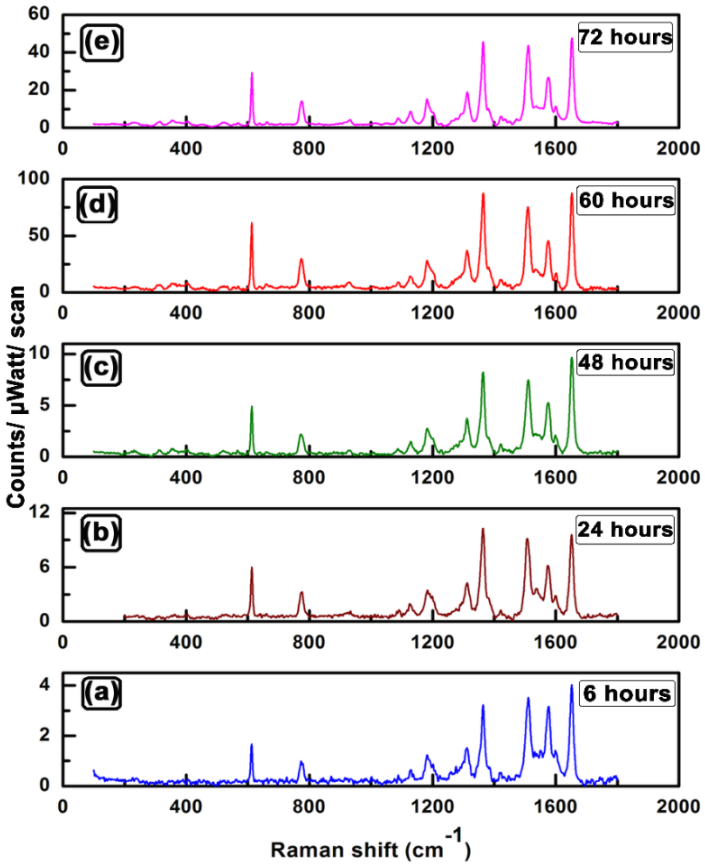

Figure 5.10: SER(R)S spectra of 1.0 x 10^{-8} M aqueous solution of R6G molecule at various DTs (λ_{ex}= 514.5 nm).

As there are limitations in determining accurately the number of molecules on the as prepared SERS active substrates, qualitative estimations have been made from the AEF calculations. AEF ranging from $\sim 10^4 - 10^{13}$ orders of magnitude have been estimated for the characteristic vibrational signatures of R6G molecule. The estimated EFs are few orders of magnitude less as reported by Kneipp et. al, [22-25] and are few orders higher with the reports of Etchegoin et. al. [26-29].

In this connection, it may be relevant to mention that the EFs ranging from $10^6 - 10^{10}$ orders of magnitude have been reported for R6G molecule when adsorbed on AuNP film surface [30-35]. Moreover, the EFs of the characteristic Raman bands of R6G molecule on the as prepared substrates are $\sim 10^1 - 10^3$ orders of magnitude higher in comparison to that on Au@Ag nanocolloidal substrates reported elsewhere [7,13,36-38]. The colossal enhancement factors may also prove the superiority of the as prepared substrates over others.

The SER(R)S spectra of 1.0×10^{-8} M R6G molecule adsorbed on the as prepared bilayer substrate of SA incubated in Au@AgNC solutions for 6 hours to 72 hours of DTs are shown in Figure 5.10. The enhancements of almost all the bands, characteristic of R6G molecule, further corroborates the proficiency of the as prepared substrates as effective SERS sensing platforms.

5.2.3 Surface characterization study of the as prepared substrates

In order to estimate a correlation between the surface morphology and roughness features, the FESEM and AFM images of the as prepared SER(R)S active substrates have been recorded. Figure 5.11 shows the FESEM images of the bare quartz slide, bilayer SA LB film and the as prepared bilayer LB films of SA incubated in Au@AgNCs at various DTs ranging from 6 hours to 72 hours. The FESEM images reveal that the nano aggregated structures of the Au@AgNCs incubated for 6 - 48 hours of DTs are interlaced and exhibit fractal like patterns. Interestingly, the FESEM image of as prepared substrate incubated for 24 hours of DT, exhibits the most homogenous feature characterized by small fractal like aggregated structures. The homogeneity of the as prepared substrate impels us to record the SER(R)S spectra of R6G molecule at various concentrations of the adsorbate as shown in Figure 5.5 (vide ante). However, with the increase in DTs (ca. 60 and 72 hours), the overall morphology changes to lumpy structures manifesting more of Euclidean features. These changes in the morphological features may be attributed to the

formation of oxides on the Au@Ag aggregated surfaces [14]. Moreover, with the increase in DTs, the density of the nano aggregated particles on the surface of the substrate increases with the concomitant decrease in the interstitial gap between the particles. These perturbation in the morphological features of the as prepared substrates may result in broadening of the absorption spectra as discussed earlier (Figure 5.2 (c) - (g); vide ante). To verify the elemental identity of the

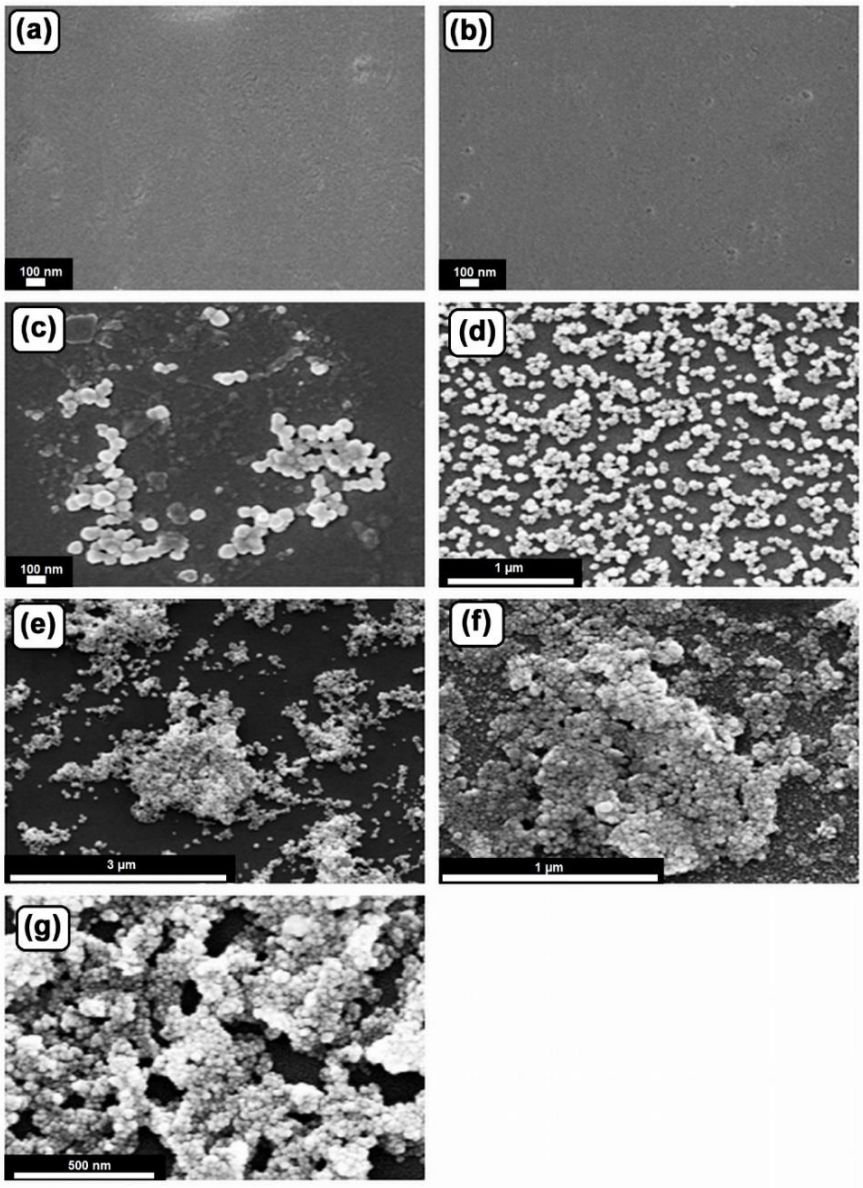

Figure 5.11: FESEM images of the as prepared substrates at various DTs. (a) Bare quartz glass slide, (b) Bilayer LB film of SA lifted at 25 mN/m surface pressure. Bilayer LB film of SA incubated in Au@ Ag NCs at (c) 6 hrs (d) 24 hrs (e) 48 hrs (f) 60 hrs (g) 72 hrs. of DTs.

as prepared substrate, the EDX analysis has been done and is shown in Figure 5.12. The EDX analysis confirm the expected existence of gold, silver and oxygen on the as prepared film substrate, together with the presence of Na emanating from the quartz slide.

Figure 5.13 shows the 2D and 3D AFM images of the bilayer LB film of SA incubated in Au@AgNCs at various DTs. The images divulge the formation of fractal like nano aggregated

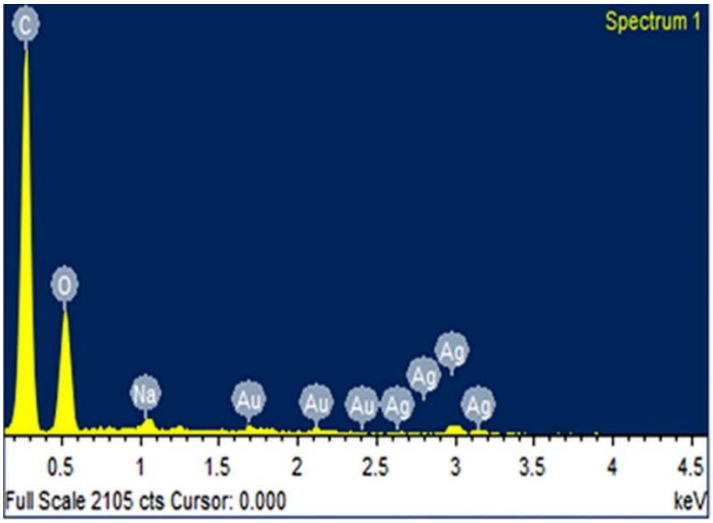

Figure 5.12: EDX analysis of the as prepared substrate.

patterns on the surface of the as prepared films. In this connection, it may be worth to mention, that the bilayer LB film substrate dipped for 60 hours in the nano colloidal solution exhibits the most enhanced SER(R)S bands of R6G molecule (vide supra, Figure 5.10). The normalized SER(R)S spectra of 1.0×10^{-8} M R6G molecule, recorded from six different spots of the as prepared substrate incubated in Au@Ag nanocolloidal solutions for 60 hours of DT, are shown in Figure 5.14. The spectra are highly reproducible and exhibit no noticeable band shift. The corresponding morphological features of the substrate may be associated with SER(R)S efficacy from the 3D AFM image. The image [Figure 5.13 (c), (C)] clearly smears the aggregation of Au@AgNC particles on the film surface with distinct sharp tips and precise interparticle spacings. The sharp tips may sustain the lightening rod effect, while the precise interparticle spacings favour the coupling of the LSPs to generate the necessary hot spots responsible for the gigantic SER(R)S enhancements.

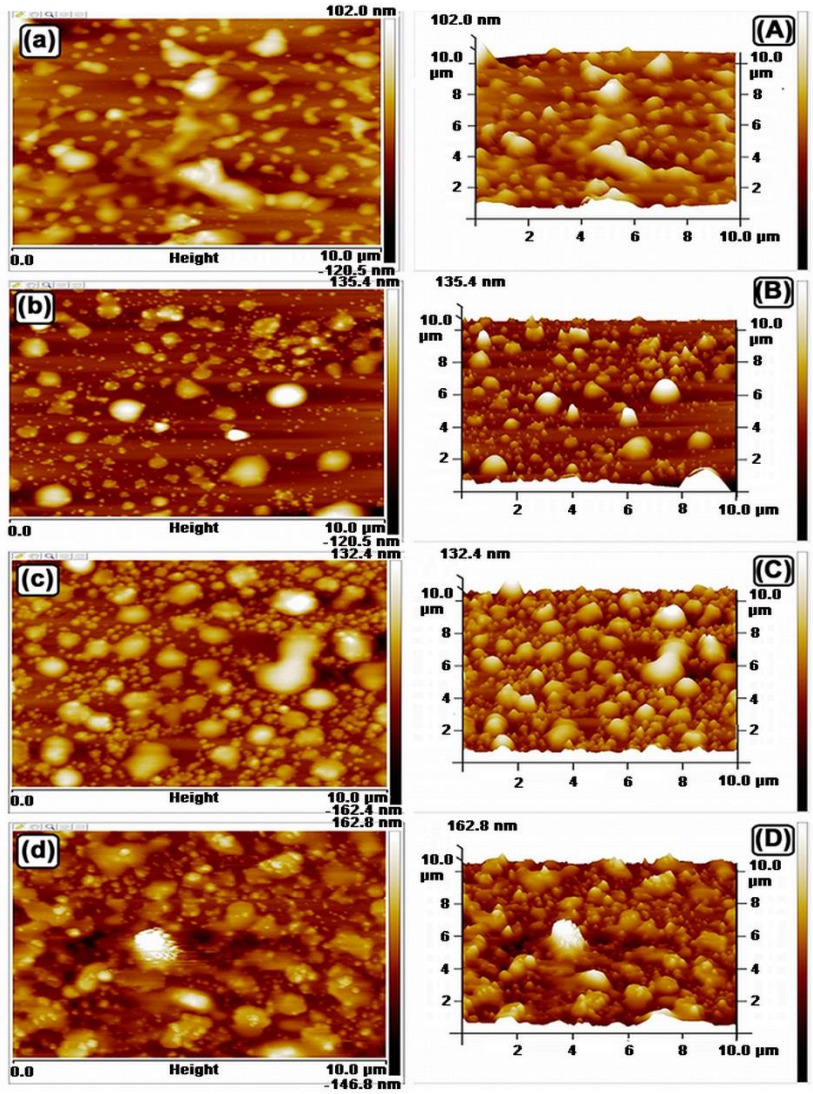

Figure 5.13: AFM images of the as prepared substrates. The left column contains topographic 2D AFM images at (a) 6 hrs, (b) 24 hrs, (c) 60 hrs and (d) 72 hrs of DTs. The right column shows the 3D AFM images of the same samples at (A) 6 hrs, (B) 24 hrs, (C) 60 hrs and (D) 72 hrs of DTs.

The root mean square (RMS) roughness of the as prepared substrates has been estimated using the relation,

$$R_q = \sqrt{\sum (z_i)^2 / N} \qquad (5.3)$$

where Z_i is the current value of peak-to-valley difference in height within the analyzed region and N is the number of points within the box cursor. Figure 5.15 shows the variations in the roughness features of the bilayer LB film of SA incubated in the nanocolloids at various DTs. The plots

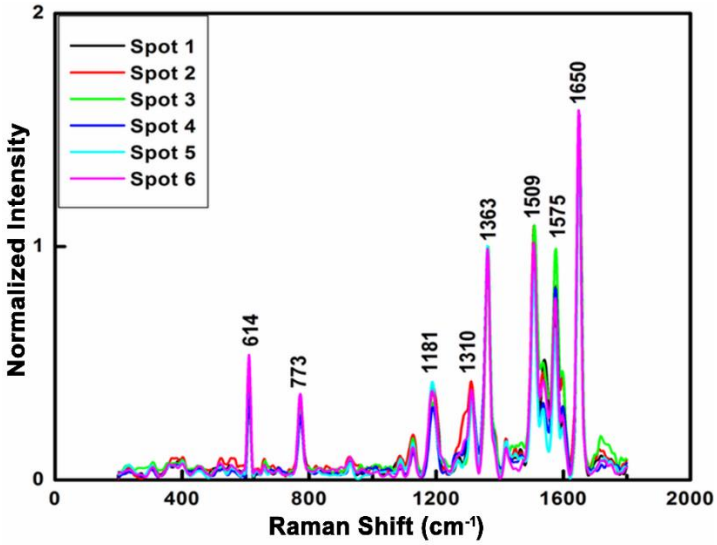

Figure 5.14: Normalized SER(R)S spectra of 1.0×10^{-8} M R6G molecule, recorded from six different spots of the as- prepared substrate incubated in Au@Ag nanocolloidal solutions for 60 hrs of DT (λ_{ex}= 514.5nm) [Normalization has been done with respect to 1363 cm^{-1} band].

indicates monotonic increase in the roughness features of the as prepared substrates with increase in DTs. The increase in surface roughness with DT may auger variations in the morphological features of the as prepared substrates. The RMS roughness has been estimated to be ~ 32.13 nm for the bilayer LB film of SA dipped for 60 hours in the Au@AgNC solution. This RMS roughness

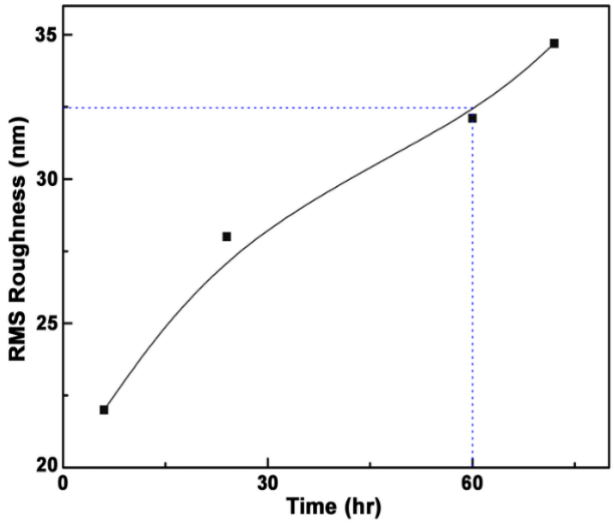

Figure 5.15: Variation in the RMS values of surface roughnesses of the as prepared substrates with various DTs in Au@AgNCs.

may be considered to be the optimum roughness feature for the as prepared substrate to generate the most enhanced Raman bands in the SER(R)S spectrum of R6G molecule [Figure 5.10 (d)].

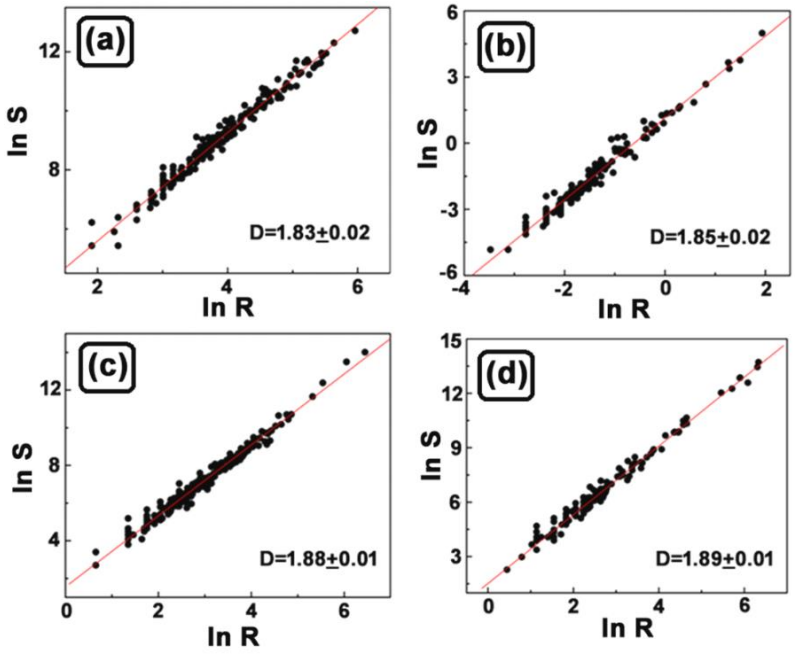

Figure 5.16: Ln R vs Ln S plots of the as prepared samples at various DTs inorder to explore fractal dimension. The error of the slope determination is coming from line fitting; (a) 24 hours, (b) 48 hours, (c) 60 hours, (d) 72 hours.

In order to elucidate fractal dimensions of the as prepared nano aggregated structures, radial mass distribution method has been applied. The area covered by each structure, S and the Hausdroff dimension, D are related as

$$S \infty R^{D} \qquad (5.4)$$

where, R is the average distance from the centre of mass of each structure to its perimeter [39]. The slopes of ln S vs ln R plots will allow us to estimate the fractal dimensions of the nanoaggregated assembles. Points are taken from different regions of the FESEM topographies and are fitted to straight lines by least square method. They are shown in Figure 5.16. From Figure 5.16, the fractal dimensions are estimated to be 1.83 ± 0.02, 1.85 ± 0.02, 1.88 ± 0.01 and 1.89 ± 0.01 for the as prepared bilayer LB film of SA dipped in 24 hours, 48 hours, 60 hours and 72 hours DTs respectively. These results are in accordance with our previous conjecture depicting the variations in the morphological features of the as prepared substrates from fractals to Euclidian patterns with the increase in DTs.

5.2.4 Estimation of EM enhancement

The electric field ($\vec{E}$) distributions around the metallic nanoparticles have been estimated to explore the genesis of enhancements of the SER(R)S bands of R6G molecule adsorbed on bilayer LB film of SA incubated for 60 hours of DT. The $\vec{E}$- field distributions are estimated directly from the FESEM topography of the as prepared substrate, and are shown in Figure 5.17. The FESEM image as shown in Figure 5.17, exhibits large number of densed nano aggregated structures in which each particle may interact through dipole- dipole coupling that may be considered favourable for the generation of hot spots. The as prepared films may have hot/ cold spots characteristic of the fractal nature of the aggregated nanocolloids. As the aggregates are fractal in nature, the normal modes of the surface plasmon oscillations are localized within these hot specks that carry the full excitation [40]. The hot spots localized in the fractal aggregates may exhibit enormous electromagnetic enhancements in comparison to non-fractal aggregates. Moreover, the surface roughness of the as prepared films may result in aggregation of fractal nature that may help to excite the localized surface plasmons by the application of electric fields. Figure 5.18 shows the spatial distributions of $\vec{E}$- fields around some selected hot geometries which are marked in the FESEM image. From Figure 5.18 (a), it is seen that the hottest among the hot spots is spatially confined in the inter particle gap ~ 1.8 nm where the spatial distribution of $\vec{E}$- field is extended over an approximate length of ~ 22 nm. The $|\vec{E}|$ fields for this hottest geometry are

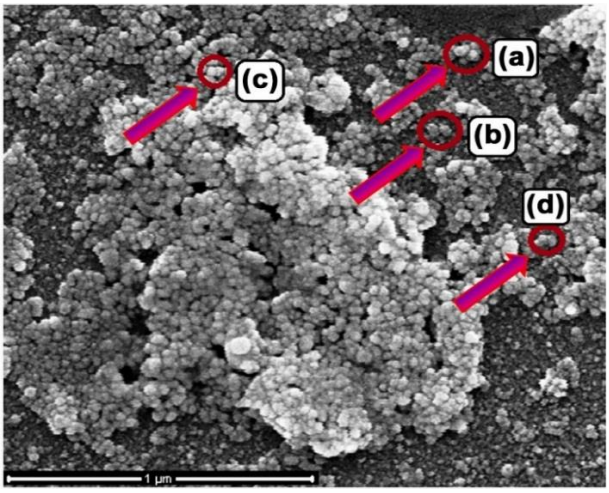

Figure 5.17: Selected Au@Ag nanoaggregated geometries of the as prepared substrates used for 3D-FDTD simulation.

estimated to be ~ 30 volt/ m [Figure 5.18 (a)], which approximately corresponds to the SE(R)RS enhancement factor $[G'(\omega, \omega')]$ ~ 10^5 orders of magnitude following the plane wave (PW) approximation. However, the variance of the estimated $G'(\omega, \omega')$ with those predicted from the experimental observations may be attributed to the resonance and the CT effect to SER(R)S apart from the EM mechanism. Thus, the EM, CT and resonance effect significantly contribute towards the enhancements of Raman bands in the SER(R)S spectra of R6G molecule. Tuning the interparticle plasmon coupling may be accomplished by lifting the bilayer LB film of SA at different surface pressures followed by the self-assembly of the nanocolloidal particles. The aspect of controlling the interparticle coupling of the surface plasmons may be an interesting issue to be focussed in our future publications.

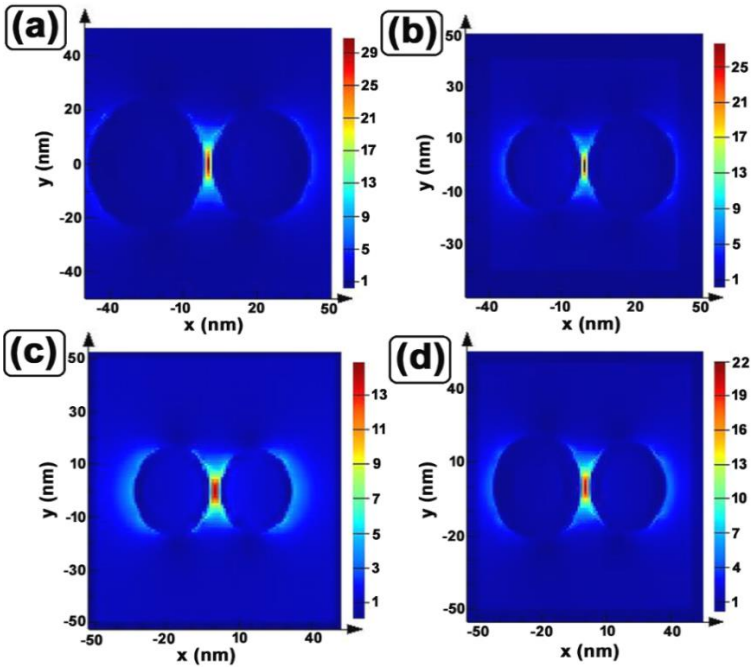

Figure 5.18: Electric field distribution around the hot-spots as estimated from 3D- FDTD simulations (λ_{ex}= 514.5 nm, the polarization of the incident light wave is along x- axis).

5.3 Conclusion

Au@Ag nanocolloids entrapped in the bilayer LB film of SA matrix has been established as an excellent SERS active substrate. Enhancement factors ranging from $10^4 - 10^{13}$ orders of magnitude have been estimated for the characteristic SER(R)S bands of R6G molecule. Correlations between the surface morphologies, fractal dimensions and roughness features of the

established SERS active substrates have been drawn. The spatial distribution of electric fields around the aggregated nanocolloids entrapped in the SA matrix has been estimated with the aid of 3D- FDTD simulations. The localized surface plasmons coupling between the aggregated nanocolloids may be controlled by lifting the LB film of SA at different surface pressures. This aspect of controlling the architecture of the as prepared substrate will be focused in the future publication.

References

1. N. R. Jana, T. Pal, *Adv. Mater*., 2007, **19**, 1761.
2. J. Bian, S. Shu, J. Li, C. Huang, Y. Y. Li, R. Q. Zhang, *Appl. Surf. Sci*., 2015, **333**, 126.
3. C. L. Nehl, J. H. Hafner, *J. Mater. Chem*., 2008, **18**, 2415.
4. Y. Yang, J. Liu, Z. W. Fu, D. Qin, *J. Am. Chem. Soc*., 2014, **136**, 8153.
5. Z. Zhang, W. Zhu, *Appl. Surf. Sci*., 2015, **333**, 214.
6. A. Roguska, A. Kudelski, M. Pisarek, M. Opara, M. J. Czachor, *Appl. Surf. Sci*., 2011, **257**, 8182.
7. N. R. Jana, *Analyst*, 2003, **128**, 954.
8. P. Pienpinijtham, X. X. Han, S. Ekgasit, Y. Ozaki, *Phys. Chem. Chem. Phys*., 2012, **14**, 10132.
9. M. A. Mahmoud, C. E. Tabor, M. A. El- Sayed, *J. Phys. Chem. C*, 2009, **113**, 5493.
10. A. Tao, F. Kim, C. Hess, J. Goldberger, R. He, Y. Sun, Y. Xia, P. Yang, *Nano Lett*., 2003, **3**, 1229.
11. M. J. Hwang, K. Kim, *Langmuir*, 1999, **15**, 3563.
12. G. Frens, *Nat. Phys. Sci*., 1973, **241**, 20.
13. A. Saha, S. Palmal, N. R. Jana, *Nanoscale*, 2012, **4**, 6649.
14. J. Sarkar, P. Pal, G. B. Talapatra, *Chem. Phys. Lett*., 2005, **401**, 400.
15. K. L. Kelly, E. Coronado, L. L. Zhao, G. C. Schatz, *J. Phys. Chem. B*, 2003, **107**, 668.
16. W. Gotschy, K. Vonmetz, A. Leitner, F. R. Aussenegg, *Optics Lett*., 1996, **21**, 1099.
17. J. R. Heath, C. M. Knoblerdaniel, V. Leff, *J. Phys. Chem. B*, 1997, **101**, 189.
18. P. Hildebrant, M. Stockburger, *J. Phys. Chem*., 1984, **88**, 5935.
19. J. Chowdhury, M. Ghosh, *J. Colloid Interface Sci*., 2004, **277**, 121.
20. J. Chowdhury, M. Ghosh, P. Pal, T. N. Misra, *J. Colloid Interface Sci*., 2003, **263**, 318.

21. J. Sarkar, J. Chowdhury, M. Ghosh, R. De, G. B. Talapatra, *J. Phys. Chem. B*, 2005, **109**, 12861.
22. K. Kneipp, H. Kneipp, I. Itzkan, R. R. Dasari, M. S. Feld, *Chem. Rev*., 1999, **99**, 2957.
23. J. Kneipp, H. Kneipp, K. Kneipp, *Chem. Soc. Rev*., 2008, **37**, 1052.
24. K. Kneipp, Y. Wang, H. Kneipp, L. T. Perelman, I. Itzkan, R. R. Dasari, M. S. Feld, *Phys. Rev. Lett*., 1997, **78**, 1667.
25. K. Kneipp, H. Kneipp, I. Itzkan, R. R. Dasari, M. S. Feld, *Chem. Phys*., 1999, **247**, 152.
26. E. C. Le Ru, P. G. Etchegoin, *MRS Bulletein*, 2013, **38**, 631.
27. P. G. Etchegoin, P. D. Lacharmoise, E. C. Le Ru, *Anal. Chem*., 2009, **81**, 682.
28. E. J. Blackie, E. C. Le Ru, P. G. Etchegoin, *J. Am. Chem. Soc*., 2009, **131**, 14466.
29. P. G. Etchegoin, E. C. Le Ru, *Phys. Chem. Chem. Phys*., 2008, **10**, 6079.
30. M. Suzuki, Y. Niidome, Y. Kuwahara, N. Terasaki, K. Inoue, S. Yamada, *J. Phys. Chem. B*, 2004, **108**, 11660.
31. D. S. dos Santos, Jr., P. J. G. Goulet, N. P. W. Pieczonka, O. N. Oliveira, Jr., R. F. Aroca, *Langmuir*, 2004, **20**, 10273.
32. L. Polavarapu, Q. H. Xu, *Langmuir*, 2008, **24**, 10608.
33. R. Que, M. Shao, S. Zhuo, C. Wen, S. Wang, S. T. Lee, *Adv. Funct. Mater*., 2011, **21**, 3337.
34. A. M. Schwartzberg, C. D. Grant, A. Wolcott, C. E. Talley, T. R. Huser, R. Bogomolni, J. Z. Zhang, *J. Phys. Chem. B*, 2004, **108**, 19191.
35. S. Q. Zhu, T. Zhang, X. L. Guo, X. Y. Zhang, *Nanoscale Res. Lett*., 2014, **9**, 114.
36. E. Kirubha, P. K. Palanisamy, *Adv. Nat. Sci.: Nanosci. Nanotechnol*., 2014, **5**, 045006.
37. L. Lu, H. Wang, Y. Zhou, S. Xi, H. Zhang, J. Hu, B. Zhao, *Chem. Commun*., 2002, 144.
38. Y. Yang, J. Shi, G. Kawamura, M. Nogami, *Scripta. Materiala*, 2008, **58**, 862.
39. C. Haley, J. H. Weaver, *Surf. Sci*., 2002, **518**, 243.
40. V. A. Markel, V. M. Shalaev, P. Zhang, W. Huynh, L. Tay, T. L. Haslett, M. Moskovits, *Phys. Rev. B*, 1999, **59**, 10903.

Chapter 6: Infused self-assembly on Langmuir- Blodgett Film: Fabrication of highly efficient SERS active substrates with controlled plasmonic aggregates

---

6.1 Introductory Remarks

The basic snag of the SERS phenomenon and the blazing issue of concern is the intrinsic reproducibility of the SERS active substrates. The huge enhancement of the SERS signals of probe molecules are often identified with the pragmatic fabrications of SERS active substrates having high density of aggregated plasmonic nanoparticles (Nps) architectures. The Np aggregates are believed to have the largest contribution to SERS by harvesting the electric field at the nano gaps or clefts (hot spots) of the aggregate, promoting gigantic Raman signals. On the basis of these considerations, great deal of current research efforts are focused on the fabrication of plasmonic nanostructures that produce hot geometries, wherein the probe molecules can entrap for giant Raman enhancements [1-3]. However, unfortunately, most of these substrates fail to overcome the "SERS uncertainty principle" which predicts the reproducibility of the substrates at the expense of the enhancement factor of the Raman vibrational signatures [4,5]. Thus, more reproducible a substrate is, less is the corresponding amplification (Enhancement Factor) of the Raman signal.

In the present chapter, LB technique in conjunction with the self-assembly of nanocolloids has been used to fabricate highly reproducible SERS active substrates that can sense 4-mercapto pyridine (4-MPy) molecule at ultrasensitive concentrations. Self-assembly is an elegant technique in which molecules or nanocolloids spontaneously interact with one another via unbiased attractive and repulsive interactions to form organized molecular or colloidal ensembles [6,7]. These molecular or nano colloidal ensembles are generally guided by non-covalent interactions leading to thermodynamically stable organized structures or patterns having lower Gibbs free energies. The plasmonic architectures of the as prepared substrates can be tuned at will to control the gap plasmons and hence the overall enhancement of SERS signals. To our knowledge, this genre of SERS active substrates with facile control over plasmonics facilitated by the aggregation of the nanocolloidal particles is expected to provide a new rostrum towards successful fabrication of next generation SERS sensing platforms.

6.2 Results and Discussions

6.2.1 Room temperature pressure-area isotherm of Langmuir monolayer

PMMA is known to form floating monolayer at the air-water interface. The room temperature surface pressure (π) – area (A) compression isotherm of PMMA at the air-water

interface is shown in Figure 6.1. Under isothermal compression, the PMMA monolayer at the air-water interface undergoes several phase transitions of 1st order. No trace of gaseous phase transition is observed in the isotherm plot. The proportional increase in surface pressure with decreasing area is first observed in the surface pressure range ~ 0 to 14 mN/ m indicating the existence of liquid expanded (LE) phase. Thereafter a small plateau like region in the curve is

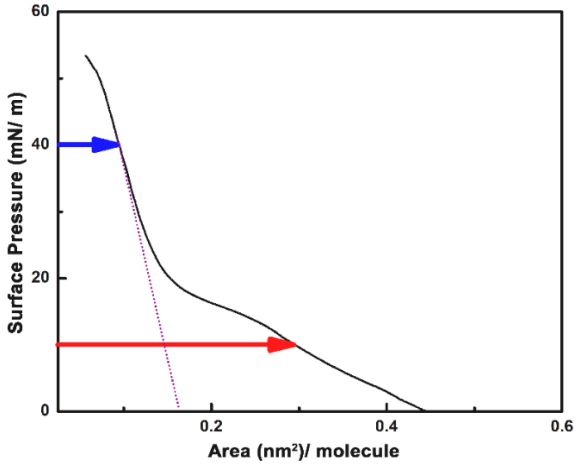

Figure 6.1: Room temperature surface pressure (π) – area (A) compression isotherm of a Langmuir monolayer of PMMA in pure water sub phase (pH ~ 6.8).

observed, followed by a sharp rise in surface pressure at ~ 21 mN/ m proceeding to collapse of the monolayer. Significant increase in the surface pressure with small decrease in area marks the second phase transition, representing liquid condensed (LC) state of the monolayer assemblies at the air- water interface. The nature of the isotherm is in accordance with the earlier reports [8] and the area/ PMMA molecule is estimated to be ~ 0.16 nm^2/ molecule. The monolayer LB films of PMMA were lifted at 40 and 10 mN/ m surface pressures on pre cleaned quartz slides (Tedpella, Inc) of area ~ 2 x 1 cm^2 by Y- type deposition technique. The as prepared LB film substrates covering ~ 2 x 1 cm^2 area of the quartz slides were then immersed in the AuNCs for various incubation times (ITs) ranging from 2 hours to 48 hours at room temperature under normal atmospheric pressure. The Au nanoparticles (AuNps) get adsorbed to the PMMA matrix of the LB film probably through its carbonyl group. Monomer unit of PMMA molecule consists of one carbonyl $(C = O)$ group and the other ester functional group containing oxygen atom. The oxygen atom of the $C = O$ group has higher negative charge density in contrast to the $C - O$ bond of the ester group. Thus, it is more likely that AuNps may bind with PMMA through the lone pair

electrons of oxygen atom associated with the $C = O$ group of the polymer. Moreover, the interactions between the AuNps and PMMA have also been investigated in detail from the XPS studies, reported elsewhere [9,10]. The survey scans of pure PMMA and Au- PMMA composites show the existence of carbon (C), oxygen (O) and gold (Au) atoms only. The XPS scans of C1s, O1s and Au4f provide specific idea about the interaction. The relative intensity ratio of the $C = O$ peak to the $C - O - C$ peak of PMMA in the XPS spectra increases with increase in concentration of gold nanoparticles in PMMA. These results signify interaction between Au and oxygen atoms through the $C = O$ groups of PMMA. Moreover, the shift of the Au4f doublet peak towards the higher binding energies in case of higher Au concentrated samples further corroborates the interaction between Au and O via the carbonyl $(C = O)$ group of PMMA. The films were then removed from the colloid, washed thoroughly with deionized water and allowed to dry in hot air oven. This process helps to eliminate the excess unreduced gold ions from the as prepared film surface. Finally, 25 µl aqueous solution of 4-MPy with varied concentrations ranging from $1.0 \times 10^{4} - 1.0 \times 10^{-12}$ M have been adsorbed on the as prepared substrates, dried in hot air oven before recording its SERS spectra.

6.2.2 UV- Vis spectra of the as-prepared substrates

Figure 6.2 (a) shows the room temperature UV- Vis electronic absorption spectrum of pristine AuNCs. The absorption spectrum of AuNC, as shown in Figure 6.2 (a), exhibits a strong absorption maximum centered at ~ 534 nm, along with broad humps at ~ 262 nm and 375 nm. The former band has been broadly ascribed to localized surface Plasmon resonance (LSPR) while the later pair is owed due to the intra- band electronic transitions of gold nanoparticles [11,12]. Figure 6.2 [(b) - (d)] shows the corresponding absorption spectra of AuNC immersed in the monolayer LB film of PMMA for various ITs ranging from 12 hours to 36 hours. The LSPR peaks of AuNC adsorbed in the LB films of PMMA are decreased in intensity, red shifted with respect to 534 nm band of pure AuNC and appear as shoulder ~ 548 - 554 nm in the UV-Vis spectra. Additionally, broad absorption maxima ranging from ~ 594 - 674 nm for AuNC self-assembled in the LB films of PMMA have been observed. The broad bands ~ 594 - 674 nm primarily mark the existence of various aggregated states of the AuNCs self-assembled in the PMMA matrix of the monolayer LB film [13,14]. These low energy bands in the UV- Vis absorption spectra are now specifically

ascribed to surface like surface Plasmon resonance (SL-SPR) and their appearance are intimately related with the degrees of aggregation of the AuNCs [15].

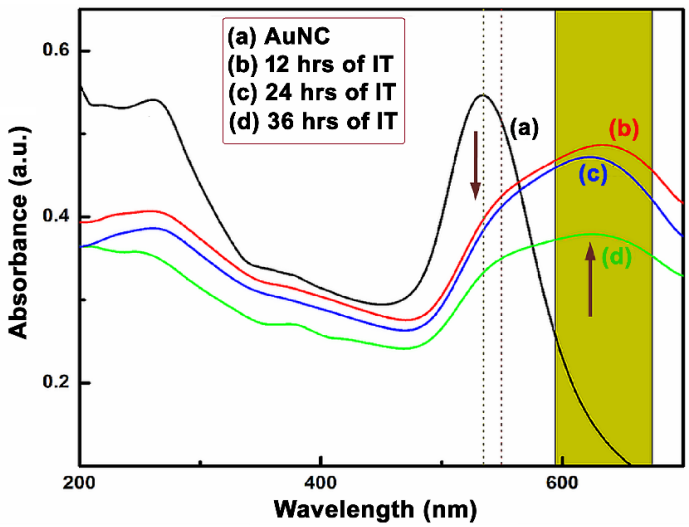

Figure 6.2: Room temperature UV- Vis electronic absorption spectra of (a) AuNC and [(b) - (d)] AuNC self-assembled in the monolayer LB film of PMMA at various ITs.

The interplay between short range nanoparticle- nanoparticle (F_{NNA}), nanoparticle-monolayer (F_{NMA}), monolayer- monolayer (F_{MMA}) attractive and dipolar long-range nanoparticle-nanoparticle repulsive (F_{NNR}) forces may favour the self-assembly of the AuNC over the monolayer LB film matrix of PMMA. The precise balance between the attractive and repulsive forces provides the necessary thermodynamic stability towards the generation of gold nanocolloidal aggregates of different degrees on the PMMA matrix, each of whose optical responses is characterized by their respective low energy bands. The broadening and the LSPR shifts, together with the appearance of low energy bands in the UV- Vis absorption spectra thus steer us to introspect the morphological and topographical details of the aggregated nanocolloids entrapped in the monolayer LB film of PMMA.

6.2.3 Morphological and topographical features of the as-prepared substrates

The morphological features of the as prepared substrates are visualized from the FESEM images. The FESEM images of the bare glass slide and the monolayer LB film of PMMA lifted at 40 mN/ m surface pressure are shown in Figure 6.3 (a) and (b) respectively. Figure 6.3 (b) shows the compact arrangement of monolayer PMMA on the quartz glass slide structured with aggregated

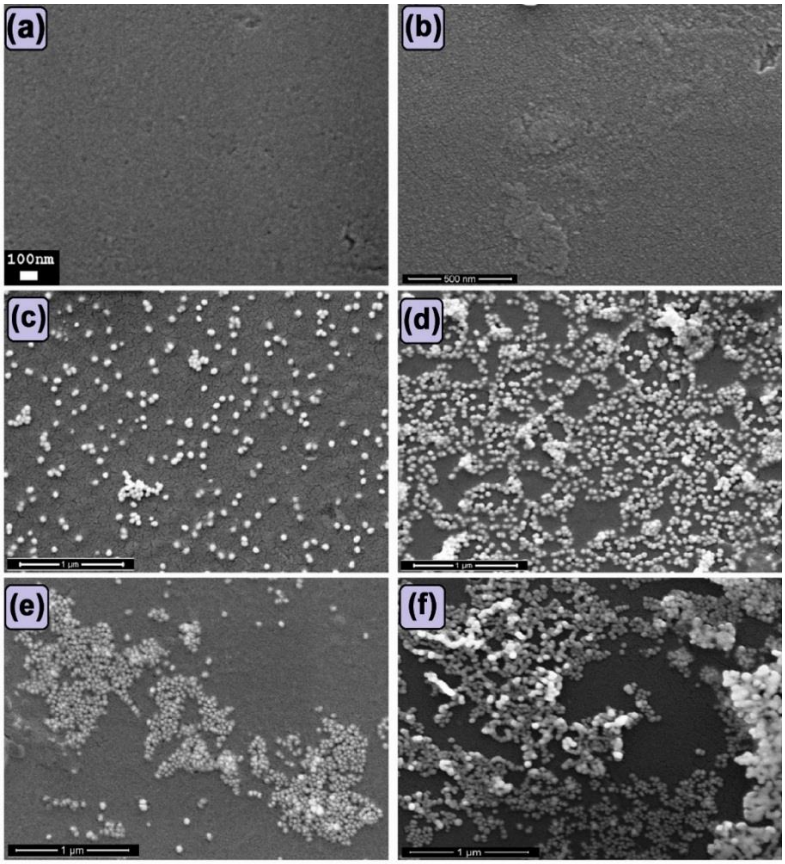

Figure 6.3: FESEM images of (a) bare quartz slide, (b) as prepared substrate of class "A"; modified substrates of class "A" after incubation in AuNC for (c) 2 hrs (d) 24 hrs (e) 36 hrs (f) 48 hrs of ITs.

domains of sizes ~ 50 - 420 nm. The 2D and 3D AFM images of the same film, scanned over 5 μm × 5 μm, surface area as shown in Figure 6.4 (a) and (A), also corroborates this observation. The monolayer LB film substrate of PMMA lifted at 40 mN/ m surface pressure will henceforth be designated as substrate of class "A". The FESEM images of the substrates of class "A" immersed in AuNCs over various ITs are shown in Figure 6.3 [(c) - (f)]. After 2 hours of IT, segregated gold nanocolloidal particles are seen to remain embedded on the monolayer LB film matrix of PMMA [Figure 6.3 (c)]. Interestingly, with increase in IT, Nps begin to form aggregated domains. The FESEM image of the substrate, captured after 24 hours of IT [Figure 6.3 (d)], depicts high density aggregated patterns of AuNps interlaced to form chain like structures. With further increase in IT, the chain like pattern turns to archipelago, stuffed with densely packed aggregated domains of the AuNps. The FESEM image of the as prepared substrate, accomplished after 48 hours of IT, is depicted by further agglomeration of gold nanocolloidal particles on the monolayer

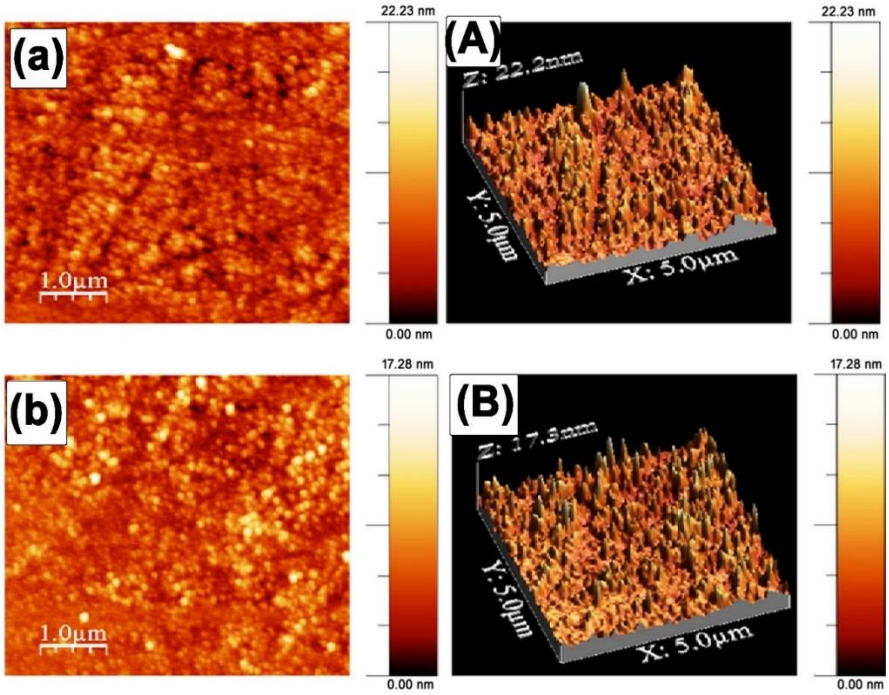

Figure 6.4: Left column: (a) and (b) 2D AFM images; Right column: (A and B) corresponding 3D AFM images of the substrates of classes "A" & "B" respectively.

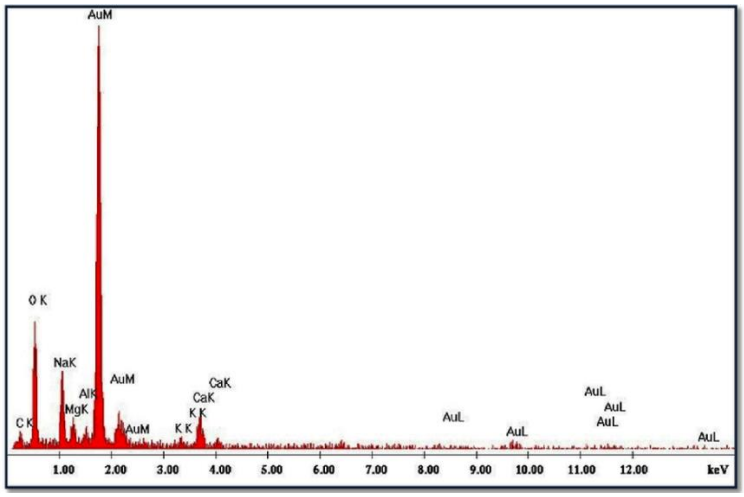

Figure 6.5: EDX analyses of the as prepared modified substrate.

LB film of PMMA matrix. The elemental analysis of the monolayer LB film substrate of PMMA incubated in AuNC for 24 hours of IT is shown in Figure 6.5. The EDX analysis confirms the expected existence of gold, oxygen and carbon on the as prepared film substrate, together with the presence of Na, Mg, Ca, K atoms, stemming from the quartz slide. We will call the as prepared substrates as "modified substrates of class A".

Close inspection of the FESEM images, as shown in Figure 6.3 [(c) - (f)], indicate that upon changing the ITs of AuNC in PMMA matrix, the plasmonic architectures of the modified substrates of class "A" can be controlled with precise ease. Controlling the plasmonic architectures of the substrates through aggregation and segregation of the Nps are fundamental towards the possible generation of hot geometries and hence ushers in greater possibilities for the probe molecules to get betwixed within the hot spots. Interestingly, apart from changing the IT of the nanocolloids on the PMMA template, the plasmonic architecture of the substrates can also be tuned by lifting the monolayer LB film of PMMA at lower surface pressure (~10 mN/ m). The FESEM image of the monolayer LB film of PMMA lifted at 10 mN/ m surface pressure is shown in Figure 6.6 (a). We name this as substrate of class "B". The FESEM image of the substrate of class "B" exhibit less compact structure containing granules, free from aggregated domains. The 2D and 3D AFM images of the same structure, as shown in Figure 6.4 (b) and (B) respectively is in accordance with the FESEM observation. Figure 6.6 (b) shows the FESEM image of the class "B" substrate, incubated in AuNCs for 24 hours of IT. Alike substrate of class "A", we designate this as "modified substrate of class "B". The final image of the as prepared modified substrate of class "B" exhibits segregated domains mostly of dimeric or trimeric AuNps that remain dispensed on the monolayer LB film template of PMMA. Significantly, this disposition closely resembles the plasmonic

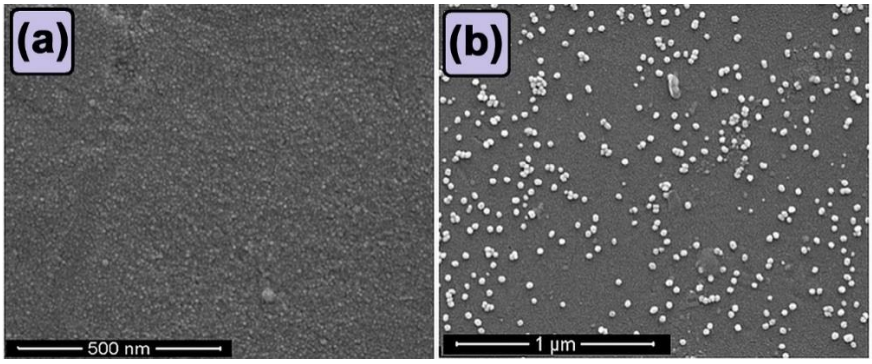

Figure 6.6: FESEM images of (a) as prepared substrate of class "B", (b) as prepared modified substrate of class "B" after incubation in AuNC for 24 hrs of IT.

architecture of the monolayer LB film substrate of PMMA lifted at 40 mN/ m surface pressure when dipped in gold nanocolloidal solution for 2 hours of IT [Figure 6.3 (c) (vide ante)]. The electronic absorption spectrum of the modified substrate of class "B" is shown in Figure 6.7, along with that recorded for pristine AuNC. Interestingly as observed for the modified substrate of class

"A", this substrate also exhibits weak LSPR band at ~ 548 nm along with low energy SL-SPR band peaked at ~ 634 nm. The SL-SPR band for the modified substrate of class "B" is less broadened in comparison with that for the modified substrate of class "A" (Figure 6.2). This result may signify apparent perturbations in the dipole- dipole interactions among the segregated and aggregated domains of the nano antennas prevalent in the modified substrates of classes "B" and "A" respectively.

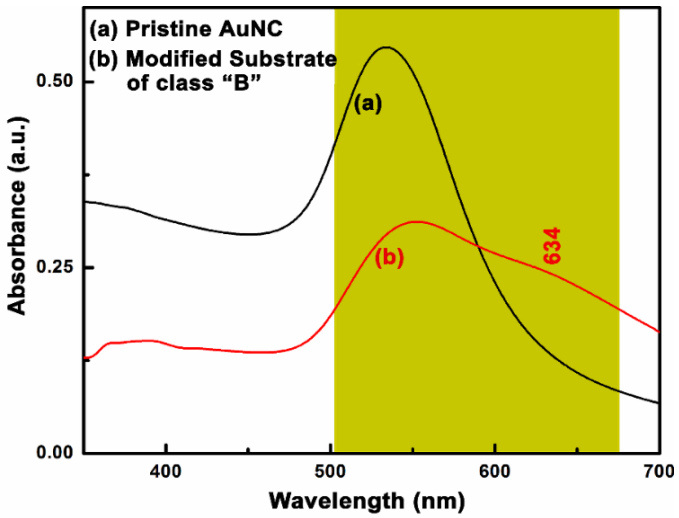

Figure 6.7: Room temperature UV- Vis electronic absorption spectra of (a) AuNC and (b) modified substrate of Class B.

Thus, the organized molecular architectures of the ultrathin LB films of PMMA in the form of aggregated and segregated domains lifted separately at 40 and 10 mN/ m surface pressures respectively in the backdrop, dominated by F_{MMA}, together with F_{NNA}, F_{NMA}, F_{NNR} from the self-assembly of the AuNC, play a pivotal role in controlling the aggregated or segregated behaviors of gold nanocolloids. Power of the LB technique in conjunction with the self-assembly of nanocolloids, thus provides a unique way to generate the interstitial gaps $< 2.14(\pm 0.679)$ nm within the dimeric or trimeric Nps. These interstitial plasmon gaps $< \pm 2.14(\pm 0.679)$ nm can act as hot sites for the protrusion of probe molecules to exhibit enhanced vibrational signatures in the SERS spectra. In this connection, it may be emphasized that such small and controlled interstitial gap plasmons are unique in nature and are not achievable from any other soft lithographic techniques or even with the aid of Anodic Aluminum Oxide (AAO) templates [16-18]. This can only be accomplished through the LB technique.

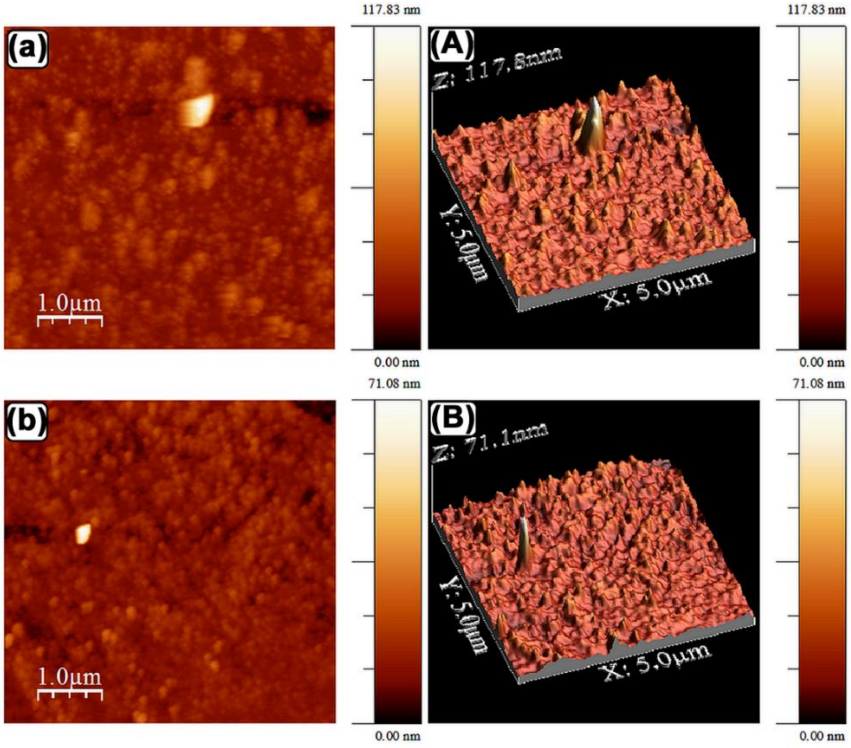

Figure 6.8: Left column: (a) and (b) 2D AFM images; Right column: (A and B) corresponding 3D AFM images of the modified substrates of classes "A" & "B" respectively.

The AFM images of the as prepared modified substrates of classes "A" and "B", are shown in Figure 6.8 (a, A) and Figure 6.8 (b, B) respectively. These images clearly mark the presence of intermittent aggregated and segregated domains of nanocolloidal particles dispensed on the monolayer LB film substrates of PMMA lifted at 40 mN/ m and 10 mN/ m surface pressures respectively. The topographical features are in accordance with the corresponding FESEM images as shown in Figure 6.3 (d) and 6.6 (b). The nanoaggregated domains, embedded in the monolayer LB film matrix of PMMA, may act as possible hot sites for harvesting enormous near- field within the interstitial gaps of the AuNps.

6.2.4 Efficacy of the as-prepared substrate for SERS

The efficacies of the as prepared modified substrates of classes "A" and "B" for detecting SERS signals are tested with 4-MPy as reporter molecule. The 4-MPy molecule has two pKa values, one at 1.43 and the other at 8.83 [19,20]. The molecule is known to exist as protonated-deprotonated and in thiol- thione tautomeric forms. They are shown in Figure 6.9. The NRS of 4-

MPy in aqueous medium (pH~ 7) at 1 M concentration is shown in Figure 6.10. The NRS spectrum shows distinct vibrational signatures at 429, 723, 1001, 1053, 1114, 1207, 1589, 1614 and 1621 cm^{-1} characteristic of 4-MPy molecule. The band at 429 cm^{-1} owes to out of plane δ(C-S)/ γ(CCC) vibrational signature. The Raman signals at 1114 and 723 cm^{-1} are the X- sensitive bands where the υ(C-S) stretching vibrations are coupled with the ring breathing and in-plane β(CC) bending modes of the molecule respectively [21-23]. Strong and intense ring breathing vibration (υ_1) appears at 1001 cm^{-1} together with the medium intense band at 1621 cm^{-1}. The appearance of

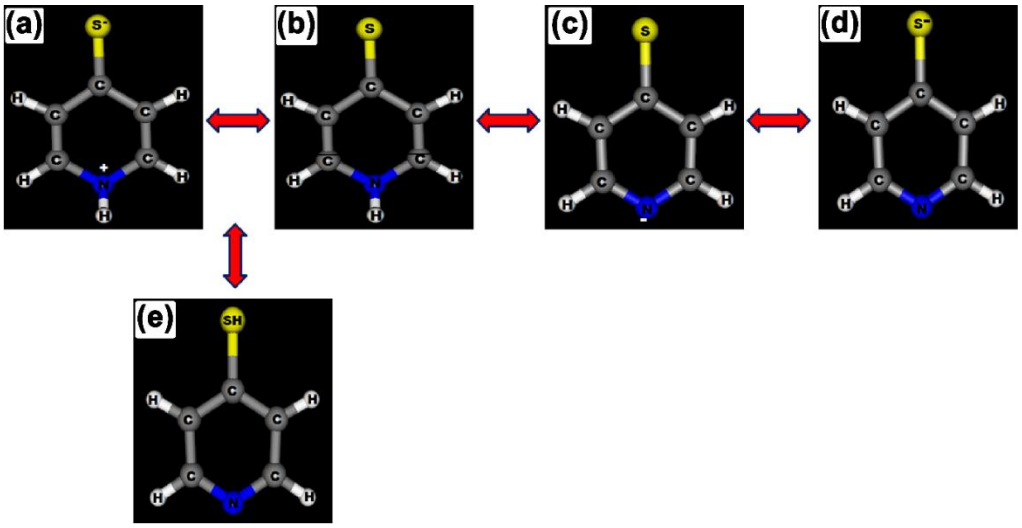

Figure 6.9: Optimized molecular structure of 4-MPy showing protonated, deprotonated thione and thiol forms of the molecule.

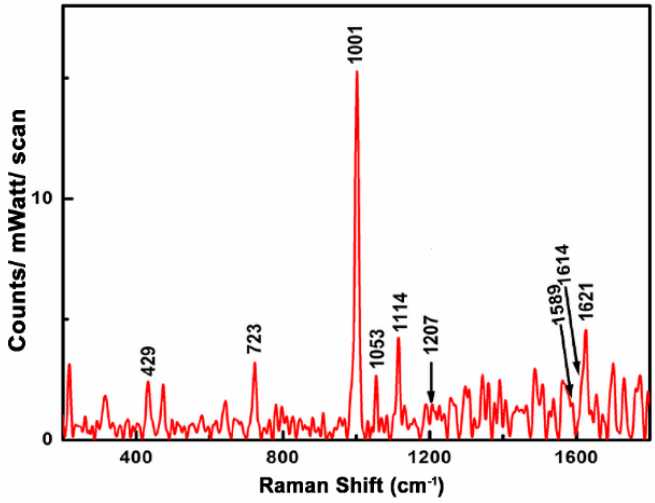

Figure 6.10: Background corrected normal Raman (NR) spectrum of 1 M 4-MPy in aqueous solution ($\lambda_{ex} = 632.8$ nm).

Table 6.1: Enhancement Factors (EFs) of SER bands of 4- MPy molecule adsorbed on the as prepared modified substrates of classes "A" and "B"

NRS (cm^{-1})	Adsorbate Concentrations									Assignment [a]
	Substrate	10^{-4} M		10^{-6} M		10^{-10} M		10^{-12} M		
		SERS	EF	SERS	EF	SERS	EF	SERS	EF	
1001	Class A	1006	3.03×10^2	1005	8.92×10^4	1006	3.86×10^8	1008	1.43×10^9	Ring Breathing (ν_1)
	Class B	1004	7.94×10^2	1004	8.19×10^4	1009	1.05×10^7	----	----	
1114	Class A	1092	2.23×10^3	1092	4.73×10^5	1092	1.01×10^9	1094	7.07×10^9	Trigonal ring-breathing with C=S deformation (ν_{12})
	Class B	1094	4.01×10^3	1094	5.70×10^5	1094	4.47×10^7	1097	4.11×10^9	
1207	Class A	1210	2.36×10^3	1207	4.69×10^5	1210	1.60×10^9	1210	1.49×10^{10}	$\beta_{(C-H)}$ (ν_9)
	Class B	1209	3.93×10^2	1205	6.67×10^5	1210	5.92×10^7	1213	1.16×10^{10}	
1589	Class A	1574	2.98×10^3	1579	3.83×10^5	1581	7.43×10^9	1576	2.96×10^{10}	$\nu_{(C-C)}$ (ν_8)
	Class B	1576	3.89×10^2	1579	7.25×10^5	1580	1.39×10^8	1572	2.47×10^{10}	
1621	Class A	1610	1.45×10^3	1610	3.13×10^5	1608	1.83×10^9	1608	1.08×10^{10}	$\nu_{(C-C)}$ (ν_8)
	Class B	1610	2.45×10^3	1611	3.81×10^5	1616	1.46×10^7	----	----	

Note: NRS: normal Raman spectrum; SERS: surface-enhanced Raman spectroscopy.

[a] ν – stretching; β - in-plane bending.

Raman band at 1621 cm^{-1}, assigned to $\nu(C-C)$ stretching vibrations of the pyridine ring of the molecule [22,24,25] marks the presence of the protonated form of 4-MPy molecule in aqueous solution. Table 6.1 shows the vibrational assignments of some specific Raman and SERS bands of protonated and deprotonated forms of 4-MPy molecule, whose detailed analysis are reported elsewhere [22-28].

Figure 6.11 shows the SERS spectra of 1.0×10^{-6} M 4-MPy molecule at pH ~ 7 adsorbed on the as prepared modified substrates of class "A" incubated in AuNC for various ITs spanning

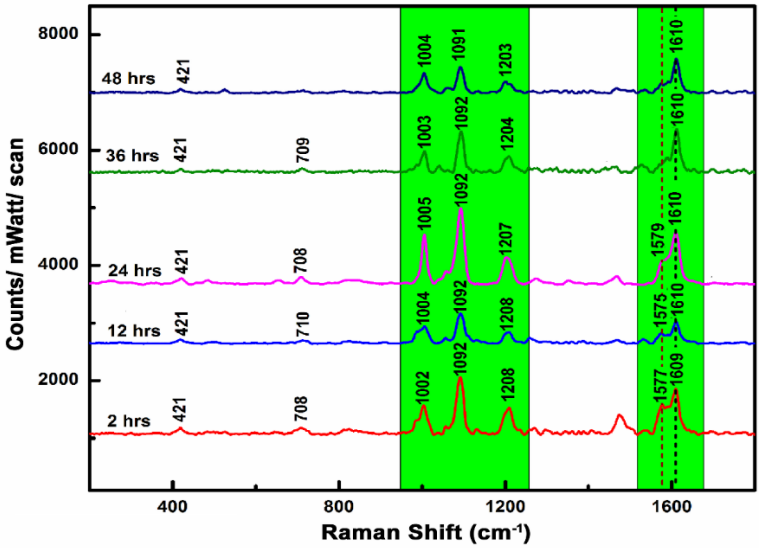

Figure 6.11: SERS spectra of 1.0×10^{-6} M 4-MPy molecule at pH ~ 7 adsorbed on the as prepared modified substrates of class "A" incubated in AuNC for various ITs ($\lambda_{ex} = 632.8$ nm).

from 2 to 48 hours. All the substrates of class "A" dipped in AuNC for various ITs act as effective SERS sensing scaffolds, albeit the spectrum recorded after 24 hours of IT exhibits the best execution of signal to noise ratio. The SERS spectra show enhancements of Raman bands centered at around 1005, 1092, 1207, 1579 and 1610 cm^{-1}. Among them, the X- sensitive bands at ~ 708 and 1092 cm^{-1} are remarkably down shifted with respect to the NRS counterpart at 721 and 1114 cm^{-1} respectively.

The enormous downshift of the X- sensitive bands together with no trace of $\nu(S-H)$ stretching vibration at ~ 2575 cm^{-1} [25] in the SERS spectra (not shown in the Figure) primarily suggest the existence of protonated state of the thione form of 4-MPy molecule. Presence of protonated form of the molecule is further substantiated by the appearance of enhanced Raman bands at ~ 1204 cm^{-1} and ~ 1610 cm^{-1}. The 1204 cm^{-1} has been assigned to mixed vibrations from the CH in-plane and $N-H$ out of plane bends and is associated with the protonated form of the 4-MPy molecule [23-27]. Interesting observation can be drawn from the enhancements and relative intensities for the pair of bands centered at ~ 1610 and 1577 cm^{-1}. Both these bands are ascribed to $\nu(C-C)$ stretching vibrations, however the former, originating from the protonated while the

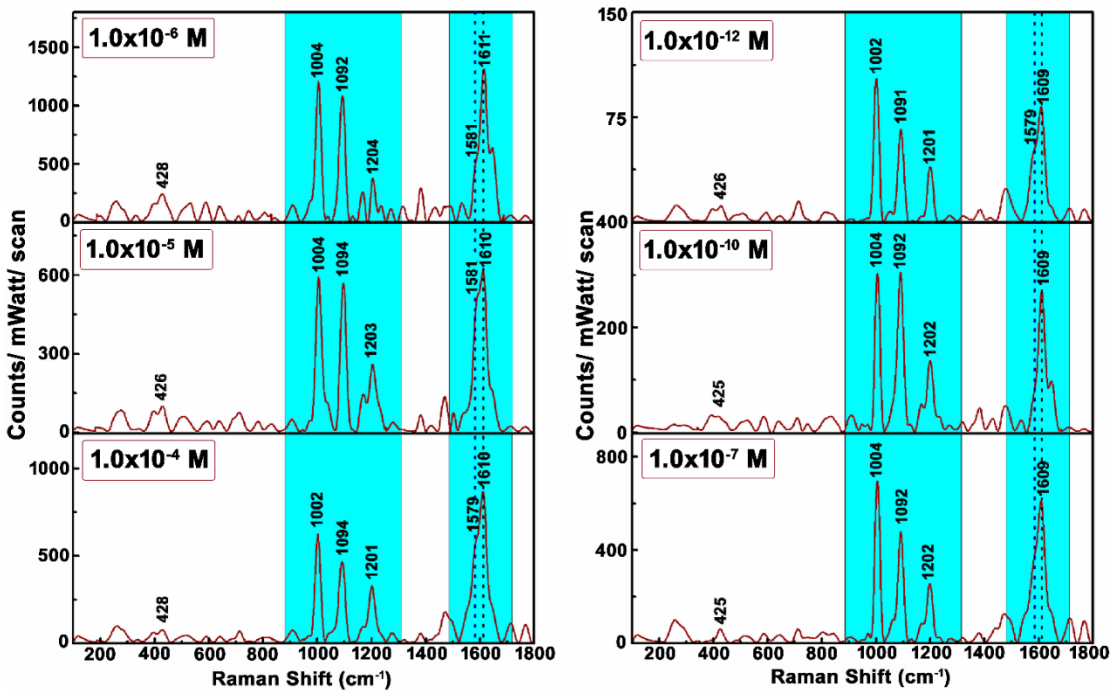

Figure 6.12: Concentration dependent SERS spectra of 4-MPy molecule at pH ~ 1 adsorbed on the modified substrates of class "A" incubated in AuNC for 24 hours of IT ($\lambda_{ex} = 632.8$ nm).

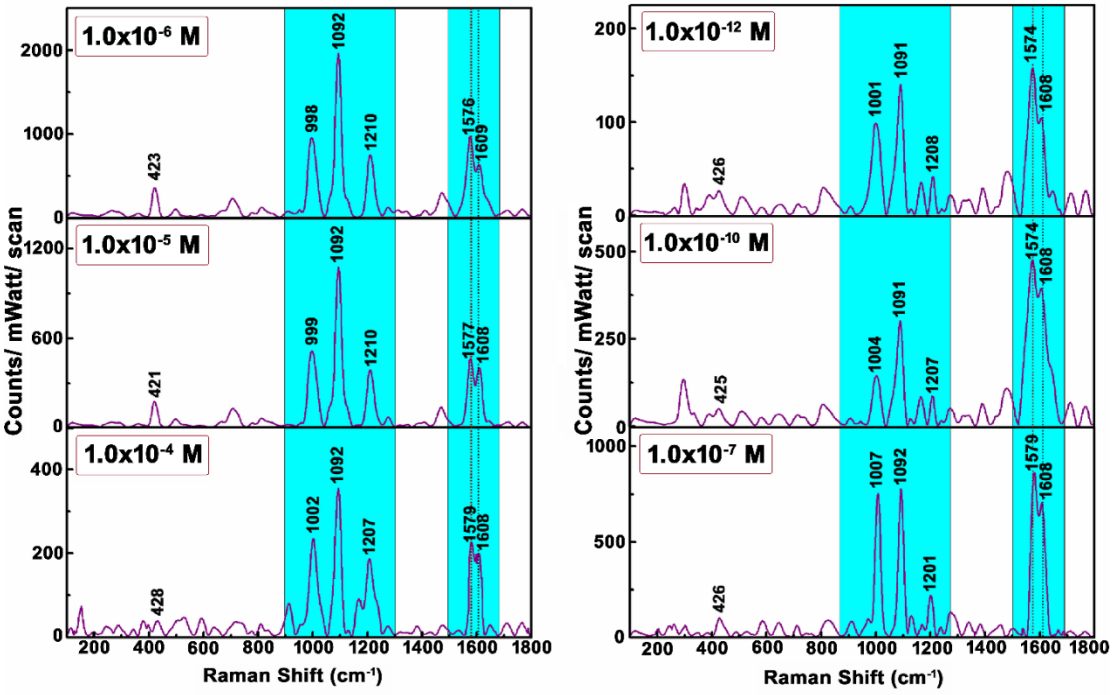

Figure 6.13: Concentration dependent SERS spectra of 4-MPy molecule at pH ~ 10 adsorbed on the modified substrates of class "A" incubated in AuNC for 24 hours of IT ($\lambda_{ex} = 632.8$ nm).

later from the deprotonated species of 4-MPy molecule [23-25,29]. Strong enhancements of 1610 cm^{-1} band in comparison to that of 1577 cm^{-1} further justify the preponderance of protonated species in comparison to the deprotonated one in the surface adsorbed state. Interestingly, span in the ITs of the nanocolloids on pristine LB film substrates of PMMA is correlated with the existence of mixed or protonated form of the reporter molecule. At lower ITs (2- 24 hours), the SERS spectra exhibit the presence of both the protonated and the deprotonated forms while for the higher ITs (36- 48 hours), explicit presence of the protonated form of 4-MPy molecule are suggested.

The concentration dependent SERS spectra of 4-MPy molecule at pH ~ 1 and pH ~ 10 are shown in Figure 6.12 and 6.13 respectively. Concentration dependent SERS spectra of 4-MPy molecule at pH ~ 1, adsorbed on the modified substrate of class "A" (Figure 6.12) is marked by the presence of enhanced Raman bands centered at ~ 1610, 1201, 1094 and 1002 cm^{-1} together with weak hump at ~ 1579 cm^{-1}. The appearance of bands centered at ~ 1610 and 1201 cm^{-1} signify the predominant existence of the protonated form of the probe molecule in the surface adsorbed state at pH ~ 1. Interestingly, the SERS spectra of 4-MPy molecule recorded at pH ~ 10 for various concentrations of the adsorbate are dominated by the Raman bands centered at ~ 1576, 1210, 1092 and 1002 cm^{-1}. In addition to these, a band at ~ 1609 cm^{-1}, weaker in intensity in comparison to the intense band at ~ 1576 cm^{-1} is observed. They are shown in Figure 6.13. However, the presence of 1576 and 1210 cm^{-1} bands in the entire concentration dependent SERS spectral profile presage the predominant existence of the deprotonated form of the 4-MPy molecule at alkaline pH (pH ~ 10). Considering the two pKa values of 4-MPy (at 1.43 and 8.83) [19,20] this is an expected observation, where the protonated form of the molecule is expected to be dominant at lower pH (pH ~ 1), while at higher pH value (pH ~ 10), the deprotonated form of the molecule is preponderant. The expected observation is in harmony with the enhanced vibrational signatures of 4-MPy molecule, as recorded from the pH dependent SERS spectra.

Figure 6.14 shows the concentration dependent SERS spectra of the reporter 4-MPy molecule at pH ~ 7 adsorbed on the modified substrates of class "A". The spectra show remarkable changes in features of enhanced Raman bands. At higher concentrations (ca. 1.0×10^{-4} to 1.0×10^{-6} M), the spectra are dominated by the enhanced bands centered at ~ 1005, 1092, 1208 and 1610 cm^{-1}. The appearance of the above-mentioned bands signify the existence of protonated form of the molecule, which get adsorbed through its sulphur atom on the substrate. The

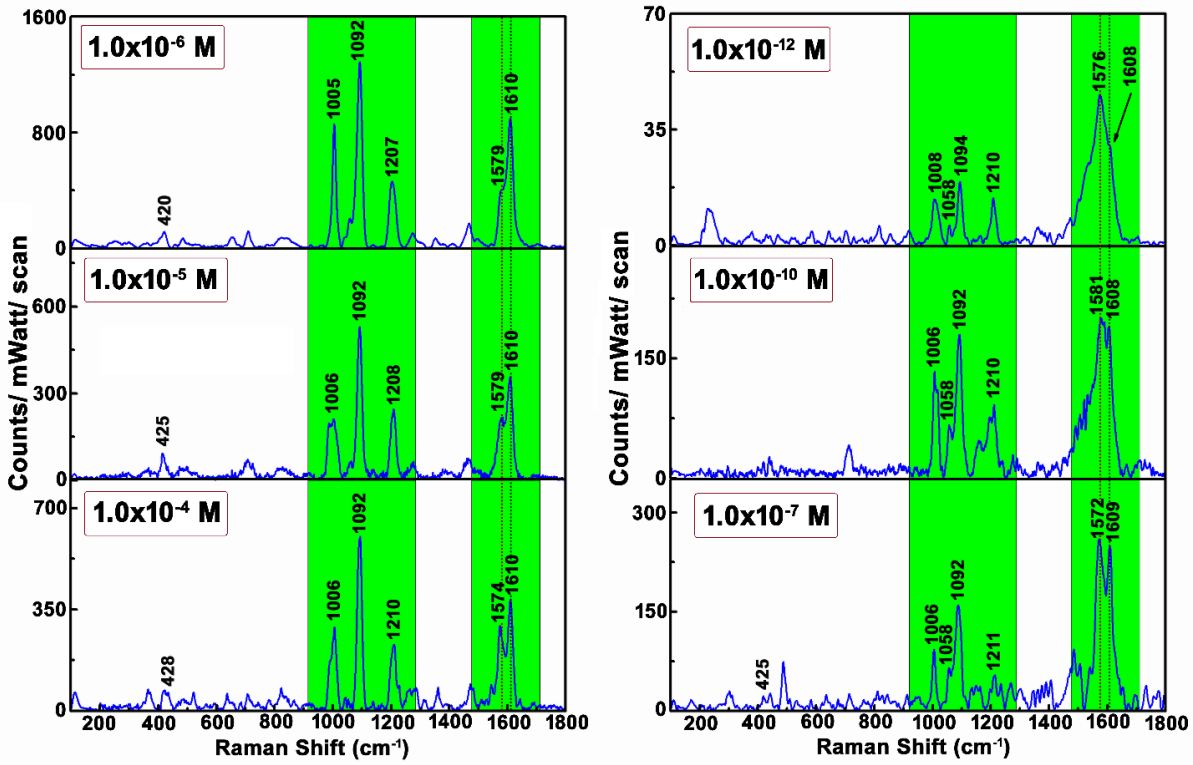

Figure 6.14: Concentration dependent SERS spectra of 4-MPy molecule at pH ~ 7 adsorbed on the modified substrates of class "A" incubated in AuNC for 24 hours of IT ($\lambda_{ex} = 632.8$ nm).

enhancements of in-plane vibrational modes together with the moderate enhancement of Raman band at ~ 425 cm^{-1}, ascribed to $\delta(C-S)/\gamma(C-C-C)$ out-of-plane vibration [21,24,30] may signify tilted adsorptive stance of 4-MPy molecule on the modified substrate of class "A" through the lone pair electrons of sulphur atom. However, in the lower concentration domain (1.0×10^{-7} to 1.0×10^{-12} M), the SERS spectra are remarkably different from those recorded at higher concentrations of the adsorbate. Significant observation can be drawn from the intensity reversal between the pair of bands at 1572 and 1610 cm^{-1}.

With decrease in concentration, the band ~ 1572 cm^{-1} gains in intensity with concomitant weakening of the other band at 1610 cm^{-1}. At 1.0×10^{-10} and 1.0×10^{-12} M concentrations, the strongest band appears in the SERS spectra at ~ 1576 - 1581 cm^{-1}. The presence of the bands at ~ 1572 - 1581 cm^{-1} and at ~ 1058 cm^{-1} together with the upshift of the 1210 cm^{-1} band, mark the existence of the deprotonated form of 4-MPy molecule at lower concentrations of the adsorbate. Thus, the modified substrate of class "A" can act as exclusive sensor for detections of protonated and deprotonated forms of 4-MPy molecule at trace concentrations. At higher concentrations of

the adsorbate (ca. 1.0×10^{-4} to 1.0×10^{-6} M), predominant existence of the protonated forms of the molecule are estimated, while at lower concentrations (ca 1.0×10^{-10} to 1.0×10^{-12} M), the presence of the deprotonated forms of 4-MPy are explicitly detected. At the intermediate concentration ~ 1.0×10^{-7} M, both the forms of the molecule are found to co-exist.

Interesting conclusion may be extended from the SERS spectra of the molecule adsorbed on the modified substrate of class "B". They are shown in Figure 6.15. At higher concentrations of the adsorbate (~ 1.0×10^{-4} M), strong enhancements of 1576, 1209 and 1057 cm^{-1} bands mark the presence of deprotonated form of 4-MPy molecule [29]. The substantial red shift of enhanced Raman bands centered at ~ 713 cm^{-1} and at 1094 cm^{-1} again presage the adsorption of the molecule on the substrate through the lone pair electrons of the sulphur atom. Interestingly, reversal in intensities between the pair of bands at 1578 and 1611 cm^{-1} are observed at 1.0×10^{-5} and 1.0×10^{-6} M concentrations of the adsorbate. With decrease in concentration of the adsorbate, 1611 cm^{-1} gains in intensity, with progressive downshift of the band at ~ 1205 cm^{-1}, and weakening in the intensity of 1057 cm^{-1}. These results signify the existence of both the protonated and deprotonated forms of the molecule. At relatively lower concentration of the adsorbate (ca ~ 1.0×10^{-7} M), the band centered at ~ 1579 cm^{-1} disappears with distinct enhanced vibrational signatures recorded only at 1614, 1203, 1092, 1006 cm^{-1}. The enhancements of these specific Raman bands envisage exclusive presence of the protonated form of 4-MPy molecule on the modified substrate of class "B". Interestingly, further lowering in the adsorbate concentrations (ca ~1.0×10^{-10} to 1.0×10^{-12} M) exhibit the reappearance of the band centered at ~1572- 1580 cm^{-1}. The reappearance of the band centered at ~ 1572- 1580 cm^{-1}, together with the upshift of 1210 cm^{-1} band, albeit weak in intensity, presage the presence of deprotonated form of 4-MPy adsorbate on modified substrate of class "B" at lower concentrations (ca ~ 1.0×10^{-10} to 1.0×10^{-12} M) of the adsorbate. However, substantial downshifts of enhanced Raman bands at ~ 713, 1094 cm^{-1} in conjunction with the enhancements of both in-plane and out-of-plane vibrational modes at ~ 713, 1006, 1057, 1094, 1210, 1576, 1611 and 424 cm^{-1} respectively in the entire concentration dependent SERS spectral profile favour tilted adsorption stances of both the protonated and deprotonated forms of 4-MPy molecule through the lone pair electrons of sulphur atom on the modified substrate of class "B".

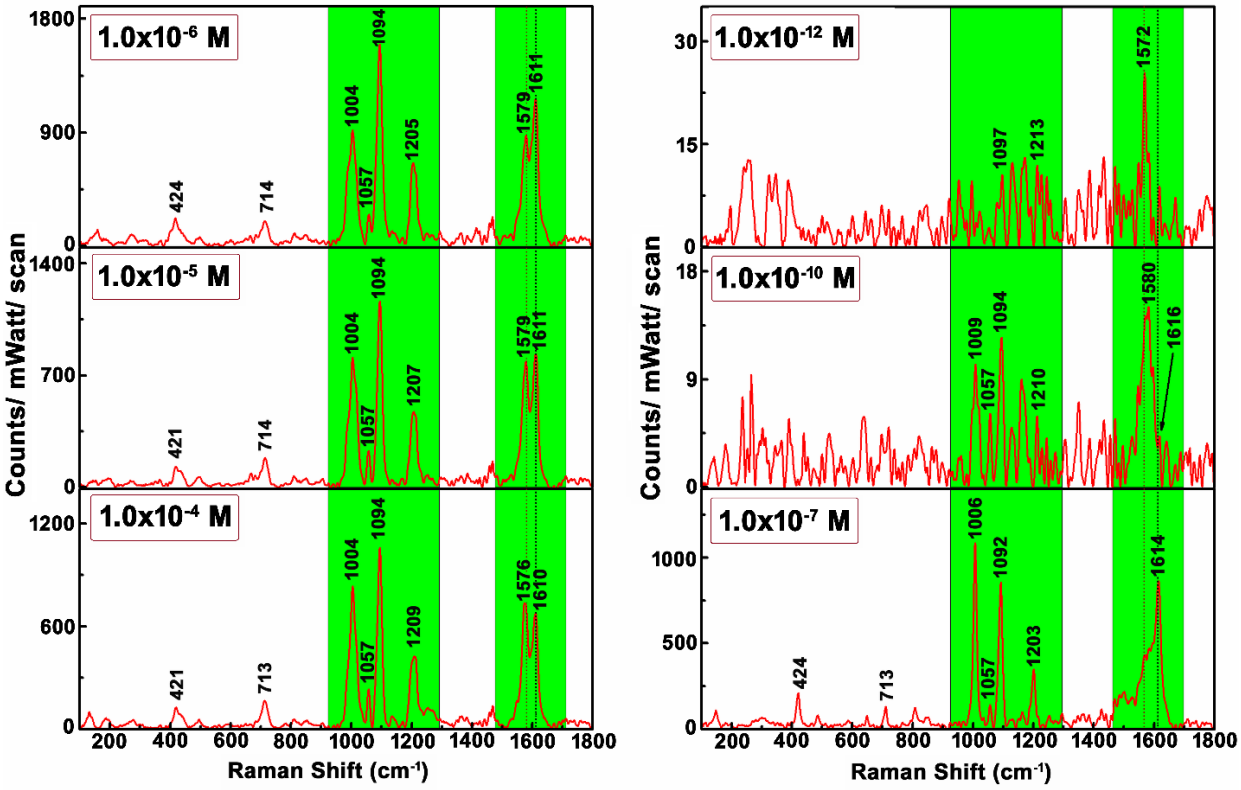

Figure 6.15: Concentration dependent SERS spectra of 4-MPy molecule at pH ~ 7 adsorbed on the modified substrates of class "B" incubated in AuNC for 24 hours of IT (λ_{ex} = 632.8 nm).

In this connection, discussions concerning simultaneous or explicit presence of protonated, deprotonated forms of the 4-MPy molecule in the adsorbed state with the corresponding pKa values demand considerable attention. In free state the pKa values of 4-MPy are at 1.43 and 8.83, involving dissociation of proton attached to -SH and –NH groups of the molecule respectively (vide supra, Figure 6.9). Thus, in neutral pH medium 4-MPy molecule may co-exist in (a) ↔ (b) thione tautomeric forms and/ or its corresponding thiol form. They are shown in Figure 6.9. However, the vibrational signatures of enhanced Raman bands as depicted in Figure 6.14 & 6.15 preclude the existence of thiol and presage the presence of protonated and deprotonated thione forms of the molecule (vide ante). The possible protonated and deprotonated thione forms of the molecule in the surface adsorbed state are [(a), (b)] and [(c), (d)] respectively as shown in Figure 6.9. The existence of deprotonated (c) ↔ (d) forms of the 4-MPy molecule in the surface adsorbed state clearly indicates significant effect on its pKa (~ 8.83) value upon absorption. This means 4-MPy molecule adsorbed on the as prepared modified substrates of classes "A" and "B" is ionized

at neutral pH which is essentially lower than what is required to deprotonate the species. The lowering in pKa values of molecules in surface adsorbed state in comparison to its free form is a well-known observation and are reported elsewhere [31].

Thus, the as prepared modified substrates of classes "A" and "B" both show their respective efficacies as efficient SERS sensing scaffolds for detecting 4-MPy molecule at ultrasensitive concentrations. Moreover, these substrates are unique of their kinds, where explicit presence of protonated and deprotonated forms of 4-MPy can be detected at trace concentrations for the first time. The as prepared substrates covering 2 × 1 cm^2 area of the quartz slides, however not only can explicitly sense different tautomeric species of 4-MPy molecules at trace concentrations, but also exhibit remarkable spectral reproducibility.

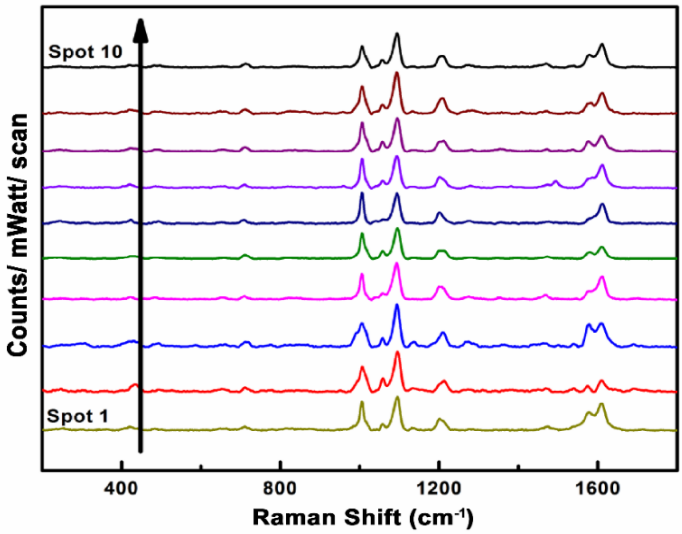

Figure 6.16: Representative SERS spectra of 1.0×10^{-6} M 4-MPy at pH ~ 7, recorded for 10 distinct spots from the as prepared modified substrate of class "A" ($\lambda_{ex} = 632.8$ nm).

The reproducibility of the as prepared substrates has been checked and the relative standard deviation (RSD) have been estimated from the SERS spectra of 4-MPy by probing the laser beam on ten different spots covering a wide zone ~ 2 × 1 cm^2 surface area of the substrate. The spectra are shown in Figure 6.16. The RSD values for the prominent and well resolved SER bands of 4-MPy molecule centered at ~ 1006, 1092 and 1210 cm^{-1} are estimated to be 10.94%, 12.93% and 17.91% respectively. The average estimated RSD value < 15% indicate good reproducibility of the as prepared substrates as effective SERS sensing scaffold for future state-of-art sensing

applications. To our knowledge the unique reproducibility of the as prepared substrates for detecting probe molecules at ultrasensitive concentrations, in cohesion with their reproducibility per se, may be the first report of SERS active substrates which have the potential to overcome the "SERS uncertainty Principle".

The Enhancement Factors (EFs) of the SER bands of 4-MPy molecule adsorbed on two different modified substrates of classes "A" and "B" have been separately calculated using the relation [32,33]

$$EF = \frac{I_{SERS}}{I_{bulk}} \times \frac{N_{bulk}}{N_{SERS}} \tag{6.1}$$

where, N_{bulk} and N_{SERS} represent the number of probe molecule that contribute to the normal Raman and SERS signals. I_{bulk} and I_{SERS} are the corresponding normal Raman and SERS intensities measured from the baseline. The N_{bulk} has been estimated using the following relation,

$$N_{bulk} = C_{bulk} A h N_A \tag{6.2}$$

C_{bulk} is the concentration of the probe molecule in the normal Raman spectrum. As 50x objective lens has been employed in the present experimental work with confocal depth (h) ~ 1.4 μm, the laser spot area (A) ~ 8.31×10^{-13} m^2 has been estimated for the excitation wavelength (λ_{ex}) ~ 632.8 nm. N_{SERS} is calculated using the relation,

$$N_{SERS} = C_{SERS} V N_A A/A^{/} \tag{6.3}$$

where, A is the area of the laser spot as estimated earlier to be ~ 8.31×10^{-13} m^2, C_{SERS} is the concentration of 4-MPy molecule at SERS measurement, N_A is the Avogadro number and V is the volume of the probe molecule which is ~ 25 μl for this experimental work and $A^{/}$ is the area of the probe molecule drop casted on the substrate which traces a circular deposit of ~ 5 mm diameter. The EFs for the SER bands of 4-MPy molecule adsorbed both on the modified substrates of classes "A" and "B" are shown in Table- 6.1. Enhancement factors ranging from ~ 10^2 to 10^{10} orders of magnitude have been estimated for the bands centered at ~ 1006, 1092, 1210, 1574, and 1610 cm^{-1} contributing to in-plane vibrational signatures. The enhancements of SER bands of 4-MPy adsorbed on the modified substrates of classes "A" and "B" with limit of detection (LOD) ~ 1.0×10^{-12} M concentration corroborate the superiority of the as prepared substrates in comparison with other substrates reported elsewhere [34-40].

6.2.5 Near- field distributions of the aggregated AuNCs on the substrates of classes "A" and "B"

Near- field distributions around the nanoaggregates on the substrates of classes "A" and "B" are estimated from 3D- FDTD simulation. Both the substrates are dipped in AuNC for 24 hours of IT. Simulations are mapped directly from the respective zones of the FESEM images,

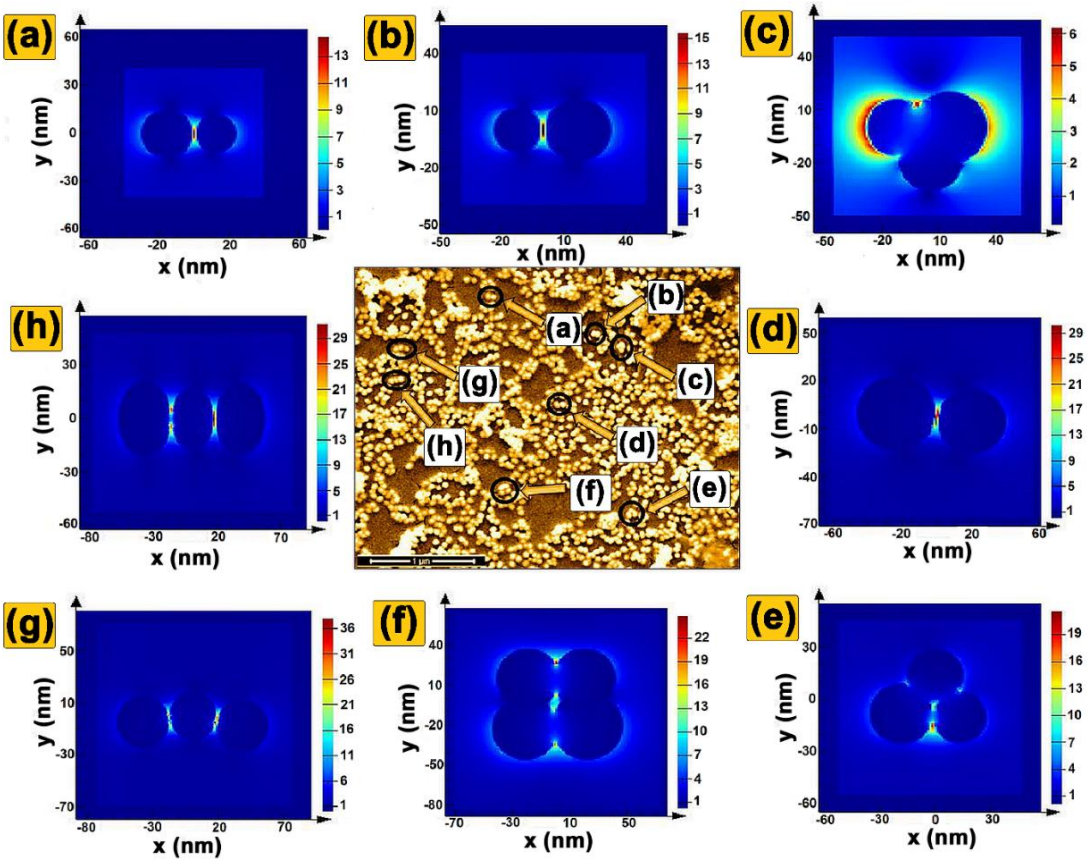

Figure 6.17: [(a) - (h), clockwise ↷] Electric field distribution around the hot-spots as estimated from 3D-FDTD simulations for as prepared modified substrate of class "A" incubated in AuNC for 24 hours of IT ($(\lambda_{ex} = 632.8$ nm), the polarization of the incident light wave is along x- axis). The corresponding FESEM image, with false color representation is shown in the middle.

marked as (a)- (h) in clockwise direction. They are shown in Figure 6.17 and 6.18. The 3D- FDTD simulations, as shown in Figure 6.17 and 6.18 exhibit specific regions of intense electric fields, mostly confined within the nanogaps of the aggregated domains. These zones are referred as "hot spots" in SERS, and molecules entrapped in these regions encounter gigantic enhancements. The hottest among the "hot spots" have been identified.

The maximum confinement of electric field is estimated for the trimeric [$|\vec{E}|$ ~ 30 volt/m; zone: (h)] and dimeric [$|\vec{E}|$ ~ 30 volt/m; zone: (b)] domains of the nano aggregates, which correspond to the EF $G(\omega, \omega') \sim 8.1 \times 10^5$ orders of magnitude, following PW approximation. The EF as obtained from 3D-FDTD simulations are much smaller in comparison with the average experimental EFs ~ 10^{10} for the SERS spectra of probe molecules adsorbed on the modified

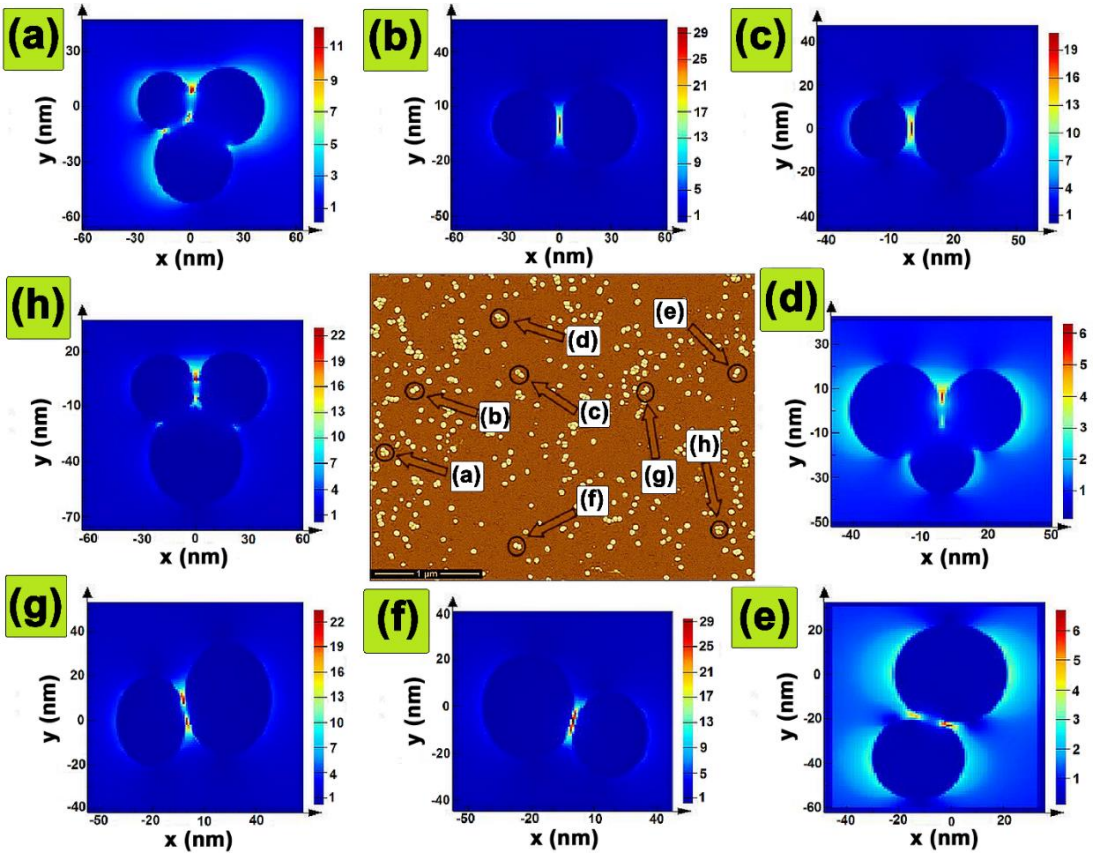

Figure 6.18: [(a) – (h), clockwise ↷] Electric field distribution around the hot-spots as estimated from 3D- FDTD simulations for as prepared modified substrate of class "B" incubated in AuNC for 24 hours of IT ($(\lambda_{ex} = 632.8$ nm), the polarization of the incident light wave is along x- axis). The corresponding FESEM image, with false color representation is shown in the middle.

substrates of classes "A" and "B". The apparent diminution in the EF value may be due to the intrinsic approximation in PW calculations and oversimplification of 3D-FDTD simulations per se. However, in this connection it is worth to mention that, the diffraction limit of the laser spot diameter (Δx) may be estimated as

$$\Delta x = \frac{1.22\lambda}{\text{N.A.}} \qquad (6.4)$$

where, N.A. is the numerical aperture of the objective lens and λ is the excitation wavelength used in the Raman spectral measurement. With 50x objective lens corresponding to N.A. ~ 0.75, the laser spot diameter has been estimated to ~ 1 μm. Thus, the laser spot that is focused at different positions on the as prepared modified substrates of classes "A" and "B" covers an area A ~ 0.831 μm^2 which is much smaller in area as depicted in the respective FESEM images [Figure 6.3(d) and 6.6(b)]. The discrepancy between theoretically estimated and experimentally-determined EFs may also arise due to the cumulative signals in the SERS spectra which are averaged out from small number of molecules residing in hot-spots and the rest emanating from much weaker enhancing sites, apart from the CT contribution to SERS.

Moreover, the limitations of PW approximation per se as and the non- incorporation of dipole re- radiation (DR) theory may be the other possible consequence for underestimation of simulated EF from experimental observations. Closer look on the correlation between the near-field optical response of the as prepared substrates with the far- field SERS spectra will also be explored in detail from wavelength scanned surface enhanced Raman spectroscopic studies.

6.3 Conclusion

This chapter is focused on the fabrication of efficient SERS sensing platforms through coherent integration of LB and self-assembly technique. The plasmonic architectures of the as prepared substrates can be tuned with precise ease to control the gap plasmons and hence the overall enhancements of SERS signal. Power of the LB technique in conjunction with the self-assembly of nanocolloids, provide a unique way to generate the interstitial gaps $< 2.14(\pm 0.679)$ nm within the dimeric or trimeric nanoparticles. These interstitial gaps can act as hot sites for the protrusion of probe molecules to exhibit enhanced SERS signal. The as prepared substrates of classes "A" and "B" immersed in AuNC over various ITs have the unique ability to detect the explicit or concomitant presence of protonated and deprotonated forms of 4-MPy at trace concentrations. Moreover, the substrates exhibit remarkable spectral reproducibility and show early promise to overcome the "SERS uncertainty Principle". The spatial distributions of the electric fields in an around the probable hot spots have been estimated from 3D-FDTD simulations. To our knowledge, this genre of SERS active substrates with facile control over plasmonics, is not

reported earlier and is expected to open new windows towards successful fabrication of next generation SERS sensing scaffolds.

References

1. M. B. Ross, M. J. Ashley, A. L. Schmucker, S. Singamaneni, R. R. Naik, G. C. Schatz, C. A. Mirkin, *J. Phys. Chem. C*, 2016, **120**, 20789.
2. C. Hou, D. D. Galvan, G. Meng, Q. Yu, *Phys. Chem. Chem. Phys*., 2017, **19**, 24126.
3. A. R. L. Marshall, J. Stokes, F. N. Viscomi, J. E. Proctor, J. Gierschner, J. S. G. Bouillard, A. M. Adawi, *Nanoscale*, 2017, **9**, 17415.
4. E. C. Le Ru, P. G. Etchegoin, *Principles of surface-enhanced Raman spectroscopy and related plasmonic effects*, Elsevier, Amsterdam, 2009.
5. E. C. Le Ru, P. G. Etchegoin, *MRS Bulletein*, 2013, **38**, 631.
6. M. Mastrangeli, S. Abbasi, C. Varel, C. V. Hoof, J-P. Celis, K. F. Bohringer, *J. Micromech. Microeng*., 2009, **19**, 083001.
7. G. M. Whitesides, B. Grzybowski, *Science*, 2002, **295**, 2418.
8. P. K. Paul, S. A. Hussain, D. Bhattacharjee, *J. of Luminesc*., 2008, **128**, 41.
9. M. K. Abyaneh, R. Pasricha, S. W. Gosavi, S. K. Kulkarni, *Nanotech*., 2006, **17**, 4129.
10. M. K. Abyaneh, D. Paramanik, S. Varma, S. W. Gosavi, S. K. Kulkarni, *J. of Phys. D: Appl Phys*., 2007, **40**, 3771.
11. S. D. Roy, M. Ghosh, J. Chowdhury, *J. Raman Spectrosc*., 2015, **46**, 451.
12. S. Basu, S. K. Ghosh, S. Kundu, S. Panigrahi, S. Praharaj, S. Pande, S. Jana, T. Pal, *J. Colloid Inter. Sci*., 2007, **313**, 724.
13. T. J. Norman, C. D. Grant, D. Magana, J. Z. Zhang, J. Liu, D. Cao, F. Bridges, A. Van Buuren, *J. Phys. Chem. B*, 2002, **106**, 7005.
14. W. Yang, K. Liu, D. Song, Q. Du, R. Wang, H. Su, *J. Phys. Chem. C*, 2013, **117**, 27088.
15. S. D. Roy, M. Ghosh, J. Chowdhury, *J. Phys. Chem. C*, 2018, **122**, 10981.
16. H. Zhan, F. Cheng, Y. Chen, K. W. Wong, J. Mei, D. Hui, W. M. Lau, Y. Liu, *Composites Part B*, 2016, **84**, 222.
17. Q. Hao, H. Huang, X. Fan, Y. Yin, J. Wang, W. Li, L. Ma, P. K. Chu, O. G. Schmidt, *ACS Appl. Mater. Inter*., 2017, **9**, 36199.

18. C. Wang, G. Wang, R. Yang, X. Sun, H. Ma, S. Sun, *Langmuir*, 2017, **33**, 503.
19. A. Albert, G. B. Barlin, *J. Chem. Soc*., 1959, **0**, 2384.
20. K. Kishore, G. R. Dey, D. B. Naik, *Res. Chem. Intermed*., 2002, **28**, 29.
21. J. A. Baldwin, B. Vlckova, M. P. Andrews, I. S. Butler, *Langmuir*, 1997, **13**, 3744.
22. X. Fu, F. Bei, X. Wang, X. Yang, L. Lu, *J. Raman Spectrosc*., 2009, **40**, 1290.
23. H. S. Jung, K. Kim, M. S. Kim, *J. mol. Struc*., 1997, **407**, 139.
24. Y. Wang, H. Hu, S. Jing, W. Wang, Z. Sun, B. Zhao, C. Zhao, J. R. Lombardi, *Anal. Sci*., 2007, **23**, 787.
25. J. Hu, B. Zhao, W. Xu, B. Li, Y. Fan, *Spectrochim Acta A Mol Biomol Spectrosc*., 2002, **58**, 2827.
26. W. H. Do, C. J. Lee, D. Y. Kim, M. J. Jung, *J. Indust. Engg. Chem*., 2012, **18**, 2141.
27. Z. Ling, Y. Bai, Z. Shang, Y. Zhang, Y. Mo, *J. Raman Spectrosc*., 2007, **38**, 1106.
28. M. Pradhan, J. Chowdhury, S. Sarkar, A. K. Sinha, T. Pal, *J. Phys. Chem. C*, 2012, **116**, 24301.
29. Y. Chao, Z. Qun, Y. Li, Y. Yan, Y. Wu, J. Zheng, *J. Phys. Chem. C*, 2007, **111**, 16990.
30. H. Guo, L. Ding, Y. Mo, *J. Mol. Struc*., 2011, **991**, 103.
31. E. Tourwe, K. Baert, A. Hubin, *Vib. Spectrosc*., 2006, **40**, 25.
32. N. D. Jayram, S. Sonia, P. S. Kumar, L. Marimuthu, Y. Masuda, D. Mangalaraj, N. Ponpandian, C. Viswanathan, S. Ramankrishna, *RSC Adv*., 2015, **5**, 46229.
33. W. Song, W. Ji, S. Vantasin, I. Tanabe, B. Zhao, Y. Ozaki, *J. Mater. Chem. A*., 2015, **3**, 13556.
34. Y. Zheng, W. Wang, Q. Fu, M. Yu, K. Shayan, K. M. Wong, S. Singh, A. Schober, P. Schaaf, Y. Lei, *Chem. Plus Chem*., 2014, **79**, 1622.
35. W. Yue, Z. Wang, Y. Yang, L. Chen, A. Syed, K. Wong, X. Wang, *J. Micromech. Microeng*. 2012, **22**, 125007.
36. E. N. Esenturk, A. R. Hight Walker, *J. Raman. Spectrosc*., 2009, **40**, 86.
37. Q. Yu, P. Guan, D. Qin, G. Golden, P. M. Wallace, *Nano Lett*., 2008, **8**, 1923.
38. L. Zhang, L. Dai, Y. Rong, Z. Liu, D. Tong, Y. Huang, T. Chen, *Langmuir*, 2015, **31**, 1164.
39. J. Tao, D. He, B. Tang, L. Kong, P. Zhao, W. Gang, Z. Peng, *RSC Adv*., 2015, **5**, 49168.
40. Y. Pan, X. Wang, H. Zhang, Y. Kang, T. Wu, Y. Du, *Anal. Methods*, 2015, **7**, 1349.

Chapter 7: Decoding the topographical features of more realistic SERS active substrates in presence of the probe molecules from statistical considerations: An in-depth study bridging Microscopy with Spectroscopy

---

Chapter 7: Decoding the topographical features of more realistic SERS active substrates in presence of the probe molecules from statistical considerations: An in-depth study bridging Microscopy with Spectroscopy

7.1 Introductory Remarks

Recently, major focus in the research activities on SERS has been devoted towards the fabrications of robust SERS active substrates that exhibit colossal enhancements of Raman signals from the adsorbed probe molecules [1-10]. While fabrications of such substrates using various top-down and bottom-up approaches continue to be the focal point in this area of research [1-14], however reports on understanding the topographical features of those substrates from statistical considerations in terms of lateral correlation length (ξ), Hurst or roughness exponents (α), root mean square surface roughnesses (ω), fractal dimensions (D_f) etc. are surprisingly rare. The importance of some of these parameters have long been recognized to elucidate the enhancement mechanism of SERS [15-17], but to our knowledge, the first systematic studies to understand the topographical features of SERS active substrates in terms of ξ, α, ω and D_f were recently addressed by our research group [2,18,19]. Those studies reveal that certain range of values associated with the topographical parameters (ca. ξ, α, ω and D_f) favor the efficacies of the SERS active substrates under investigations [2,18,19]. Though the above referred topographical parameters for the substrates primarily allow us to understand their morphological features, however correlating their topographical parameters with the corresponding SERS responses were rather incomplete and imprecise. The obvious reason is that the topographical parameters of the SERS active substrates were estimated in the absence of probe molecules, but in reality, the SERS signals are collected from the probe molecules only upon adsorption on the substrates. The adsorption of probe molecules on the substrates can alter their overall morphological features in comparison to the pristine counterparts. This will lead to the changes in ξ, α, ω and D_f values and will help us to correlate the corresponding SERS responses more precisely under real experimental conditions.

This present chapter is focused to explore in details the topographical features of SERS active substrates, fabricated through Langmuir-Blodgett (LB) and self-assembly techniques, in presence of the probe 4- Mercapto Pyridine (4-Mpy) molecules. The statistical parameters (ca. ξ, α, ω and D_f) associated with the topographical features of the bare SERS active substrate are also compared with the same substrate in presence of 4-Mpy. We believe that the present report will help to correlate the topographical features of more realistic SERS active substrates in presence of

probe molecules with their corresponding SERS activities and render significant advancement towards successful fabrications of efficient SERS active substrates in future endeavours.

7.2 Results and Discussions

7.2.1 Pressure- area isotherm plot and fabrication of the substrate

The surface pressure (π) – area (A) compression isotherm plot of Stearic acid (SA) at room temperature is shown in Figure 7.1. The π – A isotherm plot of SA shows a distinct condensed phase at an area/ SA molecule ~ 0.20 nm^2/ molecule. The bilayer LB film of SA was lifted on quartz slide at a constant surface pressure of 25 mN/ m by Y-type deposition technique. This deposition technique allows Head (H) -Tail (T) and Tail (T) – Head (H) configuration of the molecular architecture, leaving behind the polar COO^- head groups of SA to remain suspended in air. The bilayer LB film of SA was then dipped in AuNCs for 24 hours and finally dried in hot air oven to remove the excess metal ions from the surface of the film. We call this LB film substrate, so recovered after dipping in AuNC, as the "As Prepared Substrate (APS)."

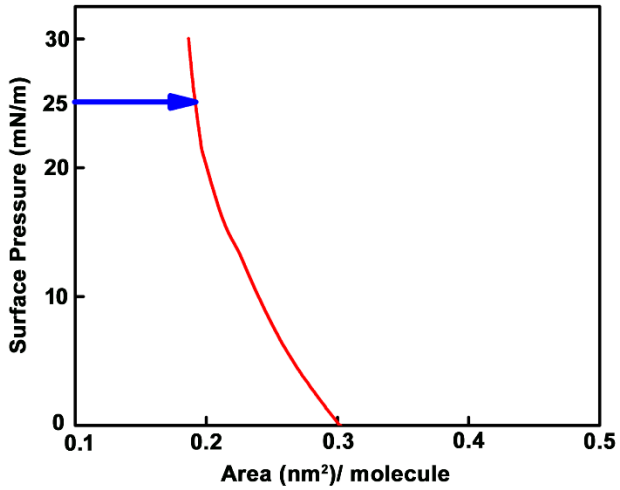

Figure 7.1: Room temperature surface pressure – area (π − A) compression isotherm of Stearic Acid.

The APS substrates were then soaked in the aqueous solution of the Raman probe 4-MPy molecule [$\sim 1.0 \times 10^{-9}$ M (pH ~ 6.8)] for 1 hr, 1.5 hrs and 2 hrs. After the pre-referred soaking times (STs), the respective substrates were removed and kept undisturbed for 18 hours before recording the FESEM, AFM, XPS and SERS spectra. These substrates will henceforth be referred as the "Modified As Prepared Substrates (M-APSs)" to distinguish them from the APS.

Furthermore, the M-APSs which were soaked in the aqueous solution of 4-Mpy for 1 hr, 1.5 hrs and 2 hrs are designated as M-APS (1), M-APS (1.5) and M-APS (2) respectively.

7.2.2 Morphological Characterizations of APS, M-APSs and SERS responses

The FESEM and the corresponding fast fourier transform (FFT) images in the reciprocal k space of APS and M-APSs soaked in the aqueous solution of 4-Mpy ($\sim 1.0 \times 10^{-9}$ M; pH ~ 6.8) for 1, 1.5 and 2 hrs are shown in Figure 7.2 (a, A), (b, B), (c, C) and (d, D) respectively. The FFT images primarily portray random textures of all the substrates [20]. Closer inspections of the FESEM image of the APS [Figure 7.2 (a)] show tethering of gold nanoparticles (AuNps) in the bilayer LB film matrix of SA. The elemental compositions of the APS have been envisaged from the survey scan XPS spectrum, covering the wide binding energy (BE) window ranging from 0 to 1100 eV. The spectrum, as shown in Figure 7.3 (a) (maroon trace), clearly shows the presence of prominent peaks characteristic of Au4f, C1s, Au4d and O1s elements apart from the explicit appearance of Si2p, Si2s bands. The peaks associated with Si2p, Si2s bands at ~ 103, 154 eV BEs respectively emanate from the quartz slide upon which the bilayer LB film of SA has been deposited [21,22]. The prominent XPS peaks with BEs ascribed to Au4f, C1s, Au4d and O1s bands [23,24] confirm the presence of carbon (C), oxygen (O) and gold (Au) atoms in the APS.

The FESEM image further unveils dense aggregated clustered domains of plasmonic nanoparticles. The aggregated domains of AuNps may favour the development of hot geometries which in turn promote the generation of "hot spots" responsible for the origin of SERS spectra. The agglomerated domains of the plasmonic AuNps may evolve as a result of interplay between the short-range nanoparticle- nanoparticle (NN) attractive F_{NNA}, bilayer– bilayer (BB) attractive F_{BBA}, nanoparticle- bilayer (NB) attractive F_{NBA} and long range NN dipolar repulsive forces F_{NNR} prevalent in the APS [25,26].

The FESEM images of the M-APSs, so attained after soaking in the aqueous solution of 4-Mpy for 1 hr, 1.5 hrs and 2 hrs are shown in Figure 7.2 (b), (c) and (d) respectively. To confirm the adsorption of 4-MPy on APS, the wide scan XPS analyses have also been performed on the M-APS (2) so attained after soaking in the aqueous solution of 4-Mpy for 2 hours. The wide range survey scan XPS spectrum for the M-APS (2), as shown in Figure 7.3 (b) (green trace), is markedly different in contrast to that recorded for the APS substrate [Figure 7.3 (a) (maroon trace)]. The

intensities of the XPS peaks originating from Au4f, $Au4d_{5/2}$ and $Au4d_{3/2}$ are strongly enhanced and slightly shifted to higher BEs in comparison to those recorded for the APS. Furthermore, new peaks assigned to the BEs of S2p and N1s are also noted. All these observations may indicate not only the presence of 4-Mpy but also its possible interaction with the AuNps that remain embedded in the M-APS. The XPS analyses of the substrates in detail involving high resolution narrow scan

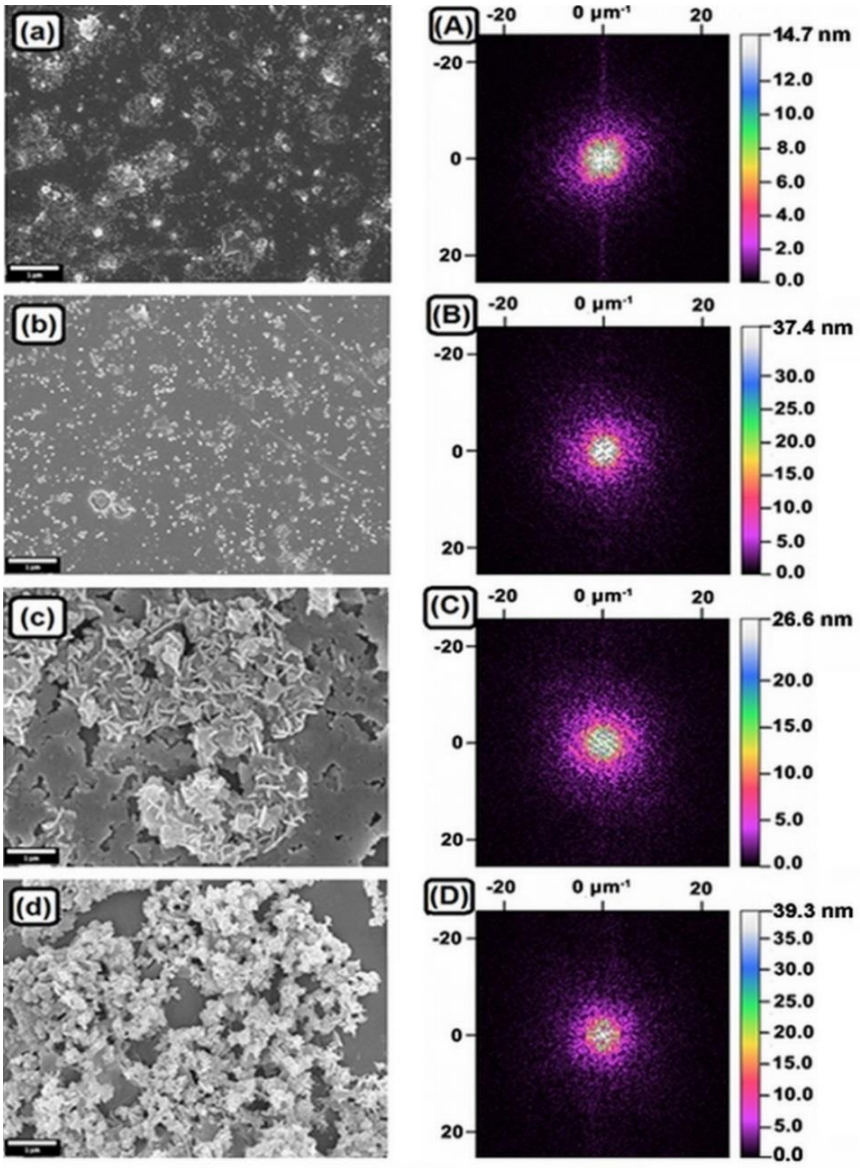

Figure 7.2: Left Column: Micrometer scale FESEM images of **(a)** APS and **(b)** M-APS (1), **(c)** M-APS (1.5) and **(d)** M-APS (2). Right Column [A-D]: The corresponding FFT images of the substrates in the reciprocal k- space.

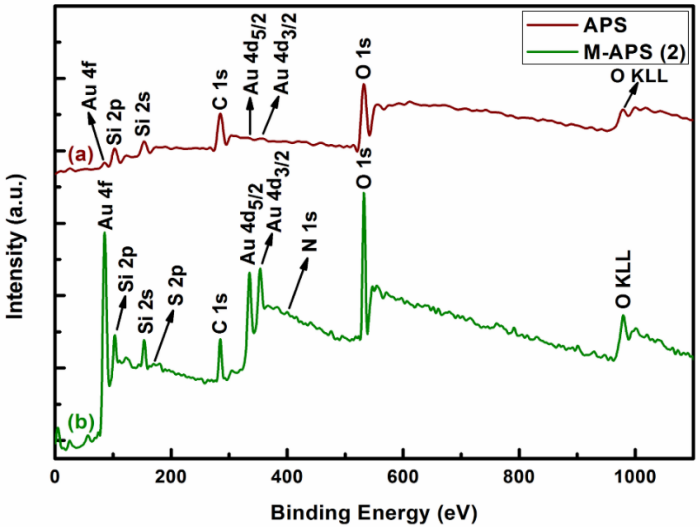

Figure 7.3: The survey scan XPS spectra of **(a)** APS (Maroon trace) and **(b)** M-APS (Green trace).

XPS spectra are beyond the scope of the present study, and are elaborately considered in a separate publication [27].

The FESEM image of the M-APS (1) soaked for 1 hr in 4-MPy solution closely resembles with the morphological features of the APS [Figure 7.2 (a)]. However, surface morphologies of the M-APSs, so accomplished after soaking in the aqueous solution of 4-MPy for 1.5 and 2 hrs show contrasting features. While the FESEM image of the former M-APS (1.5) exhibits clove like aggregated patterns of AuNps [Figure 7.2 (c)], the later M-APS (2) substrate shows sprouted aggregated domains of plasmonic nanoparticles [Figure 7.2 (d)]. These results suggest that adsorption of the probe 4-Mpy molecule on the APS for an extended period of time ($\geq$ 1.5 hrs) can perturb the overall surface morphologies of the M-APS.

Figure 7.4 shows the 2D and 3D- AFM images scanned over 5 μm × 5 μm surface area of the APS as well as of the M-APS substrates soaked in 4-Mpy for 1 hr, 1.5 hrs and 2 hrs. Figure 7.4 (a, A) shows distinct agglomeration of AuNps in the APS and is in line with the observation as perceived from the corresponding FESEM image [Figure 7.2 (a)]. The AFM images of M-APSs soaked in 4-Mpy solution over various STs ranging from 1 to 2 hrs exhibit noticeable differences in the aggregated features of the plasmonic AuNps [Figure 7.4 (b, B), (c, C) and (d, D)]. With increase in ST, the agglomerated domains of AuNps are distinctively localized showing large surface bumps on specific areas of the M-APSs. These results are again in concordance with the

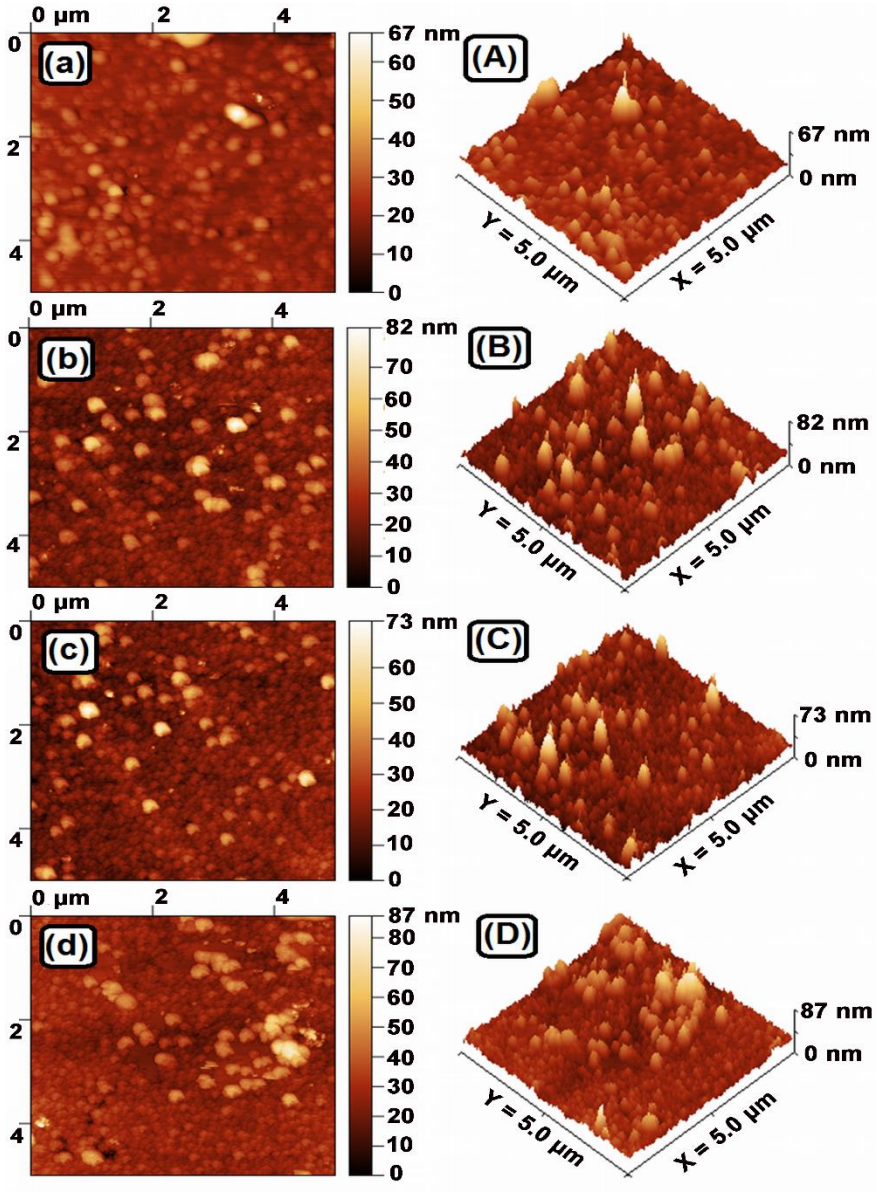

Figure 7.4: Left Column: 2D AFM images of **(a)** APS and **(b)** M-APS (1), **(c)** M-APS (1.5) and **(d)** M-APS (2). Right Column [A-D]: The corresponding 3D AFM images of the the APS and M-APSs.

corresponding FESEM images of the substrates [Figure 7.2; (*vide supra*)]. However, in this connection it may be worth to mention that the height of the M-APS (1.5) as reflected from its AFM image [Figure 7.4 (c, C)] is lower than that of M-APS (1) and M-APS (2) [Figure 7.4 (b, B) and (d, D)]. The rationale behind it may be the fact that the height of the clove like patterns of this plasmonic substrate, as reflected from the corresponding FESEM image [Figure 7.2 (c)], is much

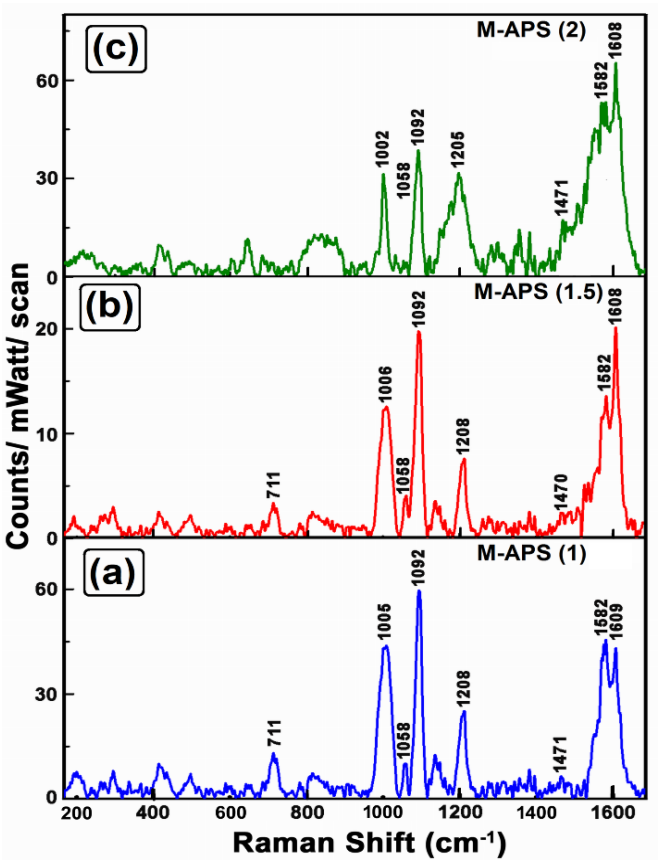

Figure 7.5: SERS spectra of 4- MPy molecule (~1.0×10^{-9} M, pH ~ 6.8) as obtained from **(a)** M-APS (1) **(b)** M-APS (1.5) and **(c)** M-APS (2) (λ_{ex}= 632.8 nm).

lower than the respective heights of the dense and sprouted aggregated domains of the plasmonic nanoparticles in M-APS (1) and M-APS (2) respectively [Figure 7.2 (b) and (d)].

The SERS spectra from the M-APSs so accomplished after soaking in 1.0×10^{-9} M aqueous solution (pH ~ 6.8) of probe 4-MPy for 1 hr, 1.5 hrs and 2 hrs are shown in Figure 7.5 (a), (b) and (c) respectively. All the spectra exhibit enhanced Raman bands at ~ 711, 1005, 1058, 1092, 1208, 1471, 1582 and 1609 cm^{-1} with appreciable S/N ratio. These vibrational signatures are well recognized and are known to originate from the in-plane bending, ring breathing and stretching modes of the 4-MPy molecule [5, 27-29]. The SERS spectral responses of 4-Mpy molecule at nanomolar concentration from three different M-APS substrates thus unarguably demonstrate their efficacies as efficient SERS sensing scaffolds. However, closer inspection of the SERS spectra as shown in Figure 7.5 (a) – (c) reveals that the SERS intensity of the 4-MPy molecule upon

adsorption on M-APS (1.5) is poorer than that of M-APS (1) and M-APS (2). In general SERS intensities of the probe molecules depend upon the surface morphologies of the SERS active substrates. Surface morphologies of the substrates in turn rely on the size, shape and interparticle distances between the plasmonic nanoparticles. The dimeric, trimeric or higher aggregated plasmonic nanostructured domains are known to promote the generation of hot spots, which are now considered to be responsible for the colossal enhancements of SERS signals [30-32]. The FESEM image of the M-APS (1.5) shows clove like aggregated patterns of AuNps [Figure 7.2 (c)]. This type of aggregated clove like patterns may not support the generation of larger hot spot densities in comparison to those of M-APS (1) and M-APS (2). This may result in poorer SERS intensity of the 4-MPy molecule upon adsorption on M-APS (1.5). Moreover, Figure 7.5 (c) reveals that the SERS background signal of M-APS (2) is higher than that of M-APS (1) and M-APS (1.5) [Figure 7.5 (a) and (b)] particularly in ~ 1300 – 1685 cm^{-1} wavenumber window. This broad SERS background signal of M-APS (2) is attributed to amorphous carbon and is now well recognized as potential contaminant that results in intense broad background signals ~ 1300 - 1685 cm^{-1} wavenumber window of the SERS spectra [33-38]. The amorphous carbon signals in the SERS spectra are known to emanate from surface carbon contamination of the organic molecules on the metal surface [39], or may be generated *in situ* due to their photodegradation in the vicinity of highly enhanced localized electric fields [34,35,40]. The appearance of this broad background from the SERS signal of 4-MPy molecule upon adsorption on M-APS (2) may be due to amorphous surface contamination or the same may be generated *in situ* from unwanted photodegradation. The SERS background signal of M-APS (2) is thus accounted for the typical “cathedral peaks” of amorphous carbon which are reported to arise ~ 1580 and 1350 cm^{-1} in the Raman spectra [33]. This may further infer that in comparison to M-APS (1) and M-APS (1.5), the sprouted aggregated domains of plasmonic nanoparticles M-APS (2) may favour surface carbon contamination of the 4-Mpy molecules on the metal surface or may promote their undesired photodegradation. However, to have deeper understanding on the hidden correlations between the topographical features of the APS and M-APSs with their corresponding SERS responses, the substrates have been analysed in view of statistical considerations.

7.2.3 Understanding the topographical features of APS and M-APSs from statistical considerations

Topographical features of the SERS active substrates primarily depend on the surface roughnesses and fractal dimensions of the plasmonic nanoparticles [15,16,41-50]. Optimum roughness features and fractal dimensions of the SERS active substrates are intrinsically linked with the SERS signals [2,18,19]. However, SERS signals in general are known to increase with the optimum roughness features of the roughened electrode surfaces mostly of gold and silver [42,45,46] and also on the fractal nature of the colloidal substrates [15,51]. Topographies of the SERS active substrates on the other hand are closely related with the statistical parameters such as lateral correlation length (ζ), the root-mean-square (RMS) roughness or interface width (ω) and the Hurst (roughness) exponent (α) of the substrate. The Hurst exponent (α) in turn is directly related to the local surface fractal dimension (D_f), which can thus be enumerated thereon [18,19].

The AFM images are not limited to understand the morphological features of the substrates qualitatively but they foster wealth of hidden information which can be extracted precisely from the statistical considerations. While the lateral correlation length (ζ) between the surface heights at any two points on the random rough substrates can be estimated from the auto correlation function, the height-height correlation function (HHCF) helps to envisage the root-mean-square (RMS) roughness or interface width (ω) and the Hurst (roughness) exponent (α) of the substrate. The lateral correlation length (ζ) is known to be one of the most important parameters of random substrate and the heights of any two surface points within spatial separation < ζ are considered to be correlated [52]. However, if they are spatially far apart exceeding the value of ζ, no correlation between the heights of the concerned surface points can be drawn. The lateral correlation length (ζ) has been estimated from the AFM images of the APS and M-APSs with the aid of the auto-correlation function $R(\vec{\rho}_1, \vec{\rho}_2)$, mathematically expressed as [52]

$$R(\vec{\rho}_1, \vec{\rho}_2) = \frac{G(\vec{\rho}_1, \vec{\rho}_2)}{\omega^2} \qquad (7.1)$$

where $\vec{\rho}_1$ and $\vec{\rho}_2$ are the two different surface points on the substrate and $G(\vec{\rho}_1, \vec{\rho}_2)$ is the auto-covariance function of the pre-referred surface points. The auto-covariance function $G(\vec{\rho}_1, \vec{\rho}_2)$ is represented as [52],

$$G(\vec{\rho}_1, \vec{\rho}_2) = E\{h(\vec{\rho}_1)h(\vec{\rho}_2)\} = \int_{-\infty}^{+\infty}\int_{-\infty}^{+\infty} h_1 h_2 p_j(h_1, h_2; \vec{\rho}_1, \vec{\rho}_2) dh_1 dh_2 \qquad (7.2)$$

where h_1 and h_2 are the corresponding surface heights at the locations $\vec{\rho}_1$ and $\vec{\rho}_2$ of the substrate respectively, $p_j(h_1, h_2; \vec{\rho}_1, \vec{\rho}_2)$ is the joint distribution probability density function and ω^2 is the auto-covariance function at zero lag when $\vec{\rho}_1$ and $\vec{\rho}_2$ are superimposed. Thus G(0) is the second order moment or the variance of a surface height and physically represents mean square surface roughness (ω^2) of the substrate concerned. For rough surfaces, the auto-correlation function $R(\vec{\rho}_1, \vec{\rho}_2)$ and the auto-covariance function $G(\vec{\rho}_1, \vec{\rho}_2)$ depend explicitly on the intermediate distance ρ or lag between the two surface points $\vec{\rho}_1$ and $\vec{\rho}_2$. Thus, both these functions can be expressed as

$$G(\vec{\rho}_1, \vec{\rho}_2) = G|\vec{\rho}_1 - \vec{\rho}_2| = G(\rho);\ \&\ R(\vec{\rho}_1, \vec{\rho}_2) = R|\vec{\rho}_1 - \vec{\rho}_2| = R(\rho) \qquad (7.3)$$

The variations of the auto-correlation function R(ρ) with lag $|\vec{\rho}_1 - \vec{\rho}_2|$= ρ have been estimated from the AFM images of the APS and M-APSs and are shown in Figure 7.6 (a), (b), (c) and (d) respectively. The lateral correlation lengths (ζ) for all the substrates are appraised from the respective values of R(ρ) where it drops to $(1/e)$ th of its value at zero lag (i.e., at ρ= $|\vec{\rho}_1 - \vec{\rho}_2|$= 0). The estimated values of ζ for the APS and M-APSs soaked in 4-Mpy solution for 1, 1.5 and 2 hrs of STs are shown in Figure 7.6. No appreciable changes in ζ values for the APS and for the M-APS (1), so attained after 1 hr of ST, have been noticed. These results are in line with the small differences in the morphological features of the APS and the M-APS (1), as recorded from their respective FESEM images [Figure 7.2 (a) and (b)]. Although topographies of the above referred substrates [ca. APS and M-APS (1)] have not much of difference, yet such small difference is clearly reflected in their respective ζ values [~ 151 nm for APS and ~ 141 nm for M-APS (1)]. Interestingly, the ζ values for M-APS (1.5) and M-APS (2) are markedly different from those of APS and M-APS (1). Sharp drop in ζ (~ 125 nm) is observed for M-APS (1.5), whose FESEM image shows clove like aggregated patterns of AuNps. However, much increase in the ζ value (~180 nm) is noted for M-APS (2) whose corresponding FESEM image exhibits profound and sprouted aggregation of plasmonic nanoparticles (*vide ante*).

The above estimations of ζ values for the APS and M-APSs may be linked with their corresponding surface roughnesses, albeit qualitatively. Lower the value of ζ, higher is the surface

roughness. From this consideration, the M-APS (1.5) happens to be most rough while the roughness for the M-APS (2) is least. There are not much prominent differences in the roughness features between the APS and M-APS (1), as their respective ζ values [~ 151 nm for APS and ~ 141 nm for M-APS (1)] are estimated to be nearly same. As surface roughness plays a pivotal role

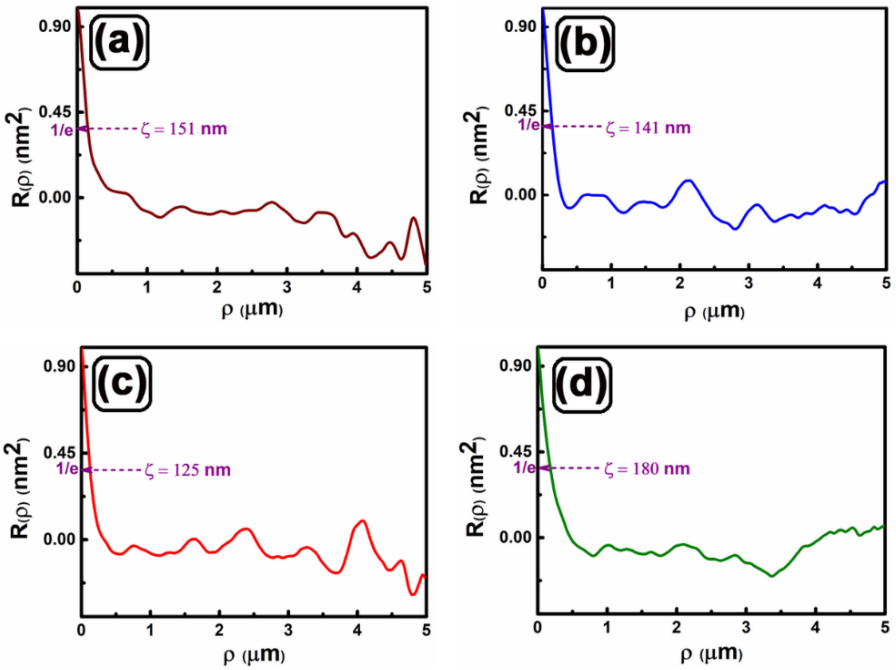

Figure 7.6: The auto- correlation function R(ρ) as a function of displacement vector $\vec{\rho}$ for **(a)** APS and **(b)** M-APS (1), **(c)** M-APS (1.5) and **(d)** M-APS (2).

in the fabrication of SERS active substrates, we believe that estimated ζ values in the range ~ 125 - 180 nm for the M-APSs are enough to exhibit good SERS responses, as depicted in Figure 7.5.

For precise estimation of the roughness features of the APS and M-APSs, the root-mean-square (RMS) roughness or interface width (ω) and the Hurst (roughness) exponent (α) of the substrates have been determined from height- height correlation function (HHCF) H(r). For self-affine surfaces HHCF is mathematically represented as [52],

$$H(r) = 2\omega^2\left[1 - e^{\left(-\frac{r}{\zeta}\right)^{2\alpha}}\right]$$

$$= 2\omega^2 f\left(\frac{r}{\zeta}\right) \qquad (7.4)$$

where $\vec{r}$ represents the position vector on the surface, ω^2 and α signify the RMS roughness or interface width and Hurst or roughness exponent respectively, while $(0 \leq \alpha \leq 1)$ and ζ refers to the lateral correlation length. We designate f(x) as the scaling function of $f(x) = f\left(\frac{r}{\zeta}\right)$ with the following properties,

$$f(x) = x^{2\alpha}, \text{for } x \ll 1$$
$$f(x) = 1, \text{for } x \gg 1 \qquad (7.5)$$

Within the lateral correlation length $(r \ll \zeta)$, H(r) obeys the power law and the Hurst (roughness) exponent (α) determines how much ragged the concerned surface is? However, beyond the correlation length $(\text{i. e for } r \gg \zeta)$, H(r) reaches the asymptotic limit $(\sim 2\omega^2)$ in the form of a plateau and allows one to estimate the RMS roughness or interface width (ω) of the substrate. Figure 7.7 shows the HHCF plots depicting the variation of $\log_{10}H(r)$ as a function of $\log_{10}r$ plot for the APS and M-APSs. The data for the above referred plots is accomplished from the AFM

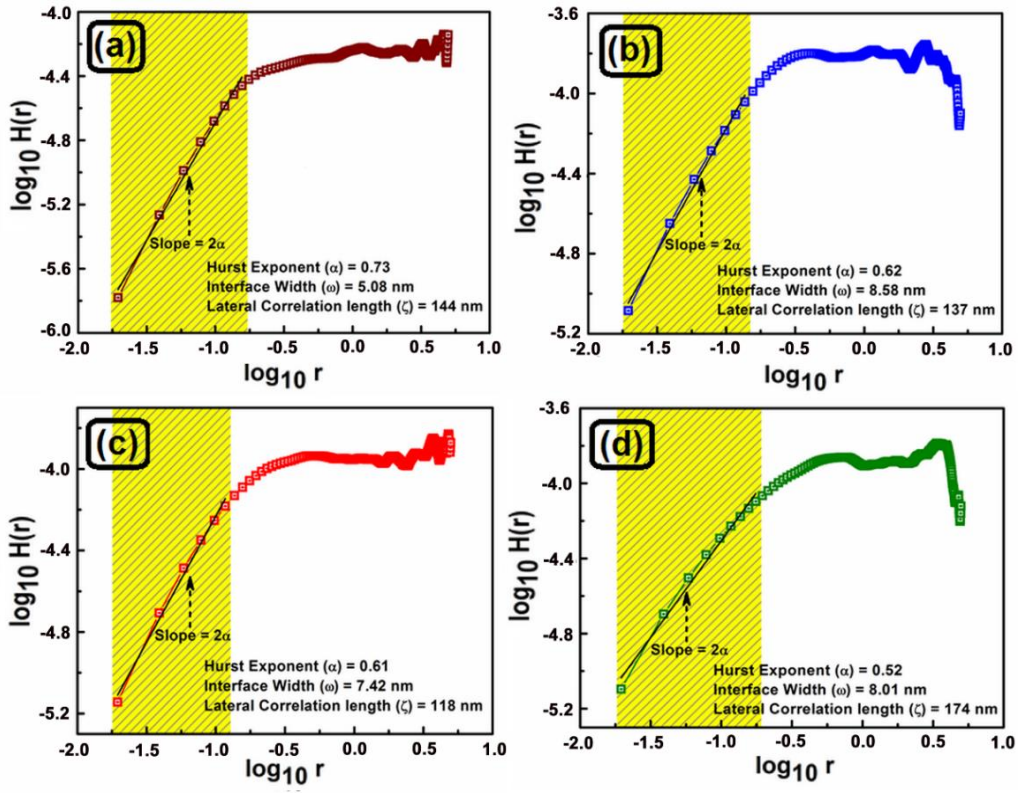

Figure 7.7. Variation of $\log_{10}H(r)$ as a function of $\log_{10}r$ for **(a)** APS and **(b)** M-APS (1), **(c)** M-APS (1.5) and **(d)** M-APS (2).

images of the substrates recorded from five different domains of $5\ \mu m \times 5\ \mu m$ scan area. Interestingly, while the log-log plots for APS as well as for the M-APSs show linear rise obeying the power law at shorter length scales for $r \ll \zeta$, however at larger length scales for $r \gg \zeta$, the HHCF curves attain the saturation limit showing their asymptotic nature. The values of ξ for the APS, M-APS (1), M-APS (1.5) and M-APS (2) have also been estimated from the HHCF plots. The correlation lengths (ξ) for the APS, M-APS (1), M-APS (1.5) and M-APS (2) are noted to be ~ 144 nm, 137 nm, 118 nm and 174 nm respectively, which are in good agreement with the results as estimated from the auto-correlation function R(ρ).

The Hurst or roughness exponent (α), as determined from the respective HHCF plots, are estimated to be ~ 0.73 for the APS and ~ 0.62, 0.61 and 0.52 for the M-APS (1), M-APS (1.5) and M-APS (2) respectively. These results suggest that M-APSs exhibit more jagged local surface morphologies in comparison to the APS. The adsorption of the probe 4-Mpy molecules on the APS substrates thus promote surface roughness which may favour improved plasmonic coupling of AuNps leading to the generation of "hot spots". "Hot spots" are the special locations on the M-APS substrates, where in the electric fields are strongly localized satisfying the plasmon dispersion relation. Probe molecules snared in these "hot spots" experience huge electric field resulting in colossal enhancements of Raman bands as observed in the SERS spectra of 4-Mpy at nanomolar concentration [Figure 7.5 (*vide ante*)].

The Hurst exponents (α) so obtained for the APS and M-APSs are further utilized to enumerate the fractal dimensions (D_f) of the plasmonic AuNps that remain entrapped within the bilayer LB matrix of SA. The Hurst exponent (α) in terms of D_f can be expressed as [52],

$$\alpha = d + 1 - D_f \qquad (7.6)$$

where the dimension of the embedded space is represented by $(d + 1)$. Considering the dimension of the embedded space of the substrates to be (2 + 1) [52], the values of D_f are estimated to be 2.27 (± 0.021) for the APS and 2.38 (± 0.025), 2.39 (± 0.022) and 2.48 (± 0.020) for M-APS (1), M-APS (1.5) and M-APS (2) respectively. These results signify that regardless of different surface morphologies, as observed in APS and M-APSs, there is no significant alteration in the D_f values of the plasmonic AuNps. These observations may further invoke us to conclude that for our APS

and M-APSs, variation in surface morphologies, correlation lengths or surface roughnesses have limited influence on the overall fractal nature of the substrates.

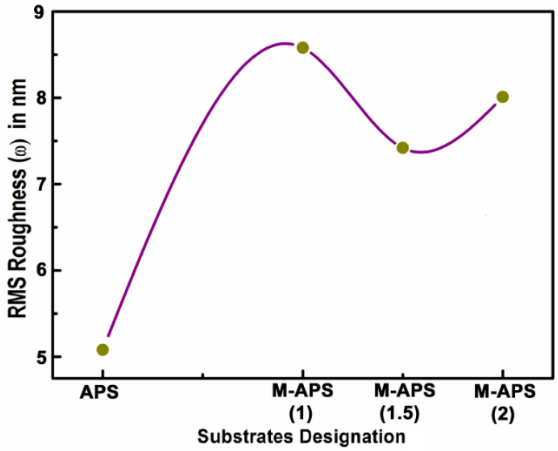

Figure 7.8. RMS roughness or interface widths (ω) plot for APS and M-APSs.

The RMS roughnesses or interface widths (ω) for the substrates have been estimated from the respective HHCF plots and their variations for the APS and M-APS (1), M-APS (1.5) and M-APS (2) are shown in Figure 7.8. The higher values of ω for the M-APSs at various STs with respect to the APS primarily indicate that the former substrates are rougher than the later one. These results are almost in line with their corresponding roughness exponents (α) and the correlation lengths (ξ), as discussed earlier (*vide ante*). Interestingly, the lateral correlation length (ξ) for the M-APS (2), as obtained from R(ρ) (HHCF) is estimated to be 180 nm (174 nm) [Figure 7.7 (d)]. This value of ξ is higher in comparison with APS, M-APS (1) and M-APS (1.5), albeit its roughness exponent (α) is least and the RMS roughness (ω) is considerably large (*vide ante*). The observed disparity in the apparently interrelated α, ω and ξ values of the M-APS (2) relating its surface roughness features in comparison with the APS, M-APS (1) and M-APS (1.5) may primarily signify the existence of chaotic patterns on the surfaces of the substrates that may remain ingrained within the correlation length.

7.2.4 Estimation of Lyapunov exponents, phase space trajectories of APS and M-APSs

The chaotic features of the substrates have been estimated from the Lyapunov exponents (λ). The Lyapunov exponents of the substrates are estimated from TISEAN software package applying Rosenstein's method [53,54]. In non-linear dynamics, this parameter provides a measure

of exponential divergence or convergence of trajectories in phase space as a function of time. While the magnitude of λ signifies unpredictability of the system dynamics, its positive sign refers a chaotic system involving the divergence of two states with the evolution of time. Here, the time series is replaced by the spatial series and value of λ denotes the rate of loss of predictability of heights of APS and M-APSs over space.

The evolution of trajectories over space due to the variations of the surface heights h(r) for successive iterations is represented as [18,19,55]

$$|\delta_l| \approx |\delta_0| e^{\lambda l} \qquad (7.7)$$

where $\delta_0 = h_n - h_{n'}$; h_n and $h_{n'}$ are the surface heights of any two points on the substrate located very close to each other at the onset of the iteration step and l denotes the number of steps involving with the space iteration. The height profiles h(r) for the APS and M-APS substrates were extracted along the breadth of the respective AFM images and were subsequently linked together in series. The values of λ for all the pre-referred substrates were found to saturate after stitching with five successive lines of the respective AFM images. Figure 7.9 shows the plot of < ln (divergence) > as a function of iterations. The positive values of λ, as estimated from the slopes of the different

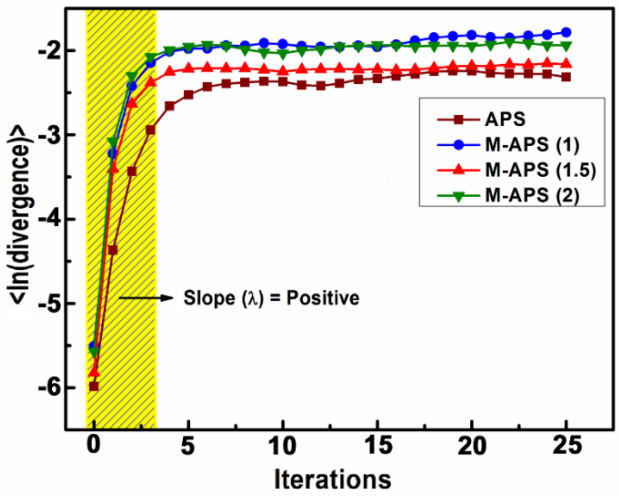

Figure 7.9. < ln (divergence) > vs iteration plot for the APS and M-APSs. The shaded portion shows the linear regime of the plot.

plots associated with APS and M-APSs, indicate the prevalence of chaos with various degrees in all the substrates. The average height profiles h along six typical lines traced over the AFM images

of APS and M-APSs as a function of r, are shown in the left column of Figure 7.10 (a-d). The spatial derivatives h'(r) vs h(r) plots of the respective height profiles are shown in the corresponding right column of the same figure (Figure 7.10). Variation of h'(r) as a function of h(r) represents the 2D- phase space diagrams of the substrates. The phase space diagrams, as shown in Figure 7.10 for the APS and M-APSs, mark the presence of non-periodic orbits, distinctively disposed on the respective phase spaces. The traces of non-periodic close orbits for APS and M-

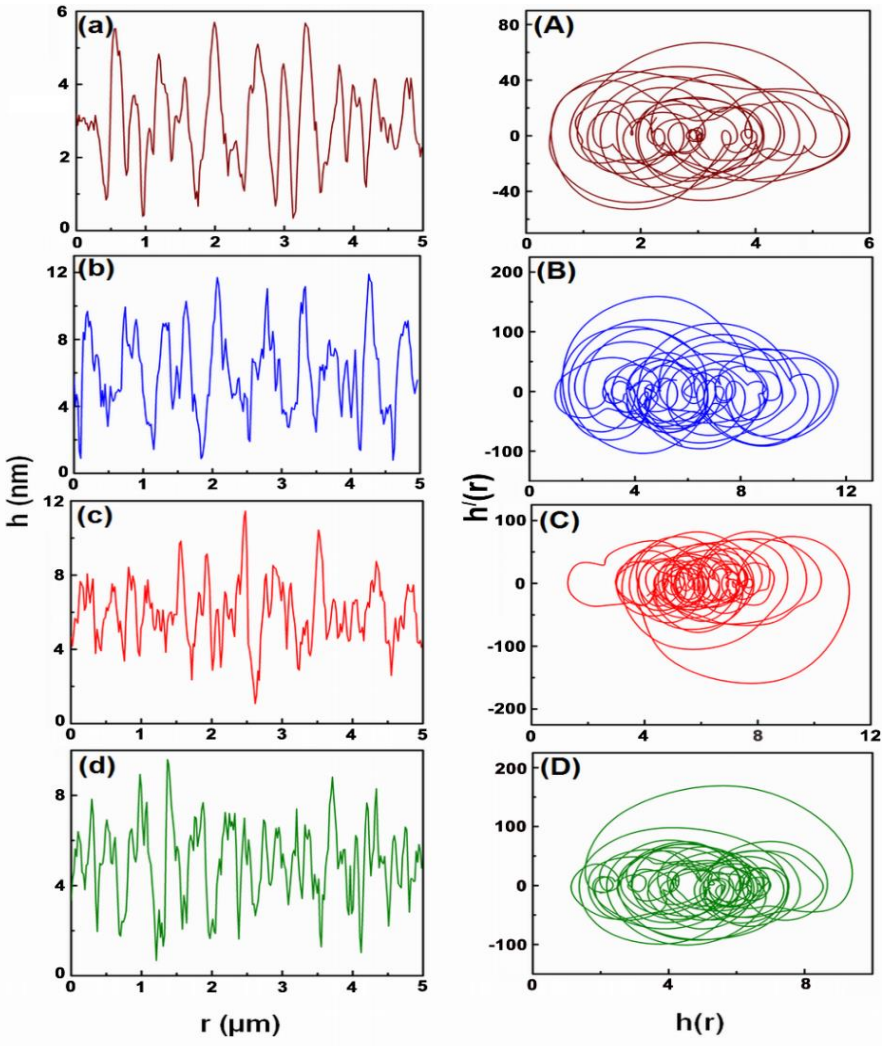

Figure 7.10 Left Column: Average height profile [h(r) vs. r plot] along six typical lines drawn from the AFM images of **(a)** APS and **(b)** M-APS (1) **(c)** M-APS (1.5) and **(d)** M-APS (2). Right Column [**(A)** – **(D)**]: Spatial derivatives h′(r) as a function of h(r) of the corresponding height profiles for the above-mentioned substrates.

APS (1) [Figure 7.10 (A) and (B)] look similar with almost equal densities of low and large amplitude structures. The phase space diagrams for the APS and M-APSs (1) may be closely linked with their nearly identical morphological features as observed from their FESEM images [Figure 7.2 (a) and (b), *vide ante*)]. Interestingly, the general features of the phase space trajectories for M-APS (1.5) and M-APS (2) share fair amount of similarities. For both these substrates, large density of low amplitude structures prevails in certain spatial locations of the phase space, while the large amplitude one with low density are seen to surround them. The spatial distribution of the phase space trajectories for M-APS (1.5) and M-APS (2) can again be mapped with the corresponding FESEM images [Figure 7.2 (c) and (d)], which show clove like and sprouted aggregated patterns of plasmonic gold nanoparticles (*vide ante*). All the above observations collectively suggest that the APS and M-APSs are spatially chaotic of different natures. Reproducible SERS responses from all the M-APSs may further accentuate the importance of chaotic substrates towards successful accomplishment of enhanced Raman signals.

7.3 Conclusion

Detail topographical features of SERS active substrates, fabricated through Langmuir-Blodgett and self-assembly techniques in presence of probe 4-MPy molecules, have been explored. Earlier studies [2,18,19] were devoted to estimate the topographical parameters of bare SERS active substrates in the absence of probe molecules. However, correlating SERS responses with the topographical parameters of bare SERS active substrates may be imprecise, as in real experimental conditions the SERS signals are collected from the probe molecules only upon adsorption on the substrates. The topographical features of the substrates in presence of 4-MPy molecules have been elucidated from the statistical considerations in terms of lateral correlation length (ξ), Hurst or roughness exponents (α), root mean square surface roughnesses (ω) and fractal dimensions (D_f). Correlations between the topographical features of the substrates in presence of the 4-Mpy molecule and their corresponding SERS responses have been mapped. Detail investigations from the FESEM, AFM images and XPS studies reflect noticeable changes in the surface morphologies of the substrates upon the adsorption of probe 4-Mpy molecule. The present study reveals that the lateral correlation length (ζ) in the range ~ 118 - 180 nm for the M-

APSs is enough to exhibit good SERS responses. Moreover, the Hurst (roughness) exponent (α) and the root-mean-square (RMS) roughness or the interface width (ω) of the as prepared substrates so determined from height- height correlation function (HHCF) H(r) show that the optimum values of α and ω in the range ~ 0.52 - 0.62 and 7.42 nm - 8.58 nm respectively favour appreciable SERS responses. The local surface fractal dimensions (D_f) of the as prepared substrates are estimated to lie within 2.38 (± 0.025) to 2.48 (± 0.020). These results further justify the importance of fractal nature of the substrates to foster appreciable SERS signals. The chaotic features of the substrates have also been estimated from the respective Lyapunov exponents and the corresponding 2D phase space trajectories. We believe that the present chapter will provide the fundamental link that connects the topographical features of more realistic SERS active substrates in presence of probe molecules with their corresponding SERS activities. This in turn will render significant advancement towards successful fabrications of efficient SERS sensing platforms in future endeavours.

References

1. S. K. Das, K. Pal, T. S. Bhattacharya, P. Karmakar, J. Chowdhury, *Sens. Actuators B*, 2019, **299**, 126962.
2. S. K. Das, M. Ghosh, S. Ghosh, J. Chowdhury, *Appl. Surf. Sci*., 2019, **484**, 1263.
3. Z. Tang, J. Xu, X. Yu, R. Hong, X. Zu, X. Lin, H. Luo, W. Lin, G. Yi, *ACS Appl. Mater. Inter*., 2021, **13**, 9281.
4. O. Volochanskyi, M. Svecova, V. Bartunek, V. Prokopec, *Coll. Surf. A*, 2021, **616**, 126310.
5. S. Saha, M. Ghosh, J. Chowdhury, *J. Raman Spectrosc*., 2019, **50**, 330.
6. S. Saha, M. Ghosh, B. Dutta, J. Chowdhury, *Appl. Surf. Sci*., 2016, **362**, 364.
7. S. Saha, M. Ghosh, B. Dutta, J. Chowdhury, *J. Raman Spectrosc*., 2016, **47**, 168.
8. J. Li, H. Yan, X. Tan, Z. Lu, H. Han, *Anal. Chem*., 2019, **91**, 3885.
9. S. Yadav, J. Satija, *J. Mater. Chem. B*, 2021, **9**, 267.
10. M. Sakir, S. Salem, S. T. Sanduvac, E. Sahmetlioglu, G. Sarp, M. S. Onses, E. Yilmaz, *Coll. Surf. A*, 2020, **585**, 124088.
11. A. B. Zrimsek, A. I. Henry, R. P. Van Duyne, *J. Phys. Chem. Lett*., 2013, **4**, 3206.

12. T. Wu, Y. W. Lin, *Appl. Surf. Sci*., 2018, **435**, 1143.
13. D. Caprara, F. Ripanti, A. Capocefalo, A. Sarra, F. Brasili, C. Petrillo, C. Fasolato, P. Postorino, *Col. Surf. A*, 2020, **589**, 124399.
14. V. Suresh, L. Ding, A. B. Chew, F. L. Yap, *ACS Appl. Nano Mater*., 2018, **1**, 886.
15. M. I. Stockman, V. M. Schalaev, M. Moskovits, R. Botet, T. F. George, *Phys. Rev. B*, 1992, **46**, 2821.
16. C. Douketis, Z. Wang, T. L. Haslett, M. Moskovits, *Phys. Rev. B*, 1995, **51**, 11022.
17. P. Zhang, T. L. Haslett, C. Douketis, M. Moskovits, *Phys. Rev. B*, 1998, **57**, 15513.
18. S. K. Das, M. Ghosh, J. Chowdhury, *Appl. Surf. Sci*., 2018, **439**, 1.
19. S. K. Das, S. Saha, M. Ghosh, J. Chowdhury, *Vib. Spec*., 2020, **107**, 103031.
20. K. L. Lee, L. H. Chen, *Patt. Recog. Image Anal*., 2002, **12**, 400.
21. K. Shimoda, J.-S. Park, T. Hinoki, A. Kohyama, *Appl. Surf. Sci*., 2007, **253**, 9450.
22. D. Xu, L. Sun, H. Li, L. Zhang, G. Guo, X. Zhao, L. Gui, *New J. Chem*., 2003, **27**, 300.
23. S. Caporali, F. Muniz- Miranda, A. Pedone, M. Muniz-Miranda, *Sensors*, 2019, **19**, 2700.
24. Z. Wang, X. Shen, Y. Yan, T. Qian, J. Wang, Q. Sun, C. Jin, *Appl. Surf. Sci*., 2018, 450, 387.
25. M. Choudhuri, A. Datta, *Soft Mat*., 2016, **12**, 5867.
26. J. N. Israelachvili, *Intermolecular and Surface Forces*, Academic Press, USA, 2010.
27. H. S. Jung, K. Kim, M. S. Kim, *J. Mol. Struc*., 1997, 407, 139.
28. J. Hu, B. Zhao, W. Xu, B. Li, Y. Fan, *Spectrochim. Acta Part A*, 2002, **58**, 2827.
29. M. Pradhan, J. Chowdhury, S. Sarkar, A. K. Sinha, T. Pal, *J. Phys. Chem. C*, 2012, **116**, 24301.
30. S. D. Roy, M. Ghosh, J. Chowdhury, *J. Phys. Chem. C*, 2018, 122, 10981.
31. S. D. Roy, M. Ghosh, J. Chowdhury, *J. Raman Spectrosc*., 2015, **46**, 451.
32. J. P. Camden, J. A. Dieringer, Y. Wang, D. J. Masiello, L. D. Marks, G. C. Schatz, R. P. Van Duyne, *J. Am. Chem. Soc*., 2008, **130**, 12616.
33. A. Ferrari, J. Robertson, *Phys. Rev. B*, 2000, **61**, 14095.
34. T. Sang, J. E. Demuth, P. N. Sanda, J. R. Kirtley, *Chem. Phys. Lett*., 1980, **76**, 54.
35. G. M. Goncher, C. A. Parsons, C. B. Harris, *J. Phys. Chem*., 1984, **88**, 4200.
36. J. Chowdhury, M. Ghosh, T. N. Misra, *J. Col. Inter. Sci*., 2000, **228**, 372.
37. J. Chowdhury, M. Ghosh, T. N. Misra, *Spectrochim. Acta Part A*, 2000, **56**, 2107.

38. J. Chowdhury, M. Ghosh, *J. Raman Spectrosc*., 2004, **35**, 1023.
39. C. E. Taylor, S. D. Garvey, J. E. Pemberton, *Anal. Chem*., 1996, **68**, 2401.
40. J. S. Suh, M. Moskovits, J. Shakhesemampour, *J. Phys. Chem*., 1993, **97**, 1678.
41. Y. Zhao, X. Liu, D. Y. Lei, Y. Chai, *Nanoscale*, 2014, **6**, 1311.
42. S. Kruszewski, *Surf. Inter. Anal*., 1994, **21**, 830.
43. G. Macias, M. Alba, L. F. Marsal, A. Mihi, *J. Mater. Chem. C*, 2016, **4**, 3970.
44. C. Lee, C. S. Robertson, A. H. Nguyen, M. Kahraman, S. Wachsmann-Hogiu, *Sci. Rep*., 2015, **5**, 11644.
45. D. D. Tuschel, J. E. Pemberton, J. E. Cook, *Langmuir*, 1986, **2**, 380.
46. A. G. Brolo, D. E. Irish, G. Szymanski, J. Lipkowski, *Langmuir*, 1998, **14**, 517.
47. C. Douketis, T. L. Haslett, Z. Wang, M. Moskovits, S. Iannotta, *Prog. In Surf. Sci*., 1995, **50**, 187.
48. S. M. Novikov, S. Boroviks, A. B. Evlyukhin, D. E. Tatarkin, A. V. Arsenin, V. S. Volkov, S. I. Bozhevolnyi, *ACS Photonics*, 2020, **7**, 1708.
49. D. Risovic, H. Gebavi, M. Ivanda, *Appl. Surf. Sci*., 2021, **537**, 147915.
50. G. Q. Wallace, F. Lagugné- Labarthet, *Analyst*, 2019, **144**, 13.
51. J. Zhu, M. J. Liu, J. J. Li, X. Li, J. W. Zhao, *Spectrochim. Acta Part A*, 2018, **189**, 586.
52. Y. Zhao, G. C. Wang, T. M. Lu, *Experimental Methods in the Physical Sciences*, Academic Press, San Diego, USA, 2001.
53. R. Hegger, H. Kantza, *Chaos*, 1999, **9**, 413.
54. M. T. Rosenstein, J. J. Collins, C. J. De Luca, *Physica D*, 1993, **65**, 117.
55. S. H. Strogatz, *Nonlinear dynamics and chaos with applications to physics, biology, chemistry and engineering*, Perseus, Cambridge, UK, 1994.

Chapter 8: Adsorption of 4-Mercapto Pyridine with Gold Nanoparticles embedded in the Langmuir-Blodgett Film matrix of stearic acid: SERS, XPS studies aided by Born-Oppenheimer on the fly dynamics, Time–Resolved Wavelet Transform Theory and DFT

Chapter 8: Adsorption of 4-Mercapto Pyridine with Gold Nanoparticles embedded in the Langmuir-Blodgett Film matrix of stearic acid: SERS, XPS studies aided by Born-Oppenheimer on the fly dynamics, Time–Resolved Wavelet Transform Theory and DFT

8.1 Introductory Remarks

Surface-enhanced Raman scattering (SERS) spectroscopy [1] has opened up new horizons not only in the offing of analytical sciences but also in elucidating the physics and chemistry of the surfaces [2-7]. Although the underlying reason behind colossal enhancements in the Raman signals have now been unanimously acclaimed to originate broadly from electromagnetic (EM) and charge transfer (CT) mechanisms, however there have been renewed interest to fabricate new SERS active substrates and to understand their adsorptive behaviors with the aid of improved adatom models [8-11]. While fabrications of new SERS active substrates that offer promising applications in the real-world diagnostics and in forensic sciences have gained significant attentions to the material scientists these days [12-15], improved ad-cluster molecule – Metal (M_n , $n = 1$ to 20) models from quantum chemical calculations proved to be effective in understanding their adsorptive behaviors [16-21].

This chapter reports facile fabrication of SERS active substrate through integration of self-assembly and Langmuir-Blodgett (LB) deposition techniques. Efficacy of the as fabricated substrate has been tested from the SERS spectra of the analyte 4-Mercaptopyridine (4MPy) molecule. The adsorptive site of the analyte molecule with the substrate has been investigated in detail from the X-ray photoelectron spectroscopy (XPS) studies. The experimental observations are aided by Born-Oppenheimer on the fly Molecular Dynamics (BO-OF-MD), time resolved wavelet transform theory and Density Functional Theory (DFT) calculations based on analyte molecule- metal adcluster models. To the best of our knowledge this chapter may be considered as the first ever report where the most probable molecule-adcluster model has been proposed from BO-OF-MD followed by DFT calculations. The CT contribution to the overall enhancement of the SERS spectra of 4MPy molecule has also been envisaged from electron density difference (EDD) studies.

8.2 Results and Discussions

8.2.1 Pressure- area isotherm plot and fabrication of the substrate

The room temperature surface pressure (π) – area (A) compression isotherm of SA is shown in Figure 8.1. The bilayer LB film of SA was deposited on the previously cleaned quartz substrates at a constant surface pressure of 25 mN/m by Y-type deposition technique. The LB film of SA was

then dipped in AuNCs for 24 hours and finally dried in the hot air oven to remove the excess metal ions from the surface of the film. We designate this final LB film substrate so accomplished after dipping in AuNC as "As Prepared substrate (APS)".

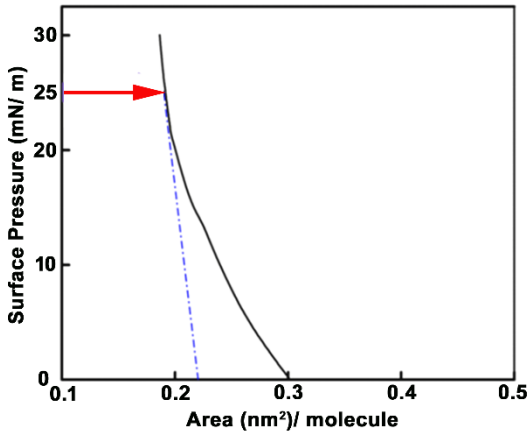

Figure 8.1: Room temperature surface pressure (π) – area (A) compression isotherm of SA in pure water sub phase (pH ~ 6.8).

8.2.2 UV-Vis electronic absorption spectra of the AuNC and APS

The room-temperature UV-Vis absorption spectrum of the as synthesized AuNC is shown in Figure 8.2. AuNCs show single absorption maximum peaked at ~ 534 nm. This band is well ascribed to bulk-like surface plasmon resonance (BL-SPR) and had been extensively reported

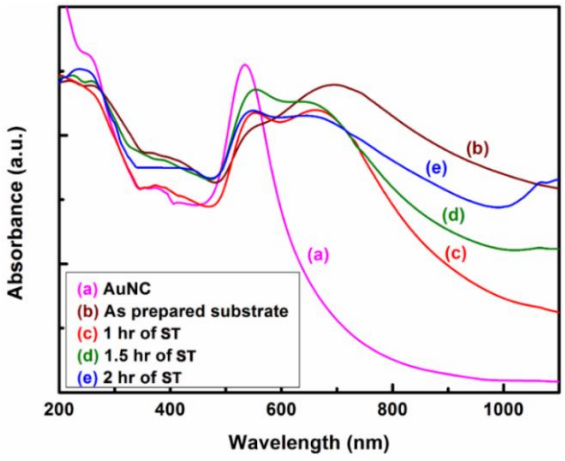

Figure 8.2: Room temperature UV-Vis electronic absorption spectra of (a) AuNC, (b) the APS and the modified M-APS so attained after (c) 1 hr, (d) 1.5 hr and (e) 2 hrs of ST in 1.0×10^{-9} M aqueous solution of 4MPy.

elsewhere [22,23]. The electronic absorption spectrum of the APS is shown in Figure 8.2 (b). The spectrum is marked by the decrease in intensity of BL-SPR band at ~ 538 nm along with the appearance of intense broad maximum at ~ 692 nm in the low energy window. The low energy band at ~ 692 nm is attributed to the surface-like surface plasmon resonance (SL-SPR) and is known to arise due to dipole-dipole interaction of the aggregated AuNPs on the bilayer LB film matrix of SA [22-24]. The optical signature of this low energy band in the UV-Vis electronic absorption spectrum primarily transpires the existence of gap- plasmonic domains of gold nanoparticles which in turn is known to promote the generation of "hot spots" on the APS. These "hot spots" are recognized to be the special locations on the substrate where the electric fields are strongly localized and the probe molecules trapped within those spots exhibit colossal SERS enhancements [23,25]. However, such conjecture needs to be correlated with the morphology of the substrate from the FESEM and AFM images.

8.2.3 Characterization of the bilayer LB film of SA and APS

The FESEM images of the bare quartz slide, bilayer LB film of SA and that of the APS are shown in Figure 8.3 (a), (b) and (c) respectively. While LB film shows compact arrangement of bilayer SA with uniform texture [Figure 8.3 (b)], the FESEM image of the APS [Figure 8.3 (c)] however marks the entrapment of gold nanoparticles (AuNPs) that remain embedded on the bilayer LB film matrix of SA in the form of dense aggregated clustered domains. The aggregated domains of AuNPs stand responsible for the generation of gap plasmons on the as prepared substrate leading to the appearance of SL-SPR band in the low energy window of the corresponding absorption spectrum [Figure 8.2; *vide supra*)] [22-24].

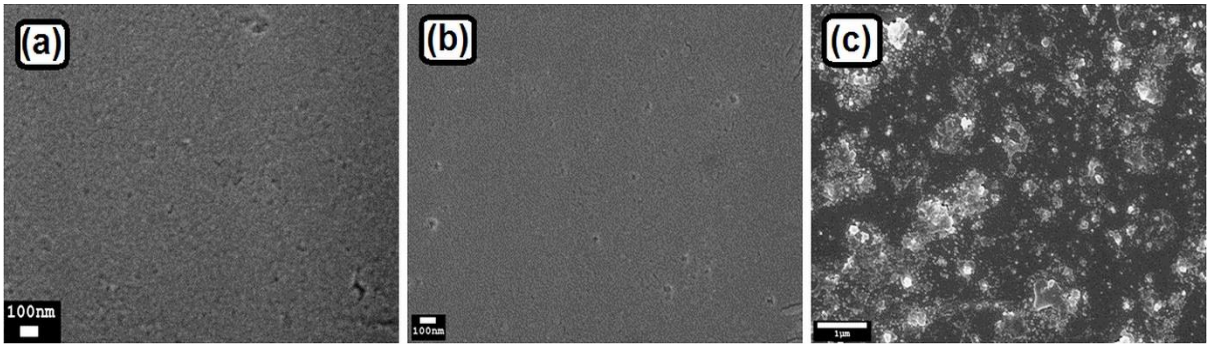

Figure 8.3: FESEM images of (a) bare quartz slide, (b) SA bilayer LB film and (c) AuNPs self-assembled on the LB film matrix of SA.

The 2D and 3D- AFM images of the APS, as shown in Figure 8.4 (a) and (b) respectively also clearly fleck the existence of aggregated AuNPs over the bilayer LB film of SA, as envisaged from the FESEM image.

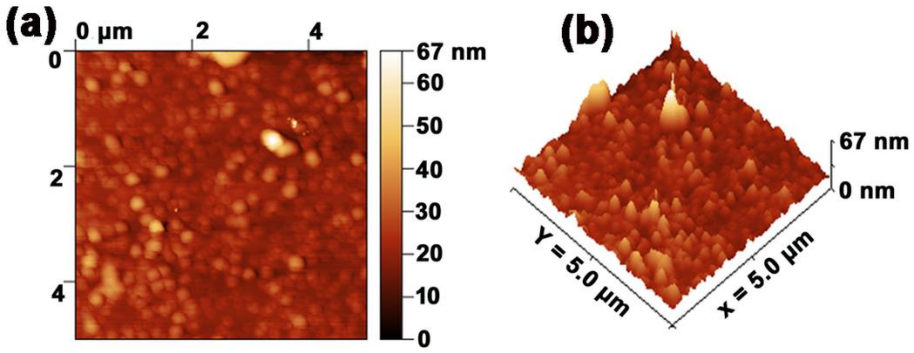

Figure 8.4: (a) 2D and (b) 3D AFM images of the APS.

To gain precise information about the elemental composition of APS and to unveil the chemical state and bonding configuration of Au with SA, XPS analyses have been performed. Being a surface sensitive technique and normally probes to a depth of ~ 10 nm, we believe for the LB film substrates XPS technique may be reckoned to be the method of choice for such characterizations. The wide range survey scan XPS spectrum of the APS is shown in Figure 8.5 (a). Full survey scan spectrum shows the presence of prominent peaks characteristic of Au4f, Si2p, Si2s C1s, Au4d and O1s elements along with Auger peaks O KLL in the order of increasing binding energy (BE) associated with gradual stepwise increase in background. The XPS survey scan thus primarily confirms the presence of carbon (C), oxygen (O) and gold (Au) atoms in the APS. The presence of Si in the bare glass slide upon which the bilayer LB film of SA has been deposited is marked by the appearance of Si2p and Si2s peaks. The atomic percentages of Au^0 and Au^+ in the substrates have been specifically estimated using the relation [26],

$$C_i = \left\{ \frac{I_i/X_i}{\sum_j \left(I_j/X_j \right)} \right\} \times 100\% \qquad (8.1)$$

where, $i, j = Au^0,\ Au^+$. In equation 8.1, "I_i" represents the intensity of the Au^0 and Au^+ peaks while the "$\sum_j I_j$" depicts the summation of intensities contributing from Au^0 and Au^+ peaks in the XPS spectrum. The intensities I_i and I_j have been enumerated from the estimation of the areas

under the respective XPS peaks. The atomic sensitivity factor is represented by X_i, X_j which for the Au4f peak is considered to be 6.250 [26].

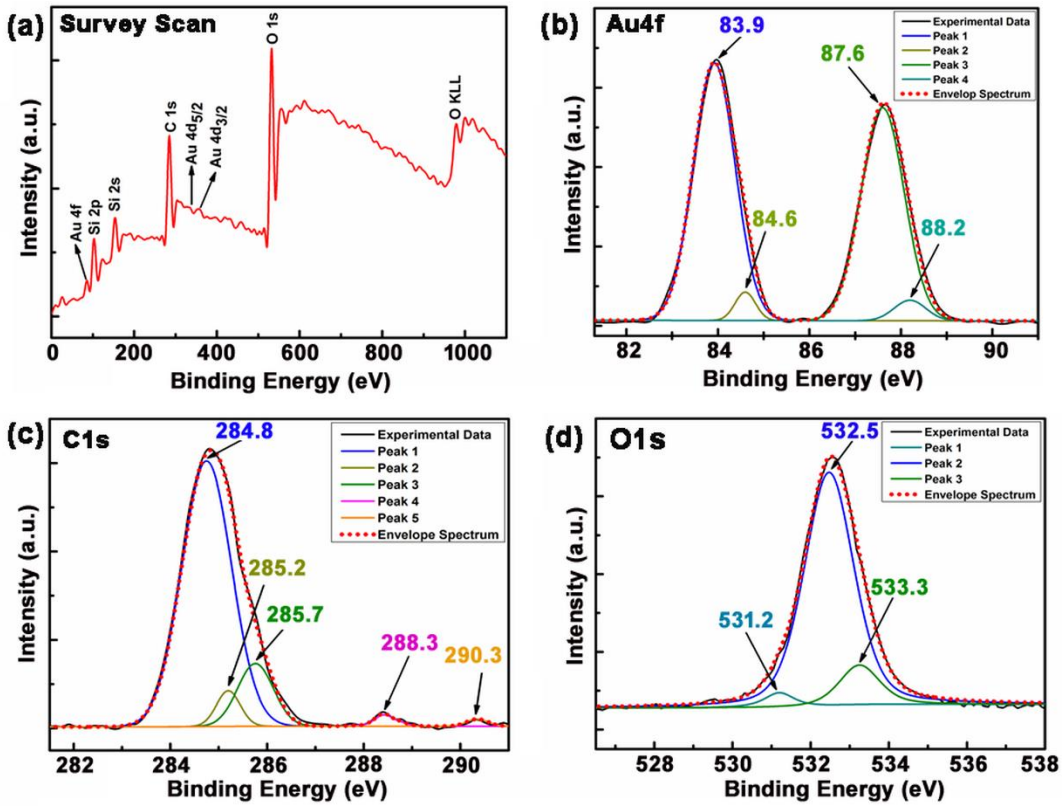

Figure 8.5: (a) The XPS survey scan of the APS. Narrow scan XPS spectra of the APS in the binding energy windows that represent (b) Au4f, (c) C1s and (d) O1s regions.

High resolution narrow scan XPS spectra exhibiting in the BE windows of Au4f, C1s and O1s peaks are shown in Figure 8.5 (b) – (d) respectively. The XPS spectrum in the BE of the Au4f region has been closely monitored and is shown in Figure 8.5 (b). Distinct doublets at ~ 83.9 and 87.6 eV with characteristic energy separation (ΔE) ≈ 3.66 eV are observed for the Au4f peak. Deconvolution of the doublet peaks mark the appearance of two pairs of bands centered at ~ 83.9, 84.7 eV and 87.6, 88.3 eV owed to $Au^0 4f_{7/2}$, $Au^+ 4f_{7/2}$, and $Au^0 4f_{5/2}$, $Au^+ 4f_{7/2}$ respectively. These results primarily signify the presence of both the neutral Au^0 atoms and positively charged Au^+ ions on the surface of AuNPs that remain entrapped in the bilayer LB film matrix of SA. However, intensity ratios of the deconvoluted doublet XPS peaks ($IAu^0 4f_{7/2}$ / $IAu^+ 4f_{7/2}$ = 12.57;

$IAu^0 4f_{5/2}$ / $IAu^+ 4f_{5/2}$ = 7.78) imply the preponderance of neutral Au^0 atoms (~ 81.57%), albeit the explicit presence of positively charged Au^+ ions (~ 18.43 %) on the APS cannot be neglected.

The narrow scan XPS spectrum in the C1s region [Figure 8.5 (c)] is characterized by intense and well resolved peak at ~ 284.85 eV together with weak but prominent bands peaked at ~ 288.3 and 290.3 eV. Upon deconvolution of the experimental data, three peaks appear at ~ 284.8, 285.2 and 285.7 eV, while the other two peaks in the higher BE region retain their peak positions at ~ 288.3 and 290.3 eV as were recorded in the unconvoluted spectrum. The most prominent peak at ~ 284.8 eV originates from the $C-C$ and $C-H$ groups, representing the long aliphatic chain of SA [27], while the relatively weaker peak at 285.2 eV is attributed to the carbon atoms that are located near the carboxylic group [28]. The peak at 285.7 eV corresponds to the BE associated with the $C-O$ group of SA [29,30]. Weak but distinct peak at ~ 288.3 eV is owed to $Au-COO^-$[27,31]. while the XPS signal at 290.3 eV suggests the presence of COOH group non-bonded to the AuNPs [27]. High resolution narrow surface scan in the BE window of C1s not only justifies the presence of SA but also may point towards probable interaction of its carboxylate group (which remain exposed to air in the bilayer LB film of SA deposited through Y- type deposition technique) with the Au^+ ions. This interaction in turn may promote the possible entrapment of AuNPs in the bilayer LB film matrix of SA.

Considerable attention may also be drawn from the narrow scan XPS spectrum representing the O1s signal in the BE window spanning in the range of 526.5 to 538 eV. The spectrum is shown in Figure 8.5 (d). Deconvolution of the O1s peak exhibits three bands peaked at 531.2, 532.5 and 533.3 eV. Two weak peaks ~ 531.2 and 533.3 eV may be ascribed to the BEs associated with $Au-O$ and $C=O$ bonds of the carbonyl group respectively [32,33], while the most intense peak at 532.5 eV is owed to the $C-O$ bond. These results further indicate the presence of SA in the LB film substrate and their interaction with AuNPs in agreement with our earlier conjecture.

8.2.4 Adsorption of the probe 4MPy molecule on the APS and their corresponding absorption spectra

Aqueous solution ~ 1.0×10^{-9} M (pH ~ 7) of probe 4MPy molecule is soaked on the APSs for 1 hr, 1.5 hrs and 2 hrs of soaking times (STs). The delays in the various STs may allow the

probe molecules to penetrate deep into the substrate through gradual diffusion. Figure 8.2 (c – e) show the UV-Vis electronic absorption spectra of the substrates obtained after soaking in 4Mpy solution for 1 hr, 1.5 hrs and 2 hrs. In comparison to the APS [Figure 8.2 (b)], the BL-SPR band in the absorption spectra of the substrate upon soaking in the probe molecule for various STs gains in intensities without any significant alterations in the peak positions (λ_{max} ~ 550 nm). However, remarkable down shift of the broad SL-SPR band (λ_{max} ~ 665 nm) is noticed in the absorption spectra of the substrate in presence of the probe molecule in comparison to the APS. The substantial blue shifts of the SL-SPR band signify facile adsorption of the probe molecules on the APS which in turn may alter the respective dielectric environments of the plasmonic AuNPs, resulting in appreciable downshifts [34,35]. The as substrate so obtained upon soaking in the solution of the probe 4Mpy molecules will henceforth be designated as "modified-as prepared substrate (M-APS)" to distinguish it from the "as prepared substrate (APS)" so fabricated from LB and self-assembly techniques without any adsorption of the probe molecules.

8.2.5 Characterization of the M-APS: FESEM, AFM and XPS studies

The FESEM images of the M-APS, so obtained upon soaking in the probe 4Mpy molecules (~ 1.0×10^{-9} M concentration at pH ~ 7) for 1 hr, 1.5 hrs and 2 hrs of STs, are shown in Figure 8.6 (a), (b) and (c) respectively. After 1 hr of ST [Figure 8.6 (a)], the FESEM image of the M-APS looks almost similar as was recorded for the APS without the adsorption of the probe molecules. However, the morphological features of the "modified substrates", so attained after soaking in the aqueous solution of 4MPy for 1.5 and 2 hrs of STs are remarkably different. The M-APS incubated in the 4Mpy solutions for 1.5 hrs show clove like aggregated patterns of AuNPs [Figure 8.6 (b)].

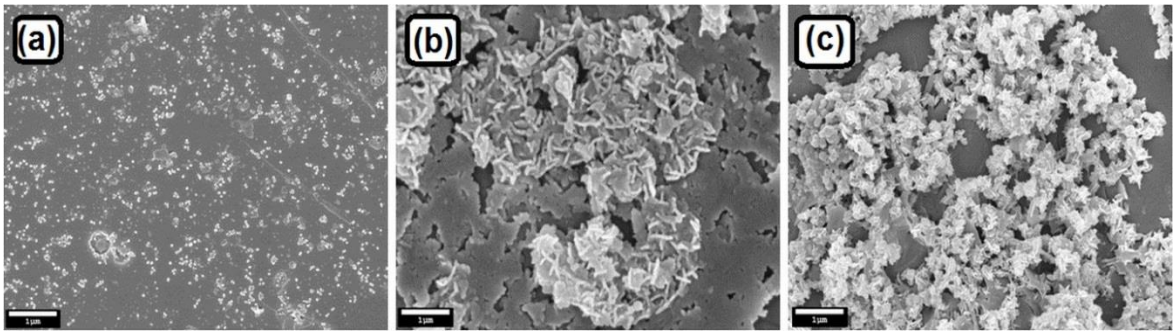

Figure 8.6: Micrometer scale Field Emission Scanning Electron Microscopy (FESEM) images of the M-APS so attained after (a) 1 hr, (b) 1.5 hrs, (c) 2 hrs of STs in 1.0×10^{-9} M aqueous solution of 4MPy.

The aggregation becomes even more profound for the M-APS that remain soaked in the aqueous solution of 4Mpy for 2 hrs of STs [Figure 8.6 (c)]. These results indicate that adsorption of the probe 4Mpy molecule on the APS for an extended period of ST (ST ≥ 1.5 hrs) has remarkable

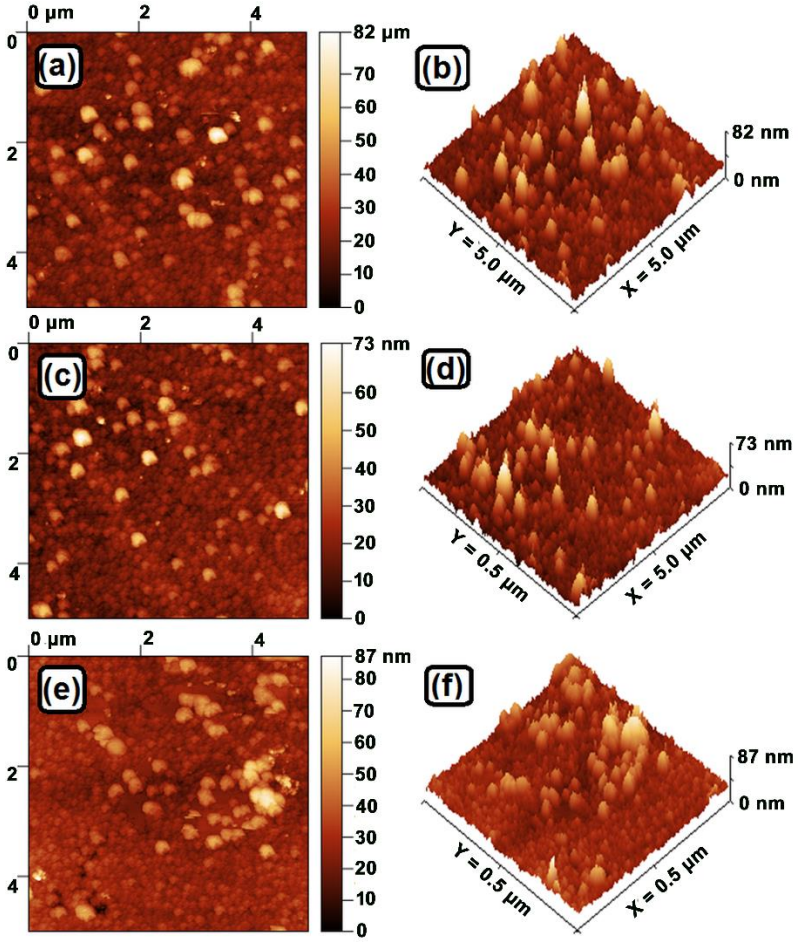

Figure 8.7: Left column: (a), (c) and (e) 2D AFM images; Right column: (b), (d) and (f) corresponding 3D AFM images of the M-APSs so recovered after 1 hr, 1.5 hrs and 2 hrs of STs respectively in 1.0×10^{-9} M aqueous solution of 4MPy.

effect in controlling the overall morphology of the M-APS. Such variations in the morphological features of the M-APSs are also reflected from the 2D- and 3D- AFM images, as shown in Figure 8.7 (a, c, e) and 8.7 (b, d, f) respectively. With increase in STs, the AFM images of the M-APSs exhibit sharp differences in the aggregated features of the plasmonic AuNPs. These results are

again in harmony with that as observed in the corresponding FESEM images [Figure 8.6; (*vide supra*)].

To understand the adsorption of 4Mpy molecule on M-APS so obtained after 2 hrs of ST, the XPS analyses have been performed. The corresponding spectra are shown in Figure 8.8. The wide range survey scan XPS spectrum for the M-APS [Figure 8.8 (a)] is markedly different in contrast to the APS substrate as discussed earlier [Figure 8.5 (a); *vide supra*]. Prominent distinctions are noticed for the Au4f, $Au4d_{5/2}$ and $Au4d_{3/2}$ XPS peak intensities which appear as weak signals for the APS. The pronounced increase in intensities of these bands, together with small but definite peak shifts towards higher BE in the XPS spectrum of the M-APS substrate in comparison to that of APS may signify considerable interaction of 4Mpy with Au. Moreover, the deconvoluted high resolution narrow scan XPS spectrum in the BE window of the Au4f peak [Figure 8.8 (b)] further suggests the existence of neutral Au^0 atoms (~ 83.52 %) in the M-APS,

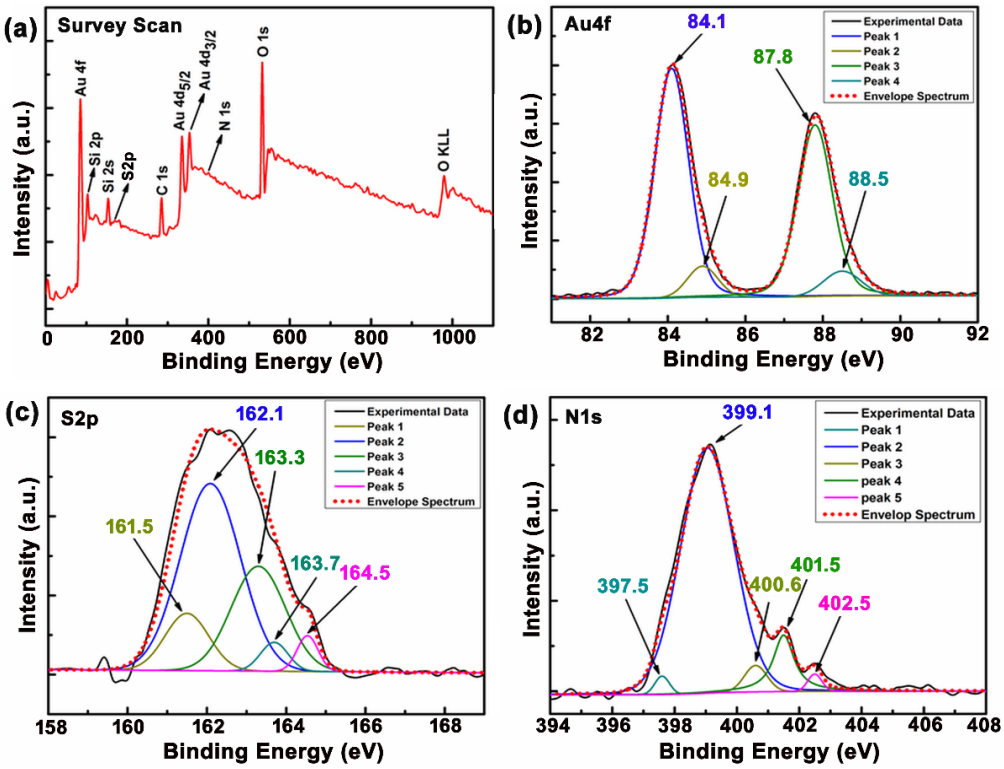

Figure 8.8: (a) The XPS survey scan of the M-APS so obtained after 2 hrs of ST. Narrow scan XPS spectra of the M-APS so obtained after 2 hrs of ST in the binding energy windows that represent (b) Au4f, (c) S2p and (d) N1s regions.

although the presence of Au^+ ions (~ 16.48 %) on the substrate cannot be ignored. Other contrasting features that are noticed in the survey scan spectrum of M-APS are the presence of S2p and N1s XPS peaks. These peaks are not observed in APS, thereby indicating their origin to be explicitly owed to the probe 4MPy molecule that gets adsorbed in the M-APS.

Close observation may be drawn from the narrow scan XPS spectrum covering the S2p BE window ranging from 158 to 169 eV [Figure 8.8 (c)]. The narrow scan XPS signal in the S2p region shows broad spectral signature, distinctively dissimilar with that reported for free 4MPy molecule in the same BE window [29]. This spectral feature not only just suggest the interaction of 4Mpy with the M-APS but also may signify different chemical states of the sulfur atom [36]. Subsequent deconvolution results in five probable peaks centered at ~ 161.5, 162.1, 163.3, 163.7 and 164.5 eV. The peaks at ~ 161.5 eV and 164.5 eV are characteristic to the $S2p_{3/2}$ level while the peak at 163.7 eV is known to originate from the $S2p_{1/2}$ level of the sulfur atom [37]. The other two peaks at ~ 162.1 and 163.3 eV are owed to $2p_{3/2}$ and $2p_{1/2}$ levels of sulfur respectively and their relative intensity ratio ~ 2:1 may presage the existence of the thiolate form of the molecule [38,39]. The presence of S^- in the thiolate form of 4Mpy may involve in the adsorption process with the Au atoms of the AuNPs that remain embedded on the substrate. This conjecture is further substantiated by the absence of any S2p peak at the higher BE beyond 167 eV, primarily suggesting that the sulfur atom of the 4MPy molecule has not probably been oxidized [36].

The high resolution XPS spectrum in the N1s peak region has been recorded and is shown in Figure 8.8 (d). The N1s spectrum has been deconvoluted into five peaks. Among them, the peak centered at ~ 397.5 eV is attributed to the BE of $C-N$ bond associated with the 4MPy molecule [39]. The other deconvoluted peaks at ~ 399.1 and 400.6, 401.5 eV are reported to emanate from the 4MPyD and 4MPyH forms of 4MPy molecule respectively [38]. Interestingly, weak but prominent band which appears in relatively higher BE and peaked at ~ 402.5 eV is ascribed to the oxidized N atom of the 4MPyD form of 4Mpy molecule [40].

The above XPS analyses thus collectively suggest the presence of both the 4MPyH and 4MPyD thiolate forms of 4MPy molecule that remain adsorbed on the M-APS. No evidence presaging the oxidation of sulfur atom and the presence of the thiolate S^- form together with the presence of N1s peak at ~ 402.5 eV may signify the adsorption of the 4MPyH and 4MPyD thiolate

forms of 4MPy molecule with the M-APS substrate via the sulfur atom leaving the nitrogen atom free to oxidize [37,38]. However, the conjecture may be further strengthened from the SERS spectra of the M-APS substrate and have been depicted in the following section.

8.2.6 SERS spectra of M-APS

The SERS spectra from the M-APS so obtained after soaking in 1.0×10^{-9} M aqueous solution (pH ~7) of 4MPy molecules for 1 hr, 1.5 hrs and 2 hrs of STs are shown in Figure 8.9 (a), (b) and (c) respectively. The spectra are marked by distinct vibrational signatures ~ 416, 711, 1002, 1058, 1092, 1208, 1582 and 1608 cm^{-1}, characteristic of the 4MPy molecules [41-43]. These observations clearly indicate appreciable efficacies of all the M-APSs as good SERS sensing

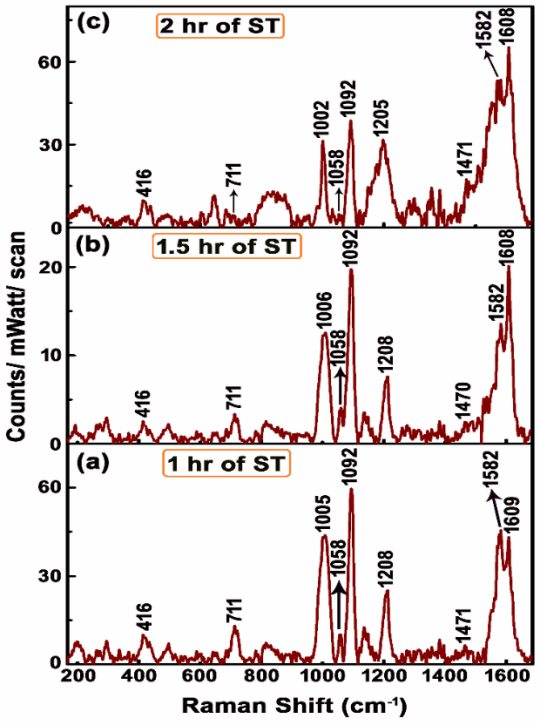

Figure 8.9: SERS spectra of 1.0×10^{-9} M aqueous solution of 4MPy molecule at various STs ($\lambda_{ex} = 632.8$ nm).

platforms. In order to establish the spectral reproducibility, the relative standard deviation (RSD) of the SERS spectra from the M-APS after 2 hrs of ST has been evaluated. Figure 8.10 shows the SERS spectra of 1.0×10^{-9} M 4MPy molecule so attained after interrogating the laser spot on ten random regions of the M-APS. The calculated RSD values of the well resolved marker bands of

4-MPy centered at ~ 1002, 1092, 1582 and 1608 cm^{-1} are 11.88%, 9.19%, 11.19% and 12.34% respectively. The estimated RSD value < 13% marks the reproducibility of the as prepared M-

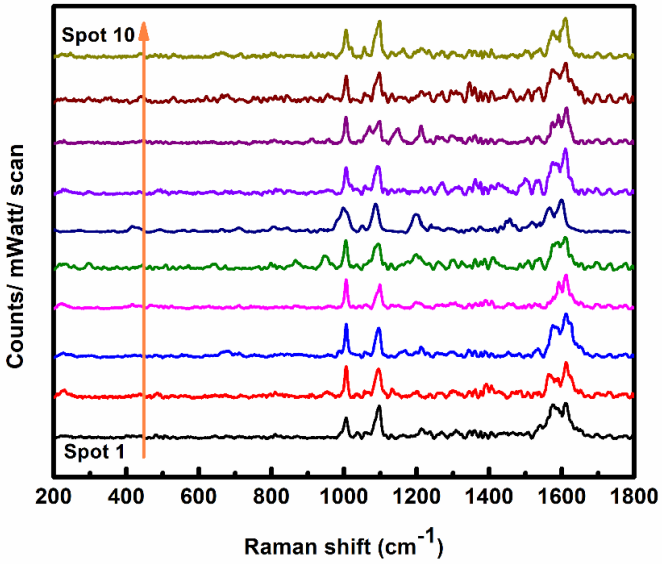

Figure 8.10: SERS spectra of 1.0×10^{-9} M 4MPy at pH ~ 7, recorded from 10 distinct spots of the M-APS so obtained after 2 hrs of ST.

APS. The NRS of 4MPy in aqueous medium (pH ~ 7) at 1 M concentration is also recorded and is shown in Figure 8.11. The NRS spectrum exhibit Raman modes of vibrations centered at around ~ 429, 723, 1001, 1053, 1114, 1207, 1589 and 1621 cm^{-1}, all known to emanate from the 4MPy molecule [42,44-46]. Interestingly, appreciable changes in relative intensities are noted for the SERS bands of the 4MPy molecules centered at ~ 1002, 1092, 1208, 1582 and 1609 cm^{-1} depending upon the STs of the probe molecule on the M-APSs. Among them 1582 cm^{-1} SERS band belongs to B_2 irreducible representation while the rest are linked with A_1 symmetry species. These changes may primarily signify the presence of both the 4MpyH and 4MpyD thione forms of 4Mpy molecule, which are known to coexist in different proportions under similar experimental conditions and have been extensively reported in our earlier publication [41]. Alternatively, the selective enhancements of Raman bands in the SERS spectra belonging to A_1 and B_2 irreducible representations (*vide supra*) may account from the CT interaction between the probe molecule and the AuNP systems. Since the concentration (~ 1.0×10^{-9} M) and pH of the adsorbate 4Mpy molecules in aqueous solution remains same, we believe the variations in the intensities of the

enhanced bands in the SERS spectra may be due to CT interactions between AuNPs and the existing 4MPyH and 4MPyD forms of the 4Mpy molecule in the surface adsorbed state.

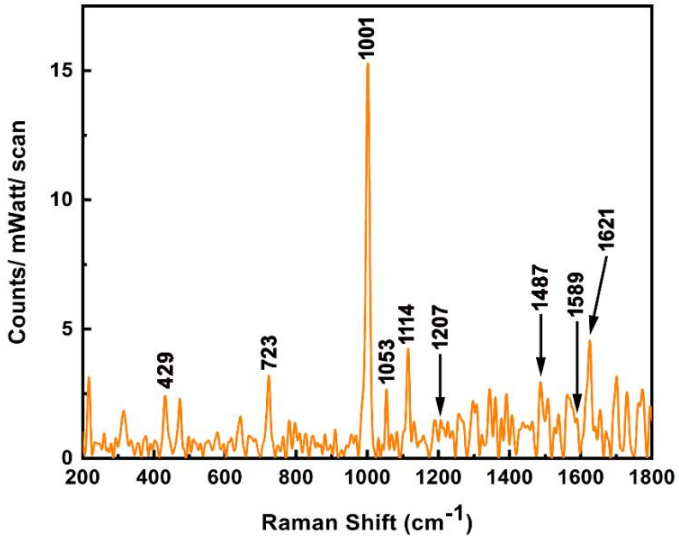

Figure 8.11: Background corrected normal Raman spectrum (NRS) of 1 M 4MPy in aqueous solution ($\lambda_{ex} = 632.8$ nm).

The prevalence of CT interaction is further substantiated by appreciable downshifts of SERS bands at around ~ 711 and 1092 cm^{-1} whose NRS counterparts are recorded at 723 and 1114 cm^{-1} respectively. The bands at ~ 711 and 1092 cm^{-1} are assigned to mixed $\upsilon(C-S)$ stretching, in – plane $\beta(C-C)$ bending (ν_6) and ring breathing mode [$12a_1$] coupled with $\upsilon(C-S)$ stretching vibrations respectively [41,47]. Furthermore, remarkable downshifts of both these bands may signify plausible interaction of the 4MPy molecule with the AuNPs through lone pair electrons of the sulfur (S) atom. This conjecture is in line with the observation as predicted from the XPS studies (*vide supra*). The rationale behind the CT interaction may be further extended from the intensity reversals between the pair of bands ~ 1582 and 1608 cm^{-1} in the SERS spectra of 4Mpy molecule [Figure 8.9 (a-c)] belonging to B_2 and A_1 irreducible representations respectively [48,49]. The intensity reversals between these pair of bands owing to B_2 and A_1 irreducible representations are attributed to CT interactions driven by intensity borrowing from strongly allowed molecular transition of 4MPy molecule [48]. To gain deeper insights into the adsorption behaviour of the 4Mpy with M-APS, BO-OF-MD and DFT calculations have been further

explored with the aid of molecule-metal adatoms models [38,50-52]. The results of the pre-referred calculations are depicted in the following section.

8.2.7 Born Oppenheimer Molecular Dynamics and DFT Calculations on the Molecule- Au cluster Models

To corroborate the CT effect of SERS, as evinced from the experimental observations (*vide supra)*, the adatom or small metal cluster models have been adopted to understand the Au-4Mpy interactions from the DFT calculations [38,50-52]. These adatom or adcluster models ensure the importance of specific surface-active site/ sites on the metal nanoparticles that are explicitly involved in the chemisorption processes with the external probe molecules [19,53]. The surface active adatoms or adclusters contain single or few metal atoms or ions and remain relatively isolated from the bulk metal [54]. Recent reports suggest pragmatic applications of such models have the real power to reproduce the experimentally observed SERS spectra of various metal-molecule systems both in terms of their vibrational frequencies and relative intensities [8-11,16-21,27,55,56].

However, to envisage a reliable model of the metal adcluster that can get involved in the binding processes with both the existing 4MpyH and 4MpyD forms of the 4MPy molecule on the "M-APSs", the partial radial distribution function g(r) between the Au and the sulfur (S1), nitrogen (N9) atoms of the probe molecule have been estimated from BO-OF-MD simulations. The partial radial distribution function not only provides a firm basis to enumerate the composition of atom/atoms in the Au adcluster but also help to understand their interactions with the specific atom/ atoms of the probe molecule, useful for the ensuing DFT calculations. Figure 8.12 (a) and 8.12 (b) shows the variation of g(r) as a function of radial distances between the $S1-Au$ for 4MpyH and the $N9-Au$, $S1-Au$ atoms for 4MpyD forms of the molecule respectively. The radial distributions show one prominent peak [Figure 8.12 (a)], centered at ~ 2.53 Å, signifying the average distance between S1 of 4MpyH and the Au atoms of the adcluster. Such close distance ~ 2.53 Å between S1 and Au atoms may primarily indicate probable involvement of sulfur (S1) atom of 4MpyH molecule in the adsorption process with AuNPs. Interestingly, the variations of $g_{S1-Au}(r)$ and $g_{N9-Au}(r)$ as a function of distance for the 4MpyD molecule, as shown in Figure 8.12 (b), divulge some interesting observations. While, $g_{S1-Au}(r)$ exhibits the most prominent

peak at a distance ~2.35 Å, the first prominent maximum of $g_{N9-Au}(r)$ however appears at comparatively larger distance ~ 4.02 Å. These results may signify the involvement of sulfur (S1) instead of nitrogen (N9) atom even in the adsorption of 4MpyD forms of the probe molecule with AuNPs, as being suggested for its 4MPyH form (vide *supra, cf.* Figure 8.8). Integrating the areas

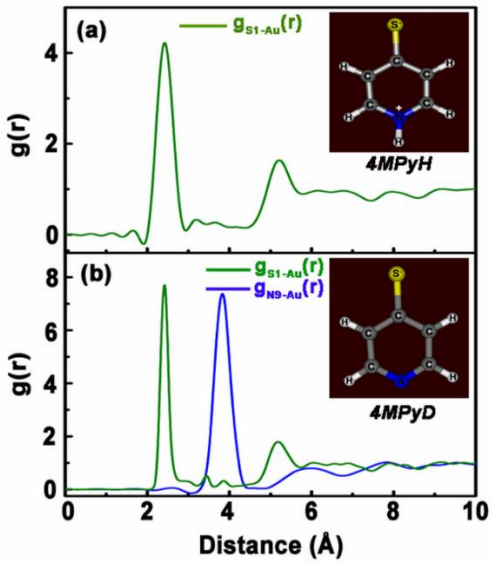

Figure 8.12: Partial radial distribution function g(r) for (a) 4MpyH and (b) 4MpyD forms of the molecule in presence of surrounding Au atoms as estimated from BO-OF-MD simulation.

under the curves represented by the first distinct peak of the $g_{S1-Au}(r)$ plots [Figure 8.12 (a) and 8.12 (b)] for the 4MpyH and 4MpyD forms of the molecule yield the integration number ~ 2.81 and 2.96 respectively. These results suggest the existence of maximum three or minimum of two Au atoms in the first neighbouring shell near the sulfur (S1) atom of both the 4MPyH and 4MPyD forms of the 4Mpy molecule. Thus 3 or 2 Au atoms in neutral or in positively charged forms may constitute the Au_n adcluster (n = 3, 2) model to best represent the surface-active site of the AuNPs.

The energy of the Au_3 cluster has been equilibrated over a period of time ranging from 0 to 30 picosecond with the aid of BO-OF-MD calculation. The results are shown as blue trace in Figure 8.13 (a). After initial structural flexing and relaxations, the energy of the Au_3 cluster system is noted to be stabilized after 10 ps of the simulation run. The probable structure of the Au_3 cluster evolved at ~ 12 ps is shown the inset of Figure 8.13 (a). The frequency distributions showing variations of $r(Au-Au)$ bond length and $\angle Au-Au-Au$ bond angle as obtained from the

corresponding BO-OF-MD trajectory are shown in Figure 8.13 (b) and (c) respectively. The weighted average values of the $r(Au - Au)$ bond length and $\angle\, Au - Au - Au$ bond angle for the Au_3 cluster are estimated to be ~ 2.595 Å and 136^0 respectively. The initial structural parameters

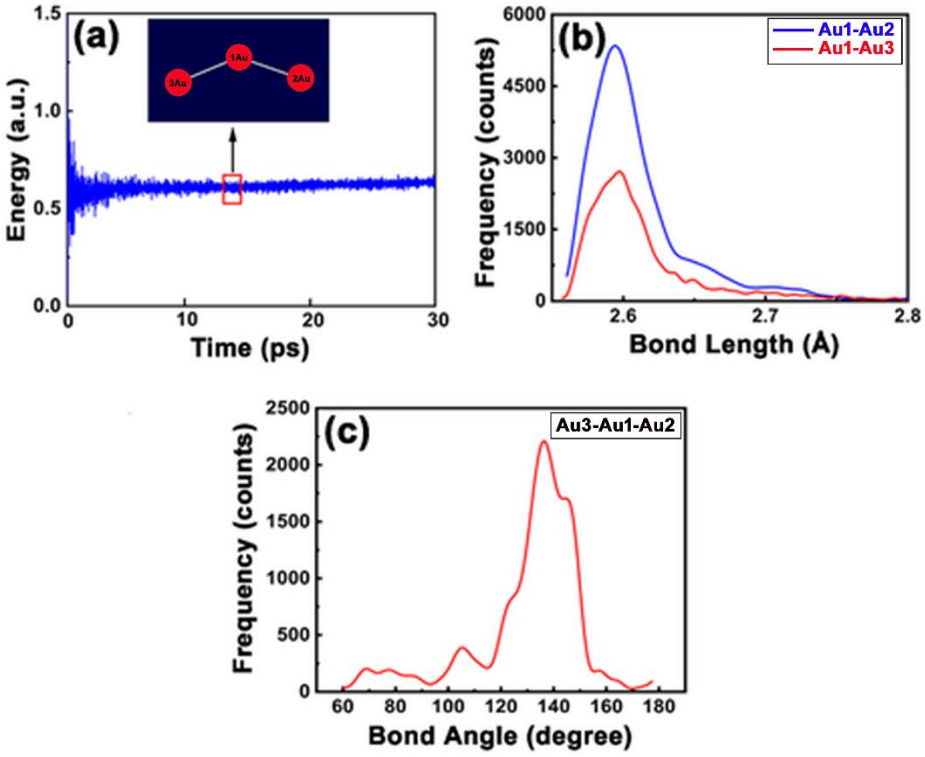

Figure 8.13 (a) Energy vs time plot of Au_3 cluster over 30 ps time scale as obtained from the BO-OF-MD calculations. Statistical distributions of (b) Au – Au bond lengths and (c) Au – Au – Au bond angle.

Table 8.1. Optimized structural parameters of Au_3 cluster as obtained from BO-OF-MD and DFT calculations with B3LYP/ Lanl2DZ level of theory. Figures in the parenthesis represent the standard deviations of the respective estimated values.

Bond length (in Å)/ bond angle (in degree)	**BO-OF-MD**	**DFT**
$Au_1 - Au_2$	2.71($\pm$0.065)	2.75
$Au_1 - Au_3$	2.73 ($\pm$0.044)	2.75
$\angle\, Au_3 - Au_1 - Au_2$	138.32 ($\pm$2.39)	144.2

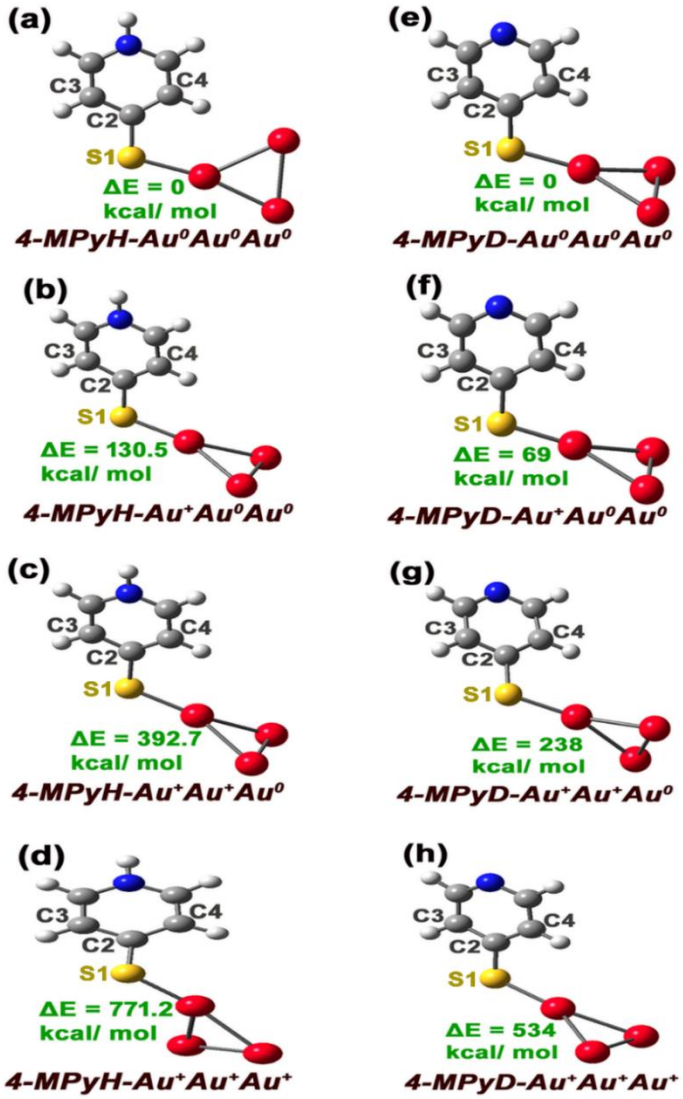

Figure 8.14 Optimized geometries of the model complexes of (a) 4MPyH-$Au^0Au^0Au^0$, (b) 4MPyH-$Au^+Au^0Au^0$, (c) 4MPyH-$Au^+Au^+Au^0$, (d) 4MPyH-$Au^+Au^+Au^+$, (e) 4MPyD-$Au^0Au^0Au^0$, (f) 4MPyD-$Au^+Au^0Au^0$, (g) 4MPyD-$Au^+Au^+Au^0$ and (h) 4MPyD-$Au^+Au^+Au^+$ adclusters so obtained from DFT calculations with B3LYP / 6-31++g(d,p) [for C, H, N and S] / LANL2DZ (for Au atoms) level of theory.

of Au_3 cluster, as obtained from BO-OF-MD simulation, has been fed for further geometry optimization using DFT calculations with B3LYP/ LANL2DZ level of theory. The optimized structural parameters of Au_3 cluster as estimated from BO-OF-MD and DFT calculations are shown Table 8.1. Figure 8.14 shows different adsorptive stances of neutral (Au_3^0) as well as

charged $Au^{+}Au^{0}Au^{0}$, $Au^{+}Au^{+}Au^{0}$ and $Au^{+}Au^{+}Au^{+}$cluster systems with 4MpyH and 4MpyD forms of the probe molecule. The inclusion of neutral and charged Au atoms in various Au_3

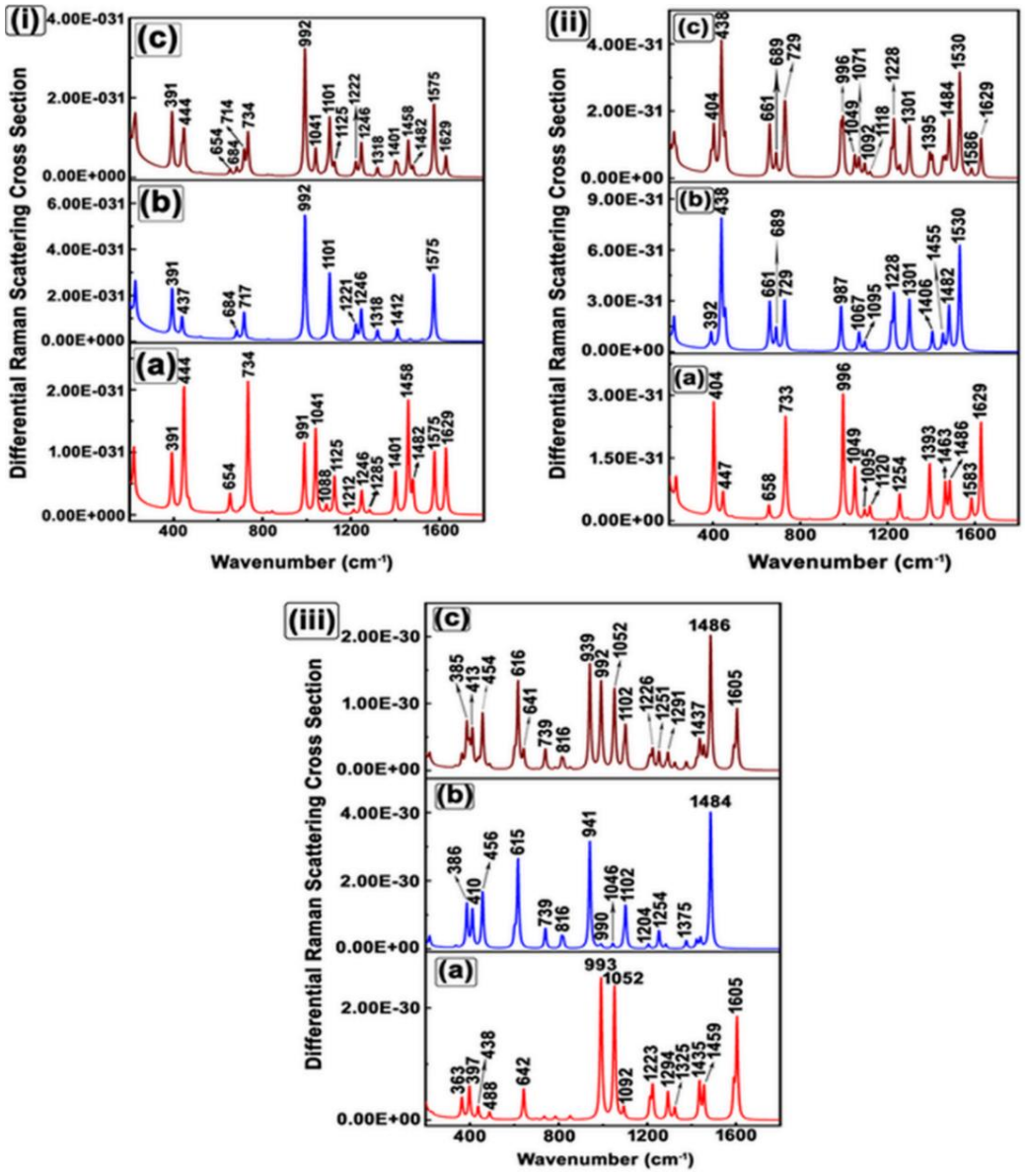

Figure 8.15: Theoretically simulated Raman spectra of **(i)** (a) 4MPyH – $Au^{0}Au^{0}Au^{0}$, (b) 4MPyD – $Au^{0}Au^{0}Au^{0}$ and (c) Mixed -$Au^{0}Au^{0}Au^{0}$ adclusters; **(ii)** (a) 4MPyH – $Au^{+}Au^{0}Au^{0}$, (b) 4MPyD – $Au^{+}Au^{0}Au^{0}$ and (c) Mixed –$Au^{+}Au^{0}Au^{0}$adclusters; **(iii)** (a) 4MPyH – $Au^{+}Au^{+}Au^{+}$, (b) 4MPyD – $Au^{+}Au^{+}Au^{+}$ and (c) Mixed – $Au^{+}Au^{+}Au^{+}$ adclusters using B3LYP / 6-31++g(d,p) [for C, H, N and S] / LANL2DZ (for Au atoms) level of theory.

adcluster models stem from the XPS spectra of M-APS that marks the presence of both neutral (Au^0) and charged Au^+ ions as discussed earlier (cf. section 8.2.5). Significantly enough, among the estimated self-consistent field (SCF) energies of the probable Au_3 - molecule adatom models, the 4MpyH-$Au^0Au^0Au^0$ and 4MpyD–$Au^0Au^0Au^0$ surface complexes are found to be thermodynamically most stable. These results are in line with the XPS studies that smears the presence of Au^0 atoms in abundance on the M-APS (*vide ante*; c*f.* section 8.2.5). Figure 8.15 shows the theoretically simulated Raman spectra of 4MpyH-$Au^0Au^0Au^0$, 4MpyH-$Au^+Au^0Au^0$, 4MpyH-$Au^+Au^+Au^+$, 4MpyD-$Au^0Au^0Au^0$, 4MpyD-$Au^+Au^0Au^0$, 4MpyD-$Au^+Au^+Au^+$ and their corresponding mixed forms. Interestingly, neither of the calculations can reproduce the experimentally recorded SERS spectra, although among them the 4MPyH/ 4MPyD – $Au^0Au^0Au^0$ adcluster models are estimated to be most stable from theromdynamical considerations. On the contrary, the Raman spectra of the mixed 4MpyH– $Au^+Au^+Au^0$ and 4MpyD– $Au^+Au^+Au^0$ forms, as estimated from the DFT calculations, are shown in Figure 8.16 which is in close agreement with the experimentally observed SERS spectra of the molecule. The

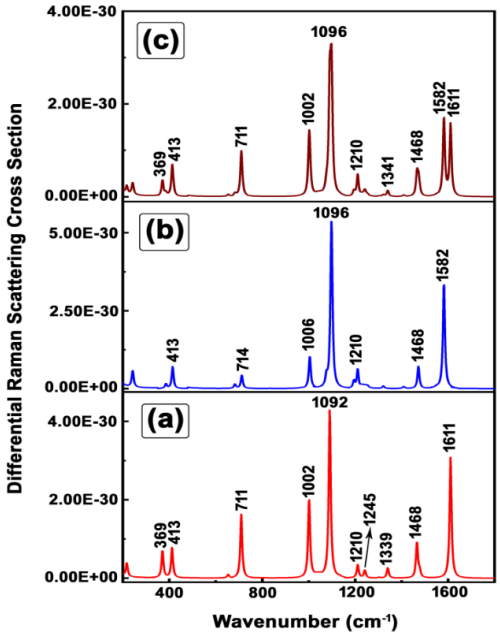

Figure 8.16: Theoretically simulated Raman spectra of (a) 4MPyH–$Au^+Au^+Au^0$, (b) 4MPyD–$Au^+Au^+Au^0$ and (c) Mixed form–$Au^+Au^+Au^0$ adcluster models as estimated from B3LYP / 6-31++g(d,p) [for C, H, N and S] / LANL2DZ (for Au atoms) level of theory.

Table 8.2: Simulted frequencies of 4MPyH-$Au^+Au^+Au^0$ and 4MPyD-$Au^+Au^+Au^0$ complexes compared with the experimentally observed SERS frequencies of 4MPy adsorbed on Au nanoparticles surface at different STs along with their tentative assignments[a]

NRS (1 M)	**SERS (1.0×10^{-9}M)**			**4MpyH–** $Au^+Au^+Au^0$	**4MpyD–** $Au^+Au^+Au^0$	**Symmetry**	**Assignment**
	ST =1 hr	**ST = 1.5 hr**	**ST = 2 hr**				
				180			Au– Au/Au– S stretch
				224	231		Au– S stretch
				372	381		Ring stretch with C– S/ C– C– C
429 (ms)	416	416	416	413	413	A_1	CC out-of-plane bend
				662	670		Ring stretch with CC asym wag
723 (ms)	711	711	711	711	714	A_1	β (C – C)/ν (C – S)[ν_6]
1001 (vs)	1005	1006	1002	1002	1006	A_1	Ring Breathing [ν_1]
1053 (w)	1058	1058	1058			A_1	β (C – H)[ν_{18}]
1114 (ms)	1092	1092	1092	1092	1096	A_1	Trigonal ring-breathing with C=S deformation [ν_{12}]
1207 (vw)	1208	1208	1205	1210	1210	------	β (C – H)/δ (NH)
				1244	1248		N– H in-plane wag
1487 (w)	1471	1470	1471	1477	1468	A_1	ν(C=C/C=N)[ν_{19}]
1589 (w/k)	1582	1582	1582		1582	B_2	ν(C – C)[ν_8] with deprotonated nitrogen
1621 (ms)	1609	1608	1608	1611		A_1	ν (C – C)[ν_8] with protonated nitrogen

[a]ms-medium strong; vs- very strong; w- weak; vw- very weak, k- kink.

calculated vibrational frequencies of $4MpyH-Au^{+}Au^{+}Au^{0}$, $4MpyD-Au^{+}Au^{+}Au^{0}$ model complexes along with the experimentally observed SERS bands at various STs are shown in Table 8.2 along with some of their tentative assignments. The optimized geometrical parameters of some selected bond lengths and bond angles of $4MpyH-Au^{+}Au^{+}Au^{0}$, $4MpyD-Au^{+}Au^{+}Au^{0}$ model complexes as estimated from the DFT calculations are shown in the Table 8.3.

Interesting observations may be drawn from the results of WT theory, which can estimate the fluctuations of $Au-S1$ bond length as a function of time. The temporal variations of the $Au-S1$ bond length for $4MpyH-Au^{+}Au^{+}Au^{0}$ and $4MpyD-Au^{+}Au^{+}Au^{0}$ model complexes in the pico second time scale are shown in the Figure 8.17 (a, e). The VDOS of the ν_6 [$\beta\,(C-C)/\nu\,(C-S)$] and ν_{12} [Trigonal ring- breathing with $C=S$ deformation] normal mode

Table 8.3: Relevant structural parameters of $4MpyH/\,4MpyD-Au^{+}Au^{+}Au^{0}$ model complexes as obtained from DFT calculations with B3LYP/ 6-31++g(d,p) [for C, H, N and S] / LANL2DZ (for Au atoms) level of theory.

Bond length (in Å)/ bond angle (in degree)	**DFT**	
	4MpyH– $Au^{+}Au^{+}Au^{0}$	**4MpyD–** $Au^{+}Au^{+}Au^{0}$
S1----Au	2.36	2.37
S1 – C2	1.76	1.73
S1 – C2 – C4	116.07	116.67

for $4MpyH-Au^{+}Au^{+}Au^{0}$ and $4MpyD-Au^{+}Au^{+}Au^{0}$ model complexes have been also estimated from WT theory and are also shown in Figure 8.17(b, c) and (f, g) respectively. From Figure 8.17 (a-c) and 8.17 (e-g), it is clearly seen that the vibrational frequencies of the normal modes ν_6 and ν_{12} are significantly downshifted from ~ 728 to 707 cm^{-1} (~ 721 to 710 cm^{-1}) and ~1105 to 1087 cm^{-1} (~1100 to 1091 cm^{-1}) as the Au atom approaches in the close proximity of S1 atom for the 4MPyH (4MPyD) forms of the 4MPy molecule. These results collectively suggest the probable adsorption of S1 atom with Au not only for the 4MPyH and 4MPyD, but for the mixed form of the 4MPy molecule as well. The time resolved vibrational frequencies, as estimated from VDOS, further corroborate the experimentally recorded SERS spectra of the 4MPy molecule, which show significant red shifts of the enhanced vibrational frequencies at ~ 711 and 1092 cm^{-1}

compared to its NRS counterpart at ~ 721 and 1114 cm^{-1} respectively (*vide supra. cf.* Figure 8.9). The discrete snapshots of the 4MPyH----$Au^{+}Au^{+}Au^{0}$ and 4MPyD----$Au^{+}Au^{+}Au^{0}$ model systems

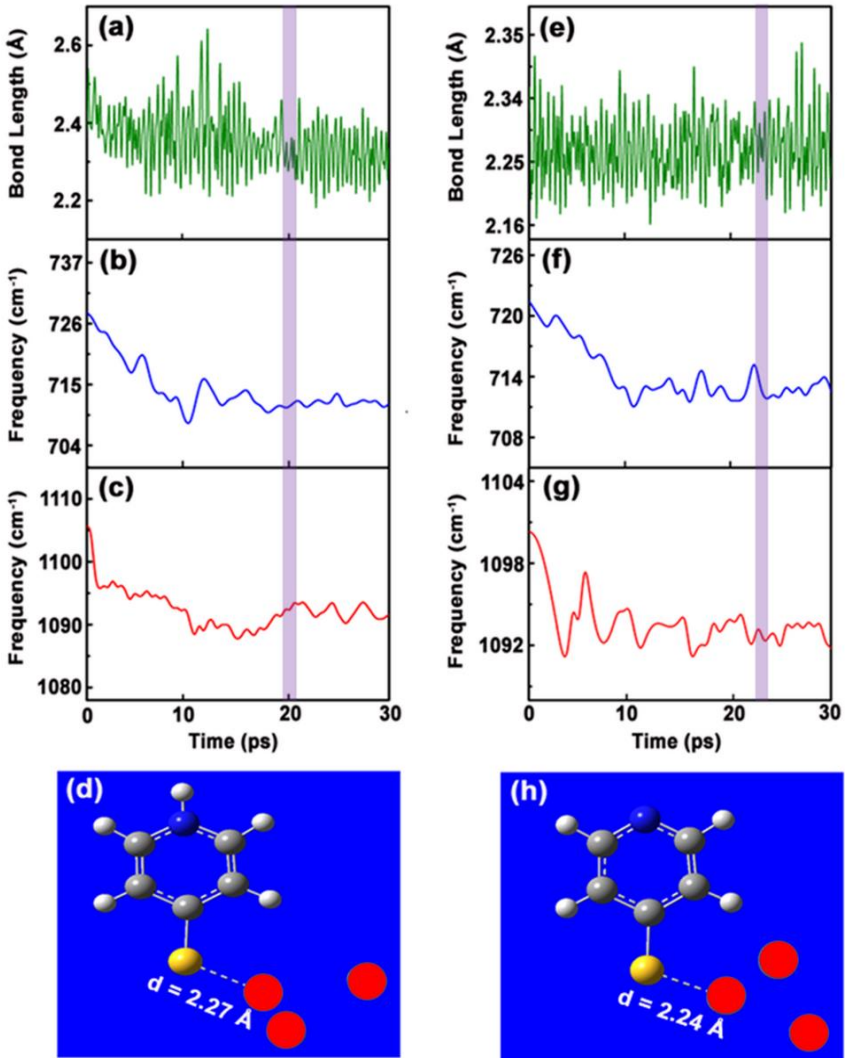

Figure 8.17: Time evolution of Au – S1bond length of (a) 4MPyH – $Au^{+}Au^{+}Au^{0}$ and (e)4MPyH – $Au^{+}Au^{+}Au^{0}$clusters as obtained from BO-OF-MD simulations. Time resolved band stretching frequencies of C2 – S1 bond of (b, c) 4MpyH – $Au^{+}Au^{+}Au^{0}$ and (f, g) 4MPyD – $Au^{+}Au^{+}Au^{0}$ clusters as obtained from Wavelet Transform Theory. Discrete snapshots of the BO-OF-MD simulations for (d) 4MpyH----$Au^{+}Au^{+}Au^{0}$ and (h) 4MpyD----$Au^{+}Au^{+}Au^{0}$ models captured at 20 and 23 pico second time scale respectively at T= 300 K.

captured at 20 and 23 picosecond time scale of the simulation run are shown in Figure 8.17 (d) and (h) respectively. Interestingly, from BO-OF-MD simulations, the Au----S1 distances for 4MpyH----$Au^+Au^+Au^0$/ 4MPyD----$Au^+Au^+Au^0$ model systems are estimated to be 2.27(± 0.017)/ 2.24(± 0.014) Å is in close harmony with that estimated from DFT calculations 2.36/ 2.37 Å for the most probable 4MpyH– $Au^+Au^+Au^0$/ 4MPyD – $Au^+Au^+Au^0$ adcluster models.

The electron densities that are harboured in the 4MPyH, 4MPyD molecule and in the $Au^+Au^+Au^0$ metal cluster models are shown in Figure 8.18 (a), (b) and (c) respectively. From Figure 8.18 (a) and (b), it is clearly seen that the electron densities are strongly localized on C, N and S atoms of the respective aromatic rings of the 4MPyH and 4MPyD molecule. The electron densities for the $Au^+Au^+Au^0$ clusters are however confined on the Au atoms [Figure 8.18 (c)]. Figure 8.18 (d) and (e) shows the EDDs that are perceived in 4MPyH – $Au^+Au^+Au^0$ and 4MPyD – $Au^+Au^+Au^0$ molecule-Au cluster models respectively. Figure 8.18 (d) and (e) clearly

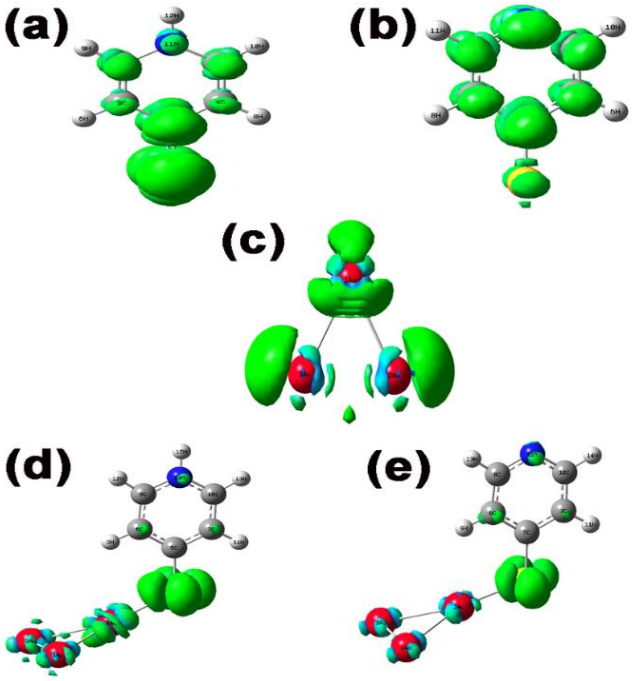

Figure 8.18: Electron density of (a) 4MPyH, (b) 4MPyD (c) $Au^+Au^+Au^0$ metal and Electronic density differences of (d) 4MPyH – $Au^+Au^+Au^0$ and (e) 4MPyD – $Au^+Au^+Au^0$ adclusters as estimated from B3LYP / 6-31++g(d,p) [for C, H, N and S] / LANL2DZ (for Au atoms) level of theory (iso surface value = 0.005 a.u).

reveals depletion of charge clouds on the respective aromatic rings of 4MPyH and 4MPyD molecules and accumulation of electron density clouds on their respective S atoms and on the Au atoms of the adclusters. These observations may signify appreciable shifts of electron clouds from the aromatic rings of the molecule to the Au metal atoms, there by suggesting molecule → metal CT interaction. The molecule → metal CT contribution to SERS may be envisaged from the broadening and appreciable downshifts of the enhanced Raman bands centered at ~ 711 and 1092 cm^{-1} (*vide supra, cf.* Figure 8.9) whose NRS counterparts are recorded at 723 and 1114 cm^{-1} [*vide supra*, *cf.* Figure 8.11] respectively [57]. Moreover, selective enhancements and considerable shifts of the Raman bands at ~ 1582 and 1608 cm^{-1} in the SERS spectra further signify the involvement of CT interaction in the overall enhancement of the Raman bands of 4MPy molecule [48].

8.3 Conclusion

Facile fabrication of an efficient and reproducible SERS active substrate has been reported through the integration of self-assembly and LB deposition techniques. Efficacy of the as fabricated substrate has been tested from the SERS spectra of 4MPy molecule upon adsorption with the metallic AuNPs entrapped within the bilayer LB film template of SA. The wide range survey scan XPS spectrum for the M-APS is noticeably different compared to the APS signifying considerable interaction of 4Mpy with the embedded AuNPs. Detail analysis of the XPS and SERS spectral features further indicate the adsorption of 4MPy molecule with the AuNPs via the sulfur atom of the analyte 4MPy molecule. The experimental observations are corroborated by BO-OF-MD, time resolved wavelet transform theory and DFT calculations based on analyte molecule-metal adcluster models. The time resolved vibrational frequency calculations reveal that the 711 and 1092 cm^{-1} bands are significantly down shifted compared to its NRS counterparts as the Au atom approaches close to the sulfur atom of the analyte 4MPy molecule. The direction of the CT interaction towards the overall SERS enhancement in case of the 4MPy-Au complex has been estimated from the EDD calculations.

References

1. M. Fleischmann, P. J. Hendra, A. J. McQuillan, *Chem. Phys. Lett*., 1974, **26**, 163.
2. S. K. Das, T. S. Bhattacharya, M. Ghosh, J. Chowdhury, *New. J. Chem*., 2021, **45**, 2670.

3. G. Cabello, K. C. Nwoko, J. F. Marco, M. Sanchez-Arenillas, A. M. Mendez-Torres, J. Feldmann, C. Yanez, T. A. D. Smith., *J. Alloys and Compounds*, 2019, **791**, 184.
4. S. Yadav, M. A. Sadique, P. Ranjan, N. Kumar, A. Singhal, A. K. Srivastava, R. Khan, *ACS Appl. Bio Mater*., 2021, **4**, 2974.
5. C. Fan, X. J. Zhang, M. Lv, J. Bai, Z. Qiu, Y. M. Zhao, Z. L. Wu, H. J. Xu, *Anal. Methods*, 2021, **13**, 3274.
6. A. Pramanik, Y. Gao, S. Patibandla, D. Mitra, M. G. McCandless, L. A. Fassero, K. Gates, R. Tandon, P. C. Ray, *Nanoscale Adv*., 2021, **3**, 1588.
7. M. Lee, K. Oh, H. K. Choi, S. G. Lee, H. J. Youn, H. L. Lee, D. H. Jeong, *ACS Sens*., 2018, **3**, 151.
8. D. B. Grys, B. D. Nijs, A. R. Salmon, J. Huang, W. Wang, W. H. Chen, O. A. Scherman, J. J. Baumberg, *ACS Nano*, 2020, **14**, 8689.
9. M. Muniz-Miranda, F. Muniz-Miranda, A. Pedone, *Chem. Select*, 2018, **3**, 8698.
10. M. Muniz-Miranda, F. Muniz- Miranda, S. Caporali, S. Calisi, A. Pedone, *Appl. Surf. Sci*., 2018, **457**, 98.
11. A. Tsunoi, G. Lkhamsuren, E. A. Q. Mondarte, S. Asatyas, M. Oguchi, J. Noh, T. Hayashi, *J. Phys. Chem. C*, 2019, **123**, 13681.
12. M. Muhammad, C. Shao, Q. Huang, *Spectrochem. Acta Part A*, 2019, **223**, 117282.
13. X. Su, Y. Xu, H. Zhao, S. Li, L. Chen, *Talanta*, 2019, **194**, 903.
14. H. Wang, Z. Xue, Y. Wu, J. Gilmore, L. Wang, L. Fabris, *Anal. Chem*., 2021, **93**, 9373.
15. M. Velicka, E. Zacharovas, S. Adomaviciute, V. Sablinskas, *Spectrochem. Acta Part A*, 2021, **246**, 118956.
16. D. Q. Dao, T. C. Ngo, T. T. H. Le, Q. T. Trinh, T. L. A. Nguyen, B. T. Huy, N. N. Trei, N. T. Trung, M. T. Nguyen, *J. Phys. Chem. A*, 2021, **125**, 8529.
17. T. C. Ngo, Q. T. Trinh, N. T. T. An, Tri, N. T. Trung, D. H. Truong, B. T. Huy, B. T. Nguyen, D. Q. Dao, *J. Phys. Chem. C*, 2020, **124**, 21702.
18. R. L. Birke, J. R. Lombardi, W. A. Saidi, P. Norman, *J. Phys. Chem. C*, 2016, **120**, 20721.

19. I. Lopez-Tocon, S. Valdivia, J. Soto, J. C. Otero, F. Muniz-Miranda, M. C. Menziani, M. Muniz-Miranda, *Nanomat*., 2019, **9**, 1211.
20. A. Zoppi, S. Caporali, F. Muniz-Miranda, A. Pedone, M. Muniz-Miranda, *ACS Appl. Nanomater.*, 2019, **2**, 7319.
21. R. Wang, X. R. Shen, M. Zhang, R. Devasenathipathy, R. Pang, J. Zhang, J. Ulstrap, Z. Q. Tian, *J. Phys. Chem. C*, 2019, **123**, 23026.
22. S. Dutta Roy, M. Ghosh, J. Chowdhury, *J. Phys. Chem. C*, 2018, **122**, 10981.
23. E. C. Le Ru, C. Galloway, P.G. Etchegoin, *Phys. Chem. Chem. Phys*., 2006, **8**, 3083.
24. S. K. Das, T. S. Bhattacharya, J. Chowdhury, *Phys. Chem. Chem. Phys*., 2020, **22**, 8719.
25. S. K. Das, S. Saha, M. Ghosh, J. Chowdhury, *Vib. Spectrosc*., 2020, **107**, 103031.
26. R. Chadha, A. Das, A. K. Debnath, S. Kapoor, N. Maiti, *Col. Surf. A*, 2021, **615**, 126279.
27. S. Caporali, F. Muniz-Miranda, A. Pedone, M. Muniz-Miranda, *Sensors*, 2019, **19**, 2700.
28. G. Gabka, P. Bujak, K. Giedyk, K. Kotwica, A. Ostrowski, K. Malinowka, W. Lisowski, J. W. Sobczak, A. Pron, *Phys. Chem. Chem. Phys*., 2014, **16**, 23082.
29. C. Su, Z. Lu, H. Zao, H. Yang, R. Chen, *Appl. Surf. Sci*., 2015, **353**, 735.
30. E. Desimoni, B. Brunetti, *Chemosensors*, 2015, **3**, 70.
31. J. W. Park, J. S. Shumaker-Parry, *ACS Nano*, 2015, **9**, 1665.
32. Z. Wang, X. Shen, Y. Yan, T. Qian, J. Wang, Q. Sun, C. Jin, *Appl. Surf. Sci*., 2018, **450**, 387.
33. C. Li, B. Xie, Z. He, J. Chen, Y. Long, *Renewable Energy*, 2019, **140**, 862.
34. M. A. Mahmoud, C. E. Tabor, M. A. El- Sayed, *J. Phys. Chem. C*, 2009, **113**, 5493.
35. J. R. Heath, C. M. Knoblerdaniel, V. Leff, *J. Phys. Chem. B*, 1997, **101**, 189.
36. Y. Wang, Z. Sun, Y. Wang, H. Hu, B. Zhao, W. Xu, J. R. Lombardi, Spectrochem. *Acta Part A*, 2007, **66**, 1199.
37. H. L. Zhang, S. D. Evans, J. R. Henderson, R. E. Miles, T. Shen, *J. Phys. Chem. B*, 2003, **107**, 6087.
38. S. Herrera, F. Tasca, F. J. Williams, E. J. Calvo, P. Carro, R. C. Salvarezza, *Langmuir*, 2017, **33**, 9565.
39. Q. Liu, T. Liu, Q. F. Fang, F. J. Liang, J. X. Wang, *Thin Solid Films*, 2006, **503**, 79.

40. D. Chen, S. Wang, Z. Zhang, H. Quan, Y. Wang, Y. Jiang, M. J. Hurlock, Q. Zhang, *Environ. Sci.: Nano*, 2020, **7**, 1205.
41. S. Saha, M. Ghosh, J. Chowdhury, *J. Raman Spectrosc*., 2019, **50**, 330.
42. H. S. Jung, K. Kim, M. S. Kim, *J. Mol. Struc*., 1997, **407**, 139.
43. J. Hu, B. Zhao, W. Xu, B. Li, Y. Fan, *Spectrochem. Acta Part A*, 2002, **58**, 2827.
44. K. Kishore, G. R. Dey, D. B. Naik, Res. *Chem. Intermed*., 2002, **28**, 29.
45. J. A. Baldwin, B. Vlckova, M. P. Andrews, I. S. Butler, *Langmuir*, 1997, **13**, 3744.
46. X. Fu, F. Bei, X. Wang, X. Yang, L. Lu, *J. Raman Spectrosc*., 2009, **40**, 1290.
47. Y. Chao, Q. Zhou, Y. Li, Y. Yan, Y. Wu, J. Zheng, *J. Phys. Chem. C*, 2007, **111**, 16990.
48. M. Pradhan, J. Chowdhury, S. Sarkar, A. K. Sinha, T. Pal, *J. Phys. Chem. C*, 2012, **116**, 24301.
49. H. Guo, L. Ding, Y. Mo, *J. Mol. Struc*., 2011, **991**, 103.
50. A. Otto, J. Billmann, J. Eickmans, U. Erturk, C Pettenkofer, *Surf. Sci*., 1984, **138**, 319.
51. R. Chadha, A. Das, S. Kapoor, N. Maiti, *J. of Mol. Liq*., 2021, **322**, 114536.
52. E. A. Ramirez, E. Cortes, A. A. Rubert, P. Carro, G. Benitez, M. E. Vela, R. C. Salvarezza, *Langmuir*, 2012, **28**, 6839.
53. D. Roy, T. E. Furtak, *Phys. Rev. B Condens Matter*., 1986, **34**, 5111.
54. M. Pagliai, S. Caporali, M. Muniz-Miranda, G. Pratesi, V. Schettino, *J. Phys. Chem. Lett*., 2012, **3**, 242.
55. N. Maiti, R. Chadha, A. Das, S. Kapoor, *RSC Adv*., 2016, **6**, 62529.
56. M. Muniz- Miranda, F. Muniz-Miranda, A. Pedone, *Phys. Chem. Chem. Phys*., 2016, **18**, 5974.
57. J. Chowdhury, J. Sarkar, T. Tanaka, G. B. Talapatra, *J. Phys. Chem. C*, 2008, **112**, 227.

Conclusion and future plans of the research work

Conclusion

Fabrication of highly sensitive and reproducible SERS active substrates on metallic nanocolloids entrapped in the monolayer/ bilayer Langmuir- Blodgett (LB) film matrix of Poly(methyl-methacrylate) [PMMA]/ Stearic acid (SA) molecules have been reported. The SERS efficacies of the as prepared substrates have been verified with various concentrations of Rhodamine 6G (R6G) and 4-Mercaptopyridine (4MPy) molecules. Enormous enhancement factors ranging from ~ $10^4 - 10^{13}$ orders of magnitude have been estimated for the characteristic vibrational signatures of R6G and 4MPy molecules. This colossal enhancement factors also substantiate the superiority of the as prepared SERS active substrates. The optical responses and the morphological features of the substrates are envisaged using UV- Vis absorption spectra and FESEM, AFM images respectively. The plasmonic architectures of the SERS active substrates have been altered at will to control the hot spots and hence the overall enhancements of SERS signal. Correlations have been drawn between the SERS efficacies and the corresponding surface morphologies, fractal dimensions and roughness features of the as prepared substrates. The spatial distributions of the $|\vec{E}|$ fields around the aggregated geometries of the plasmonic nanoparticles have been estimated with the aid of Three-Dimensional Finite Difference Time Domain (3D-FDTD) simulation studies. The topographical features of the SERS active substrates have been envisaged from statistical considerations in terms of lateral correlation length (ξ), Hurst or roughness exponents (α), root mean square surface roughnesses (ω) and fractal dimensions (D_f). Moreover, correlations have been drawn between the topographical features of the substrates with their corresponding SERS responses. The adsorptive behaviour of the analyte 4MPy molecule with the AuNPs entrapped in the monolayer LB film template of SA has been envisaged using the SERS and XPS characterization techniques. The experimental observations have been further substantiated with the aid of Born-Oppenheimer on the fly dynamics (BO-OF-MD), Time–Resolved Wavelet Transform (WT) theory and Density Functional Theory (DFT) simulations. The direction of the charge transfer (CT) mechanism has been estimated from the Electron Density Difference (EDD) calculations.

Future plans of the research work

Efforts will be given to use the as fabricated SERS active substrates as “Lab on a chip” for the sensing of various pesticides, drugs and real-world sensing applications. More efforts will be made to fabricate template driven SERS active substrates of varying surface roughnesses by changing the LB film templates using binary mixtures of various fatty acids (ca. Stearic acid, Arachidic acid etc) and polymer molecule (ca. PMMA, Chitosan etc) at different molar ratios. The morphological features and relative merits of those SERS active substrates will be investigated from various experimental and theoretical considerations. Also, Multifractal Detrended Fluctuation Analysis (MFDFA) will be introduced to decipher the multifractal features of the as prepared SERS substrates. Moreover, substrates containing smooth surfaces, which are known to exhibit poor SERS signals, will also be explored to correlate with the MF-DFA results. Furthermore, the synthesis of 2D Transition Metal Dichalcogenides (TMDs) and fabrication of efficient and reproducible SERS active substrates using the 2D-TMDs materials will be the keen interest of future research.

APPENDIX

List of publications

1. Self-assembly of silver nanocolloids in the Langmuir- Blodgett Film of stearic acid: Evidence of an efficient SERS sensing platform; **Somsubhra Saha**, Manash Ghosh, Bipan Dutta, Joydeep Chowdhury. *Journal of Raman Spectroscopy*, 2016, **47**, 168 - 176.

2. Silver coated gold nanocolloids entrapped in organized Langmuir- Blodgett Film of stearic acid: Potential evidence of a new SERS active substrate; **Somsubhra Saha**, Manash Ghosh, Bipan Dutta, Joydeep Chowdhury. *Applied Surface Science*, 2016, **362**, 364 - 373.

3. Infused self- assembly on Langmuir–Blodgett Film: Fabrication of highly efficient SERS active substrates with controlled plasmonic aggregates; **Somsubhra Saha**, Manash Ghosh, Joydeep Chowdhury. *Journal of Raman Spectroscopy*, 2019, **50**, 330 - 344.

4. Decoding the topographical features of more realistic SERS active substrates in presence of the probe molecules from statistical considerations: An in-depth study bridging Microscopy with Spectroscopy; **Somsubhra Saha**, Manash Ghosh, Subhendu Chandra, Joydeep Chowdhury. *Colloids and Surfaces A: Physicochemical and Engineering Aspects*, 2021, **628**, 127319-127330.

5. Adsorption of 4-Mercapto Pyridine with Gold Nanoparticles embedded in the Langmuir-Blodgett Film matrix of stearic acid: SERS, XPS studies aided by Born-Oppenheimer on the fly dynamics, Time –Resolved Wavelet Transform Theory and DFT; **Somsubhra Saha**, Bipan Dutta, Manash Ghosh, Joydeep Chowdhury **(*Communicated*)**.

6. How SERS responses of probe molecules depend on topographies of the substrates? A vis-à-vis exploration; Sumit Kumar Das, **Somsubhra Saha**, Manash Ghosh, Joydeep Chowdhury. *Vibrational Spectroscopy*, 2020, **107**, 103031 – 103038. ***(Not included in this thesis)***.

Papers presented in National/ International Conferences/ Symposium (Selected List)

1. Self-assembly of Au@Ag nanocolloids in the organised Langmuir-Blodgett film of DPPC: Evidence of an efficient SERS sensing platform; **Somsubhra Saha**, "Some recent trends in research in Physics" held on 21st March 2018 at Department of Physics, Jadavpur University, India. **(Poster Presentation)**

2. Self-assembly of metal nanocolloids entrapped in Langmuir-Blodgett Film templates: Evidence of efficient SERS sensing platforms; Joydeep Chowdhury, **Somsubhra Saha**, Manash Ghosh. *Materials Today: Proceedings*, 2018, **5**, 10071–10076.

3. Controlled Aggregation of Gold NanoParticles in the Langmuir-Blodgett Film Matrix of PMMA: An Efficient SERS Sensing Platform with Unique Molecular Selectivity; **Somsubhra Saha**, "7th International Conference on Perspectives in Vibrational Spectroscopy (ICOPVS 2018) held on 25 -29 November, 2018 at BARC Mumbai, India. **(Poster Presentation)**

4. Overcoming the SERS uncertainty principle: Fabrication of highly reproducible SERS active substrate with controlled plasmonics; **Somsubhra Saha**, International Conference on "90 Years of Raman Effect: Current Status and Future Directions" held on 27th February –2nd March 2018 at Indian Institute of Science, Bengaluru, India. **(Poster Presentation)**

5. Decoding the self-affine properties of SERS active substrates: Experimental vis à vis theoretical investigations; **Somsubhra Saha**, "VISPEC 2019: Emerging Trends in Vibrational Spectroscopy" held on 11th-13th September, 2019 at University of Brescia Engineering Campus, Brescia, Italy. **(Poster Presentation)**

6. Investigation of surface parameters of self-affine surfaces on SERS response; **Somsubhra Saha**, **"**National Seminar on Emerging Frontiers in Materials Science" held on 14 -15 February, 2019 at Behala College, Kolkata, India. **(Oral Presentation)**

Research article

Journal of RAMAN SPECTROSCOPY

Received: 3 April 2015 Revised: 20 July 2015 Accepted: 21 July 2015 Published online in Wiley Online Library: 24 August 2015

(wileyonlinelibrary.com) DOI 10.1002/jrs.4771

Self-assembly of silver nanocolloids in the Langmuir–Blodgett Film of stearic acid: Evidence of an efficient SERS sensing platform

Somsubhra Saha,[a] Manash Ghosh,[b] Bipan Dutta[a] and Joydeep Chowdhury[a]*

Highly sensitive surface-enhanced Raman scattering active substrate obtained by self-assembly of silver nanocolloids (AgNCs) in the bilayer Langmuir–Blodgett (LB) film of stearic acid (SA) has been reported. Rhodamine 6G (R6G) has been used as the probe molecule to test the efficacy of the *as prepared* substrate. Gigantic enhancement factors ~10^{12} orders of magnitude have been estimated from the surface-enhanced resonance Raman scattering [SER(R) S] spectrum of R6G, which proves that the *as prepared* substrate is superior or comparable with silver nanoparticle as dried AgNC solutions on microscopic slides. The optical properties of the *as prepared* substrates have been envisaged by ultraviolet-visible absorption spectra, while their morphological features are mapped through field emission scanning electron microscopy (FESEM) and atomic force microscopy (AFM) images. A correlation has been drawn between the SER(R) S efficacy and the corresponding FESEM and AFM images of the *as prepared* substrates. Electric field distributions around the aggregated AgNCs have been estimated with the aid of three-dimensional finite difference time domain simulation studies. Localized surface plasmon coupling between the nanoaggregated geometries may be altered by lifting the LB film of SA at various surface pressures. Copyright © 2015 John Wiley & Sons, Ltd.

Additional supporting information may be found in the online version of this article at the publisher's web-site.

Keywords: Langmuir–Blodgett film; silver nanocolloid; surface-enhanced resonance Raman scattering; rhodamine 6G; 3D-FDTD

Introduction

Surface-enhanced Raman scattering (SERS) is a powerful and surface-sensitive tool that enhances Raman signals of probe molecules when they are adsorbed on the rough nanostructure surfaces.[1–3] It enables one to determine the molecular orientations as well as to detect trace concentrations of molecules down to single molecule detection limit.[4–7] The origin of SERS is still unclear. However, it is widely recognized that both the electromagnetic (EM) and charge transfer mechanisms are concurrently responsible for this enormous enhancement.[8,9] The long-range EM enhancement is more dominant and originates from the excitation of localized surface plasmons.[10] On the other hand, the short-range chemical enhancement mechanism arises from the interaction between the metal and the adsorbate molecules.[11]

Noble metallic nanoparticles of different geometries[12–20] have been used for the fabrication of SERS active substrates because of their interesting tunable plasmonic behaviors and prospective applications. Among many different noble metals, silver nanoparticles (AgNPs) have been established as an efficient SERS active substrate since decades.[21,22] There has been an incessant wave in this area of research aiming towards the fabrication of novel and efficient SERS active substrates, which can be readily used for trace analysis and ultrasensitive detection.

Since the pioneering work of Aroca *et al.*,[23–25] the Langmuir–Blodgett (LB) technique has been successfully utilized to record the SERS spectra of texas red, perylene, methacrylate, phthalocyanine, xanthene derivatives adsorbed on island films and silver-coated tin spherical surface.[26–30] In these reports, the LB films have been used as integral parts of molecular architectures for SERS active substrates.

Interestingly, SERS spectra of the LB films of hemicyanine dye and 2-amino nitropyridine molecules adsorbed on smooth copper surfaces had been reported.[31] Recently, Ozaki *et al.*[32] reported an ionic surfactant-mediated LB method to fabricate gold nanoparticle films for SERS. El-Sayed *et al.*[33] estimated the SERS enhancement of poly(vinyl) pyrrolidone molecules from aggregated silver nanocubes assembled via LB technique. Yang *et al.*[34] applied LB technique to assemble monolayers of aligned silver nanowires and demonstrated its efficacy as a SERS active substrate. These reports mainly focused on the fabrication of SERS active substrate using LB technique.

Bearing these things in mind, here, we report a different technique to fabricate a novel SERS active substrate through self-assembly of silver nanocolloids (AgNCs) in the bilayer LB film of stearic acid (SA). The electrostatic interaction between the negatively charged acid group of SA and the positively charged AgNC allows the entrapment of the aggregated nanocolloids in the SA matrix. The SERS efficacy of the *as prepared* substrate has been tested with rhodamine 6G (R6G) molecules. Gigantic enhancement factors ranging from 10^7 to 10^{12} orders of magnitude have been estimated. The electric field distributions around the nanoaggregated

* *Correspondence to: Joydeep Chowdhury, Department of Physics, Sammilani Mahavidyalaya, Baghajatin Station, E. M. Bypass, Kolkata 700094, India. E-mail: joydeep72_c@rediffmail.com*

a *Department of Physics, Sammilani Mahavidyalaya, Baghajatin Station, E. M. Bypass, Kolkata 700094, India*

b *Department of Spectroscopy, Indian Association for the Cultivation of Science, Jadavpur, Kolkata 700032, India*

colloids have been envisaged from three-dimensional finite difference time domain simulation studies.

Experimental section

Materials and methods

Spectral grade R6G molecule, ~95% dye content, and SA, >99% purity, were purchased from Sigma-Aldrich and were used as received. Silver nitrate ($AgNO_3$), sodium borohydride ($NaBH_4$), ethanol, and acetone were purchased from E-Merck (Germany) and were used without any further purification. Spectral grade chloroform was purchased from SRL India and was used as received. All the glasswares used in the synthesis were cleaned with freshly prepared aqua-regia and were thoroughly rinsed with distilled water prior to use. The required solutions were prepared using triple distilled water subsequently deionized through Milli-Q-plus system of Millipore Corporation, USA. The pH and the resistivity of the deionized water were 6.8 and 18.2 MΩ cm, respectively.

Prior to the deposition of LB film, the substrates were washed with ethanol, chloroform, and deionized water. The LB film of SA was prepared by Y-type deposition technique in a computer-controlled fully automated Langmuir-Blodgett trough (Model No. D2007, Apex Instruments). Chloroform was used as solvent to prepare the SA solution. Triple distilled deionized water was used as sub-phase. The pressure-area (π-A) isotherm [Fig. S1 (Supporting Information)] of SA was measured with a film balance, and the surface pressure was measured by the Wilhelmy method using a filter paper. SA solution in chloroform solvent was spread drop wise on the water subphase. After a delay of 20 min, the film was compressed slowly till the surface pressure reaches ~30 mN/m. The LB bilayer film was deposited on quartz substrate at a constant surface pressure ~25 mN/m.

First layer of SA in the LB trough was deposited by upstroke, so that the polar COO^- group of SA in the second layer, accomplished by downstroke, can point outwards. AgNCs were prepared according to the recipe as prescribed by Creighton *et al.*[35] Briefly, 5 ml of 1.0×10^{-3} M aqueous solution of $AgNO_3$ was added rapidly to 15 ml ice-cooled aqueous solution of $NaBH_4$ (2.0×10^{-3} M) with vigorous stirring. A stable yellowish colloid is prepared and was kept in 5 °C for 2 weeks before the experimental use. The *as prepared* SA bilayer LB films were then incubated in the AgNCs for 24 h. The films were removed from Ag nanocolloidal solutions, washed repeatedly with deionized water, and were dried in vacuum. The surface morphology and the intrinsic roughness of the *as prepared* substrates were estimated from the field emission scanning electron microscopic and atomic force microscopic studies, respectively. The *as prepared* samples were then dipped in 1.0×10^{-8}, 1.0×10^{-10}, 1.0×10^{-12}, and 1.0×10^{-14} M aqueous solutions of R6G for an extended period of 1 h.

Instrumentation

The absorption spectra were recorded from Jasco UV-Vis Absorption Spectrometer (Model No: V-630). The resonance Raman (RR) and the surface-enhanced resonance Raman scattering [SER(R) S] spectra were recorded by J-Y Horiba Confocal Triple Raman Spectrometer (Model: T 64000) fitted with gratings of 1800 groove/mm and a TE cooled Synapse CCD detector from J-Y Horiba. For recording the RR spectrum, an aliquot containing 100 μl aqueous solution of 1.0×10^{-3} M R6G solution is drop casted on a quartz slide and then allowed to dry. The samples were then excited using a 514.5 nm green line of Ar^+ laser [Spectra Physics, USA (Model. Stabilite2017)] with spot size 1 μm in diameter incident at a power ~60 μW on the samples. The scattered signals were collected at 180° scattering angle to the excitations from an Olympus open stage microscope of 10 times objective. The detector and the data acquisition were controlled by Lab Spec 5 software as provided by Horiba. The acquisition times for recording both the RR and SER(R) S spectra were fixed at 20 s. The baseline corrections of the spectra have been performed with the tool option as implemented in the Microcal Origin version 7.0 suits of software. The reproducibility of the SERS spectra has been tested around the hot spots through rastering around the film surface. The surface morphology of the LB films was observed by field emission scanning electron microscopy (FESEM) (JEOL JSM 7600F) at 15 kV excitation energy. The surface roughnesses of the *as prepared* samples were imaged by atomic force microscopy (AFM) (Vecco dilnnova), operated in the tapping mode. Antimony doped silicon tip with typical resonant frequency 300 kHz, force constant 40 N/m, was used.

Theoretical model

The spatial distributions of electric fields, around the nanoparticle aggregates, were estimated from three-dimensional finite difference time domain simulations, with the aid of Lumerical Solutions, Inc.[36] The dimension of the Yell cell for the simulation run was fixed at $1\times1\times1$ nm^3. The dielectric function for silver was imported from the Johnson–Christy data, and water with real refractive index 1.33 was chosen for the background medium. The models chosen for the simulations were excited with plane polarized light of wavelength 514.5 nm whose amplitude of electric field is 1 V/m. Perfectly matched layer boundary condition was introduced to avoid reflection and back scattering of electric field from the pre-selected boundary. The durations of all the simulations were fixed at 500 fs to ensure full convergence of the calculations. The fractal dimensions were estimated using 'Image J'[37] software considering around 300–350 nanoparticles.

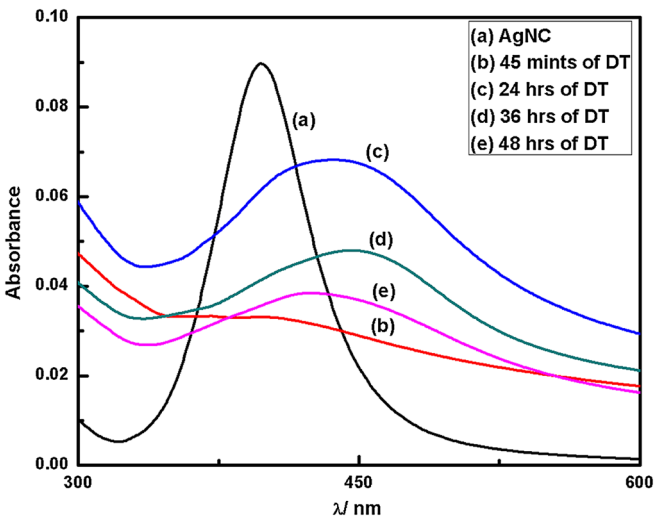

Figure 1. Room temperature ultraviolet-visible electronic absorption spectra of (a) silver nanocolloid (AgNC) and [(b)–(e)] AgNC self-assembled in the bilayer Langmuir–Blodgett film of stearic acid at various dipping times (DTs).

Results and discussions

Pressure-area isotherm of Langmuir monolayer

Room temperature surface pressure (π) – area (A) compression isotherm of a Langmuir monolayer of SA in pure water sub-phase has been recorded and is shown in Fig. S1 (Supporting Information). The nature of the isotherm is in accordance with that reported elsewhere.[38] The area/SA molecule is estimated to be ~0.22 (nm^2)/molecule. Bilayer LB film of SA molecule is then lifted on the pre-cleaned quartz substrate at a constant surface pressure of 25 mN/m by Y-type deposition technique. This preferred technique allows tail–tail architecture thereby favoring the polar COO^- group of SA molecule in the second layer to point outwards. The bilayer LB films of SA were subsequently dipped in the *as synthesized* nanocolloidal silver solutions at various dipping times (DTs) ranging from 45 min to 48 h. The bilayer LB films were then repeatedly washed with deionized water to remove the excess silver ions that may get adsorbed on the surface of the SA films and are allowed to dry in a vacuum chamber.

Absorption spectrum of the *as prepared* substrates

Figure 1 shows the room temperature ultraviolet-visible electronic absorption spectrum of AgNCs. The yellowish AgNC shows a single

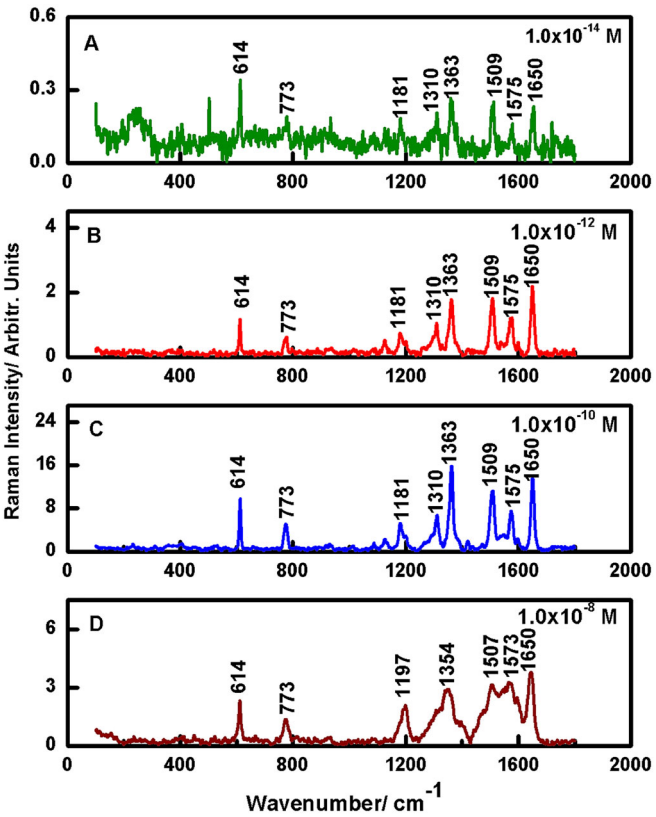

Figure 2. Surface-enhanced resonance Raman scattering spectra of rhodamine 6G molecule at varied concentrations of the adsorbate (λ_{ex} = 514.5 nm).

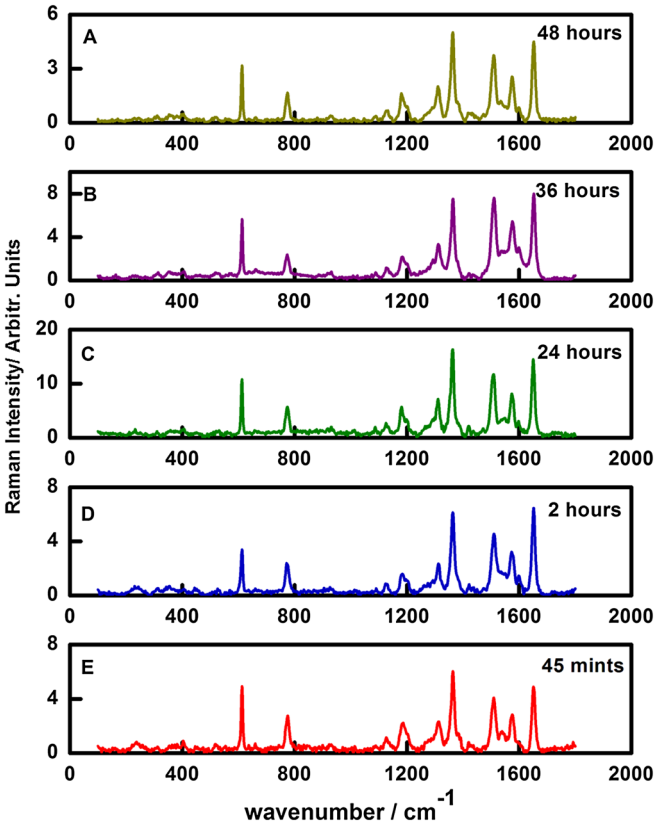

Figure 3. Surface-enhanced resonance Raman scattering spectra of rhodamine 6G molecule at various dipping times (λ_{ex} = 514.5 nm).

Table 1. Analytical enhancement factors of SER bands of R6G molecule adsorbed on the *as prepared* substrates

NRS (cm^{-1})	Adsorbate concentrations								Assignment
	10^{-8} M		10^{-10} M		10^{-12} M		10^{-14} M		
	SERS	AEF	SERS	AEF	SERS	AEF	SERS	AEF	
614	614	2.01×10^{7}	614	6.69×10^{9}	614	6.05×10^{10}	614	1.99×10^{12}	α (C–C–C)
776	773	1.95×10^{7}	773	6.79×10^{9}	773	7.31×10^{10}	773	1.07×10^{12}	γ (C–H)
1187	1197	2.12×10^{8}	1181	3.40×10^{10}	1181	1.51×10^{11}	1181	6.52×10^{12}	β (C–H)
1312	—	—	1310	5.78×10^{10}	1310	1.42×10^{11}	1310	8.81×10^{12}	
1365	1354	1.04×10^{8}	1363	1.16×10^{10}	1363	9.10×10^{10}	1363	4.57×10^{11}	ν (C–C)
1509	1507	5.73×10^{7}	1509	8.77×10^{10}	1509	1.49×10^{12}	1509	6.02×10^{12}	ν (C–C)
1575	1573	6.59×10^{7}	1575	1.98×10^{10}	1575	4.20×10^{11}	1575	2.44×10^{12}	ν (C–C)
1652	1650	3.68×10^{7}	1650	1.17×10^{10}	1650	1.92×10^{11}	1650	8.08×10^{11}	ν (C–C)

AEF, analytical enhancement factor; SERS, surface-enhanced Raman scattering; R6G, rhodamine 6G.
α, β: in-plane bending; γ: out-of-plane bending; ν: stretching.

absorption maximum centered at ~397 nm, characteristic of Localized Surface Plasmon Resonance (LSPR).[35] However, the absorption spectra of AgNC self-assembled in the bilayer LB film of SA at various DTs (also shown in the same figure) exhibit broad and structureless features. The LSPR band of AgNC self-assembled in the bilayer LB film of SA undergoes progressive bathochromic shift with the change in the DTs from 45 min to 36 h. The general broadening of the absorption spectra may signify the possibility of silver nanocolloidal aggregates to get entrap in the bilayer LB film of SA. The rationale towards the formation of these hot aggregated geometries may be due to the neutrality of surface charges from the carboxylic ($COOH^-$) head group of SA with the unneutralized positive charges of AgNCs.[39] Strong dipole dipole coupling between the aggregated nanoparticles may be the reason for the featured red shift. However, after 48 h of DT, the LSPR band undergoes hypsochromic shift, and absorption maximum is shifted at ~421 nm. This down shift exhibited by the films may be due to the decrease in dielectric constant for metal nanoparticles surrounded by the neighboring nanoparticles.[33]

SER(R) S study and enhancement factor of Raman bands

The concentration-dependent SER(R) S spectra of R6G molecule adsorbed on AgNC dipped in bilayer LB film of SA for 24 h are shown in Fig. 2. The optical absorption maximum of R6G ~525 nm in concurrence with the availability of the laser excitation source at ~514.5 nm allows us to record the SER(R) S spectra of the molecule. The SERS spectra of R6G molecule at varied concentrations of the adsorbate under off resonant condition are also recorded with 632.8 nm red laser excitation source. The representative SERS spectra of R6G molecule at three different concentrations of the adsorbate with 632.8 nm laser excitation source are shown in Fig. S2 (Supporting Information). The spectra exhibit background noise with considerable low signal-to-noise ratio in comparison with that recorded with 514.5 nm excitation source.

Figure S3 (Supporting Information) shows the variations in intensities of 614, 773, 1363, 1509, 1575, and 1650 cm^{-1} SER(R) S bands with the logarithm of adsorbate concentrations. The SER(R) S spectra at trace concentrations of the adsorbate exhibit enhanced Raman bands characteristic of R6G molecule. The spectra are marked by enhanced Raman bands centered at ~614; 1363, 1509, 1575, 1650, and 773 cm^{-1} ascribed to in-plane α (C–C–C) bending; ν (C–C) stretching and out-of-plane γ (C–H) bending vibrations associated with the xanthenes ring moiety of the R6G molecule, respectively.[40] The adsorbate concentration dependence of SERS bands of R6G molecule, in general, arises from the surface coverage. It is now well established on silver island films and on nanocolloids[41–44] that at extremely low concentrations, the metal surface coverage by the adsorbates is submonolayer. In the absence of sufficient scattering molecules, the SER signals in this range of concentrations are weak. With increase in concentration of the adsorbate, the SERS signal increases and attains a maximum

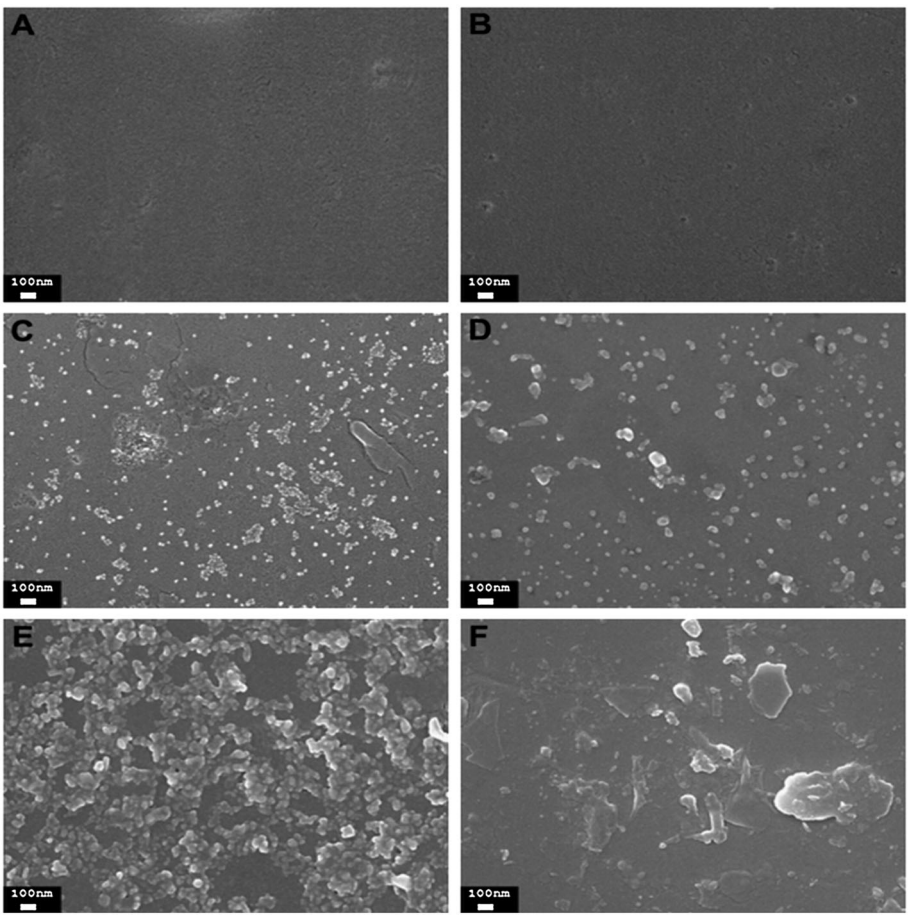

Figure 4. Nanometer scale field emission scanning electron microscopy (FESEM) images of the *as prepared* substrates. (A) Bare quartz slide, (B) bilayer Langmuir–Blodgett (LB) film of stearic acid (SA) lifted at 25 mN/m surface pressure, bilayer LB film of SA incubated in silver nanocolloid at (C) 45 min, (D) 24 h, (E) 36 h, and (F) 48 h of dipping times.

intensity at monolayer coverage, where both electromagnetic and charge transfer contributions to SERS maximize. On further increase in concentration of the adsorbates, multilayers are formed, and the SERS signal decreases in intensity. It therefore seems plausible that the monolayer coverage of the adsorbed R6G molecule may have formed on the *as prepared* substrate at a concentration

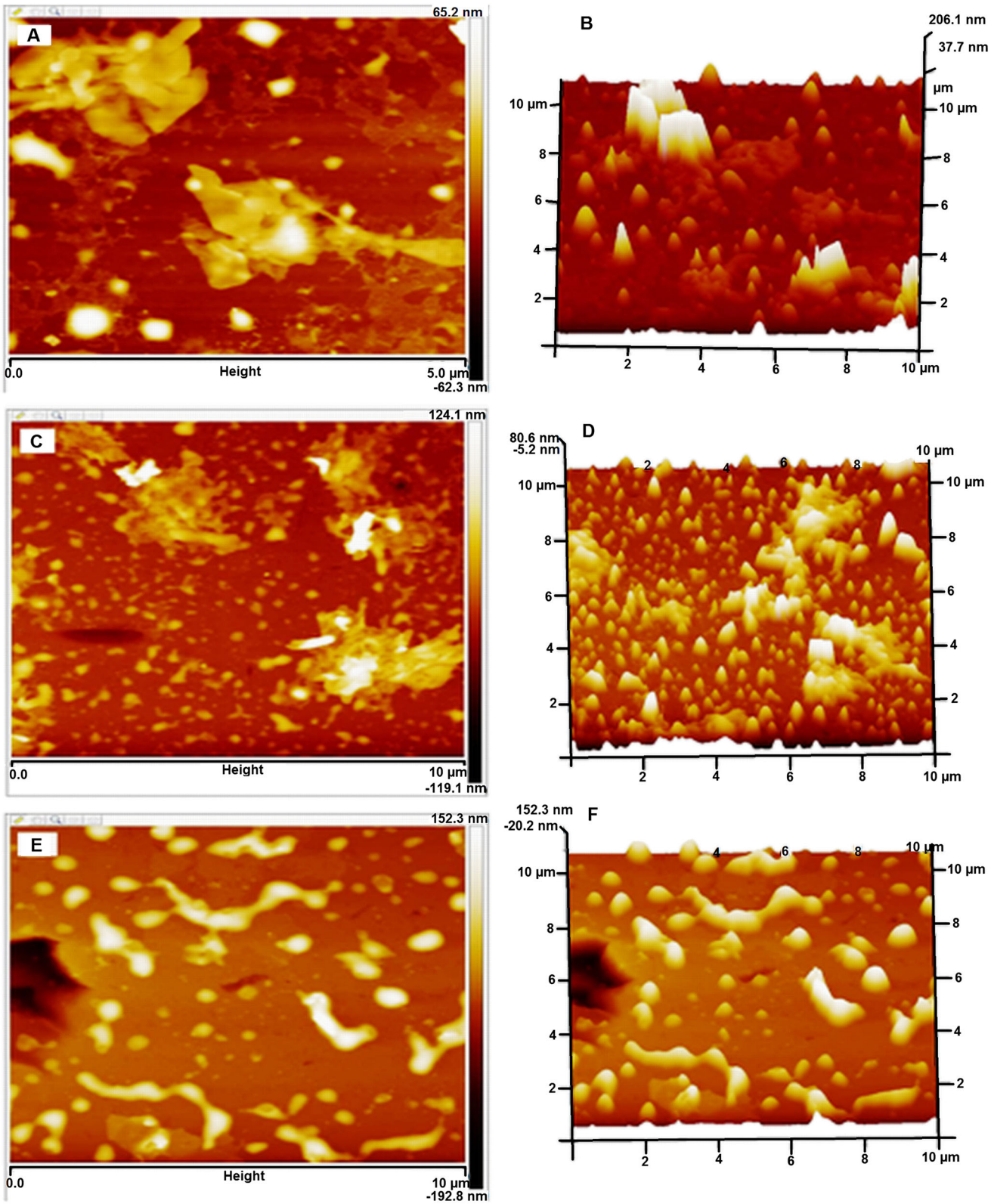

Figure 5. Nanometer scale atomic force microscopy (AFM) images of the *as prepared* substrates. The left column contains topographic two-dimensional AFM images at (A) 45 min, (C) 24 h, and (E) 48 h of dipping times (DTs). The right column shows the three-dimensional AFM images of the same samples at (B) 45 min, (D) 24 h, and (F) 48 h of DTs.

~1.0×10^{-10} M, which shows maximum enhancement of the SER(R)S signals. The analytical enhancement factors (AEFs) of the Raman bands of R6G molecule adsorbed on the *as prepared* substrates have been calculated using the relation[45]

$$AEF = \sigma_{SER(R)S}[C_{RR}]/\sigma_{RR}[C_{SER(R)S}] \quad (1)$$

where C and σ represent the concentration and the integrated peak area of the Raman bands, respectively, measured from baseline. The background corrected RR spectrum of 10^{-3} M R6G in aqueous solution is shown in Fig. S4 (Supporting Information). The AEFs for 614, 773, 1363, 1575, and 1650 cm^{-1} bands of R6G are tabulated in Table 1. Gigantic enhancement factors ranging from 10^7 to 10^{12} orders of magnitude have been estimated for the aforementioned bands.

Figure 3 shows the SER(R)S spectra of 1.0×10^{-10} M R6G adsorbed on bilayer LB film of SA dipped in AgNC at various DTs ranging from 45 min to 48 h. Strong enhancements of 614, 773, 1181, 1310, 1363, 1509, and 1650 cm^{-1} bands, all representing the vibrational signatures of R6G molecule, further substantiate the competence of the *as prepared* substrates as an efficient SERS sensing platform. In this connection, it is worth to mention that the vibrational signatures of R6G molecule exhibit enhancement factors ~3.0×10^5 orders of magnitude and the limit of detection (LOD) ~1.0×10^{-5} M, when AgNCs are adsorbed on silanized glass substrate.[46] Interestingly, self-assembled silver nanoparticle (AgNP) monolayer on glassy carbon exhibit significant SER(R) enhancement of R6G molecule with LOD ~10^{-9} M.[47] Highly efficient SERS active substrate has been reported by immersing mica modified cetyltrimethyl ammonium bromide into AgNC. The LOD of the substrate for R6G is estimated to be ~1.0×10^{-14} M.[48] SERS substrates based on the silicon–hydrogen bond assembly of AgNPs on Si wafer is reported to exhibit vibrational signatures of R6G molecule at 1.0×10^{-12} M concentration of the adsorbate.[49] The AEFs ~10^7–10^{12} orders of magnitude, estimated for the *as prepared* substrate (vide supra), suggest that it is superior or comparable with AgNP as dried AgNC solutions on microscopic slides. The LOD of R6G molecule has been estimated to be 1.0×10^{-14} M, which is reduced by five orders from its practical LOD.[50]

Silver nanoparticles films, as obtained after drying ethanol-induced AgNCs, are reported to behave as an efficient SERS active substrate that can detect R6G in the concentration range 1.0×10^{-10} to 1.0×10^{-14} M.[51] The LOD of the probe molecule on the *as prepared* substrate is also reduced by nine and five orders of magnitude in comparison with R6G on AgNC adsorbed on silanized glass and on AgNP in glassy carbon substrates, respectively.[46,47]

Surface morphology of the *as prepared* substrates

To estimate a correlation between SER(R)S efficacy and the corresponding morphological features, the FESEM and AFM images of the *as prepared* SERS active substrates have been captured. Figure 4 shows the FESEM images of the bare quartz slide, bilayer LB film of SA, and that of SA film incubated in AgNC at various DTs ranging from 45 min to 48 h. The FESEM images of the bilayer LB films of SA dipped in AgNCs at various DTs [Fig. 4(C–F)] smear distinctive entrapment of silver nanocolloidal particles within the SA matrix of the bilayer LB film. From the FESEM images (as shown in Fig. 4), it is seen that the silver clusters entrapped in the bilayer LB film of SA dipped in the colloidal solutions for 45 min and 24 h appear as small fractal aggregates. However, at 36 h of DT, larger aggregates of Ag nanoclusters are recorded, which with further increase in DT (~48 h) twirl to discrete lumps. These changes in the morphological features may be due to the aerial oxidation of silver clusters on the bilayer LB film of SA.[39] The optical responses to these changes in the morphological features of the *as prepared* substrates may result in the broadening of spectral signatures together with the bathochromic and hypsochromic shifts of the LSPR band in the electronic absorption spectra (Fig. 1) as reported earlier (vide supra).

Figure 5 shows the two-dimensional and 3D AFM images of the *as prepared* bilayer LB film of SA incubated in silver nanocolloidal solution at various DTs. The AFM topography images reveal that with the increase in DTs, the initial fractal-like features of the nanoparticles transform towards lumpy structures. The SER(R)S spectrum of 1.0×10^{-10} M R6G, adsorbed on the LB film of SA dipped in AgNCs for 24 h, exhibits the most enhanced Raman bands with high signal-to-noise ratio (Fig. 3). The corresponding 3D AFM image exhibits the entrapment of the aggregated Ag nanoparticles in the SA matrix as sharp tips and definite interparticle spacing. These precise interstitial spacing between the plasmonic nanoparticles may be the probable host for generation of hot spots responsible for gigantic SER(R)S enhancements. The root mean square (RMS) roughnesses of the bilayer LB films of SA incubated in AgNCs at various DTs are estimated using the following relation:

$$Rq = \sqrt{\frac{\sum (Z_i)^2}{N}} \quad (2)$$

where Z_i is the current value of peak-to-valley difference in height within the analyzed region and N is the number of points within the box cursor. The variations in the RMS values of surface roughness of the *as prepared* substrates with various DTs on AgNCs are

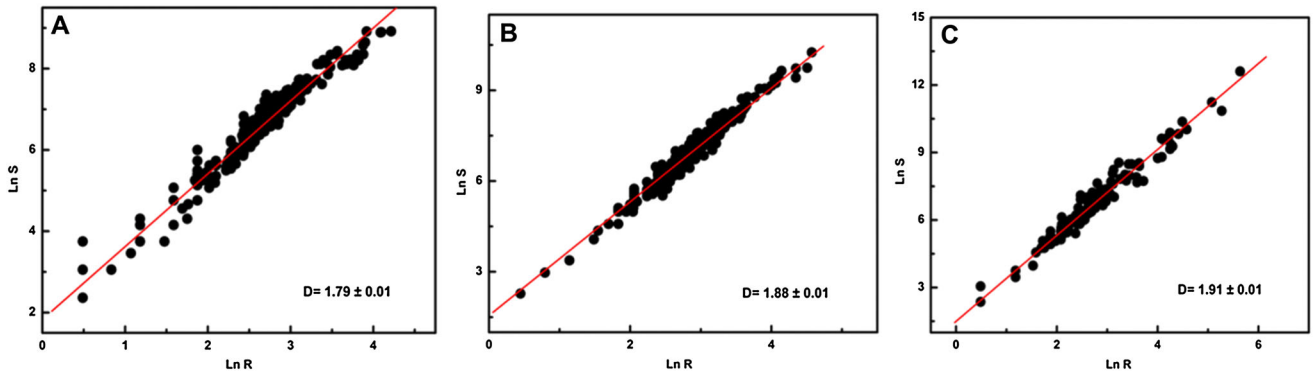

Figure 6. Ln R *versus* Ln S plot of the *as prepared* substrates incubated in silver nanocolloid at (A) 45 min, (B) 24 h, and (C) 48 h of dipping times. The error in the slope determination is coming from the line fitting.

shown in Fig. S5 (Supporting Information). The plot indicates increase in the roughness features of the *as prepared* substrates with the increase in DTs. The RMS roughness of the bilayer LB film of SA dipped for 24 h in AgNC is estimated to be 23.93 nm. This nanometer-ranged RMS roughness may be considered as the benchmark roughness feature for the *as prepared* substrate to generate the most intense vibrational signatures of R6G molecule in the SER(R) S spectrum [Fig. 5(C,D)].

The fractal dimensions of the *as prepared* substrates have also been estimated using the following relation,

$$S \alpha R^D \quad (3)$$

where S is the area of the each structure and R exhibits the average distance from the center of mass of each structure to its perimeter, and D is the Hausdroff dimension.[52] Figure 6 shows ln R *versus* ln S plots of the *as prepared* substrates with various DTs in AgNCs. The slopes of ln R *versus* ln S plot allow one to estimate the desired fractal dimension of the nanoaggregated assembles. The fractal dimensions of the bilayer LB films of SA dipped in AgNC solution for 45 min, 24 h, and 48 h of DTs are estimated to be 1.79 ± 0.01, 1.88 ± 0.01,

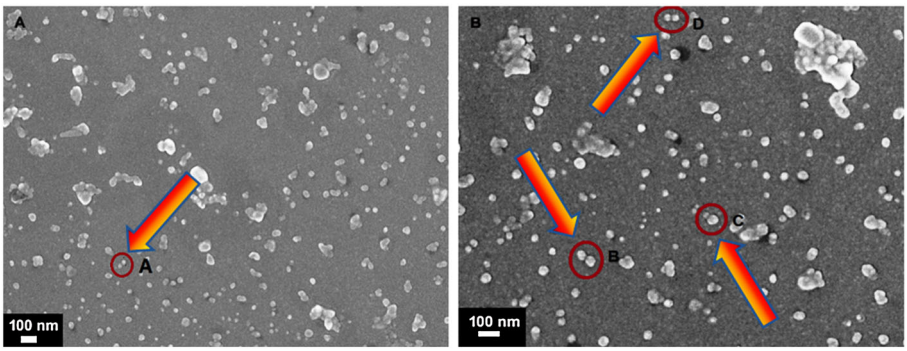

Figure 7. Selected silver nanoaggregated geometries of the *as prepared* substrates as captured from the FESEM images at (A) 30E(03), (B) 50E(03) magnifications used for three-dimensional finite difference time domain simulations.

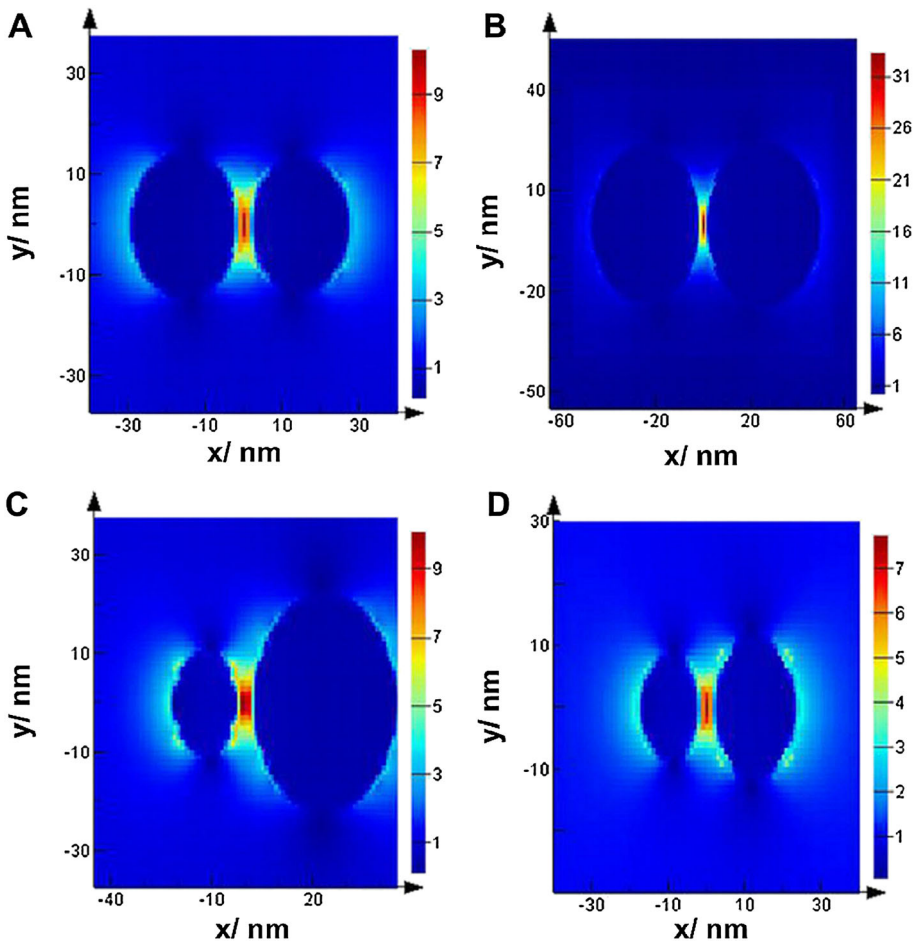

Figure 8. Electric field distribution around the hot spots as estimated from three-dimensional finite difference time domain simulations (λ_{ex} = 514.5 nm, the polarization of the incident light wave is along *x*-axis). The hot spots are envisaged at the regions A, B, C, D from the FESEM images as shown in Fig. 7.

and 1.91 ± 0.01, respectively. These results are in accordance with the morphological features of the self-assembled AgNCs on the bilayer LB film of SA as discussed earlier from the FESEM and AFM images.

Estimation of EM enhancement around the aggregated AgNCs

To envisage a correlation between the hot aggregated geometries of the plasmonic nanoparticles and the huge enhancement factors of the SER(R) S bands, the electric field distributions around the plasmonic nano particles have been estimated. LSPRs of metallic nanostructures can spawn evanescent waves containing high spatial frequency information of the interacting object. These near field waves are the standing waves leading to the confinement of large EM field responsible for the generation of hot spots. The electric fields are estimated directly from the FESEM topography of the *as prepared* bilayer LB film of SA dipped in AgNCs for 24 h. The *as prepared* films are not uniformly hot, it may have cold spots characteristic of the fractal nature of the aggregated nanocolloids.[53] The FESEM image, as shown separately in Fig. 7, however exhibits large number of aggregated structures favorable for the generation of hot geometries. The hottest among the hot spots has been identified for the interparticle gap ~1.7 nm where the spatial distribution of electric field $|\vec{E}|$ ~32 V/m is extended over an approximate length of ~20 nm. The localization of strong $|\vec{E}|$ field corresponds to ~10^6 orders of magnitude enhancement of SER(R) S bands according to the plane wave approximation (Fig. 8). From Fig. 7, it is clearly seen that the simple hetero dimeric spherical aggregates are more evident to generate the hottest spots in comparison with other homo/hetero dimeric or higher-order nanoaggregated structures. However, ~10^7–10^{12} orders of magnitude enhancements (Table 1) for almost all the Raman bands may also signify moderate involvement of resonant and charge transfer mechanism (in addition to the EM contribution) towards the overall enhancement of the SER(R) S bands of the molecule at 1.0×10^{-10} M concentration of the adsorbate.

Conclusions

Silver nanocolloids self-assembled in the bilayer LB film of SA have been established as a promising SERS active substrate. The efficacy of the *as prepared* substrate has been tested with R6G as probe molecule. Gigantic enhancement factors ranging from 10^7 to 10^{12} orders of magnitude have been reported for the characteristic vibrational signatures of R6G molecule. The optical responses, surface morphologies, and the fractal dimensions of the *as prepared* substrates have been estimated. Correlation between the hot aggregated geometries of the plasmonic nanoparticles and the huge enhancement factors of the SER(R) bands has been drawn from 3D-FDTD simulations. The interparticle coupling of the surface plasmons in the nanoaggregated domains may be tuned by lifting the LB film of SA at different surface pressures.

Acknowledgements

Authors express their thanks to the Department of Science and Technology (DST), India, for the financial support through the research projects (project no. SR/ S2/ CMP-0045/ 2012; 2012/ 37P/ BRNS). S. S. would like to thank DST, Govt. of India for the Junior Research Fellowship. Authors would like to thank Professor G. B. Talapatra, Dr Prabir Pal, Indian Association for the Cultivation of Science, Jadavpur, and Mr Dhanpal Jayram Naidu, Department of Nanoscience and Technology, Bharathiar University, Coimbatore for fruitful discussions.

References

[1] M. Fleishmann, P. J. Hendra, A. J. McQuillan, *Chem. Phys. Lett.* **1974**, *26*, 163.
[2] P. L. Stiles, J. A. Dieringer, N. C. Shah, R. P. Van Duyne, *Annu. Rev. Anal. Chem.* **2008**, *1*, 601.
[3] C. L. Haynes, R. P. Van Duyne, *J. Phys. Chem. B* **2003**, *107*, 7426.
[4] H. Liang, Z. Li, W. Wang, Y. Wu, H. Xu, *Adv. Mater.* **2009**, *21*, 1.
[5] M. Takahashi, M. Fujita, M. Ito, *Chem. Phys. Lett.* **1984**, *109*, 122.
[6] T. Vo- Dinh, M. V. K. Hiromoto, G. M. Begun, R. L. Moody, *Anal. Chem.* **1984**, *56*, 1667.
[7] Z. Y. Li, Y. Xia, *Nano Lett.* **2010**, *10*, 243.
[8] S. Chandra, J. Chowdhury, M. Ghosh, G. B. Talapatra, *J. Colloid Interface Sci.* **2013**, *399*, 33.
[9] S. D. Roy, M. Ghosh, J. Chowdhury, *J. Raman Spectrosc.* **2015**, *46*, 451.
[10] J. M. McMahan, S. Li, L. K. Ausman, G. C. Schatz, *J. Phys. Chem. C* **2012**, *116*, 1627.
[11] M. Osawa, N. Matsuda, K. Yoshii, I. Uchida, *J. Phys. Chem.* **1994**, *98*, 12702.
[12] N. R. Jana, T. Pal, *Adv. Mater.* **2007**, *19*, 1761.
[13] C. L. Nehl, H. Liao, J. H. Hafner, *Nano Lett.* **2006**, *6*, 683.
[14] X. Dong, X. Ji, J. Jing, M. Li, W. Yang, *J. Phys. Chem. C* **2010**, *114*, 2070.
[15] M. Y. Tsvetkov, B. N. Khlebtsov, V. A. Khanadeev, V. N. Bagratashvili, P. S. Timashev, M. I. Samoylovich, N. G. Khlebtsov, *Nanoscale Research Lett.* **2013**, *8*, 250.
[16] P. Rajapandiyan, J. Yang, *J. Raman Spectrosc.* **2014**, *45*, 574.
[17] K. Malek, A. Brzozka, A. Rygula, G. D. Sulka, *J. Raman Spectrosc.* **2014**, *45*, 281.
[18] Z. Hu, Z. Liu, L. Li, B. Quan, Y. Li, J. Li, C. Gu, *Small* **2014**, *10*, 3933.
[19] Y. H. Kwon, R. Ossig, F. Hubenthal, H. D. Kronfeldt, *J. Raman Spectrosc.* **2012**, *43*, 1385.
[20] D. Jana, A. Mandal, G. De, *ACS Appl. Mater. Interfaces* **2012**, *4*, 3330.
[21] J. Chowdhury, P. Pal, M. Ghosh, T. N. Misra, *J. Colloid Interface Sci.* **2001**, *235*, 317.
[22] J. Chowdhury, M. Ghosh, *J. Raman Spectrosc.* **2004**, *35*, 1023.
[23] R. Aroca, C. Jennings, G. J. Kovacs, R. O. Loutfy, P. S. Vincett, *J. Phys. Chem.* **1985**, *89*, 4051.
[24] G. J. Kovacs, R. O. Loutfy, P. S. Vincett, C. Jennings, R. Aroca, *Langmuir* **1986**, *2*, 689.
[25] R. Aroca, D. Battisti, *Langmuir* **1990**, 6, 250 and references cited therein.
[26] G. Moula, R. F. Aroca, *Anal. Chem.* **2011**, 83, 284 and references cited therein.
[27] N. P. W. Pieczonka, R. F. Aroca, *Chem. Soc. Rev.* **2008**, 37.
[28] C. J. L. Constantino, R. F. Aroca, C. R. Mendonca, S. V. Mello, D. T. balogh, O. N. Oliveira Jr, *Spectrochemica Acta Part A* **2001**, *57*, 281 and references cited therein.
[29] P. Alessio, C. J. L. Constantino, R. F. Aroca, O. N. Oliveira Jr, *J. Chil. Chem. Soc.* **2010**, 55, 469 and references cited therein.
[30] A. R. Guerrero, Y. Zhang, R. F. Aroca, *Small* **2012**, 8, 2964 and references cited therein.
[31] M. M. Miranda, M. Puggelli, R. Ricceri, G. Gabrielli, *Langmuir* **1996**, *12*, 4417.
[32] P. Pienpinijtham, X. X. Han, S. Ekgasit, Y. Ozaki, *Phys. Chem. Chem. Phys.* **2012**, *14*, 10132.
[33] M. A. Mahmoud, C. E. Tabor, *J. Phys. Chem. C* **2009**, *113*, 5493.
[34] A. Tao, F. Kim, C. Hess, J. Goldberger, R. He, Y. Sun, Y. Xia, P. Yang, *Nano Lett.* **2003**, *3*, 1229.
[35] J. A. Creighton, C. G. Blatchford, M. G. Albrecht, *J. Chem. Soc. Faraday Trans. 2.* **1979**, *75*, 790.
[36] https://www.lumerical.com/tcad-products/fdtd/
[37] http://imagej.nih.gov/ij/
[38] M. J. Hwang, K. Kim, *Langmuir* **1999**, *15*, 3563.
[39] J. Sarkar, P. Pal, G. B. Talapatra, *Chem. Phys. Lett.* **2005**, *401*, 400.
[40] P. Hildebrant, M. Stockburger, *J. Phys. Chem.* **1984**, *88*, 5935.
[41] J. Chowdhury, M. Ghosh, J. Colloid Interface, *Sci.* **2004**, *277*, 121.
[42] J. Chowdhury, M. Ghosh, P. Pal, T. N. Misra, *J. Colloid Interface Sci.* **2003**, *263*, 318.
[43] M. Moskovits, J. S. Suh, *J. Phys. Chem.* **1988**, *92*, 6327.
[44] U. K. Sarkar, A. J. Pal, S. Chakraborti, T. N. Misra, *Chem. Phys. Lett.* **1992**, *190*, 59.
[45] S. Chandra, J. Chowdhury, M. Ghowdhury, M. Ghosh, G. B. Talapatra, *J. Phys. Chem. A* **2012**, *116*, 10934.
[46] M. Culha, M. Kahraman, N. Tokman, G. Turkoglu, *J. Phys. Chem. C* **2008**, *112*, 10338.
[47] H. Chen, Y. Wang, J. Qu, S. Dang, *J. Raman Spectrosc.* **2007**, *38*, 1444.

[48] G. Wei, H. Zhou, Z. Liu, Z. Li, *Appl. Surf. Sci.* **2005**, *240*, 260.
[49] Q. Shao, R. Que, L. Cheng, M. Shao, *RSC Adv.* **2012**, *2*, 1762.
[50] Y. C. Liu, C. C. Yu, S. F. Sheu, *J. Mater. Chem.* **2006**, *16*, 3546.
[51] L. Sun, Y. Song, L. Wang, C. Guo, Y. Sun, Z. Liu, Z. Li, *J. Phys. Chem. C* **2008**, *112*, 1415.
[52] C. Haley, J. H. Weaver, *Surf. Sci.* **2002**, *518*, 243.
[53] M. Moskovits, L. L. Tay, J. Yang, T. Haslett, Proc. SPIE, Nanoparticles and nanostructured surfaces: novel reporters with biological applications, **2001**, *4258*, 43.

Supporting information

Additional supporting information may be found in the online version of this article at the publisher's web-site.

Applied Surface Science 362 (2016) 364–373

Contents lists available at ScienceDirect

Applied Surface Science

journal homepage: www.elsevier.com/locate/apsusc

Silver coated gold nanocolloids entrapped in organized Langmuir–Blodgett Film of stearic acid: Potential evidence of a new SERS active substrate

Somsubhra Saha[a], Manash Ghosh[b], Bipan Dutta[c], Joydeep Chowdhury[a,*]

[a] Department of Physics, Jadavpur University, Kolkata 700032, India
[b] Department of Spectroscopy, Indian Association for the Cultivation of Science, Jadavpur, Kolkata 700032, India
[c] Department of Physics, Sammilani Mahavidyalaya, Baghajatin Station, E. M. Bypass, Kolkata 700094, India

ARTICLE INFO

Article history:
Received 26 June 2015
Received in revised form 12 October 2015
Accepted 14 November 2015
Available online 19 November 2015

Keywords:
Langmuir–Blodgett film
Silver coated gold nanocolloid
Surface enhanced resonance Raman scattering
Rhodamine 6G
3D-FDTD

ABSTRACT

SERS active substrate containing silver coated gold (Au@Ag) nanocolloids entrapped in the Langmuir–Blodgett (LB) film matrix of stearic acid (SA) has been reported. The SERS efficacy of the *as prepared* substrate has been tested with trace concentrations of Rhodamine 6G (R6G) molecules. Enhancement factors ranging from 10^4–10^{13} orders of magnitude have been estimated for the characteristic vibrational signatures of R6G molecule. The colossal enhancement factors also signify the superiority of the *as prepared* substrate in comparison to Au@Ag nanocolloids. The optical responses and the morphological features of the substrates are estimated with aid of UV–vis absorption spectra and FESEM, AFM images respectively. Correlations between the surface morphologies, fractal dimensions and roughness features of the *as prepared* substrates are also drawn. The electric field distributions around the aggregated nanocolloids entrapped in the SA matrix have been envisaged with the aid of three dimensional finite difference time domain (3D-FDTD) simulations. Tuning the interparticle localized surface plasmon (LSP) coupling between the aggregated nanocolloids may be achieved by lifting the LB film of SA at different surface pressures.

1. Introduction

Surface-enhanced Raman scattering (SERS) spectroscopy has been established as a powerful technique which allows enormous enhancements of Raman signals from probe molecules upon their adsorption on the nano structured surfaces [1–4]. It is successfully applied to understand the orientations and trace identifications of molecules or ions down to single molecule detection limit [5–8]. The genesis behind the huge enhancements of SERS signals is still not clear. However, the general consensus is that, both the electromagnetic (EM) and the chemical enhancement (CHEM) mechanisms are simultaneously operative [9–12] The EM effect is considered to be more dominant and results from the generation of localized surface plasmons (LSPs) of the metallic nanostructures [13]. The CHEM mechanism owes to the transfer of an electron from the Fermi level (E_F) of the nanostructured substrate to the HOMO or LUMO of the adsorbed analyte or vice versa [14–16]. Size, shape and morphology of the surfaces synergistically play an important role toward the enhancements of SERS signals [17–22]. Aroca et al. [23–30] reported a series of pioneering works where Langmuir–Blodgett (LB) technique had been successfully utilized to record the SERS of monolayer and multilayered organic molecules. In those reports, LB films of organic molecules had been used as integral part of molecular architectures for the SERS active substrates. However, the recent trends of research in this area, albeit scarce, are focused toward the fabrication of new SERS sensitive substrates using LB technique, which are reproducible, facile to prepare and favor interparticle LSP couplings [31–33].

With these things in mind, here we report the fabrication of a novel SERS active substrate of silver coated gold (Au@Ag) nanocolloids (NCs) self assembled in the bilayer Langmuir–Blodgett (LB) film matrix of stearic acid (SA). The efficacy of the SERS activity has been tested with Rhodamine 6G (R6G) molecule. Enhancements of the Raman bands have been discussed in the light of EM mechanism. The spatial distribution of electric fields around the self assembled Au@Ag nanoparticles are also estimated with the

* Corresponding author.
E-mail address: joydeep72.c@rediffmail.com (J. Chowdhury).

http://dx.doi.org/10.1016/j.apsusc.2015.11.137
0169-4332/

aid of three dimensional finite difference time domain (3D-FDTD) simulation studies.

2. Experimental procedure

2.1. Materials and methods

R6G molecule; ~95% dye content, SA; >99% purity and chloroauric acid ($HAuCl_4$) of spectroscopic grades were purchased from Sigma–Aldrich and were used as received. Silver nitrate ($AgNO_3$), tri-sodium citrate, ascorbic acid (AS), ethanol and acetone were purchased from E-Merck (Germany) and were used without further purification. Spectral grade chloroform was purchased from SRL India and was used as received. All the glasswares used in the synthesis were cleaned with freshly prepared aqua-regia and were thoroughly rinsed with distilled water prior to use. The required solutions were prepared using triple distilled water subsequently deionized (18.2 MΩ cm resistivity and pH ~ 6.8) through Milli-Q-plus system of Millipore Corporation, USA.

Spherical gold nanocolloids (AuNCs) of average particle diameter ~25 nm were synthesized by citrate reduction method as reported by Frens [34]. The AuNC, thus prepared, was used as core for the synthesis of Au@Ag nanocolloid according to the recipe described by Jana et al. [35]. Briefly, 10 ml of the AuNC aqueous solution was prepared with suitable dilution. To it, 50 μL 0.1 M aqueous solution of AS was added and then 250 μL of 0.01 M aqueous solution of $AgNO_3$ was subsequently added drop wise with continuous stirring. The color of the colloidal solution turns from red to greenish yellow, indicating the formation of Au@Ag nanocolloid having ~25 nm core diameter and ~13 nm shell thickness. The HRTEM image and EDX spectra of the *as synthesized* Au@AgNC are shown in the inset of Fig. 1 and Fig. S1 (Supplementary Material) respectively. The EDX spectrum confirms the existence of silver and gold in Au@Ag nanocolloidal solution.

The quartz glass slides were cleaned vigorously with ethanol, deionized water and acetone. The bilayer LB films of SA were lifted on the quartz substrates by Y-type deposition technique using computer controlled LB trough (Model No. D2007, Apex Instruments). Chloroform was used as solvent in the spreading solution of SA. Triple distilled deionized water was used as sub phase. The pressure–area (π–A) isotherm of SA was estimated with a film balance and the surface pressure was measured by the Wilhelmy method using a filter paper. SA solution in chloroform solvent was spread drop wise by a syringe on the water subphase. After a delay of 20 min, allowing the solvent to evaporate, the film was compressed by moving the barrier at a constant speed of 2 mm/min. The pressure area (π–A) isotherm was recorded throughout the compression steps.

The first layer of the SA was lifted by upstroke and the subsequent second layer was deposited by down stroke so that the hydrophilic part of the SA molecule can point outwards. The bilayer LB films of SA were dipped in the Au@Ag nanocolloids (Au@AgNCs) for 24 h. The films were then removed from the colloid, washed thoroughly with deionized water and dried in hot air oven to remove excess silver ions from the film surface. To verify the elemental identity of the *as prepared* substrates, were identified with the aid of EDX analysis and is shown in Fig. S2 (Supplementary Material). The *as prepared* substrates were then incubated in 1.0×10^{-6} M, 1.0×10^{-8} M, 1.0×10^{-12} M and 1.0×10^{-14} M aqueous solution of R6G for 1 h.

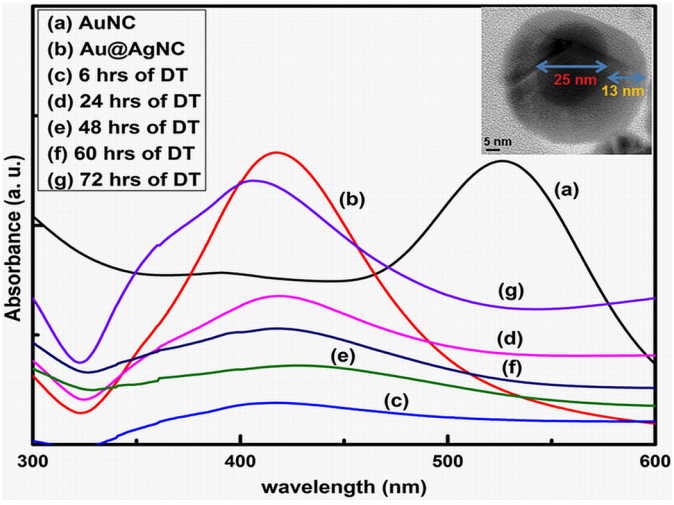

Fig. 1. Room temperature UV–vis electronic absorption spectra of (a) AuNC, (b) Au@AgNC and ((c)–(g)) Au@AgNC self-assembled in the bilayer LB film of SA at various DTs. Inset shows the HRTEM image of the *as synthesized* Au@AgNC.

2.2. Instrumentation

The absorption spectra were recorded using Jasco UV-vis Absorption Spectrometer (Model No: V-630). The surface enhanced resonance Raman scattering [SER(R)S] spectra were recorded by J–Y Horiba Confocal Triple Raman Spectrometer (Model: T 64000) fitted with gratings of 1800 groove/mm and a TE cooled synapse CCD detector from J–Y Horiba. The samples were excited using 514.5 nm green line of Ar+ laser manufactured by Spectra Physics, USA (Model.Stabilite2017) with spot size 1 μm in diameter at a laser power ~50 μW incident on the sample. The acquisition times for recording the SER(R) S spectra were fixed at 20 s. The scattered signals were collected at 180° scattering angle to the excitations from an Olympus open stage microscope of 10x objective. The detector and the data acquisition were controlled by Lab Spec 5 software as provided by Horiba. HRTEM and EDX analysis were carried out with Tecnai TF20 ST Transmission Electron Microscope with 200 KV accelerating voltage and EDAX make Si (Li) type EDX detector respectively. The surface morphology of the LB films was observed by Field Emission Scanning Electron Microscope (FESEM) (QUANTA FEG 250) at excitation energy of 10 kV. The EDX analyses of the *as prepared* substrates were performed by Quanta 200 equipped with EDAX made Si (Li) type EDX detector. The surface roughnesses of the *as prepared* samples were imaged by Atomic Force Microscope (AFM) (Vecco diInnova) operated in the tapping mode. Antimony doped silicon tip with typical resonant frequency of 300 kHz and force constant 40 N/m were used.

2.3. Theoretical calculations

The spatial distributions of electric fields around the plasmonic nanomaterials were estimated from 3D-FDTD simulations. The simulations were performed using 3D-FDTD Lumerical Solutions, Inc. [36]. The dimension of the Yell cell, used in the calculations, was fixed at 1 nm × 1 nm × 1 nm. The Johnson–Christy dielectric data for silver and gold were imported and water with real refractive index 1.33 was chosen for the back ground medium. All the models were exited with plane polarized light wave whose electric field amplitude is 1.0 V/m. Perfectly matched layer (PML) boundary condition was introduced to avoid reflection and back scattering of electric field from the pre-selected boundary. Incident light of 514.5 nm wavelength was used for the excitations and the duration of all the simulations was fixed at 500 fs to ensure full convergence of the electric field. The fractal dimensions were estimated using "Image J" [37] software considering around 300/350 nanoparticles.

3. Results and discussions

3.1. Pressure–area isotherm of a Langmuir monolayer of SA and preparation

Room temperature pressure (π)–area (A) isotherm of a Langmuir monolayer of SA at the air-water interface is shown in Fig. S3 (Supplementary Material). The nature of the isotherm is in concordance with the earlier reports [38] and the area/SA molecule is estimated to be ~0.22 (nm^2)/molecule. The bilayer LB film of SA is lifted on the pre-cleaned quartz substrate at a constant surface pressure of 25 mN/m. The film is lifted by Y-type deposition technique so that the polar COO^- group of the SA molecules point outwards in the periphery of the bilayer.

3.2. Optical and SER(R) S properties of the as prepared substrates

The room-temperature UV–vis electronic absorption spectra of the *as synthesized* Au and Au@Ag nanocolloidal particles are shown in Fig. 1. Pure Au and Au@AgNCs exhibit single absorption maximum centered at ~526 nm and 417 nm respectively, characteristic of their respective surface Plasmon (SP) electronic transitions [34,35]. The HRTEM image of the Au@AgNC having ~25 nm core diameter and ~13 nm shell thickness is shown in the inset of Fig. 1. Fig. 1 also shows the absorption spectra of Au@AgNCs self assembled in the organized bilayer LB film of SA at various dipping times (DTs) ranging from 6 h to 72 h.

Interestingly, the spectrum of the bilayer LB film of SA, incubated for 24 h in Au@AgNCs (Fig. 1(d)), is marked by broad structureless feature with no remarkable shift of the SP band. The broadening of the absorption spectra, in general, presages spontaneous aggregation of the Au@AgNCs on the bilayer LB film matrix of SA [39]. In Au@AgNC, there are residual surface charges which subsist due to incomplete reduction of metal ions in presence of reducing agent. The polar COO^- group of the bilayer LB film of SA may attract the unneutralized positively charged Au@Ag nanoparticles by virtue of charge neutrality consideration. This may lower the population of residual surface charges on the nanocolloidal surface, which in turn results in the reduction of repulsive interactions between the charged nanocolloidal particles and favors the formation of distinct aggregates in the LB film matrix of SA. The schematic representation showing the interaction between SA in the bilayer LB film and the Au@AgNC is shown in Fig. 2. The coupling of the electrostatic fields among the neighboring aggregated nanoparticles also contributes to the broadening of the electronic absorption spectra [40,41]. After 48 h of DT (Fig. 1 (e)), the SP band is remarkably red shifted and appears as distinct maximum centered at ~434 nm. This red shift may be owed to the strong dipole–dipole coupling between the neighboring Au@Ag nanoparticles. Interestingly, with further increase in DT (ca. ~60 h), this band undergoes considerable down shift and centered at ~423 nm. The blue shift is attributed to the alteration in the dielectric constant for metal nanoparticles surrounded by other metal nanoparticles [32,42]. However, at 72 h of DT, the SP band undergoes further hypsochromic shift and exhibits distinct structureless band maximum centered at ~407 nm with the appearance of a prominent hump at ~354 nm. This hump in the absorption spectrum is attributed to quadrapolar resonance which is mostly reported to appear for spherical and nearly spherical nanoparticles [40]. The optical responses of the UV–vis absorption spectra may provide an index to understand the variations in surface morphology of the aggregated nanocolloids self-assembled on the LB film of SA at various DTs.

Fig. 3 shows the concentration dependent SER(R) S spectra of R6G molecule adsorbed on the *as prepared* bilayer LB film of SA dipped in Au@AgNCs for 24 h. The electronic absorption maximum of the probe R6G at ~525 nm together with the green laser

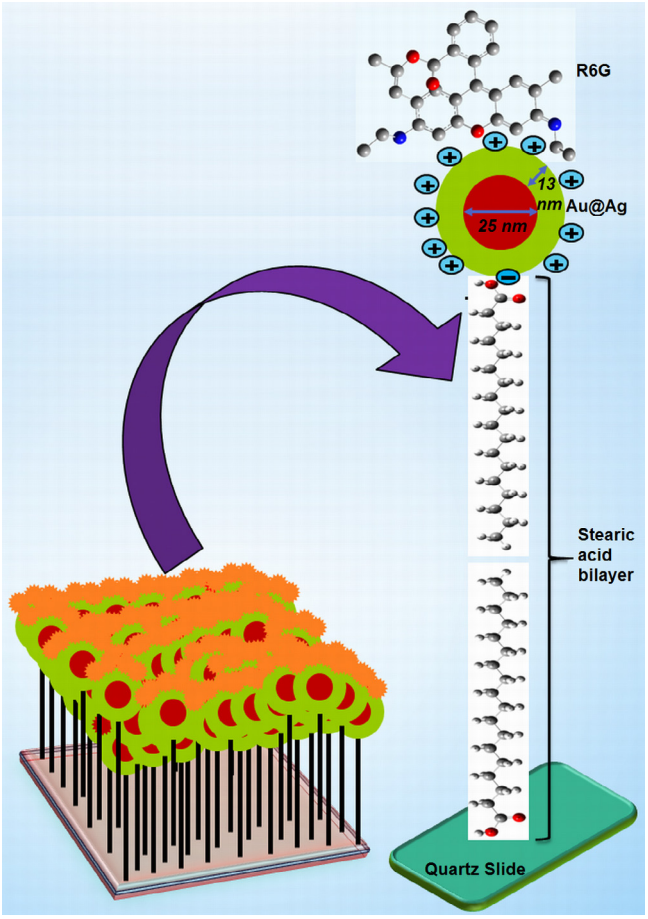

Fig. 2. Schematic representation showing the interaction between SA in the bilayer LB film and the Au@Ag nanocolloid.

excitation source allow us to record the surface enhanced resonance Raman scattering [SER(R)S] spectra of the molecule. The spectra are marked by enhanced Raman bands centered at ~614, 773, 1181, 1363, 1509, 1575 and 1650 cm^{-1} characteristic of R6G molecule [43]. The enhanced bands at ~614, 773, 1181, 1310, 1363, 1509, 1575 and 1650 cm^{-1} have been ascribed to in-plane vibrations, while 773 cm^{-1} band has been assigned to C—H out of plane mode associated with the xanthene ring plane of the R6G molecule. Fig. S4 (Supplementary Material) shows the variations in intensities of 614, 773, 1363, 1509, 1575 and 1650 cm^{-1} SER(R)S bands of R6G molecule with logarithm of the adsorbate concentrations. The concentration dependent variations in intensities of SER(R)S bands, in general, arises from surface coverage [44,45]. At extremely low concentrations, the metal surface coverage by the adsorbates is submonolayer. The SERS signal increases with increase in concentration of the adsorbate, attains a maximum intensity at monolayer coverage, where both the contributions from the EM and charge transfer (CT) effect to SERS maximize. With further increase in concentration of the adsorbates, multilayers are formed, resulting in the overall decrement of SERS signal. It therefore seems plausible that the monolayer coverage of the adsorbed R6G molecule on the *as prepared* substrate may have formed at a concentration ~1.0×10^{-8} M which exhibits maximum enhancement of the SER(R)S signals.

The SER(R)S and the RR spectra have been normalized with respect to 1363 cm^{-1} band. The relative intensity of this band does not change significantly in RR and in the SER(R)S spectra. In order to envisage the enhancements of SER(R)S bands, the apparent

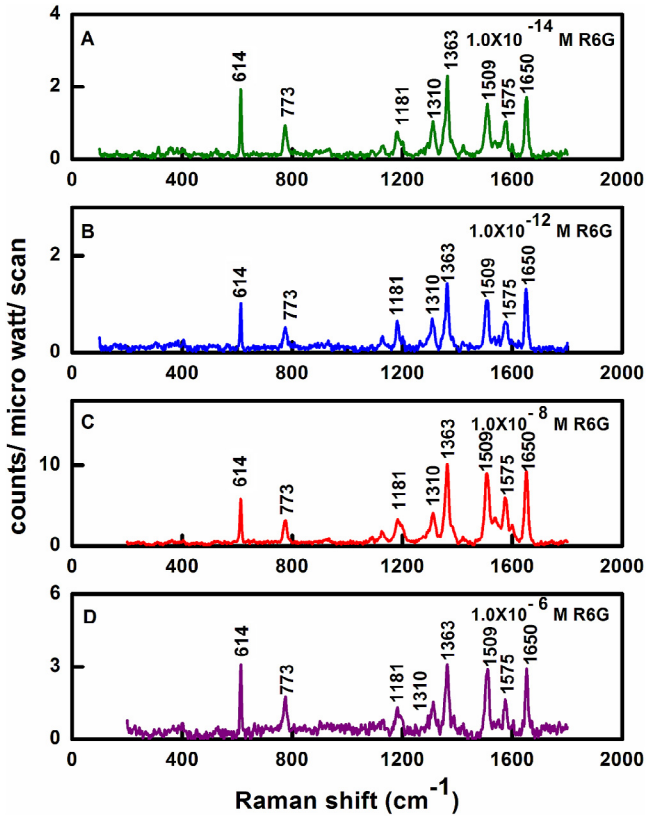

Fig. 3. SER(R) S spectra of R6G molecule at varied concentrations of the adsorbate (λ_{ex} = 514.5 nm).

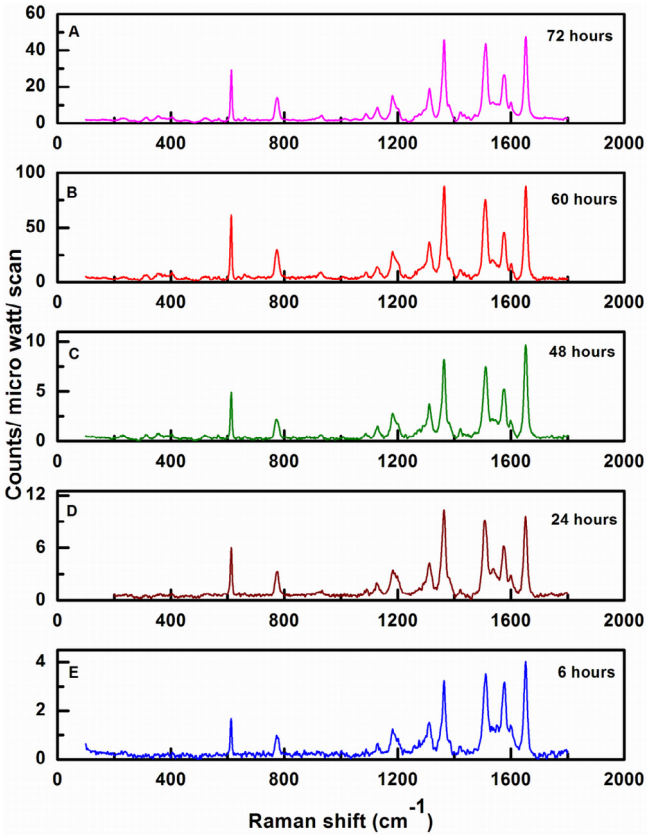

Fig. 4. SER(R) S spectra of 1.0×10^{-8} M aqueous solution of R6G molecule at various DTs (λ_{ex} = 514.5 nm).

enhancement factors (AEF) have been estimated using the following relation [46].

$$\mathrm{AFF} = \frac{\sigma_{\mathrm{SER(R)S}}[C_{\mathrm{RR}}]}{\sigma_{\mathrm{RR}}[C_{\mathrm{SER(R)S}}]} \quad (1)$$

where $[C_{\mathrm{RR/SER(R)S}}]$ and $\sigma_{\mathrm{RR/SER(R)S}}$ represent the concentrations and the integrated peak areas of the RR/SER(R)S bands respectively normalized with respect to 1363 cm^{-1} band. The integrated areas of the RR, SER(R)S bands are measured from the baseline. The background corrected normalized RR spectrum of 0.1 M R6G in aqueous solution and the normalized SER(R)S spectra of R6G at various concentration of the adsorbate are shown in Figs. S5 and S6 respectively (Supplementary Material). The apparent enhancement factors (AEFs) for 614, 773, 1181, 1363, 1509, 1575 and 1650 cm^{-1} bands have been tabulated in Table 1. Enhancement factors ranging from $\sim 10^4$ to 10^{13} orders of magnitude have been estimated for the above mentioned bands. The normalized SER(R)S spectra of 1.0×10^{-14} M R6G, recorded from 5 distinct spots each from three different *as prepared* substrates incubated in Au@Ag nanocolloidal solutions for 24 h of DT, are shown in Fig. S7 (Supplementary Material). The spectral profiles are highly reproducible and exhibit distinct vibrational signatures of R6G molecule. The AEFs of the enhanced Raman bands, as obtained from the triplicate experiments after striking at five distinct spots on the *as prepared* substrates, are shown in Table S1 in the Supplementary Material. The estimated AEFs also support the reproducibility of the SER(R)S spectra of R6G molecule adsorbed on the *as prepared* substrates. These results suggest that the *as prepared* bilayer LB film of SA dipped in Au@AgNCs for 24 h behave as an efficient SERS active substrate for sensing R6G molecules at trace concentrations.

Kneipp et al. reported SERS enhancement factor (EF) $\sim 10^{14}$ order of magnitude for NaCl activated nanocolloidal aggregates or clusters [47–50]. The EF was reported to the independent on the size of the nanoclusters. However, the huge EF ($\sim 10^{14}$) was questioned by Etchegoin et al. They suggested that the improper way of

Table 1
Apparent enhancement factors (AEF) of SER(R)S bands of R6G molecules adsorbed on the *as-prepared* substrate surface at various concentrations of the adsorbate.

NRS (cm^{-1})	Adsorbate concentrations								Assignment
	10^{-6} M		10^{-8} M		10^{-12} M		10^{-14} M		
	SERS	AEF	SERS	AEF	SERS	AEF	SERS	AEF	
614	614	1.32×10^5	614	8.72×10^6	614	1.03×10^{11}	614	1.08×10^{13}	α (C—C—C)
776	773	1.25×10^5	773	8.74×10^6	773	7.83×10^{10}	773	1.04×10^{13}	γ (C—H)
1187	1181	8.96×10^4	1181	2.30×10^6	1181	5.92×10^{10}	1181	3.38×10^{12}	β (C—H)
1363	1363	9.26×10^4	1363	9.98×10^6	1363	9.23×10^{10}	1363	8.96×10^{12}	ν (C—C)
1509	1509	1.05×10^5	1509	9.79×10^6	1509	8.13×10^{10}	1509	7.42×10^{12}	ν (C—C)
1575	1575	6.46×10^4	1575	9.43×10^6	1575	8.05×10^{10}	1575	7.26×10^{12}	ν (C—C)
1652	1650	5.81×10^4	1650	7.18×10^6	1650	6.58×10^{10}	1650	5.88×10^{12}	ν (C—C)

α, β: in-plane bending; γ: out-of-plane bending; ν: stretching.

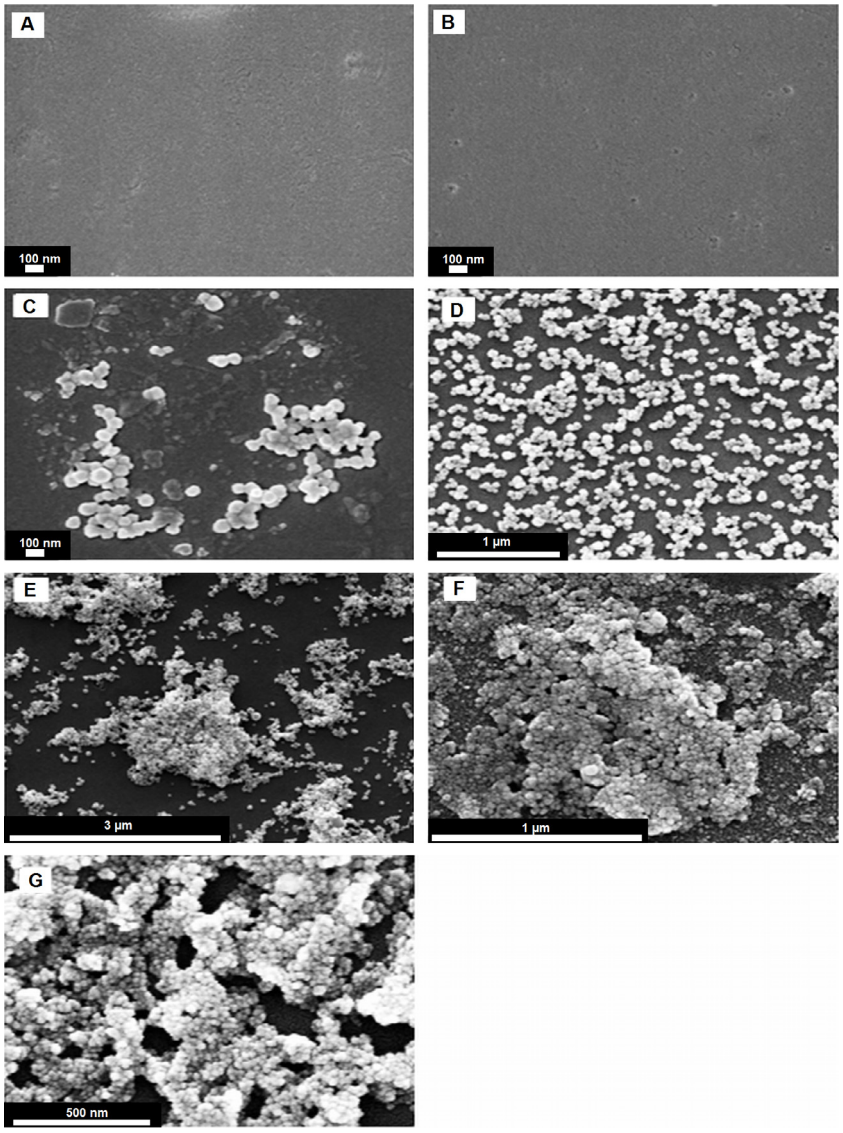

Fig. 5. Nanometer scale FESEM images of the *as prepared* substrates at various DTs. (A) Bare quartz glass slide, (B) bilayer LB film of SA lifted at 25 mN/m surface pressure. Bilayer LB film of SA incubated in Au@AgNCs at (C) 6 h, (D) 24 h, (E) 48 h, (F) 60 h, (G) 72 h of DTs.

normalization may be the genesis of the enormous claims of SERS EF $\sim 10^{14}$ orders of magnitude. Moreover, AEF as estimated from Eq. (1) [vide supra] is best suited for SERS in colloidal solutions. The intrinsic problem in the AEF definition rests in the fact that it does not recognize SERS to be a type of surface spectroscopy. The crucial step from transferring 3D solutions to 2D SERS active substrates may markedly affect the estimated AEF values by several orders of magnitude [51]. However, precise estimation of the EF may be obtained from SERS substrate EF (SSEF), defined as [51]

$$\mathrm{SSEF} = \frac{[I_{\mathrm{SERS}}/N_{\mathrm{Surf}}]}{[I_{\mathrm{RS}}/N_{\mathrm{Vol}}]} \quad (2)$$

where I_{SERS} and I_{RS} are the intensities of the SER bands and the normal Raman spectrum respectively, N_{Surf} is the number of molecules adsorbed on the SERS active substrate at respective adsorbate concentrations and N_{Vol} is the number of molecules sampled in the bulk solution.

As there are limitations in determining accurately the number of molecules on the *as prepared* SERS active substrates, qualitative estimations have been made from the AEF calculations. AEF ranging from 10^4 to 10^{13} orders of magnitude have been estimated for the characteristic vibrational signatures of R6G molecule. The estimated EFs are few orders of magnitude less as reported by Kneipp et al. [47–50] and are few orders higher with the reports of Etchegoin et al. [51–54].

In this connection, it may be relevant to mention that the EFs ranging from 10^6 to 10^{10} orders of magnitude have been reported for R6G molecule when adsorbed on AuNP film surface [55–60]. Moreover, the EFs of the characteristic Raman bands of R6G molecule on the *as prepared* substrate are $\sim 10^1$ to 10^3 orders of magnitude higher in comparison to that on Au@Ag nanocolloidal substrates reported elsewhere [35,61–64]. The colossal enhancement factors may also prove the superiority of the *as prepared* substrate over others.

The SER(R)S spectra of 1.0×10^{-8} M R6G molecule adsorbed on the *as prepared* bilayer substrate of SA incubated in Au@AgNC solutions for 6 h to 72 h of DTs are shown in Fig. 4. The enhancements of almost all the bands, characteristic of R6G molecule, further corroborates the proficiency of the *as prepared* substrates as effective SERS sensing platforms.

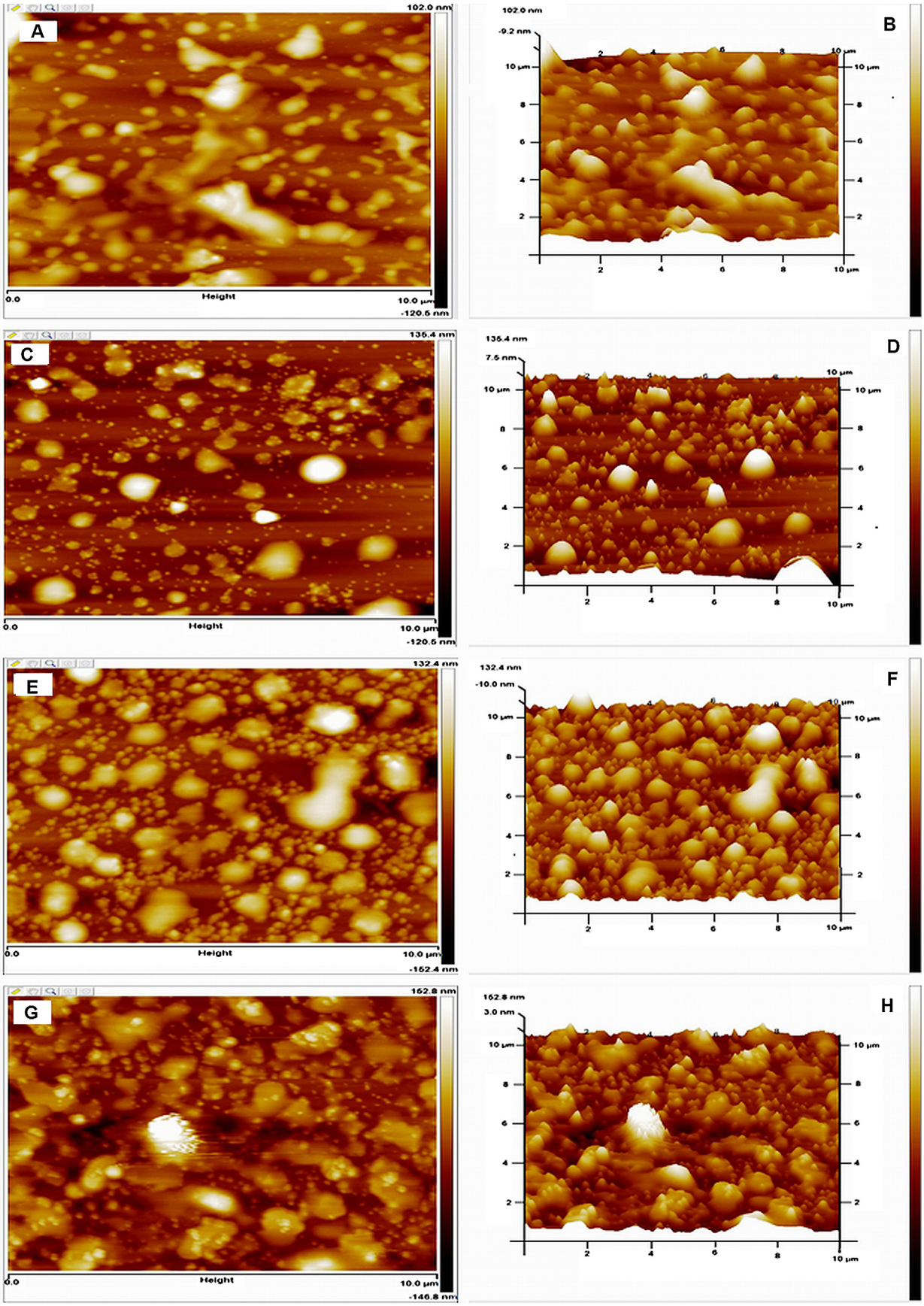

Fig. 6. Nanometer scale AFM images of the *as prepared* substrates. The left column contains topographic 2D AFM images at (A) 6 h, (C) 24 h, (E) 60 h and (G) 72 h of DTs. The right column shows the 3D AFM images of the same samples at (B) 6 h, (D) 24 h, (F) 60 h and (H) 72 h of DTs.

3.3. Surface characterization study of the as prepared substrates

In order to estimate a correlation between the surface morphology and roughness features, the FESEM and AFM images of the *as prepared* SER(R)S active substrates have been recorded. They are shown in Figs. 5 and 6 respectively. Fig. 5 shows the FESEM images of the bare quartz slide, bilayer SA LB film and the *as prepared* bilayer LB films of SA incubated in Au@AgNCs at various DTs ranging from 6 h to 72 h. The FESEM images reveal that the nano aggregated structures of the Au@AgNCs incubated for 6–48 h of DTs are interlaced and exhibit fractal like patterns. Interestingly, the FESEM image of *as prepared* substrate incubated for 24 h of DT, exhibits the most homogenous feature characterized by small fractal like aggregated structures. The homogeneity of the *as prepared* substrate impels us to record the SER(R)S spectra of R6G molecule at various concentrations of the adsorbate as shown in Fig. 3 (vide ante). However, with the increase in DTs (ca.60 and 72 h), the overall morphology changes to lumpy structures manifesting more of Euclidean features. These changes in the morphological features may be attributed to the formation of oxides on the Au@Ag aggregated surfaces [39]. More over with the increase in DTs, the density of the nano aggregated particles on the surface of the substrate increases with the concomitant decrease in the interstitial gap between the particles. These perturbation in the morphological features of the *as prepared* substrates may result in broadening of the absorption spectra as discussed earlier (Fig. 1(c)–(g); vide ante). To verify the elemental identity of the *as prepared* substrate, the EDX analysis has been done and is shown in Fig. S2 (Supplementary Material). The EDX analysis confirm the expected existence of gold, silver and oxygen on the *as prepared* film substrate, together with the presence of Na emanating from the quartz slide.

Fig. 6 shows the 2D and 3D AFM images of the bilayer LB film of SA incubated in Au@AgNCs at various DTs. The images divulge the formation of fractal like nano aggregated patterns on the surface of the *as prepared* films. In this connection, it may be worth to mention, that the bilayer LB film substrate dipped for 60 h in the nano colloidal solution exhibits the most enhanced SER(R)S bands of R6G molecule (vide supra, Fig. 4). The normalized SER(R)S spectra of 1.0×10^{-8} M R6G molecule, recorded from six different spots of the *as prepared* substrate incubated in Au@Ag nanocolloidal solutions for 60 h of DT, are shown in Fig. S8 in the Supplementary Material. The spectra are highly reproducible and exhibit no noticeable band shift. The corresponding morphological features of the substrate may be associated with SER(R)S efficacy from the 3D AFM image. The image (Fig. 6(E) and (F)) clearly smears the aggregation of Au@AgNC particles on the film surface with distinct sharp tips and precise interparticle spacings. The sharp tips may sustain the lightening rod effect, while the precise interparticle spacings favor the coupling of the LSPs to generate the necessary hot spots responsible for the gigantic SER(R)S enhancements.

The root mean square (RMS) roughness of the *as prepared* substrates have been estimated using the relation,

$$R_q = \sqrt{\sum \frac{(Z_i)^2}{N}} \tag{3}$$

where Z_i is the current value of peak-to-valley difference in height within the analyzed region and N is the number of points within the box cursor. Fig. 7 shows the variations in the roughness features of the bilayer LB film of SA incubated in the nanocolloids at various DTs. The plot indicates monotonic increase in the roughness features of the *as prepared* substrates with increase in DTs. The increase in surface roughness with DT may auger variations in the morphological features of the *as prepared* substrates.

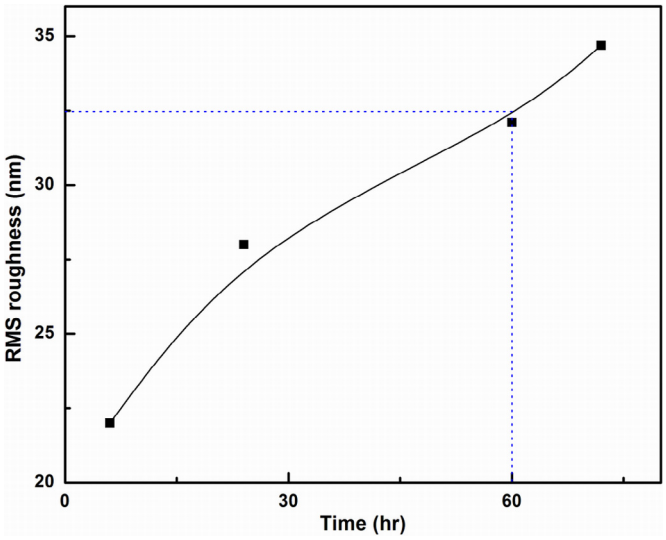

Fig. 7. Variation in the RMS values of surface roughnesses of the *as prepared* substrates with various DTs in Au@AgNCs.

The RMS roughness has been estimated to be ~32.13 nm for the bilayer LB film of SA dipped for 60 h in the Au@AgNC solution. This RMS roughness may be considered to be the optimum roughness feature for the *as prepared* substrate to generate the most enhanced Raman bands in the SER(R)S spectrum of R6G molecule (Fig. 4(B))

In order to elucidate fractal dimensions of the *as prepared* nano aggregated structures, radial mass distribution method has been applied. The area covered by each structure, S and the Hausdroff dimension, D are related as

$$S \alpha R^D \tag{4}$$

where R is the average distance from the center of mass of each structure to its perimeter [65]. The slopes of ln S vs ln R plots will allow us to estimate the fractal dimensions of the nano aggregated assembles. Points are taken from different regions of the FESEM topographies and are fitted to straight lines by least square method. They are shown in Fig. 8. From Fig. 8, the fractal dimensions are estimated to be 1.83 ± 0.02, 1.85 ± 0.02, 1.88 ± 0.01 and 1.89 ± 0.01 for the *as prepared* bilayer LB film of SA dipped in 24 h, 48 h, 60 h and 72 h DTs respectively. These results are in accordance with our previous conjecture depicting the variations in the morphological features of the *as prepared* substrates from fractals to Euclidian patterns with the increase in DTs.

3.4. Estimation of EM enhancement

The electric field (E) distribution around the metallic nanoparticles have been estimated to explore the genesis of enhancements of the SER(R)S bands of R6G molecule adsorbed on bilayer LB film of SA incubated for 60 h of DT. The E-field distributions are estimated directly from the FESEM topography of the *as prepared* substrate, and are shown in Fig. 9. The FESEM image as shown in Fig. 9, exhibits large number of densed nano aggregated structures in which each particle may interact through dipole–dipole coupling that may be considered favorable for the generation of hot spots. The *as prepared* films may have hot/cold spots characteristic of the fractal nature of the aggregated nanocolloids. As the aggregates are fractal in nature, the normal modes of the surface plasmon oscillations are localized within these hot specks that carry the full excitation [66]. The hot spots localized in the fractal aggregates may exhibit enormous electromagnetic enhancements

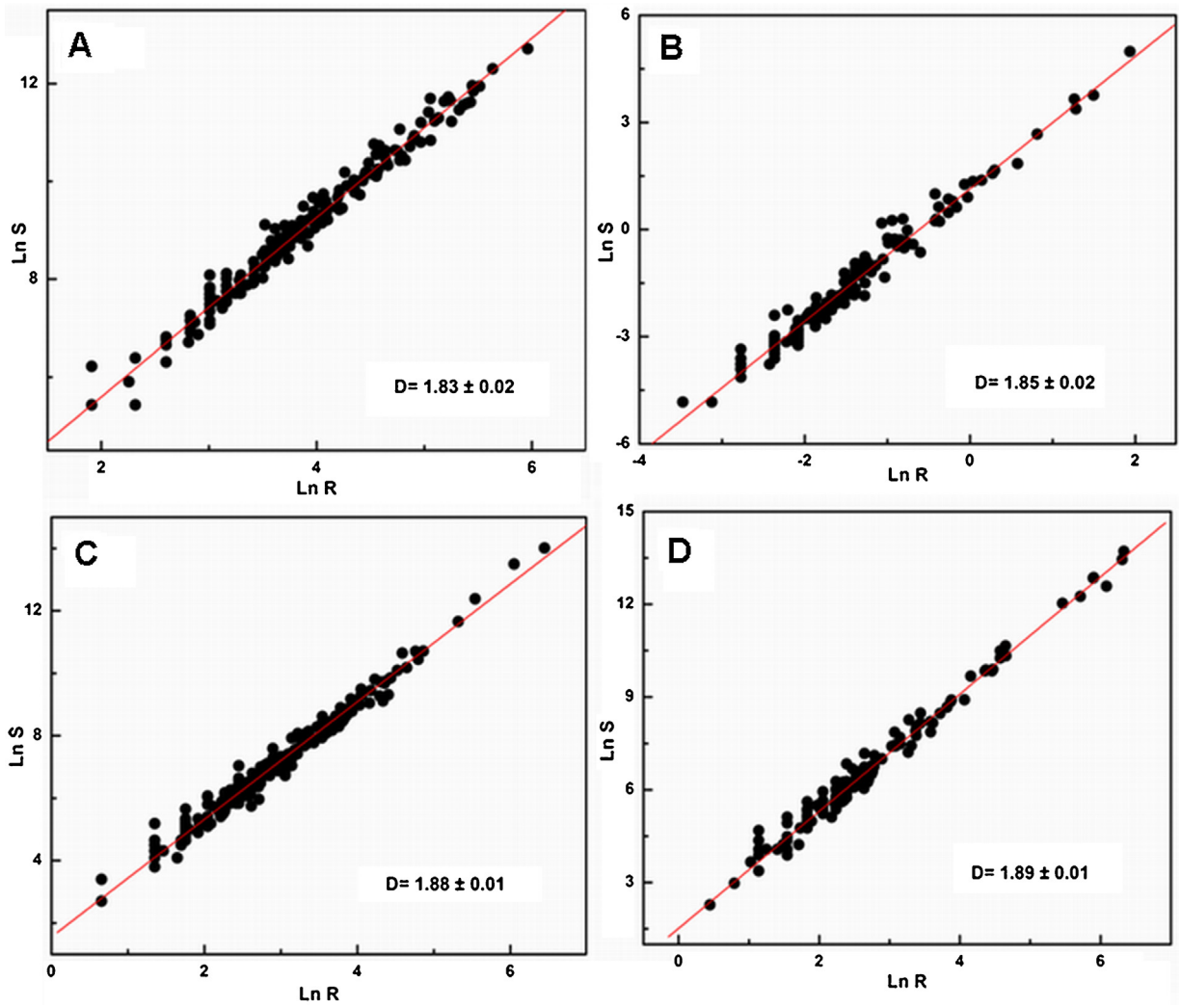

Fig. 8. Ln *R* vs Ln *S* plots of the *as-prepared* samples at various DTs inorder to explore fractal dimension. The error of the slope determination is coming from line fitting; (a) 24 h, (b) 48 h, (c) 60 h, (d) 72 h.

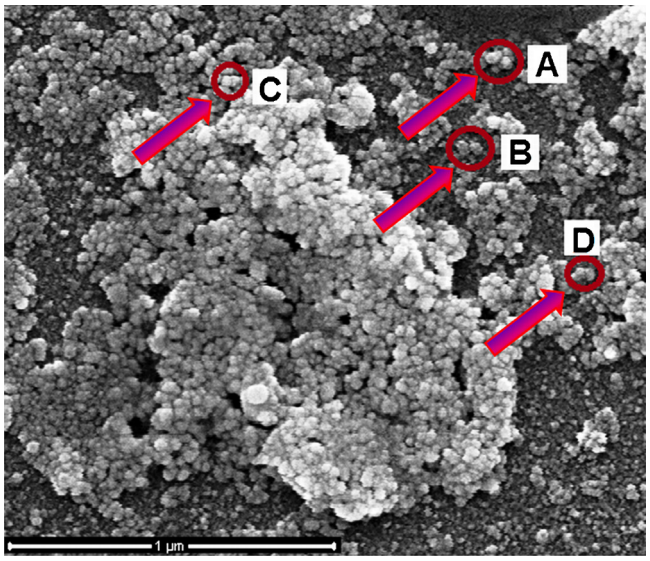

Fig. 9. Selected Au@Ag nanoaggregated geometries of the *as prepared* substrates used for 3D-FDTD simulation.

in comparison to non fractal aggregates. Moreover, the surface roughness of the *as prepared* films may result in aggregation of fractal nature that may help to excite the localized surface plasmons by the application of electric fields. Fig. 10 shows the spatial distributions of *E*-fields around some selected hot geometries which are marked in the FESEM image. From Fig. 10(A), it is seen that the hottest among the hot spots is spatially confined in the inter particle gap ~1.8 nm where the spatial distribution of *E*-field is extended over an approximate length of ~22 nm. The $|\vec{E}|$ fields for this hottest geometry is estimated to be ~30 V/m (Fig. 10(A)), which approximately corresponds to the SE(R)RS enhancement factor $[G^{/}(\omega, \omega')]$ ~10^5 orders of magnitude following the plane wave (PW) approximation. However, the variance of the estimated $G^{/}(\omega, \omega')$ with those predicted from the experimental observations may be attributed to the resonance and the CT effect to SER(R)S apart from the EM mechanism. Thus the EM, CT and resonance effect significantly contribute toward the enhancements of Raman bands in the SER(R)S spectra of R6G molecule. Tuning the interparticle plasmon coupling may be accomplished by lifting the bilayer LB film of SA at different surface pressures followed by the self-assembly of the nanocolloidal particles. The aspect of controlling the interparticle coupling of the surface plasmons may be an interesting issue to be focussed in our future publications.

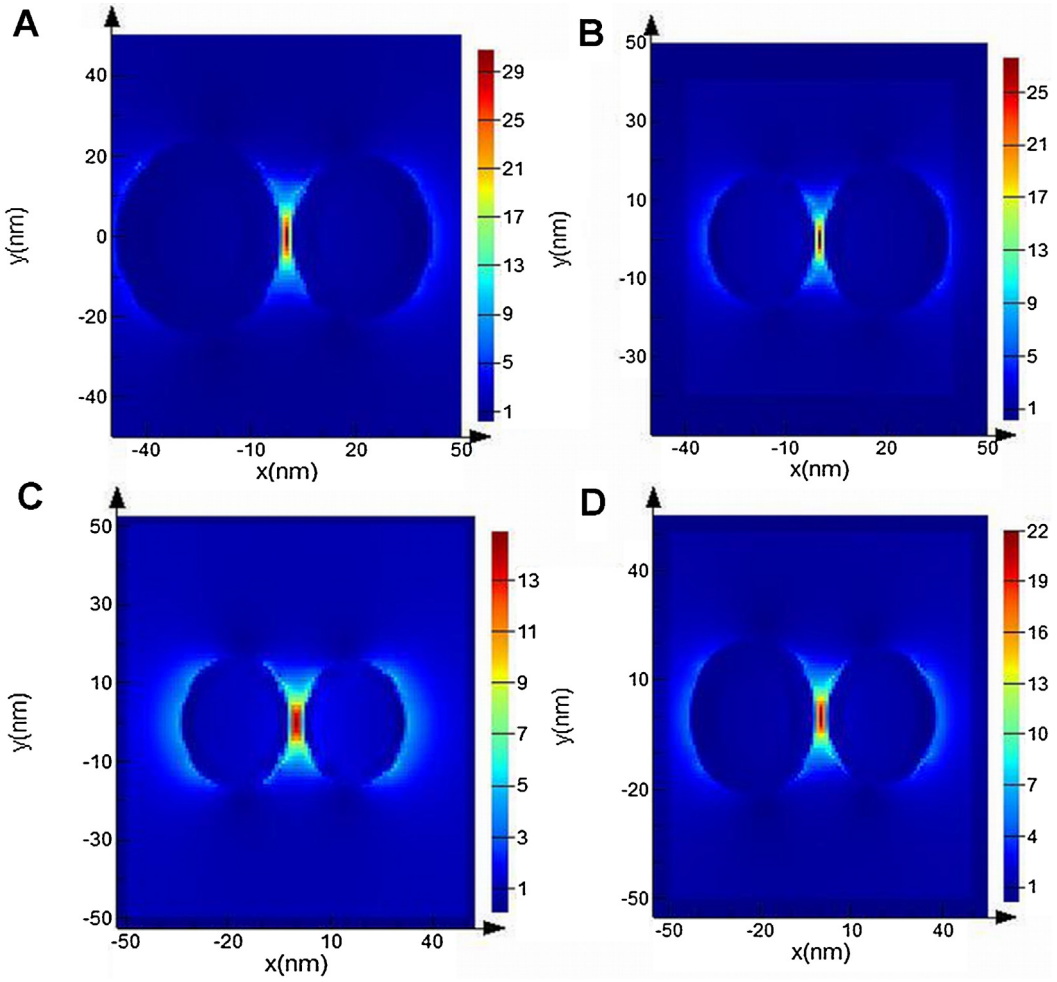

Fig. 10. Electric field distribution around the hot-spots as estimated from 3D-FDTD simulations (λ_{ex} = 514.5 nm, the polarization of the incident light wave is along *x*-axis).

4. Conclusion

Au@Ag nanocolloids entrapped in the bilayer LB film of SA matrix has been established as an excellent SERS active substrate. Enhancement factors ranging from 10^4 to 10^{13} orders of magnitude has been estimated for the characteristic SER(R)S bands of R6G molecule. Correlations between the surface morphologies, fractal dimensions and roughness features of the established SERS active substrates have been drawn. The spatial distribution of electric fields around the aggregated nanocolloids entrapped in the SA matrix has been estimated with the aid of 3D-FDTD simulations. The localized surface plasmons coupling between the aggregated nanocolloids may be controlled by lifting the LB film of SA at different surface pressures. This aspect of controlling the architecture of the *as prepared* substrate will be focused in the future publication.

Acknowledgement

Authors express their thanks to the Department of Science and Technology (DST), India for the financial support through the research projects (project no. SR/S2/CMP-0045/2012; 2012/37P/BRNS). SSS would like to thank DST, Govt. of India for the Junior Research Fellowship.

Appendix A. Supplementary data

Supplementary data associated with this article can be found, in the online version, at http://dx.doi.org/10.1016/j.apsusc.2015.11.137.

References

[1] M. Fleishmann, P.J. Hendra, A.J. McQuillan, Raman spectra of pyridine adsorbed at a silver electrode, Chem. Phys. Lett. 26 (1974) 163–166.
[2] L. Guerrini, D. Graham, Molecularly-mediated assemblies of plasmonic nanoparticles for surface-enhanced Raman spectroscopy applications, Chem. Soc. Rev. 41 (2012) 7085–7107.
[3] L. Yang, P. Li, J. Liu, Progress in multifunctional surface-enhanced Raman scattering substrate for detection, RSC Adv. 4 (2014) 49635–49646.
[4] F.J. Garcia-Vidal, J.B. Pendry, Collective theory for surface enhanced Raman scattering, Phys. Rev. Lett. 77 (1996) 1163–1166.
[5] Y. Ma, Q. Ding, L. Yang, L. Zhang, Y. Shen, Ag nanoparticles as multifunctional SERS substrate for the adsorption, degradation and detection of dye molecules, Appl. Surf. Sci. 265 (2013) 346–351.
[6] J. Chowdhury, P. Pal, M. Ghosh, T.N. Misra, Surface-enhanced Raman scattering of Rhodamine 123 in silver hydrosols and in Langmuir–Blodgett films on silver islands, J. Colloid Interface Sci. 235 (2001) 317–324.
[7] C.J.L. Constantino, T. Lema, P.A. Antunes, R. Aroca, Single-molecule detection using surface-enhanced resonance Raman scattering and Langmuir–Blodgett monolayers, Anal. Chem. 73 (2001) 3674–3678.
[8] K. Kneipp, Y. Wang, H. Kneipp, L.T. Perelman, I. Itzkan, R.R. Dasari, M.S. Feld, Single molecule detection using surface-enhanced Raman scattering (SERS), Phys. Rev. Lett. 78 (1997) 1667–1671.

[9] S.D. Roy, M. Ghosh, J. Chowdhury, Adsorptive parameters and influence of hot geometries on the SER(R) S spectra of methylene blue molecules adsorbed on gold nanocolloidal particles, J. Raman Spectrosc. 46 (2015) 451–461.
[10] P. Nordlander, C. Oubre, E. Prodan, K. Li, M.I. Stockman, Plasmon hybridization in nanoparticle dimers, Nano Lett. 4 (2004) 899–903.
[11] S. Chandra, J. Chowdhury, M. Ghosh, G.B. Talapatra, Exploring the pH dependent SERS spectra of 2-mercaptoimidazole molecule adsorbed on silver nanocolloids in the light of Albrecht's "A" term and Herzberg–Teller charge transfer contribution, J. Colloid Interface Sci. 399 (2013) 33–45.
[12] M.T. Sun, S.B. Wan, Y.J. Liu, Y. Jia, H.X. Xu, Chemical mechanism of surface-enhanced resonance Raman scattering via charge transfer in pyridine–Ag2 complex, J. Raman Spectrosc. 39 (2008) 402–408.
[13] M.C. Wu, M.P. Lin, S.W. Chen, P.H. Lee, J.H. Li, W.F. Su, Surface-enhanced Raman scattering substrate based on a Ag coated monolayer array of SiO_2 spheres for organic dye detection, RSC Adv. 4 (2014) 10043–10050.
[14] J.F. Arenas, M.K. Woolley, I.L. Tacon, J.C. Otero, I.J. Marcos, Complete analysis of the surface-enhanced Raman scattering of pyrazine on the silver electrode on the basis of a resonant charge transfer mechanism involving three states, J. Chem. Phys. 112 (2000) 7669–7683.
[15] J.R. Lombardi, R.L. Birke, A unified approach to surface-enhanced Raman spectroscopy, J. Phys. Chem. C 112 (2008) 5605–5617.
[16] M.R.L. Ramirez, C. Ruano, J.L. Castro, J.F. Arenas, J. Soto, J.C. Otero, Surface-enhanced Raman scattering of benzoate anion adsorbed on silver nanoclusters: evidence of the transient formation of the radical dianion, J. Phys. Chem. C 114 (2010) 7666–7672.
[17] N.R. Jana, T. Pal, Anisotropic metal nanoparticles for use as surface-enhanced Raman substrates, Adv. Mater. 19 (2007) 1761–1765.
[18] J. Bian, S. Shu, J. Li, C. Huang, Y.Y. Li, R.Q. Zhang, Reproducible and recyclable SERS substrates: flower-like Ag structures with concave surfaces formed by electrodeposition, Appl. Surf. Sci. 333 (2015) 126–133.
[19] C.L. Nehl, J.H. Hafner, Shape-dependent plasmon resonances of gold nanoparticles, J. Mater. Chem. 18 (2008) 2415–2419.
[20] Y. Yang, J. Liu, Z.W. Fu, D. Qin, Galvanic replacement-free deposition of Au on Ag for core–shell nanocubes with enhanced chemical stability and SERS activity, J. Am. Chem. Soc. 136 (2014) 8153–8156.
[21] Z. Zhang, W. Zhu, Controllable-density nanojunctions as SERS substrates for highly sensitive detection, Appl. Surf. Sci. 333 (2015) 214–219.
[22] A. Roguska, A. Kudelski, M. Pisarek, M. Opara, M.J. Czachor, Surface-enhanced Raman scattering (SERS) activity of Ag, Au and Cu nanoclusters on TiO_2-nanotubes/Ti substrate, Appl. Surf. Sci. 257 (2011) 8182–8189.
[23] R. Aroca, C. Jennings, G.J. Kovacs, R.O. Loutfy, P.S. Vincett, Surface-enhanced Raman scattering of Langmuir–Blodgett monolayers of phthalocyanine by indium and silver island films, J. Phys. Chem. 89 (1985) 4051–4054.
[24] G.J. Kovacs, R.O. Loutfy, P.S. Vincett, C. Jennings, R. Aroca, Distance dependence of SERS enhancement factor from Langmuir–Blodgett monolayers on metal island films: evidence for the electromagnetic mechanism, Langmuir 2 (1986) 689–694.
[25] R. Aroca, D. Battisti, SERS of Langmuir–Blodgett monolayers: coverage dependence, Langmuir 6 (1990) 250–254, and references cited therein.
[26] G. Moula, R.F. Aroca, Plasmon-enhanced resonance Raman scattering and fluorescence in Langmuir–Blodgett monolayers, Anal. Chem. 83 (2011) 284–288, and references cited therein.
[27] N.P.W. Pieczonka, R.F. Aroca, Single molecule analysis by surfaced-enhanced Raman scattering, Chem. Soc. Rev. 37 (2008) 946–954, and references cited therein.
[28] C.J.L. Constantino, R.F. Aroca, C.R. Mendonca, S.V. Mello, D.T. balogh, O.N. Oliveira Jr., Surface enhanced fluorescence and Raman imaging of Langmuir–Blodgett azopolymer films, Spectrochem. Acta Part A 57 (2001) 281–289, and references cited therein.
[29] P. Alessio, C.J.L. Constantino, R.F. Aroca, O.N. Oliveira Jr., Surface-enhanced Raman scattering: metal nanostructures coated with Langmuir–Blodgett films, J. Chil. Chem. Soc. 55 (2010) 469–478, and references cited therein.
[30] A.R. Guerrero, Y. Zhang, R.F. Aroca, Experimental confirmation of local field enhancement determining far-field measurements with shell-isolated silver nanoparticles, Small 8 (2012) 2964–2967, and references cited therein.
[31] P. Pienpinijtham, X.X. Han, S. Ekgasit, Y. Ozaki, An ionic surfactant-mediated Langmuir–Blodgett method to construct gold nanoparticle films for surface-enhanced Raman scattering, Phys. Chem. Chem. Phys. 14 (2012) 10132–10139.
[32] M.A. Mahmoud, C.E. Tabor, M.A. El-Sayed, Surface-enhanced Raman scattering enhancement by aggregated silver nanocube monolayers assembled by the Langmuir–Blodgett technique at different surface pressures, J. Phys. Chem. C 113 (2009) 5493–5501.
[33] A. Tao, F. Kim, C. Hess, J. Goldberger, R. He, Y. Sun, Y. Xia, P. Yang, Langmuir–Blodgett silver nanowire monolayers for molecular sensing using surface-enhanced Raman spectroscopy, Nano Lett. 3 (2003) 1229–1233.
[34] G. Frens, Controlled nucleation for the regulation of the particle size in monodisperse gold suspensions, Nat. Phys. Sci. 241 (1973) 20–22.
[35] A. Saha, S. Palmal, N.R. Jana, Highly reproducible and sensitive surface-enhanced Raman scattering from colloidal plasmonic nanoparticle *via* stabilization of hot spots in graphene oxide liquid crystal, Nanoscale 4 (2012) 6649–6657.
[36] https://www.lumerical.com/tcad-products/fdtd/.
[37] http://imagej.nih.gov/ij/.
[38] M.J. Hwang, K. Kim, Poly(ethylenimine) as a subphase stabilizer of stearic acid monolayers at the air/water interface: surface pressure–area isotherm and infrared spectroscopy study, Langmuir 15 (1999) 3563–3569.
[39] J. Sarkar, P. Pal, G.B. Talapatra, Self-assembly of silver nano-particles on stearic acid Langmuir–Blodgett film: evidence of fractal growth, Chem. Phys. Lett. 401 (2005) 400–404.
[40] K.L. Kelly, E. Coronado, L.L. Zhao, G.C. Schatz, The optical properties of metal nanoparticles: the influence of size, shape, and dielectric environment, J. Phys. Chem. B 107 (2003) 668–677.
[41] W. Gotschy, K. Vonmetz, A. Leitner, F.R. Aussenegg, Optical dichroism of lithographically designed silver nanoparticle films, Opt. Lett. 21 (1996) 1099–1101.
[42] J.R. Heath, C.M. Knoblerdaniel, V. Leff, Pressure/temperature phase diagrams and superlattices of organically functionalized metal nanocrystal monolayers: the influence of particle size, size distribution, and surface passivant, J. Phys. Chem. B 101 (1997) 189–197.
[43] P. Hildebrant, M. Stockburger, Surface-enhanced resonance Raman spectroscopy of Rhodamine 6G adsorbed on colloidal silver, J. Phys. Chem. 88 (1984) 5935–5944.
[44] J. Chowdhury, M. Ghosh, Concentration-dependent surface-enhanced Raman scattering of 2-benzoylpyridine adsorbed on colloidal silver particles, J. Colloid Interface Sci. 277 (2004) 121–127.
[45] J. Chowdhury, M. Ghosh, P. Pal, T.N. Misra, Concentration-dependent surface-enhanced resonance Raman scattering of a porphyrin derivative adsorbed on colloidal silver particles, J. Colloid Interface Sci. 263 (2003) 318–326.
[46] J. Sarkar, J. Chowdhury, M. Ghosh, R. De, G.B. Talapatra, Adsorption of 2-aminobenzothiazole on colloidal silver particles: an experimental and theoretical surface-enhanced Raman scattering study, J. Phys. Chem. B 109 (2005) 12861–12867.
[47] K. Kneipp, H. Kneipp, I. Itzkan, R.R. Dasari, M.S. Feld, Ultrasensitive chemical analysis by Raman spectroscopy, Chem. Rev. 99 (1999) 2957–2975.
[48] J. Kneipp, H. Kneipp, K. Kneipp, SERS – a single-molecule and nanoscale tool for bioanalytics, Chem. Soc. Rev. 37 (2008) 1052–1060.
[49] K. Kneipp, Y. Wang, H. Kneipp, L.T. Perelman, I. Itzkan, R.R. Dasari, M.S. Feld, Single molecule detection using surface-enhanced Raman scattering (SERS), Phys. Rev. Lett. 78 (1997) 1667–1670.
[50] K. Kneipp, H. Kneipp, I. Itzkan, R.R. Dasari, M.S. Feld, Surface-enhanced non-linear Raman scattering at the single-molecule level, Chem. Phys. 247 (1999) 152–160.
[51] E.C. Le Ru, P.G. Etchegoin, Quantifying SERS enhancements, MRS Bull. 38 (2013) 631–640.
[52] P.G. Etchegoin, P.D. Lacharmoise, E.C. Le Ru, Influence of photostability on single-molecule surface enhanced Raman scattering enhancement factors, Anal. Chem. 81 (2009) 682–688.
[53] E.J. Blackie, E.C. Le Ru, P.G. Etchegoin, Single-molecule surface-enhanced Raman spectroscopy of nonresonant molecules, J. Am. Chem. Soc. 131 (2009) 14466–14472.
[54] P.G. Etchegoin, E.C. Le Ru, A perspective on single molecule SERS: current status and future challenges, Phys. Chem. Chem. Phys. 10 (2008) 6079–6089.
[55] M. Suzuki, Y. Niidome, Y. Kuwahara, N. Terasaki, K. Inoue, S. Yamada, Surface-enhanced nonresonance Raman scattering from size- and morphology-controlled gold nanoparticle films, J. Phys. Chem. B 108 (2004) 11660–11665.
[56] D.S. dos Santos Jr., P.J.G. Goulet, N.P.W. Pieczonka, O.N. Oliveira Jr., R.F. Aroca, Gold nanoparticle embedded, self-sustained chitosan films as substrates for surface-enhanced Raman scattering, Langmuir 20 (2004) 10273–10277.
[57] L. Polavarapu, Q.H. Xu, Water-soluble conjugated polymer-induced self-assembly of gold nanoparticles and its application to SERS, Langmuir 24 (2008) 10608–10611.
[58] R. Que, M. Shao, S. Zhuo, C. Wen, S. Wang, S.T. Lee, Highly reproducible surface-enhanced Raman scattering on a capillarity-assisted gold nanoparticle assembly, Adv. Funct. Mater. 21 (2011) 3337–3343.
[59] A.M. Schwartzberg, C.D. Grant, A. Wolcott, C.E. Talley, T.R. Huser, R. Bogomolni, J.Z. Zhang, Unique gold nanoparticle aggregates as a highly active surface-enhanced Raman scattering substrate, J. Phys. Chem. B 108 (2004) 19191–19197.
[60] S.Q. Zhu, T. Zhang, X.L. Guo, X.Y. Zhang, Self-assembly of large-scale gold nanoparticle arrays and their application in SERS, Nanoscale Res. Lett. 9 (2014) 114–122.
[61] E. Kirubha, P.K. Palanisamy, Green synthesis, characterization of Au–Ag core–shell nanoparticles using gripe water and their applications in nonlinear optics and surface enhanced Raman studies, Adv. Nat. Sci.: Nanosci. Nanotechnol. 5 (2014) 045006–045011.
[62] L. Lu, H. Wang, Y. Zhou, S. Xi, H. Zhang, J. Hu, B. Zhao, Seed-mediated growth of large, monodisperse core–shell gold–silver nanoparticles with Ag-like optical properties, Chem. Commun. (2002) 144–145.
[63] Y. Yang, J. Shi, G. Kawamura, M. Nogami, Preparation of Au–Ag, Ag–Au core–shell bimetallic nanoparticles for surface-enhanced Raman scattering, Scr. Mater. 58 (2008) 862–865.
[64] N.R. Jana, Silver coated gold nanoparticles as new surface enhanced Raman substrate at low analyte concentration, Analyst 128 (2003) 954–956.
[65] C. Haley, J.H. Weaver, Buffer-layer-assisted nanostructure growth via two-dimensional cluster–cluster aggregation, Surf. Sci. 518 (2002) 243–250.
[66] V.A. Markel, V.M. Shalaev, P. Zhang, W. Huynh, L. Tay, T.L. Haslett, M. Moskovits, Near-field optical spectroscopy of individual surface-plasmon modes in colloid clusters, Phys. Rev. B 59 (1999) 10903–10909.

Received: 15 June 2018 | Revised: 2 November 2018 | Accepted: 9 November 2018

DOI: 10.1002/jrs.5529

RESEARCH ARTICLE

WILEY Journal of RAMAN SPECTROSCOPY

Infused self-assembly on Langmuir–Blodgett Film: Fabrication of highly efficient SERS active substrates with controlled plasmonic aggregates

Somsubhra Saha[1] | Manash Ghosh[2] | Joydeep Chowdhury[1]

[1]Department of Physics, Jadavpur University, Kolkata, India

[2]Department of Spectroscopy, Indian Association for the Cultivation of Science, Jadavpur, Kolkata, India

Correspondence
Joydeep Chowdhury, Department of Physics, Jadavpur University, 188, Raja S. C. Mallick Rd, Kolkata 700032, India.
Email: joydeep72_c@rediffmail.com; joydeepc@phys.jdvu.ac.in

Funding information
Department of Higher Education, Science and Technology and Biotechnology, Grant/Award Number: ST/P/S&T/16G-22/2017; Council of Scientific and Industrial Research (CSIR), Grant/Award Number: 03(7471)/18

Abstract

A facile procedure towards the fabrication of highly reproducible, large area surface-enhanced Raman scattering (SERS) active substrates through integration of Langmuir–Blodgett and self-assembly technique has been reported. The plasmonic architectures of the substrates can be tuned at will to control the hot spots and hence the overall enhancements of SERS signal. The as-prepared substrates of classes "A" and "B" incubated in gold nanocolloids show their respective efficacies as efficient SERS sensing scaffolds for detecting 4-MPy molecule at ultrasensitive concentrations. Moreover, these substrates are unique in their kinds, where explicit or concomitant presence of protonated and deprotonated forms of 4-MPy can be detected at trace concentrations. The substrates also exhibit remarkable spectral reproducibility and show early promise to overcome the "SERS uncertainty principle". To our knowledge, this genre of SERS active substrates with facile control over plasmonics, is the first report of its kind and are expected to provide new direction towards successful fabrication of the next generation SERS sensing platforms.

KEYWORDS

Langmuir–Blodgett film, localized surface plasmons, nanocolloids, plasmonics, SERS

1 | INTRODUCTION

Since the accidental discovery of surface enhanced Raman scattering (SERS),[1] it has been a fascinating field of study, engrossing the enriched minds of physicists, chemists, biologists, and materials scientists. In the course of scientific evolution, SERS has undergone discrete stages of development right from understanding the basic physics behind the phenomenon,[2,3] perceiving the probe substrate interactions[4,5]and their adsorption efficiencies[6,7] to the real state-of-art diagnostic applications.[8,9] The remarkable facet of SERS technique is its high specificity, providing unique "fingerprints" of molecules under study at trace concentrations. The technique can now detect vibrational signatures of molecules down to single molecule detection regime, arguably the ultimate sensitivity in terms of analytical applications.[10,11]

However, the basic snag of the phenomenon and the blazing issue of concern is the intrinsic reproducibility of the SERS active substrates. The enhancements of enormous SERS signals of probe molecules are often identified with the pragmatic fabrications of SERS active substrates having high density of aggregated nanoparticles (Nps) plasmonic architectures. The Np aggregates are believed to have the largest contribution to SERS by

harvesting the electric field at the nanogaps or clefts (hot spots) of the aggregate, promoting gigantic Raman signals. On the basis of these considerations, great deal of current research efforts are focused on the fabrication of plasmonic nanostructures that produce hot geometries, wherein the probe molecules can entrap for giant Raman enhancements.[12–14] However, unfortunately, most of these substrates fail to overcome the "SERS uncertainty principle", which predicts the reproducibility of the substrates at the expense of the enhancement factor of the Raman vibrational signatures.[15,16] Thus, more reproducible a substrate is, less is the corresponding amplification (enhancement factor) of the Raman signal.

The Langmuir–Blodgett (LB) technique has been successfully accomplished by Aroca et al. in the seminal works[17–19] to record the SERS spectra of different Raman probe molecules like texas red, perylene, methacrylate, rhodium phthalocyanine and xanthene derivatives etc. In most of those experiments, mixture of fatty acids and Raman probe molecules organized in the monolayer LB films have been deposited on metallic islands. It was established that a monolayer deposited on the silver island films exhibits homogeneous and strong SERS signals. High enhancement factors of SERS signals from probe molecules down to single molecule detection limit had been achieved by striking the nanostructure with specific excitation wavelengths in resonance with both the chromophore and the plasmon absorption peak. Moreover, the LB technique in conjunction with the bianalyte SERS together with 2D spatial mapping allow one to trace similar chemical species from multicomponent samples even at ultrasensitive concentrations.[20]

In the present manuscript, the LB technique in conjunction with the self-assembly of nanocolloids has been used to fabricate highly reproducible SERS active substrates that can sense 4-mercapto pyridine (4-MPy) molecule at ultrasensitive concentrations. Self-assembly is an elegant technique in which molecules or nanocolloids spontaneously interact with one another via unbiased attractive and repulsive interactions to form organized molecular or colloidal ensembles.[21,22] These molecular or nanocolloidal ensembles are generally guided by noncovalent interactions leading to thermodynamically stable organized structures or patterns having lower Gibbs free energies. The plasmonic architectures of the as-prepared substrates can be tuned at will to control the gap plasmons and hence, the overall enhancement of the SERS signals. To our knowledge, this genre of SERS active substrates with facile control over plasmonics facilitated by the aggregation of the nanocolloidal particles, is the first report of its kind and is expected to provide a new rostrum towards successful fabrication of next generation SERS sensing platforms.

2 | EXPERIMENTAL PROCEDURE

2.1 | Materials and methods

4-MPy molecule (~95% purity), poly (methyl methacrylate; PMMA, average molecular weight [M_w] ~1,20,000), and chloroauric acid ($HAuCl_4$) of spectroscopic grades were purchased from Sigma-Aldrich and were used as received. Tri-sodium citrate, ethanol, acetone were purchased from E-Merck (Germany) and were used without further purification. Chloroform of spectral grade was purchased from SRL, India and was used as received. Before performing the experimental work, all the glass wares used in the synthesis were cleaned with freshly prepared aqua regia and were thoroughly rinsed with distilled water. Triple distilled deionized water (resistivity ~18.2 MΩ cm, pH ~6.8) from Milli-Q plus system of Millipore Corporation, USA was used throughout the experiment.

Spherical gold nanocolloids (AuNCs) of average particle diameter ~55 nm were synthesized by citrate reduction method as reported by Frens.[23,24] Typically, 50 ml aqueous solution of $HAuCl_4$ (0.1 M), used as precursor salt, was heated up to boiling. To it 400 μl of trisodium citrate (1%) was added followed by vigorous stirring. The faint blue colored solution finally turned to pink confirming the formation of quasi spherical gold nanocolloidal particles of average particle diameter ~55 nm.

The glass slides made of quartz were cleaned vigorously with ethanol, deionized water and acetone. An alternate layer computer controlled the LB trough (model no. D2007, Apex Instruments) has been used to lift the monolayer LB film of PMMA following Y-type deposition technique. The sub phase was filled with triple distilled deionized water of 18.2 MΩ cm resistivity and pH ~6.8. The surface pressure was recorded by the Wilhelmy method using a filter paper. PMMA of concentration 0.5 mg/ml in chloroform solvent was dispensed on the air-water interface of the LB trough maintained at room temperature. After waiting for 20 min, allowing all the chloroform solvent molecules to evaporate, PMMA molecules form floating monolayer at the air-water interface. The Teflon barriers of the dual LB trough were then compressed quasistatically at a constant speed of 2 mm/min. Compression of the barriers result in the increase in surface pressure (π) with proportional decrease in area/molecule of the system. The variation in surface pressure (π) as a function of area/molecule (A) is depicted as π- A isotherm plot. The room temperature surface pressure-area (π-A) compression isotherm was monitored throughout the compression steps with the aid of a film balance.

The monolayer LB films of PMMA were lifted at 40 and 10 mN/m surface pressures on precleaned quartz

slides (Tedpella, Inc) of area ~2 × 1 cm^2 by Y-type deposition technique. The LB film substrates covering ~2 × 1 cm^2 area of the quartz slides were then immersed in the AuNCs for 24 hr at room temperature under normal atmospheric pressure. The Au nanoparticles (AuNps) get adsorbed to the PMMA matrix of the LB film probably through its carbonyl group. Monomer unit of PMMA molecule consists of one carbonyl (C=O) group and the other ester functional group containing oxygen atom. The oxygen atom of the C=O group has higher negative charge density in contrast to the C—O bond of the ester group. Thus, it is more likely that AuNps may bind with PMMA through the lone pair electrons of oxygen atom associated with the C=O group of the polymer. Moreover, the interactions between the AuNps and PMMA have also been investigated in detail from the x-ray photoelectron spectroscopy (XPS) studies, reported elsewhere.[25,26] The survey scans of pure PMMA and Au-PMMA composites show the existence of carbon (C), oxygen (O) and gold (Au) atoms only. The XPS scans of C1s, O1s and Au4f provide specific idea about the interaction. The relative intensity ratio of the C=O peak to the C—O—C peak of PMMA in the XPS spectra increases with increase in concentration of gold nanoparticles in PMMA. These results signify interaction between Au and oxygen atoms through the C=O groups of PMMA. Moreover, the shift of the Au4f doublet peak towards the higher binding energies in case of higher Au concentrated samples further corroborates the interaction between Au and O via the carbonyl C=O group of PMMA. The films were then removed from the colloid, washed thoroughly with deionized water and allowed to dry in hot air oven. This process helps to eliminate the excess unreduced gold ions from the as-prepared film surface. Finally, 25 μl aqueous solution of 4-MPy with varied concentrations ranging from 1.0 × 10^{-4}–1.0 × 10^{-12} M have been adsorbed on the as-prepared substrates, dried in hot air oven before recording its SERS spectra.

2.2 | Instrumentation

The electronic absorption spectra were recorded by the Jasco UV-Vis absorption spectrometer (Model No: V-630). The normal Raman spectrum (NRS) and SERS spectra were recorded by J–Y Horiba Confocal Triple Raman Spectrometer (Model: T 64000) attached with holographic gratings of 1800 groove/mm and a TE cooled synapse CCD detector from J–Y Horiba. The 632.8 nm red line of He-Ne laser (power ~1 mW) was used as the excitation source, both for recording the NRS and SERS spectra of the molecule. The laser was focused with an Olympus open stage microscope of 50× objective (N.A. = 0.75) lens and the scattered signals were collected at 180 degree scattering angle to the excitations. The data acquisition time for each spectrum was 20 s. The Field Emission Scanning Electron Microscope (FESEM) images were acquired with INSPECT F50 FESEM with 10 kV excitation energy. The energy-dispersive X-ray spectroscopy (EDX) analyses of the as-prepared substrates were performed by Bruker Nano, equipped with EDAX made X-Flash detector (410-M). The morphologies of the as-prepared substrates were also studied with Asylum Research (Model No. MFP-3D) atomic force microscope (AFM) procured from the Oxford Instruments.

2.3 | Theoretical calculations

The spatial distributions of electric fields around the nanoaggregated geometries were estimated with the aid of three-dimensional finite difference time domain (3D-FDTD) simulations using 3D-FDTD Lumerical Solutions, Inc.[27] The Yee cell with dimension 1 × 1 × 1 nm^3 was chosen for the calculations. The Johnson–Christy dielectric data for gold and water, with real refractive index 1.33, were introduced. In the simulation run, the amplitude of the incident plane polarized light wave was set ~1 v/m and 632.8 nm wavelength was fixed as the excitation light source. The undesired reflections and back scattering of the electric fields were avoided by introducing perfectly matched layer (PML) boundary condition. The simulation time was set at 500 fs, which assures the total concurrence of the electric field.

The spatial distributions of electric fields around the nanoaggregated domains have been further utilized to estimate the SERS enhancement factor $G(\bar{\upsilon},\bar{\upsilon}')$ following plane wave (PW) approximation. The PW approximation expresses $G(\bar{\upsilon},\bar{\upsilon}')$ as the product of electric field intensities incident at wavenumber "$\bar{\upsilon}$" [$\left|\vec{E}_{loc}(\vec{r}_0,\bar{\upsilon})\right|^2$] and the other at Stokes shifted wavenumber "$\bar{\upsilon}'$" [$\left|\vec{E}_{loc}(\vec{r}_0,\bar{\upsilon}')\right|^2$] for the location of the molecule fixed at $\vec{r}_0$. Accordingly[28,29]

$$G\left(\bar{\upsilon},\bar{\upsilon}'\right)=\left|\vec{E}_{loc}\left(\vec{r}_0,\bar{\upsilon}\right)\right|^2\left|\vec{E}_{loc}\left(\vec{r}_0,\bar{\upsilon}'\right)\right|^2. \quad (2)$$

For the zero Stokes shift approximation, the expression (2) is further reduced to[28,29]

$$G\left(\bar{\upsilon},\bar{\upsilon}'\right)=\left|\vec{E}_{loc}(\bar{\upsilon})\right|^4. \quad (3)$$

Thus the SERS enhancement factor approximately scales as fourth power of the local electric field intensity incident at wavenumber "$\bar{\upsilon}$".

3 | RESULTS AND DISCUSSIONS

3.1 | Room temperature pressure-area isotherm of Langmuir monolayer

PMMA is known to form floating monolayer at the air-water interface. The room temperature surface pressure area (π)—area (A) compression isotherm of PMMA at the air-water interface is shown in Figure 1. Under isothermal compression, the PMMA monolayer at the air-water interface undergoes several phase transitions of 1st order. No trace of gaseous phase transition is observed in the isotherm plot. The proportional increase in surface pressure with decreasing area is first observed in the surface pressure range ~0 to 14 mN/m indicating the existence of liquid expanded (LE) phase. Thereafter, a small plateau like region in the curve is observed, followed by a sharp rise in surface pressure at ~21 mN/ m proceeding to collapse of the monolayer. Significant increase in the surface pressure with small decrease in area marks the second phase transition, representing liquid condensed (LC) state of the monolayer assemblies at the air-water interface. The nature of the isotherm is in accordance with the earlier reports[30] and the area/PMMA molecule is estimated to be ~0.16 nm^2/molecule. The monolayer LB film of PMMA was first lifted by the Y-type deposition technique on the precleaned quartz substrates at a constant surface pressure of 40 mN/m. The as-prepared LB films were then immersed in the nanocolloidal gold solutions at various incubation times (ITs) ranging from 2 to 48 hr. The films were then subsequently rinsed in deionized water to remove any unneutralized ions over the surface and were finally left to dry in a vacuum chamber.

3.2 | UV–Vis spectra of the as-prepared substrates

Figure 2a shows the room temperature UV–Vis electronic absorption spectrum of pristine AuNCs. The absorption spectrum of AuNC, as shown in Figure 2a, exhibits a strong absorption maximum centered at ~534 nm, along with broad humps at ~262 and 375 nm. The former band has been broadly ascribed to localized surface plasmon resonance (LSPR) whereas the later pair is owed because of the intra band electronic transitions of gold nanoparticles.[5,24] Figures 2b–d shows the corresponding absorption spectra of AuNC immersed in the monolayer LB film of PMMA for various ITs ranging from 12 to 36 hr. The LSPR peaks of AuNC adsorbed in the LB films of PMMA are decreased in intensity, red shifted with respect to 534 nm band of pure AuNC and appear as shoulder ~548–554 nm in the UV–Vis spectra. Additionally, broad absorption maxima ranging from ~594–674 nm for AuNC self-assembled in the LB films of PMMA have been observed. The broad bands ~594–674 nm primarily mark the existence of various aggregated states of the AuNCs self-assembled in the PMMA matrix of the monolayer LB film.[31,32] These low energy bands in the UV–Vis absorption spectra are now specifically ascribed to surface like surface Plasmon resonance (SL-SPR) and their appearance are intimately related with the degrees of aggregation of the AuNCs.[3]

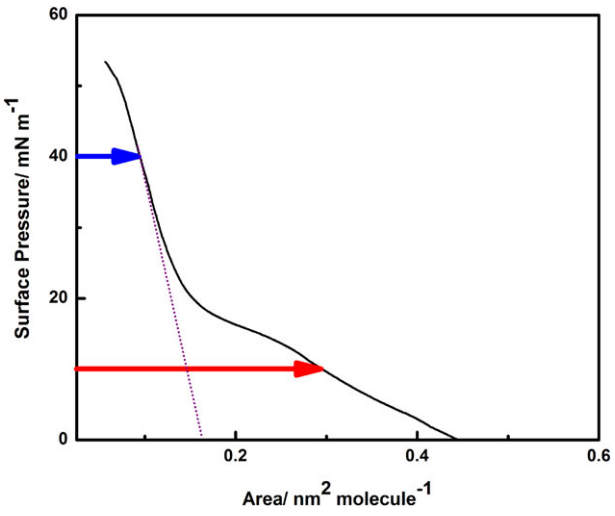

FIGURE 1 Room temperature surface pressure (π)—Area (A) compression isotherm of a Langmuir monolayer of poly (methyl methacrylate; PMMA) in pure water sub phase (pH ~6.8) [Colour figure can be viewed at wileyonlinelibrary.com]

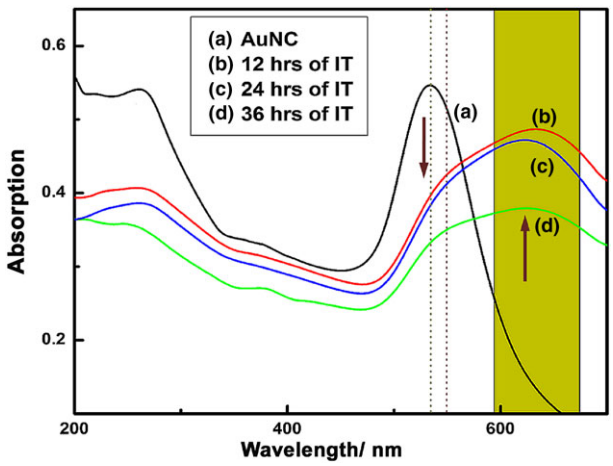

FIGURE 2 Room temperature UV–Vis electronic absorption spectra of (a) AuNC and [(b)–(d)] AuNC self-assembled in the monolayer Langmuir–Blodgett (LB) film of poly (methyl methacrylate; PMMA) at various incubation times (ITs) [Colour figure can be viewed at wileyonlinelibrary.com]

The interplay between short range nanoparticle–nanoparticle (F_{NNA}), nanoparticle–monolayer (F_{NMA}), monolayer–monolayer (F_{MMA}) attractive and dipolar long range nanoparticle–nanoparticle repulsive (F_{NNR}) forces may favor the self-assembly of the AuNC over the monolayer LB film matrix of PMMA. The precise balance between the attractive and repulsive forces provide the necessary thermodynamic stability towards the generation of gold nanocolloidal aggregates of different degrees on the PMMA matrix, each of whose optical responses is characterized by their respective low energy bands. The broadening and the LSPR shifts, together with the appearance of low energy bands in the UV–Vis absorption spectra, thus, steer us to introspect the morphological and topographical details of the aggregated nanocolloids entrapped in the monolayer LB film of PMMA.

3.3 | Morphological and topographical features of the as-prepared substrates

The morphological features of the as-prepared substrates are visualized from the FESEM images. The FESEM images of the bare glass slide and the monolayer LB film of PMMA lifted at 40 mN/m surface pressure are shown in Figures 3a and b respectively. Figure 3b shows the compact arrangement of monolayer PMMA on the quartz glass slide structured with aggregated domains of sizes ~50–420 nm. The 2D and 3D AFM images of the same film, scanned over 5 μm × 5 μm surface area, as shown in Figure S1 (i) and (I) respectively in the Supporting Information, also corroborates this observation. The monolayer LB film substrate of PMMA lifted at 40 mN/m surface pressure will henceforth be designated as substrate of class "A". The FESEM images of the substrates

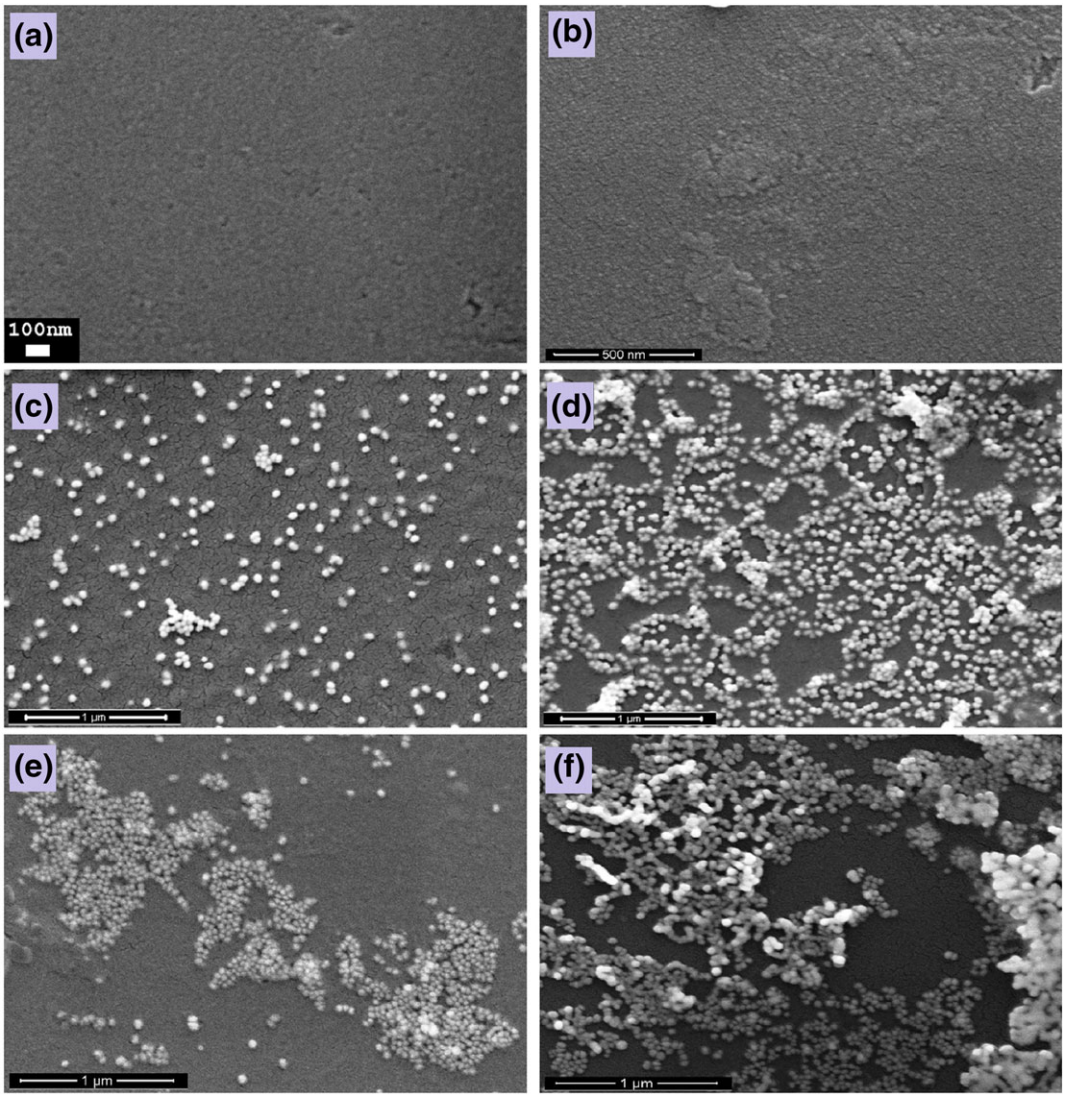

FIGURE 3 Nanometer scale Field Emission Scanning Electron Microscope (FESEM) images of (a) bare quartz slide, (b) as-prepared substrate of class "A"; modified substrates of class "A" after incubation in AuNC for (c) 2 hr, (d) 24 hr, (e) 36 hr, and (f) 48 hr of incubation times (ITs) [Colour figure can be viewed at wileyonlinelibrary.com]

of class "A" immersed in AuNCs over various ITs are shown in Figures 3c–f. After 2 hr of IT, segregated gold nanocolloidal particles are seen to remain embedded on the monolayer LB film matrix of PMMA (Figure 3c). Interestingly, with increase in IT, Nps begin to form aggregated domains. The FESEM image of the substrate, captured after 24 hr of IT, depicts high density aggregated patterns of AuNps interlaced to form chain like structures. With further increase in IT, the chain like pattern turns to archipelago, stuffed with densely packed aggregated domains of the AuNps (Figure 3d). The FESEM image of the as-prepared substrate, accomplished after 48 hr of IT, is depicted by further agglomeration of gold nanocolloidal particles on the monolayer LB film of PMMA matrix. The elemental analysis of the monolayer LB film substrate of PMMA incubated in AuNC for 24 hr of IT is shown in Figure S2 in the Supporting Information. The EDX analysis confirms the expected existence of gold, oxygen and carbon on the as-prepared film substrate, together with the presence of Na, Mg, Ca and K atoms, stemming from the quartz slide. We will call the as-prepared substrates as "modified substrates of class A".

Close inspection of the FESEM images, as shown in Figures 3c–f, indicate that upon changing the ITs of AuNC in PMMA matrix, the plasmonic architectures of the modified substrates of class "A" can be controlled with precise ease. Controlling the plasmonic architectures of the substrates through aggregation and segregation of the Nps are fundamental towards the possible generation of hot geometries and hence, ushers in greater possibilities for the probe molecules to get betwixed within the hot spots. Interestingly, apart from changing the IT of the nanocolloids on the PMMA template, the plasmonic architecture of the substrates can also be tuned by lifting the monolayer LB film of PMMA at lower surface pressure (~10 mN/m). The FESEM image of the monolayer LB film of PMMA lifted at 10 mN/m surface pressure is shown in Figure 4a. We name this as substrate of class "B". The FESEM image of the substrate of class "B" exhibit less compact structure containing granules, free from aggregated domains. The AFM images of the same structure, as shown in Figure S1 (ii) and (II) respectively in the Supporting Information is in accordance with the FESEM observation. Figure 4b shows the FESEM image of the class "B" substrate, incubated in AuNCs for 24 hr of IT. Alike substrate of class "A", we designate this as "modified substrate of class B". The final image of the as-prepared modified substrate of class "B" exhibits segregated domains mostly of dimeric or trimeric AuNps that remain dispensed on the monolayer LB film template of PMMA. Significantly, this disposition closely resembles the plasmonic architecture of the monolayer LB film substrate of PMMA lifted at 40 mN/m surface pressure when dipped in gold nanocolloidal solution for 2 hr of IT [Figure 3c (vide ante)]. The electronic absorption spectrum of the modified substrate of class "B" is shown in Figure S3 (Supporting Information), along with that recorded for pristine AuNC. Interestingly as observed for the modified substrate of class "A", this substrate also exhibits weak LSPR band at ~548 nm along with low energy SL-SPR band peaked at ~634 nm. The SL-SPR band for the modified substrate of class "B" is less broadened in comparison with that for the modified substrate of class "A" (Figure 2). This result may signify apparent perturbations in the dipole–dipole interactions among the segregated and aggregated domains of the nanoantennas prevalent in the modified substrates of classes "B" and "A" respectively.

Thus, the organized molecular architectures of the ultrathin LB films of PMMA in the form of segregated and aggregated domains lifted separately at 40 and 10 mM/m surface pressures respectively in the backdrop, dominated by F_{MMA}, together with F_{NNA}, F_{NMA} and F_{NNR} from the self-assembly of the AuNC, play a pivotal role in controlling the aggregated or segregated behaviors of gold

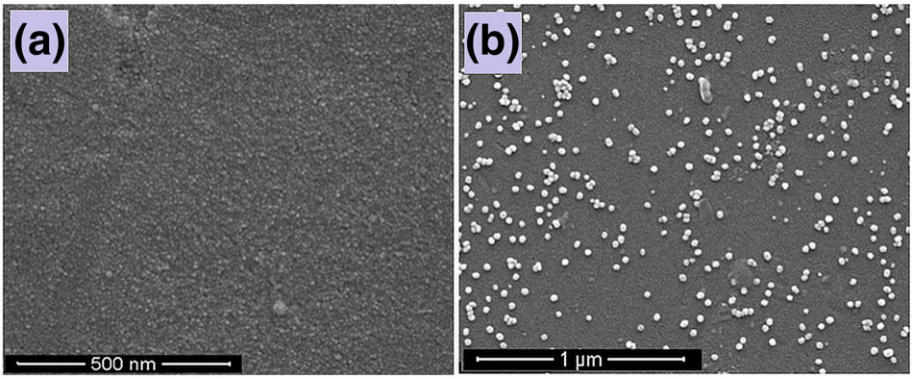

FIGURE 4 Nanometer scale Field Emission Scanning Electron Microscope (FESEM) images of (a) asprepared substrate of class "B", (b) as-prepared modified substrate of class "B" immersed in AuNC for 24 hr of incubation times (IT) [Colour figure can be viewed at wileyonlinelibrary.com]

nanocolloids. Power of the LB technique in conjunction with the self-assembly of nanocolloids, thus provides a unique way to generate the interstitial gaps less than 2.14 (±0.679) nm within the dimeric or trimeric Nps. These interstitial plasmon gaps less than ±2.14 (±0.679) nm can act as hot sites for the protrusion of probe molecules to exhibit enhanced vibrational signatures in the SERS spectra. In this connection, it may be emphasized that such small and controlled interstitial gap plasmons are unique in nature and are not achievable from any other soft lithographic techniques or even with the aid of anodic aluminum oxide (AAO) templates.[33–35] This can only be accomplished through the LB technique.

The AFM images of the as-prepared modified substrates of classes "A" and "B", are shown in Figures 5 (a,b) and 5 (c,d) respectively. These images clearly mark the presence of intermittent aggregated and segregated domains of nanocolloidal particles dispensed on the monolayer LB film substrates of PMMA lifted at 40 and 10 mN/m surface pressures respectively. The topographical features are in accordance with the corresponding FESEM images as shown in Figures 3d and 4b. The nanoaggregated domains, embedded in the monolayer LB film matrix of PMMA, may act as possible hot sites for harvesting enormous near-field within the interstitial gaps of the AuNps.

3.4 | Efficacy of the as-prepared substrate for SERS

The efficacies of the as-prepared modified substrates of classes "A" and "B" for detecting SERS signals are tested with 4-MPy as reporter molecule. The 4-MPy molecule has two pK_a values, one at 1.43 and the other at 8.83.[36,37] The molecule is known to exist as protonated–deprotonated and in thiol–thione tautomeric forms. They are shown in Figure S4 (Supporting Information). The NRS of 4-MPy in aqueous medium (pH ~7) at 1 M concentration is shown in Figure S5 (Supporting Information). The NRS spectrum shows distinct vibrational signatures at 429, 723, 1001, 1053, 1114, 1207, 1589, 1614 and 1621 cm^{-1} characteristic of 4-MPy molecule. The band at 429 cm^{-1} owes to out of plane δ(C-S)/γ

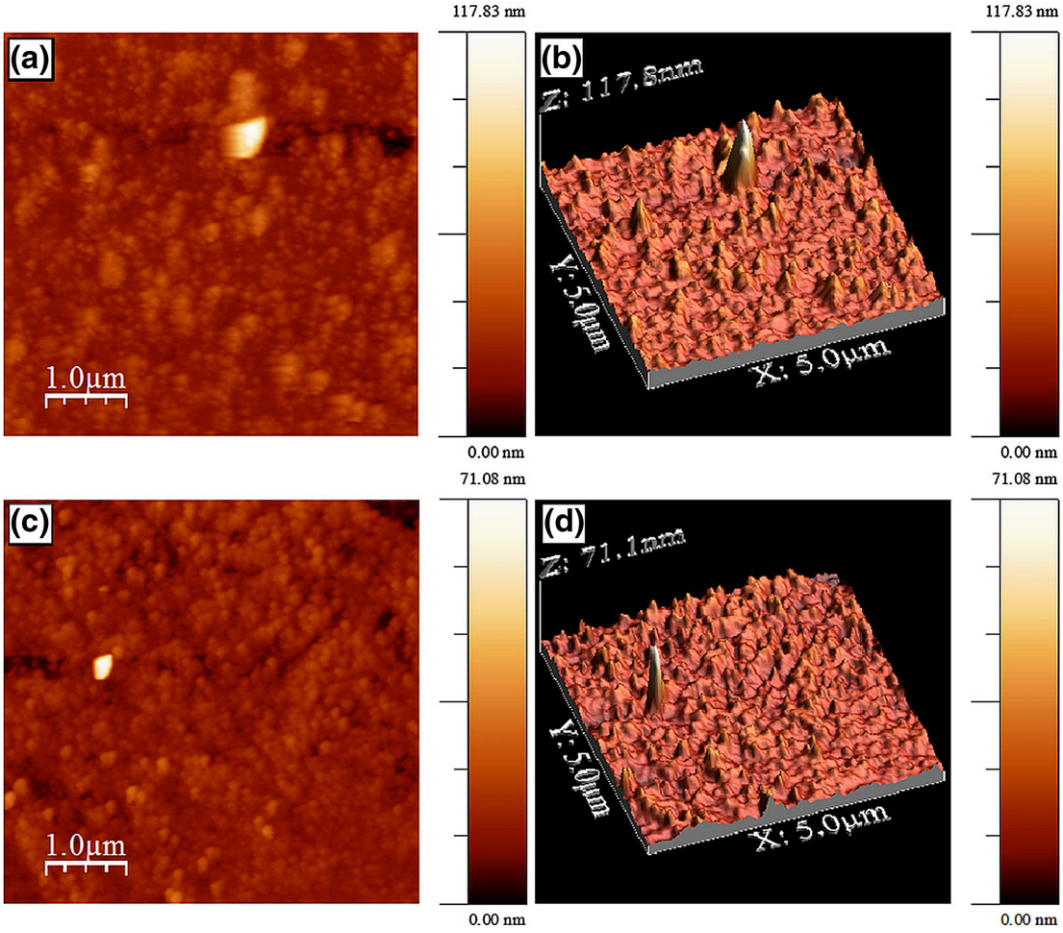

FIGURE 5 Left column: (a) and (c) 2D atomic force microscopy (AFM) images; right column: (b) and (d) corresponding 3D AFM images of the modified substrates of class "A" and "B" respectively [Colour figure can be viewed at wileyonlinelibrary.com]

(CCC) vibrational signature. The Raman signals at 1114 and 723 cm^{-1} are the X-sensitive bands where the υ(C—S) stretching vibrations are coupled with the ring breathing and in-plane β (CC) bending modes of the molecule respectively.[38–40] Strong and intense ring breathing vibration ($υ_1$) appears at 1001 cm^{-1} together with the medium intense band at 1621 cm^{-1}. The appearance of the Raman band at 1621 cm^{-1}, assigned to υ(C=C) stretching vibrations of the pyridine ring of the molecule,[39,41,42] marks the presence of the protonated form of 4-MPy molecule in aqueous solution. Table 1 shows the vibrational assignments of some specific the Raman and SERS bands of protonated and deprotonated forms of 4-MPy molecule, whose detailed analysis are reported elsewhere.[39–45]

Figure 6 shows the SERS spectra of 1.0×10^{-6} M 4-MPy molecule pH ~7 adsorbed on the as-prepared modified substrates of class "A" incubated in AuNC for various ITs spanning from 2 to 48 hr. All the substrates of class "A" dipped in AuNC for various ITs act as effective SERS sensing scaffolds, albeit the spectrum recorded after 24 hr of IT exhibits the best execution of signal to noise ratio. The SERS spectra show enhancements of Raman bands centered at around 1004, 1092 and 1205 cm^{-1}. Among them, the X-sensitive bands at ~708 and 1092 cm^{-1} are remarkably down shifted with respect to the NRS counterpart at 721 and 1114 cm^{-1} respectively. The enormous downshift of the X-sensitive bands together with no trace of υ(S—H) stretching vibration at ~2575 cm^{-1} [42] in the SERS spectra (not shown in the figure) primarily suggest the existence of protonated state of the thione form of 4-MPy molecule. Presence of protonated form of the molecule is further substantiated by the appearance of enhanced Raman bands at ~1204 and ~1610 cm^{-1}. The 1204 cm^{-1} has been assigned to mixed vibrations from the CH in-plane and N—H out of plane bends and is associated with the protonated form of the 4-MPy molecule.[40–44] Interesting observation can be drawn from the enhancements and relative intensities for the pair of bands centered at ~1610 and 1577 cm^{-1}. Both these bands are ascribed to υ(C—C) stretching vibrations, however, the former originating from the protonated whereas the later from the deprotonated species of 4-MPy molecule.[40–42,46] Strong enhancements of 1610 cm^{-1} band in comparison with that of 1577 cm^{-1} further justify the preponderance of protonated species in comparison with the deprotonated one in the surface adsorbed state. Interestingly, span in the ITs of the nanocolloids on pristine LB film substrates of PMMA is correlated with the existence of mixed or protonated form of the reporter molecule. At lower ITs (2–24 hours), the SERS spectra exhibit the presence of both the protonated and the deprotonated forms whereas for the higher ITs (36–48 hours), explicit presence of the protonated form of 4-MPy molecule are suggested.

The concentration dependent SERS spectra of 4-MPy molecule at pH ~1 and pH ~10 are shown in Figures S6 and S7 respectively in the Supporting Information. Concentration dependent SERS spectra of 4-MPy molecule at pH ~1, adsorbed on the modified substrate of class "A" (Figure S6) is marked by the presence of enhanced Raman bands centered at ~1610, 1201, 1094 and 1002 cm^{-1} together with weak hump at ~1579 cm^{-1}. The appearance of bands centered at ~1610 and 1201 cm^{-1} signify the predominant existence of the protonated form of the probe

TABLE 1 Enhancement Factors (EFs) of SER bands of 4-MPy molecule adsorbed on the as-prepared modified substrates of classes "A" and "B"

NRS (cm^{-1})	Adsorbate concentrations									
		10^{-4} M		10^{-6} M		10^{-10} M		10^{-12} M		
	Substrate	SERS	EF	SERS	EF	SERS	EF	SERS	EF	Assignment [a]
1001	Class A	1006	3.03×10^2	1005	8.92×10^4	1006	3.86×10^8	1008	1.43×10^9	Ring breathing ($ν_1$)
	Class B	1004	7.94×10^2	1004	8.19×10^4	1009	1.05×10^7	----	----	
1114	Class A	1092	2.23×10^3	1092	4.73×10^5	1092	1.01×10^9	1094	7.07×10^9	Trigonal ring-breathing with C=S deformation ($ν_{12}$)
	Class B	1094	4.01×10^3	1094	5.70×10^5	1094	4.47×10^7	1097	4.11×10^9	
1207	Class A	1210	2.36×10^3	1207	4.69×10^5	1210	1.60×10^9	1210	1.49×10^{10}	$β_{(C—H)}$ ($ν_9$)
	Class B	1209	3.93×10^2	1205	6.67×10^5	1210	5.92×10^7	1213	1.16×10^{10}	
1589	Class A	1574	2.98×10^3	1579	3.83×10^5	1581	7.43×10^9	1576	2.96×10^{10}	$ν_{(C—C)}$ ($ν_8$)
	Class B	1576	3.89×10^2	1579	7.25×10^5	1580	1.39×10^8	1572	2.47×10^{10}	
1621	Class A	1610	1.45×10^3	1610	3.13×10^5	1608	1.83×10^9	1608	1.08×10^{10}	$ν_{(C—C)}$ ($ν_8$)
	Class B	1610	2.45×10^3	1611	3.81×10^5	1616	1.46×10^7	----	----	

Note. NRS: normal Raman spectrum; SERS: surface-enhanced Raman spectroscopy.

[a]ν–stretching; β–in-plane bending.

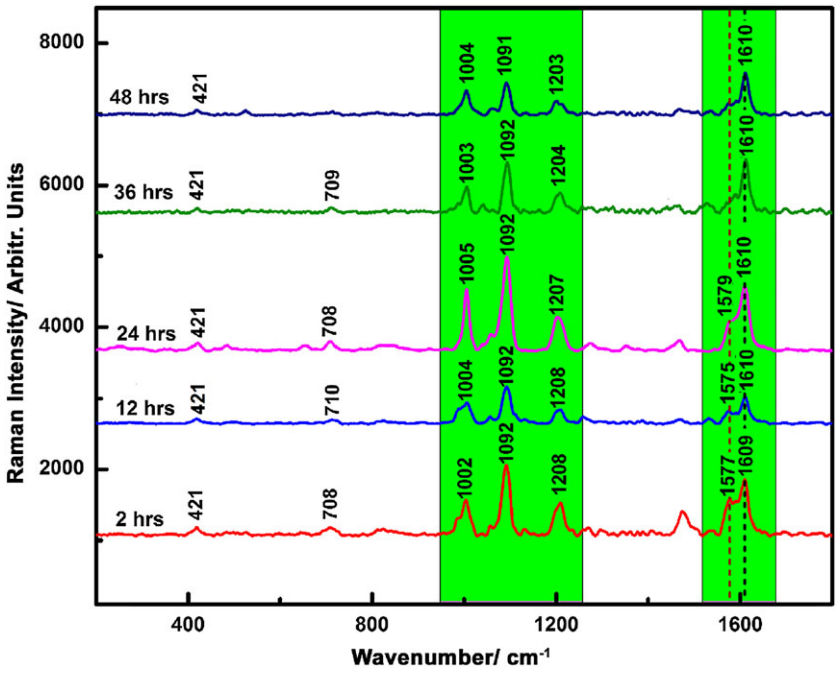

FIGURE 6 Surface-enhanced Raman spectroscopy (SERS) spectra of 1.0×10^{-6} M 4-MPy molecule at pH ~7 adsorbed on the as-prepared modified substrates of class "A" incubated in AuNC for various incubation times (ITs; λ_{ex} = 632.8 nm) [Colour figure can be viewed at wileyonlinelibrary.com]

molecule in the surface adsorbed state at pH ~1. Interestingly, the SERS spectra of 4-MPy molecule recorded at pH ~10 for various concentrations of the adsorbate are dominated by the Raman bands centered at ~1576, 1210, 1092 and 1002 cm^{-1}. In addition to these, a band at ~1609 cm^{-1}, weaker in intensity in comparison to the intense band at ~1576 cm^{-1} is observed. They are shown in Figure S7 (Supporting Information). However, the presence of 1576 and 1210 cm^{-1} bands in the entire concentration dependent SERS spectral profile presage the predominant existence of the deprotonated form of the 4-MPy molecule at alkaline pH (pH ~10). Considering the two pKa values of 4-MPy (at 1.43 and 8.83)[36,37] this is an expected observation, where the protonated form of the molecule is expected to be dominant at lower pH (pH ~ 1), whereas at higher pH value (pH ~10), the deprotonated form of the molecule is preponderant. The expected observation is in harmony with the enhanced vibrational signatures of 4-MPy molecule, as recorded from the pH dependent SERS spectra.

Figure 7 shows the concentration dependent SERS spectra of the reporter 4-MPy molecule at pH ~7 adsorbed on the modified substrates of class "A". The spectra show remarkable changes in features of enhanced Raman bands. At higher concentrations (~1.0×10^{-4} to 1.0×10^{-6} M), the spectra are dominated by the enhanced bands centered at ~1005, 1092, 1208 and 1610 cm^{-1}. The appearance of the above mentioned bands signify the existence of protonated form of the molecule, which get adsorbed through its sulfur atom on the substrate. The enhancements of in-plane vibrational modes together with the moderate enhancement of Raman band at ~425 cm^{-1}, ascribed to δ(C—S)/γ (C—C—C) out-of-plane vibration[38,41,47] may signify tilted adsorptive stance of 4-MPy molecule on the modified substrate of class "A" through the lone pair electrons of sulfur atom. However, in the lower concentration domain (1.0×10^{-7}-1.0×10^{-12} M), the SERS spectra are remarkably different from those recorded at higher concentrations of the adsorbate. Significant observation can be drawn from the intensity reversal between the pair of bands at 1572 and 1610 cm^{-1}.

With decrease in concentration, the band 1572 cm^{-1} gains in intensity with concomitant weakening of the other band at 1610 cm^{-1}. At 1.0×10^{-10} and 1.0×10^{-12} M concentrations, the strongest band appears in the SERS spectra at ~1576–1581 cm^{-1}. The presence of the bands at ~1572–1581 cm^{-1} and at ~1058 cm^{-1} together with the upshift of the 1210 cm^{-1} band, mark the existence of the deprotonated form of 4-MPy molecule at lower concentrations of the adsorbate. Thus the modified substrate of class "A" can act as exclusive sensor for detections of protonated and deprotonated forms of 4-MPy molecule at trace concentrations. At higher concentrations of the adsorbate (~1.0×10^{-4}–1.0×10^{-6} M), predominant existence of the protonated forms of the molecule are estimated, while at lower concentrations (~1.0×10^{-10}-1.0×10^{-12} M), the presence of the deprotonated forms of 4-MPy are explicitly detected. At the intermediate concentration ~1.0×10^{-7} M, both the forms of the molecule are found to coexist.

Interesting conclusion may be extended from the SERS spectra of the molecule adsorbed on the modified substrate of class "B". They are shown in Figure 8. At higher concentrations of the adsorbate (~1.0×10^{-4} M),

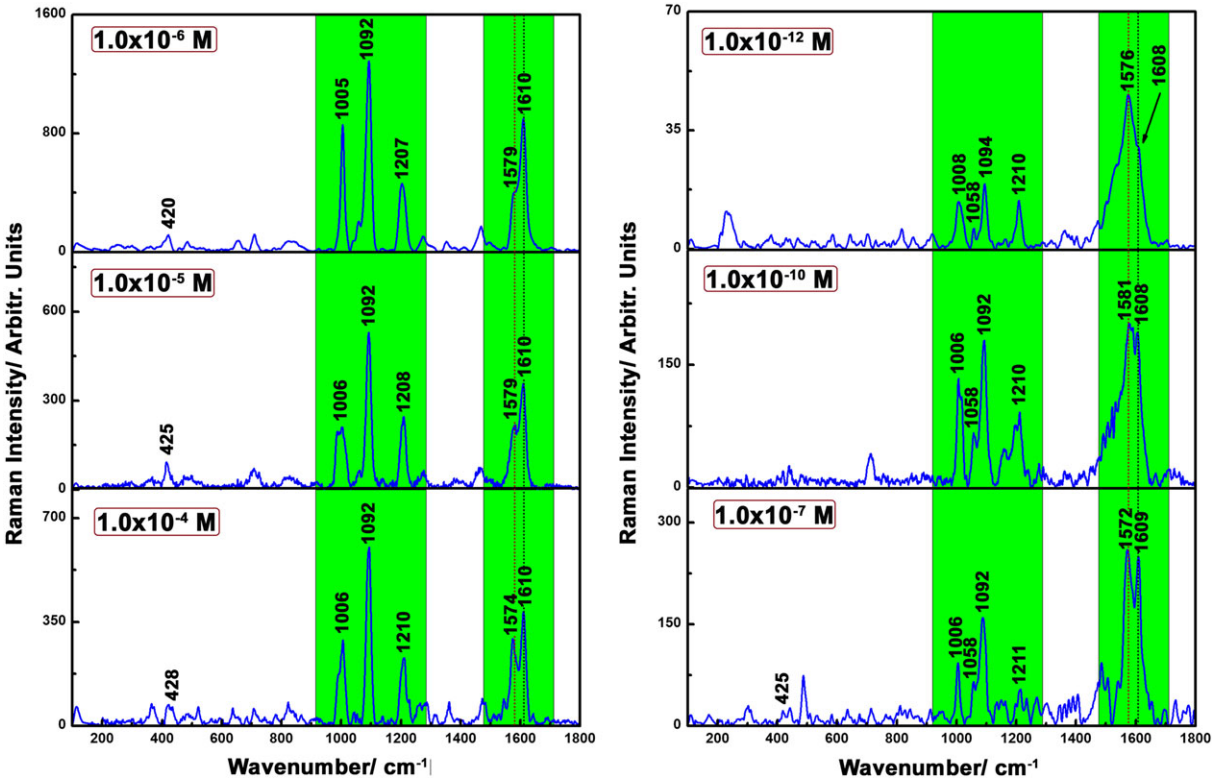

FIGURE 7 Concentration dependent Surface-enhanced Raman spectroscopy (SERS) spectra of 4-MPy molecule at pH ~7 adsorbed on the modified substrates of class "A" incubated in AuNC for 24 hr of incubation time (IT; λ_{ex} = 632.8 nm) [Colour figure can be viewed at wileyonlinelibrary.com]

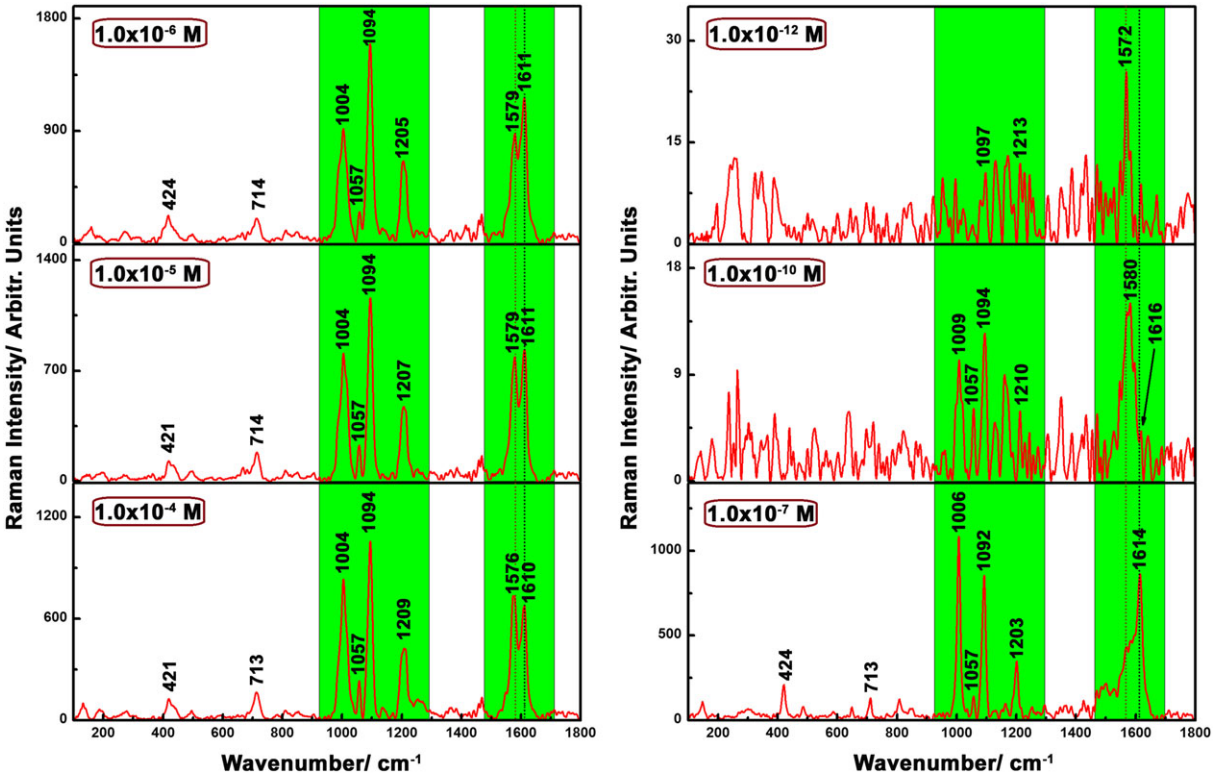

FIGURE 8 Concentration dependent Surface-enhanced Raman spectroscopy (SERS) spectra of 4-MPy molecule at pH ~7 adsorbed on the modified substrates of class "B" incubated in AuNC for 24 hr of incubation time (IT; λ_{ex} = 632.8 nm) [Colour figure can be viewed at wileyonlinelibrary.com]

strong enhancements of 1576, 1209 and 1057 cm^{-1} bands mark the presence of deprotonated form of 4-MPy molecule.[46] The substantial red shift of enhanced Raman bands centered at ~713 and at 1094 cm^{-1} again presage the adsorption of the molecule on the substrate through the lone pair electrons of the sulfur atom. Interestingly, reversal in intensities between the pair of bands at 1578 and 1611 cm^{-1} are observed at 1.0×10^{-5} and 1.0×10^{-6} M concentrations of the adsorbate. With decrease in concentration of the adsorbate, 1611 cm^{-1} gains in intensity, with progressive downshift of the band at ~1205 cm^{-1}, and weakening in the intensity of 1057 cm^{-1}. These results signify the existence of both the protonated and deprotonated forms of the molecule. At relatively lower concentration of the adsorbate (~1.0×10^{-7} M), the band centered at ~1579 cm^{-1} disappears with distinct enhanced vibrational signatures recorded only at 1614, 1203, 1092 and 1006 cm^{-1}. The enhancements of these specific Raman bands envisage exclusive presence of the protonated form of 4-MPy molecule on the modified substrate of class "B". Interestingly, further lowering in the adsorbate concentrations (~1.0×10^{-10} M–1.0×10^{-12} M) exhibit the reappearance of the band centered at ~1572–1580 cm^{-1}. The reappearance of the band centered at ~1572–1580 cm^{-1}, together with the upshift of 1210 cm^{-1} band, albeit weak in intensity, presage the presence of deprotonated form of 4-MPy adsorbate on modified substrate of class "B" at lower concentrations (~1.0×10^{-10}–1.0×10^{-12} M) of the adsorbate. However, substantial downshifts of enhanced Raman bands at ~713, 1094 cm^{-1} in conjunction with the enhancements of both in-plane and out-of-plane vibrational modes at ~713, 1006, 1057, 1094, 1210, 1576, 1611 and 424 cm^{-1} respectively in the entire concentration dependent SERS spectral profile favor tilted adsorption stances of both the protonated and deprotonated forms of 4-MPy molecule through the lone pair electrons of sulfur atom on the modified substrate of class "B".

In this connection discussions concerning simultaneous or explicit presence of protonated, deprotonated forms of the 4-MPy molecule in the adsorbed state with the corresponding pKa values demand considerable attention. In free state, the pKa values of 4-MPy are at 1.43 and 8.83, involving dissociation of proton attached to —SH and —NH groups of the molecule respectively (vide supra, Figure S4). Thus in neutral pH medium 4-MPy molecule may co-exist in A↔B thione tautomeric forms and/or its corresponding thiol form. They are shown in Figure S4. However, the vibrational signatures of enhanced Raman bands as depicted in Figures 7 and 8 preclude the existence of thiol and presage the presence of protonated and deprotonated thione forms of the molecule (vide ante). The possible protonated and deprotonated thione forms of the molecule in the surface adsorbed state are (A, B) and (C, D) respectively as shown in Figure S4. The existence of deprotonated C ↔ D forms of the 4-MPy molecule in the surface adsorbed state clearly indicates significant effect on its pKa (~8.83) value upon absorption. This means 4-MPy molecule adsorbed on the as-prepared modified substrates of classes "A" and "B" is ionized at neutral pH which is essentially lower than what is required to deprotonate the species. The lowering in pKa values of molecules in surface adsorbed state in comparison with its free form is a well-known observation and are reported elsewhere.[48]

Thus, the as-prepared modified substrates of classes "A" and "B" both show their respective efficacies as efficient SERS sensing scaffolds for detecting 4-MPy molecule at ultrasensitive concentrations. Moreover, these substrates are unique of their kinds, where explicit presence of protonated and deprotonated forms of 4-MPy can be detected at trace concentrations for the first time. The as-prepared substrates covering 2×1 cm^2 area of the quartz slides, however not only can explicitly sense different tautomeric species of 4-MPy molecules at trace concentrations, but also exhibit remarkable spectral reproducibility.

The reproducibility of the as-prepared substrates have been checked and the relative standard deviation (RSD) have been estimated from the SERS spectra of 4-MPy by probing the laser beam on ten different spots covering a wide zone ~2×1 cm^2 surface area of the substrate. The spectra are shown in Figure S8 (Supporting Information). The RSD values for the prominent and well resolved SER bands of 4-MPy molecule centered at ~1006, 1092 and 1210 cm^{-1} are estimated to be 10.94%, 12.93%, and 17.91% respectively. The average estimated RSD value less than 15% indicate good reproducibility of the as-prepared substrates as effective SERS sensing scaffold for future state-of-art sensing applications. To our knowledge the unique reproducibility of the asprepared substrates for detecting probe molecules at ultrasensitive concentrations, in cohesion with their reproducibility per se, may be the first report of SERS active substrates which have the potential to overcome the "SERS uncertainty principle".

The enhancement factors (EFs) of the SER bands of 4-MPy molecule adsorbed on two different modified substrates of classes "A" and "B" have been separately calculated using the relation,[49,50]

$$\mathrm{EF} = \frac{I_{SERS}}{I_{bulk}} \times \frac{N_{bulk}}{N_{SERS}}, \tag{4}$$

where, N_{bulk} and N_{SERS} represent the number of probe molecule that contribute to the normal Raman and SERS

signals. I_{bulk} and I_{SERS} are the corresponding normal Raman and SERS intensities measured from the baseline. The N_{bulk} has been estimated using the following relation:

$$N_{bulk} = C_{bulk}\,\mathrm{AhN_A}, \tag{5}$$

C_{bulk} is the concentration of the probe molecule in the NRS. As 50× objective lens has been employed in the present experimental work with confocal depth (h) ~1.4 μm, the laser spot area (A) ~8.31 × 10^{-13} m^2 has been estimated for the excitation wavelength (λ_{ex}) ~632.8 nm. N_{SERS} is calculated using the relation,

$$N_{SERS} = C_{SERS}\mathrm{VN_A A/A^{/}}, \tag{6}$$

where, A is the area of the laser spot as estimated earlier to be ~8.31 × 10^{-13} m^2, C_{SERS} is the concentration of 4-MPy molecule at SERS measurement, N_A is the Avogadro number and V is the volume of the probe molecule which is ~25 μl for this experimental work and $A^{/}$is the area of the probe molecule drop casted on the substrate which traces a circular deposit of ~5 mm diameter. The EFs for the SER bands of 4-MPy molecule adsorbed both on the modified substrates of classes "A" and "B" are shown in Table 1. Enhancement factors ranging from ~10^2 to 10^{10} orders of magnitude have been estimated for the bands centered at ~1006, 1092, 1210, 1574 and 1610, contributing to in-plane vibrational signatures. The enhancements of SER bands of 4-MPy adsorbed on the modified substrates of classes "A" and "B" with limit of detection (LOD) ~1.0 × 10^{-12} M concentration corroborate the superiority of the as-prepared substrates in comparison with other substrates reported elsewhere.[51–57]

3.5 | Near- field distributions of the aggregated AuNCs on the substrates of classes "A" and "B"

Near-field distributions around the nanoaggregates on the substrates of classes "A" and "B" are estimated from

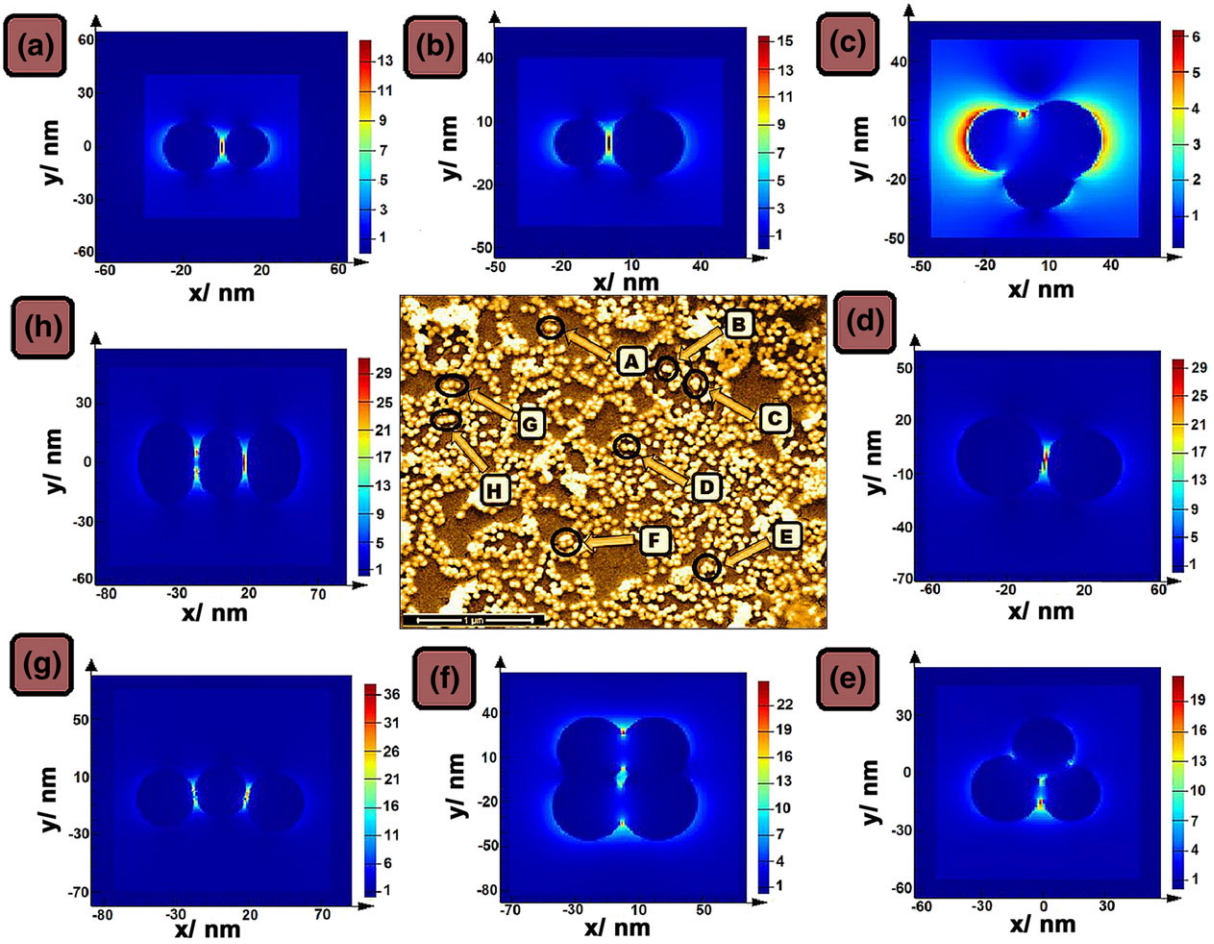

FIGURE 9 (A–H, clockwise) electric field distribution around the hot-spots as estimated from three-dimensional finite difference time domain (3D-FDTD) simulations for as prepared modified substrate of class "A" incubated in AuNC for 24 hr of incubation time (IT; λ_{ex} = 632.8 nm, the polarization of the incident light wave is along x-axis). The corresponding Field Emission Scanning Electron Microscope (FESEM) image, with false color representation is shown in the middle [Colour figure can be viewed at wileyonlinelibrary.com]

3D-FDTD simulation. Both the substrates are dipped in AuNC for 24 hr of IT. Simulations are mapped directly from the respective zones of the FESEM images, marked as A–H in clockwise direction. They are shown in Figures 9 and 10. The 3D-FDTD simulations, as shown in Figures 9 and 10 exhibit specific regions of intense electric fields, mostly confined within the nanogaps of the aggregated domains. These zones are referred as "hot spots" in SERS, and molecules entrapped in these regions encounter gigantic enhancements. The hottest among the "hot spots" have been identified.

The maximum confinement of electric field is estimated for the trimeric ($|\vec{E}|$ ~30 v/m; zone: H) and dimeric ($|\vec{E}|$ ~30 v/m; zone: B) domains of the nanoaggregates, which correspond to the EF $G(\omega, \omega') \sim 8.1 \times 10^5$ orders of magnitude, following PW approximation. The EF as obtained from 3D-FDTD simulations are much smaller in comparison with the average experimental EFs $\sim 10^{10}$ for the SERS spectra of probe molecules adsorbed on the modified substrates of classes "A" and "B". The apparent diminution in the EF value may be due the intrinsic approximation in PW calculations and oversimplification of 3D-FDTD simulations per se. However, in this connection it is worth to mention that, the diffraction limited laser spot diameter (Δx) may be estimated as follows:

$$\Delta x = \frac{1.22\lambda}{N.A.} \tag{7}$$

where, N.A. is the numerical aperture of the objective lens and λ is the excitation wavelength used in the Raman spectral measurement. With 50× objective lens corresponding to N.A. ~0.75, the laser spot diameter has been estimated to ~1 μm. Thus, the laser spot that is focused at different positions on the as-prepared modified substrates of classes "A" and "B" covers an area A ~0.831 μm^2 that is much smaller in area as depicted in the respective FESEM images (Figures 3d and 4b). The discrepancy between theoretically estimated and

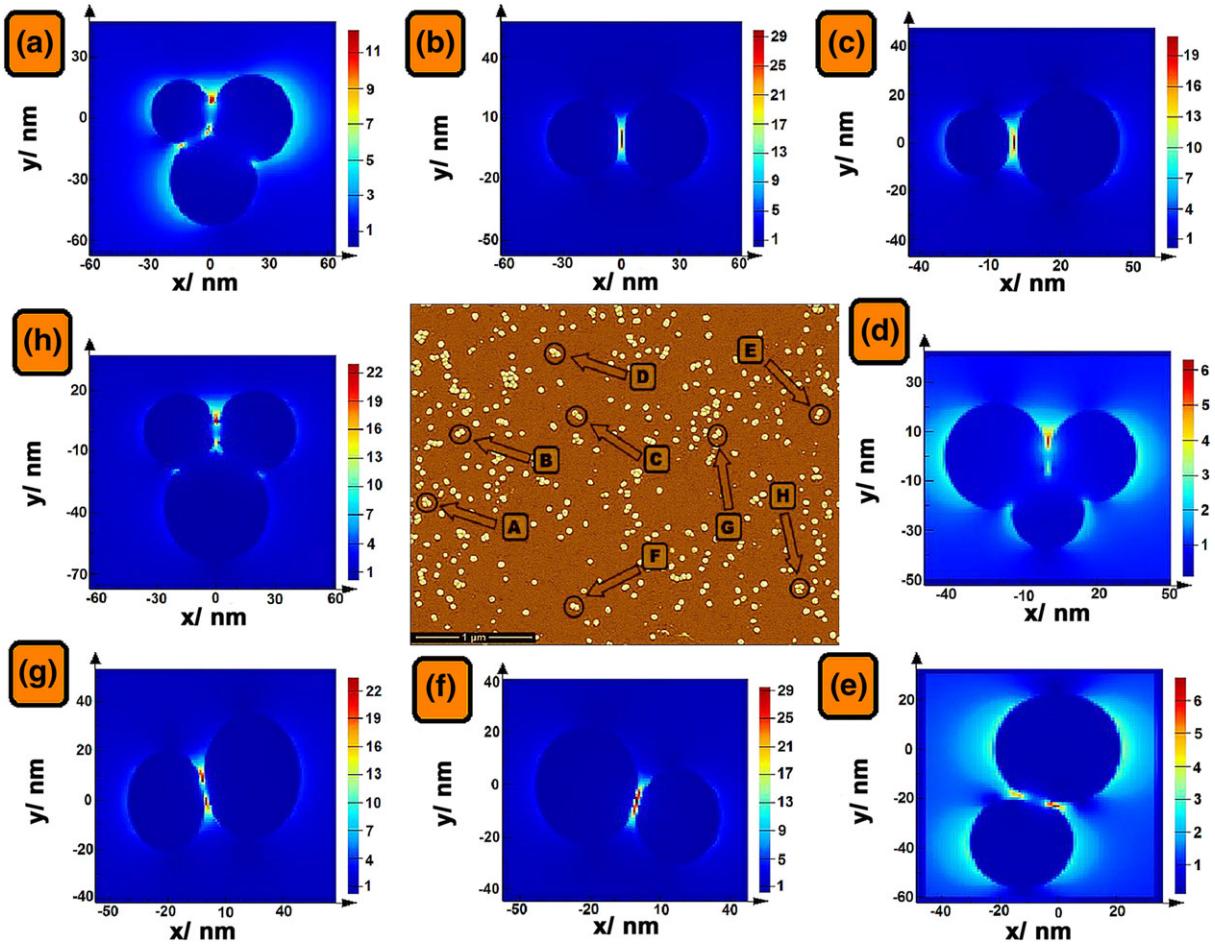

FIGURE 10 (A–H, clockwise) electric field distribution around the hot-spots as estimated from three-dimensional finite difference time domain (3D- FDTD) simulations for as prepared modified substrate of class "B" incubated in AuNC for 24 hr of incubation time (IT; λ_{ex} = 632.8 nm, the polarization of the incident light wave is along x-axis). The corresponding Field Emission Scanning Electron Microscope (FESEM) image, with false color representation is shown in the middle [Colour figure can be viewed at wileyonlinelibrary.com]

experimentally-determined EFs may also arise due to the cumulative signals in the SERS spectra, which are averaged out from small amount of molecules residing in hot-spots and the rest emanating from much weaker enhancing sites, apart from the CT contribution to SERS.

Moreover, the limitations of PW approximation per se as and the nonincorporation of dipole reradiation (DR) theory may be the other possible consequence for underestimation of simulated EF from experimental observations. Detail analysis of the EF with and without the explicit inclusion of DR theory will be focused in our future publication. Closer look on the correlation between the near-field optical response of the as-prepared substrates with the far-field SERS spectra will also be explored in detail from wavelength scanned surface enhanced Raman spectroscopic studies.

4 | CONCLUSIONS

This paper is focused on the fabrication of efficient SERS sensing platforms through coherent integration of LB and self-assembly technique. The plasmonic architectures of the asprepared substrates can be tuned with precise ease to control the gap plasmons and hence the overall enhancements of SERS signal. Power of the LB technique in conjunction with the self-assembly of nanocolloids, provide a unique way to generate the interstitial gaps less than 2.14 (±0.679) nm within the dimeric or trimeric nanoparticles. These interstitial gaps can act as hot sites for the protrusion of probe molecules to exhibit enhanced SERS signal. The as-prepared substrates of classes "A" and "B" immersed in AuNC over various ITs have the unique ability to detect the explicit or concomitant presence of protonated and deprotonated forms of 4-MPy at trace concentrations. Moreover, the substrates exhibit remarkable spectral reproducibility and show early promise to overcome the "SERS uncertainty principle". The spatial distributions of the electric fields in an around the probable hot spots have been estimated from 3D-FDTD simulations. To our knowledge, this genre of SERS active substrates with facile control over plasmonics, is not reported earlier and is expected to open new windows towards successful fabrication of next generation SERS sensing scaffolds. The as-prepared SERS active substrate can be used as "lab on a chip" for sensing applications which will be the keen interest of our future endeavors.

ACKNOWLEDGEMENTS

Authors express their thanks to the Council of Scientific and Industrial Research (CSIR) and Department of Higher Education, Science and Technology and Biotechnology, Govt. of West-Bengal for the financial support through the research projects [Project Sanction No.: 03(7471)/18; ST/P/S&T/16G-22/2017]. S. S. likes to thank UGC, Government. of India for the Junior Research Fellowship (JRF) through National Fellowship for SC students. Authors would like to thank DST-FIST facility, Departmnet of Physics, Jadavpur University for recording the FESEM images.

ORCID

Joydeep Chowdhury https://orcid.org/0000-0001-9952-9956

REFERENCES

[1] M. Fleishman, P. J. Hendra, A. J. Mc Quillan, *Chem. Phys. Lett.* **1974**, *26*, 163.

[2] B. Sharma, R. R. Frontiera, A. I. Henry, E. Ringe, R. P. Van Duyne, *Mater. Today* **2012**, *15*, 16. and references cited therein

[3] S. D. Roy, M. Ghosh, J. Chowdhury, *J. Phys. Chem. C* **2018**, *122*, 10981.

[4] M. Muniz-Miranda, M. Puggelli, R. Ricceri, G. Gabrielli, *Langmuir* **1996**, *12*, 4417.

[5] S. D. Roy, M. Ghosh, J. Chowdhury, *J. Raman Spectrosc.* **2015**, *46*, 451.

[6] M. Muniz- Miranda, F. Muniz- Miranda, A. Pedone, *Phys. Chem. Chem. Phys.* **2016**, *18*, 5974.

[7] S. D. Roy, P. Sett, M. Ghosh, J. Chowdhury, *J. Raman Spectrosc.* **2017**, *48*, 38.

[8] J. H. Granger, N. E. Schlotter, A. C. Crawford, M. D. Porter, *Chem. Soc. Rev.* **2016**, *45*, 3865. and references cited therein

[9] R. Liu, Y. Xiong, Y. Guo, M. Si, W. Tang, *J. Raman Spectrosc.* **2018**, *49*, 1426.

[10] J. Kneipp, H. Kneipp, K. Kneipp, *Chem. Soc. Rev.* **2008**, *37*, 1052. and references cited therein

[11] D. Hernandez-Sanchez, G. Villabona-Leal, I. Saucedo-Orozco, V. Bracamonte, E. Perez, C. Bittencourtd, M. Quintana, *Phys. Chem. Chem. Phys.* **2018**, *20*, 1685.

[12] M. B. Ross, M. J. Ashley, A. L. Schmucker, S. Singamaneni, R. R. Naik, G. C. Schatz, C. A. Mirkin, *J. Phys. Chem. C* **2016**, *120*, 20789.

[13] C. Hou, D. D. Galvan, G. Meng, Q. Yu, *Phys. Chem. Chem. Phys.* **2017**, *19*, 24126.

[14] A. R. L. Marshall, J. Stokes, F. N. Viscomi, J. E. Proctor, J. Gierschner, J. S. G. Bouillard, A. M. Adawi, *Nanoscale* **2017**, *9*, 17415.

[15] E. C. Le Ru, P. G. Etchegoin, *Principles of Surface-Enhanced Raman Spectroscopy and Related Plasmonic Effects*, Elsevier, Amsterdam **2009**.

[16] E. C. Le Ru, P. G. Etchegoin, *MRS Bulletein.* **2013**, *38*, 631.

[17] R. Aroca, C. Jennings, G. J. Kovacs, R. O. Loutfy, P. S. Vincett, *J. Phys. Chem.* **1985**, *89*, 4051.

[18] L. Gaffo, C. J. L. Constantino, W. C. Moreira, R. F. Aroca, O. N. Oliveira, *Spectrochem Acta Part A* **2004**, *60*, 321.

[19] G. Moula, R. F. Aroca, *Anal. Chem.* **2011**, *83*, 284. and references cited therein

[20] P. J. G. Goulet, R. F. Aroca, *Anal. Chem.* **2007**, *79*, 2728.

[21] M. Mastrangeli, S. Abbasi, C. Varel, C. V. Hoof, J.-P. Celis, K. F. Bohringer, *J. Micromech. Microeng.* **2009**, *19*, 083001.

[22] G. M. Whitesides, B. Grzybowski, *Science* **2002**, *295*, 2418.

[23] G. Frens, *Nat. Phys. Sci.* **1973**, *241*, 20.

[24] S. Basu, S. K. Ghosh, S. Kundu, S. Panigrahi, S. Praharaj, S. Pande, S. Jana, T. Pal, J. Colloid, *Interdiscip. Sci.* **2007**, *313*, 724.

[25] M. K. Abyaneh, R. Pasricha, S. W. Gosavi, S. K. Kulkarni, *Nanotechnology* **2006**, *17*, 4129.

[26] M. K. Abyaneh, D. Paramanik, S. Varma, S. W. Gosavi, S. K. Kulkarni, *J. Phys. D Appl. Phys.* **2007**, *40*, 3771.

[27] http://www.lumerical.com/tcad-products/fdtd/

[28] L. K. Ausman, G. C. Schatz, *J. Chem. Phys.* **2009**, *131*, 084708.

[29] L. K. Ausman, G. C. Schatz, *J. Phys. Chem. C* **2012**, *116*, 17318.

[30] P. K. Paul, S. A. Hussain, D. Bhattacharjee, *J. Luminesc.* **2008**, *128*, 41.

[31] T. J. Norman, C. D. Grant, D. Magana, J. Z. Zhang, J. Liu, D. Cao, F. Bridges, A. Van Buuren, *J. Phys. Chem. B* **2002**, *106*, 7005.

[32] W. Yang, K. Liu, D. Song, Q. Du, R. Wang, H. Su, *J. Phys. Chem. C* **2013**, *117*, 27088.

[33] H. Zhan, F. Cheng, Y. Chen, K. W. Wong, J. Mei, D. Hui, W. M. Lau, Y. Liu, *Composites Part B* **2016**, *84*, 222.

[34] Q. Hao, H. Huang, X. Fan, Y. Yin, J. Wang, W. Li, L. Ma, P. K. Chu, O. G. Schmidt, *ACS Appl. Mater. Interfaces* **2017**, *9*, 36199.

[35] C. Wang, G. Wang, R. Yang, X. Sun, H. Ma, S. Sun, *Langmuir* **2017**, *33*, 503.

[36] A. Albert, G. B. Barlin, *J. Chem. Soc.* **1959**, *0*, 2384.

[37] K. Kishore, G. R. Dey, D. B. Naik, *Res. Chem. Intermed.* **2002**, *28*, 29.

[38] J. A. Baldwin, B. Vlckova, M. P. Andrews, I. S. Butler, *Langmuir* **1997**, *13*, 3744.

[39] X. Fu, F. Bei, X. Wang, X. Yang, L. Lu, *J. Raman Spectrosc.* **2009**, *40*, 1290.

[40] H. S. Jung, K. Kim, M. S. Kim, *J. Mol. Struct.* **1997**, *407*, 139.

[41] Y. Wang, H. Hu, S. Jing, W. Wang, Z. Sun, B. Zhao, C. Zhao, J. R. Lombardi, *Anal. Sci.* **2007**, *23*, 787.

[42] J. Hu, B. Zhao, W. Xu, B. Li, Y. Fan, *Spectrochim. Acta Part A* **2002**, *58*, 2827.

[43] W. H. Do, C. J. Lee, D. Y. Kim, M. J. Jung, *J. Indust. Engg. Chem.* **2012**, *18*, 2141.

[44] Z. Ling, Y. Bai, Z. Shang, Y. Zhang, Y. Mo, *J. Raman Spectrosc.* **2007**, *38*, 1106.

[45] M. Pradhan, J. Chowdhury, S. Sarkar, A. K. Sinha, T. Pal, *J. Phys. Chem. C* **2012**, *116*, 24301.

[46] Y. Chao, Z. Qun, Y. Li, Y. Yan, Y. Wu, J. Zheng, *J. Phys. Chem. C* **2007**, *111*, 16990.

[47] H. Guo, L. Ding, Y. Mo, *J. Mol. Struct.* **2011**, *991*, 103.

[48] E. Tourwe, K. Baert, A. Hubin, *Vib. Spectrosc.* **2006**, *40*, 25.

[49] N. D. Jayram, S. Sonia, P. S. Kumar, L. Marimuthu, Y. Masuda, D. Mangalaraj, N. Ponpandian, C. Viswanathan, S. Ramankrishna, *RSC Adv.* **2015**, *5*, 46229.

[50] W. Song, W. Ji, S. Vantasin, I. Tanabe, B. Zhao, Y. Ozaki, *J. Mater. Chem. A* **2015**, *3*, 13556.

[51] Y. Zheng, W. Wang, Q. Fu, M. Yu, K. Shayan, K. M. Wong, S. Singh, A. Schober, P. Schaaf, Y. Lei, *Chem. Plus Chem.* **2014**, *79*, 1622.

[52] W. Yue, Z. Wang, Y. Yang, L. Chen, A. Syed, K. Wong, X. Wang, *J. Micromech. Microeng.* **2012**, *22*, 125007.

[53] E. N. Esenturk, A. R. Hight Walker, *J. Raman. Spectrosc.* **2009**, *40*, 86.

[54] Q. Yu, P. Guan, D. Qin, G. Golden, P. M. Wallace, *Nano Lett.* **2008**, *8*, 1923.

[55] L. Zhang, L. Dai, Y. Rong, Z. Liu, D. Tong, Y. Huang, T. Chen, *Langmuir* **2015**, *31*, 1164.

[56] J. Tao, D. He, B. Tang, L. Kong, Y. Luo, P. Zhao, W. Gang, Z. Peng, *RSC Adv.* **2015**, *5*, 49168.

[57] Y. Pan, X. Wang, H. Zhang, Y. Kang, T. Wu, Y. Du, *Anal. Methods* **2015**, *7*, 1349.

SUPPORTING INFORMATION

Additional supporting information may be found online in the Supporting Information section at the end of the article.

How to cite this article: Saha S, Ghosh M, Chowdhury J. Infused self-assembly on Langmuir–Blodgett Film: Fabrication of highly efficient SERS active substrates with controlled plasmonic aggregates. *J Raman Spectrosc*. 2019;50:330–344. https://doi.org/10.1002/jrs.5529

Colloids and Surfaces A: Physicochemical and Engineering Aspects 628 (2021) 127319

Contents lists available at ScienceDirect

Colloids and Surfaces A: Physicochemical and Engineering Aspects

journal homepage: www.elsevier.com/locate/colsurfa

Decoding the topographical features of more realistic SERS active substrates in presence of the probe molecules from statistical considerations: An in-depth study bridging Microscopy with Spectroscopy

Somsubhra Saha [a], Manash Ghosh [b], Subhendu Chandra [c], Joydeep Chowdhury [a,*]

[a] Department of Physics, Jadavpur University, 188, Raja S.C. Mallick Rd, Kolkata 700032, India
[b] Department of Spectroscopy, Indian Association for the Cultivation of Science, Jadavpur, Kolkata 700032, India
[c] Department of Physics, Victoria Institution (College), 78-B, A.P.C. Road, Kolkata 700009, India

HIGHLIGHTS

- Surface topographies of the SERS active substrates have been explored in detail.
- Topographical features of the substrates were mapped in presence of 4-MPy molecule.
- Bare SERS substrates are compared with the same substrate in presence of 4-Mpy.
- The chaotic behavior of the substrates has been revealed from Lyapunov exponents.

GRAPHICAL ABSTRACT

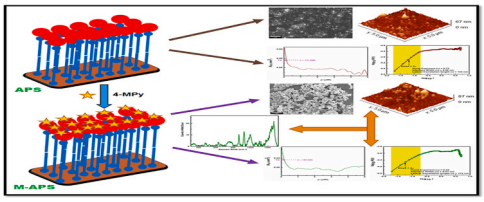

ARTICLE INFO

Keywords:
SERS
Langmuir- Blodgett Film
Height- Height Correlation Function
Hurst exponent
Plasmonic aggregation

ABSTRACT

This paper reports for the first time the topographical parameters of SERS active substrates, fabricated through Langmuir-Blodgett and self-assembly techniques, in presence of the probe 4- Mercapto Pyridine (4-Mpy) molecules. Prior to this study the topographical parameters of bare SERS active substrates in absence of probe molecules had been investigated. However, correlating the topographical parameters of bare SERS active substrates with the corresponding SERS responses may be incomplete and imprecise, as in reality the SERS signals are collected from the probe molecules only upon adsorption on the substrates. The adsorption of probe molecules on the SERS active substrates can modify their overall morphologies in comparison to the pristine counterparts. The present paper thus reports the topographical features of the SERS active substrates in presence of 4-Mpy molecule from the statistical considerations in terms of lateral correlation length (ξ), Hurst or roughness exponents (α), root mean square surface roughnesses (ω) and fractal dimensions (D_f). Attempts have been made to correlate the topographical features of the substrates in presence of 4-Mpy molecule with their corresponding SERS responses. The chaotic behaviors of the substrates in pristine form and in the presence of 4-MPy molecules are also revealed from the Lyapunov exponents and the 2D phase space trajectories. We believe that the present report will help to correlate the topographical features of more realistic SERS active substrates in presence of probe molecules with their corresponding SERS activities and render significant advancement towards successful fabrications of efficient SERS active substrates in future endeavors.

* Corresponding author.
E-mail addresses: joydeep72_c@rediffmail.com, joydeep.chowdhury@jadavpuruniversity.in (J. Chowdhury).

https://doi.org/10.1016/j.colsurfa.2021.127319
Received 6 May 2021; Received in revised form 14 July 2021; Accepted 3 August 2021
Available online 5 August 2021

1. Introduction

Over the past decades Surface-enhanced Raman scattering (SERS) spectroscopy has emerged as a potential analytical tool not only for the detection of chemicals at ultra-low concentrations in the domain of single/nearly single molecule detection limit but also find its extensive applications in the real-world diagnostics [1–11]. While understanding the effect of near–field plasmonic response on the SERS spectra of probe molecules recorded in the far-field, has been the blazing topic of contemporary research [12–14], the fabrications of efficient SERS active substrates still remain the primary concern in this area of research these days [6,15–23]. It appears that correct fabrications of SERS active substrates, fostering large number of plasmonic domains, play a pivotal role to control the enhancement of Raman signals from the probe molecules [15–25].

Recently, major focus in the research activities on SERS has been devoted towards the fabrications of robust SERS active substrates that exhibit colossal enhancements of Raman signals from the adsorbed probe molecules [6,15–23]. While fabrications of such substrates using various top-down and bottom-up approaches continue to be the focal point in this area of research [6,15–23,26–29], however reports on understanding the topographical features of those substrates from statistical considerations in terms of lateral correlation length (ξ), Hurst or roughness exponents (α), root mean square surface roughnesses (ω), fractal dimensions (D_f) etc. are surprisingly rare. The importance of some of these parameters have long being recognized to elucidate the enhancement mechanism of SERS [30–32], but to our knowledge, the first systematic studies to understand the topographical features of SERS active substrates in terms of ξ, α, ω and D_f were recently addressed by our research group [15,33,34]. Those studies reveal that certain range of values associated with the topographical parameters (ca. ξ, α, ω and D_f) favor the efficacies of the SERS active substrates under investigations [15,33,34]. Though the above referred topographical parameters for the substrates primarily allow us to understand their morphological features, however correlating their topographical parameters with the corresponding SERS responses were rather incomplete and imprecise. The obvious reason is that the topographical parameters of the SERS active substrates were estimated in the absence of probe molecules, but in reality, the SERS signals are collected from the probe molecules only upon adsorption on the substrates. The adsorption of probe molecules on the substrates can alter their overall morphological features in comparison to the pristine counterparts. This will lead to the changes in ξ, α, ω and D_f values and will help us to correlate the corresponding SERS responses more precisely under real experimental conditions.

Keeping these things in mind, this paper is focused to explore in details the topographical features of SERS active substrates, fabricated through LB and self-assembly techniques, in presence of the probe 4-Mercapto Pyridine (4-Mpy) molecules. The statistical parameters (ca. ξ, α, ω and D_f) associated with the topographical features of the bare SERS active substrate are also compared with the same substrate in presence of 4-Mpy. We believe that the present report will help to correlate the topographical features of more realistic SERS active substrates in presence of probe molecules with their corresponding SERS activities and render significant advancement towards successful fabrications of efficient SERS active substrates in future endeavors.

2. Experimental procedure

2.1. Materials and Methods

Spectroscopic grade 4-Mercaptopyridine (4-MPy; ~95% purity), stearic acid (SA; > 99% purity), chloroauric acid ($HAuCl_4$) and chloroform were purchased from Sigma- Aldrich and were used without further purification. Tri-sodium citrate dehydrate, acetone and ethanol were obtained from E- Merck (Germany) and were used as received. The glass wares used in the experiments were washed with freshly prepared aqua- regia followed by vigorous rinsing with triple distilled water. Triple distilled water subsequently deionized (18.2 MΩ cm resistivity and pH~6.8) with Milli- Q- plus system of Millipore Corporation, USA was used as subphase in the LB trough and also in preparing aqueous solutions as needed.

Quasi spherical gold nanocolloids (AuNCs) with mean particle size ~55 nm were synthesized employing the citrate reduction method as reported by Frens [35,36]. Briefly, 50 ml of aqueous solution of $HAuCl_4$ was taken in a flask and was heated till boiling. To it, 400 μl aqueous solution of 1% tri sodium citrate was added under vigorous stirring. At first the colorless solution turns deep blue and then to reddish pink indicating the formation of gold nanoparticles (AuNps).

The quartz glass slides used for LB deposition were cleaned with ethanol, acetone and deionized water. The bilayer LB films of SA were lifted on the pre- cleaned quartz glass slides by Y-type deposition technique using a computer controlled LB trough (Model No. D2007, Apex Instruments). Spectroscopic grade chloroform solvent was used to dissolve the SA molecules. The surface pressure was monitored by Wilhelmy method using a filter paper. SA solution (1 mg/ml) in chloroform solvent was dispensed dropwise by a micro syringe on the air water interface of the dual LB trough. The system was then left undisturbed for 20 min thereby allowing the chloroform solvent to evaporate. The barriers were then compressed quasistatically at a constant speed of 2 mm/min and the surface pressure-area (π-A) isotherm plot at room temperature was recorded. The bilayer LB films of SA were then dipped in AuNCs for 24 h. The LB films containing AuNCs adhered to SA bilayer were removed from the nanocolloidal suspension, washed with deionized water and dried in the hot air oven to eliminate the excess unneutralized ions. The as prepared substrates were then finally soaked in the aqueous solution of Raman probe 4-MPy molecules (~1.0×10^{-9} M) for 1, 1.5 and 2 h before recording the SERS spectra.

2.2. Instrumentation

The Field Emission Scanning Electron Microscope (FESEM) images have been recorded with JEOL JSM 7600F operating at excitation energy of 15KV. The Atomic Force Microscope (AFM) topography images of the substrates were recorded with a NTEGRA system having 1 nm resolution from NT-MDT Spectrum Instruments. The X-ray photoelectron spectroscopy (XPS) analysis of the substrates has been performed through ULVAC PHI 5000 Versa Probe- II, operating at 1.6×10^{-6} Pascal pressure. The substrates were irradiated using the Al Kα ($h\upsilon = 1486.6$ eV) X-ray source with focus area of 100 μm diameter at a fixed operating power at 25 Watt. The binding energy scale of the XPS spectra was corrected using the reference peak of C1s at 284.8 eV. The SERS spectra were recorded using J- Y Horiba Confocal Triple Raman Spectrometer (Model: T 64000) equipped with 1800 groove/mm holographic gratings and a TE cooled Synapse CCD detector from J- Y Horiba. The 632.8 nm red line of He-Ne laser (manufactured by CVI-Melles Griot) with laser power ~1 mWatt was used as the exciting source. The laser beam was focused through Olympus open stage microscope of 50x objective lens with a spot size of 1 μm in diameter. The scattered signals were collected at 180^0 scattering angle and the data acquisition time to record the SERS spectra of each sample was 20 s. The Lab Spec 5 software as provided by Horiba was used to control the detector and the subsequent data acquisition.

3. Results and discussions

3.1. Pressure- area isotherm plot and fabrication of the substrate

The surface pressure (π) – area (A) compression isotherm plot of SA at room temperature is shown in Fig. S1 of the Supplementary Material. The π – A isotherm plot of SA shows a distinct condensed phase at an area/SA molecule ~0.20 nm^2/molecule. The bilayer LB film of SA was

lifted on quartz slide at a constant surface pressure of 25 mN/m by Y-type deposition technique. This deposition technique allows Head (H) -Tail (T) and Tail (T) – Head (H) configuration of the molecular architecture, leaving behind the polar COO^{-} head groups of SA to remain suspended in air. The bilayer LB film of SA was then dipped in AuNCs for 24 h and finally dried in hot air oven to remove the excess metal ions from the surface of the film. We call this LB film substrate, so recovered after dipping in AuNC, as the "As Prepared Substrate (APS)."

The APS substrates were then soaked in the aqueous solution of the Raman probe 4-MPy molecule [$\sim 1.0 \times 10^{-9}$ M (pH~6.8)] for 1 h, 1.5 hrs and 2 hrs. After the pre-referred soaking times (STs), the respective substrates were removed and kept undisturbed for 18 h before recording

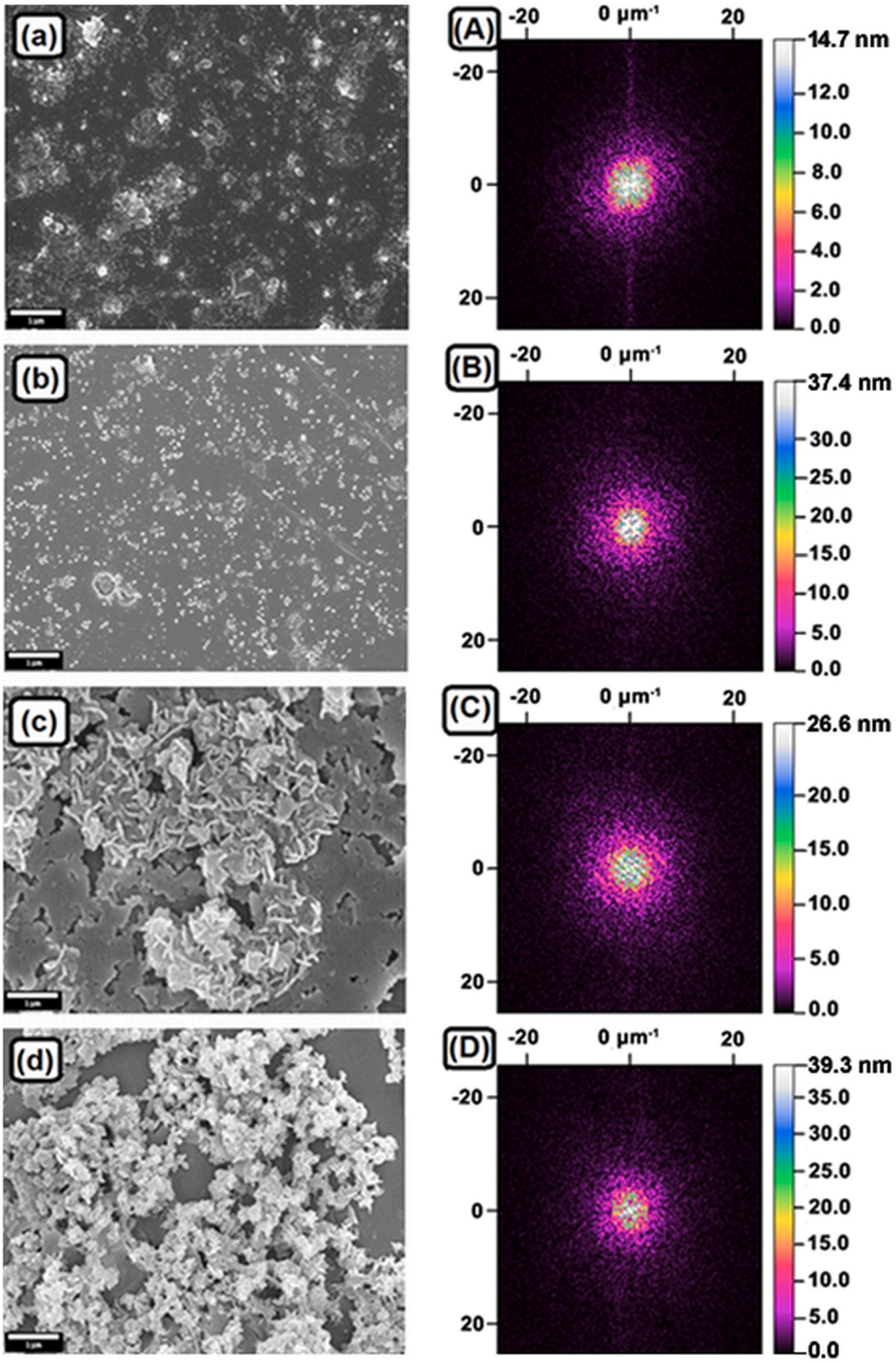

Fig. 1. Left Column: Micrometer scale FESEM images of **(a)** APS and **(b)** M-APS (1), **(c)** M-APS (1.5) and **(d)** M-APS (2). Right Column [A-D]: The corresponding FFT images of the substrates in the reciprocal k- space.

the FESEM, AFM, XPS and SERS spectra. These substrates will henceforth be referred as the "Modified As Prepared Substrates (M-APSs)" to distinguish them from the APS. Furthermore, the M-APSs which were soaked in the aqueous solution of 4-Mpy for 1 h, 1.5 hrs and 2 hrs are designated as M-APS (1), M-APS (1.5) and M-APS (2) respectively.

3.2. Morphological characterizations of APS, M-APSs and SERS responses

The FESEM and the corresponding fast fourier transform (FFT) images in the reciprocal k space of APS and M-APSs soaked in the aqueous solution of 4-Mpy (~1.0×10^{-9} M; pH~6.8) for 1, 1.5 and 2 hrs are

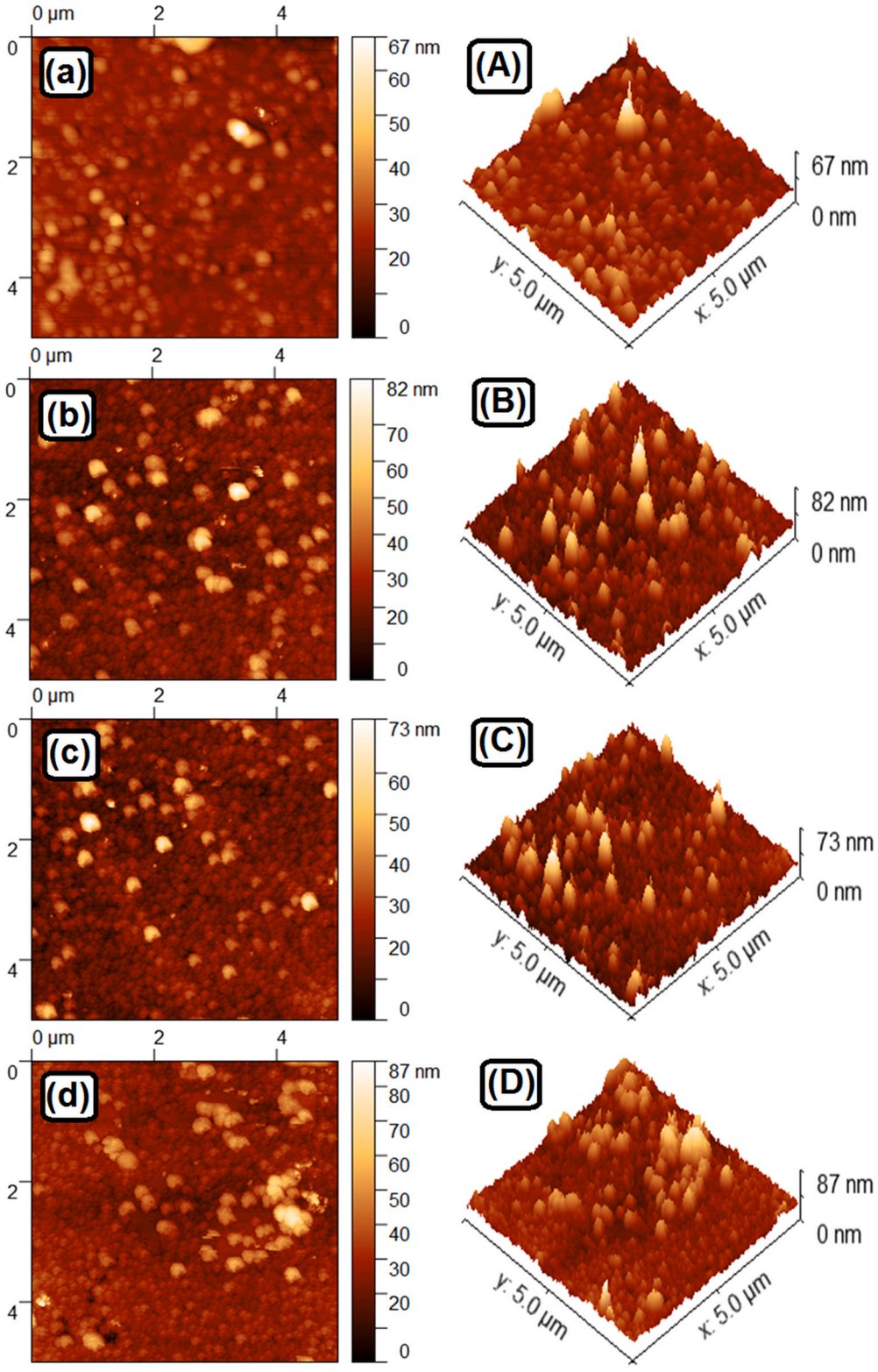

Fig. 2. Left Column: 2D AFM images of **(a)** APS and **(b)** M-APS (1), **(c)** M-APS (1.5) and **(d)** M-APS (2). Right Column [A-D]: The corresponding 3D AFM images of the APS and M-APSs.

shown in Fig. 1(a, A), (b, B), (c, C) and (d, D) respectively. The FFT images primarily portray random textures of all the substrates [37]. Closer inspections of the FESEM image of the APS [Fig. 1(a)] show tethering of gold nanoparticles (AuNps) in the bilayer LB film matrix of SA. The elemental compositions of the APS have been envisaged from the survey scan XPS spectrum, covering the wide binding energy (BE) window ranging from 0 to 1100 eV. The spectrum, as shown in Fig. S2(a) (maroon trace) in the Supplementary Material, clearly shows the presence of prominent peaks characteristic of Au4f, C1s, Au4d and O1s elements apart from the explicit appearance of Si2p, Si2s bands. The peaks associated with Si2p, Si2s bands at ~103, 154 eV BEs respectively emanate from the quartz slide upon which the bilayer LB film of SA has been deposited [38,39]. The prominent XPS peaks with BEs ascribed to Au4f, C1s, Au4d and O1s bands [40,41] confirm the presence of carbon (C), oxygen (O) and gold (Au) atoms in the APS.

The FESEM image further unveils dense aggregated clustered domains of plasmonic nanoparticles. The aggregated domains of AuNps may favor the development of hot geometries which in turn promote the generation of "hot spots" responsible for the origin of SERS spectra. The agglomerated domains of the plasmonic AuNps may evolve as a result of interplay between the short-range nanoparticle- nanoparticle (NN) attractive F_{NNA}, bilayer– bilayer (BB) attractive F_{BBA}, nanoparticle-bilayer (NB) attractive F_{NBA} and long range NN dipolar repulsive forces F_{NNR} prevalent in the APS [42,43].

The FESEM images of the M-APSs, so attained after soaking in the aqueous solution of 4-Mpy for 1 h, 1.5 hrs and 2 hrs are shown in Fig. 1 (b), (c) and (d) respectively. To confirm the adsorption of 4-MPy on APS, the wide scan XPS analyses have also been performed on the M-APS (2) so attained after soaking in the aqueous solution of 4-Mpy for 2 h. The wide range survey scan XPS spectrum for the M-APS (2), as shown in Fig. S2(b) in the Supplementary Material (green trace), is markedly different in contrast to that recorded for the APS substrate [Fig. S2(a) in the Supplementary Material (maroon trace)]. The intensities of the XPS peaks originating from Au4f, $Au4d_{5/2}$ and $Au4d_{3/2}$ are strongly enhanced and slightly shifted to higher BEs in comparison to those recorded for the APS. Furthermore, new peaks assigned to the BEs of S2p and N1s are also noted. All these observations may indicate not only the presence of 4-Mpy but also its possible interaction with the AuNps that remain embedded in the M-APS. The XPS analyses of the substrates in detail involving high resolution narrow scan XPS spectra are beyond the scope of the present study, and are elaborately considered in a separate publication [44].

The FESEM image of the M-APS (1) soaked for 1 h in 4-MPy solution closely resembles with the morphological features of the APS [Fig. 1(a)]. However, surface morphologies of the M-APSs, so accomplished after soaking in the aqueous solution of 4-MPy for 1.5 and 2 hrs show contrasting features. While the FESEM image of the former M-APS (1.5) exhibits clove like aggregated patterns of AuNps [Fig. 1(c)], the later M-APS (2) substrate shows sprouted aggregated domains of plasmonic nanoparticles [Fig. 1(d)]. These results suggest that adsorption of the probe 4-Mpy molecule on the APS for an extended period of time ($\geq$ 1.5 hrs) can perturb the overall surface morphologies of the M-APS.

Fig. 2 shows the 2D and 3D- AFM images scanned over 5 μm × 5 μm surface area of the APS as well as of the M-APS substrates soaked in 4-Mpy for 1 h, 1.5 hrs and 2 hrs. Fig. 2(a, A) shows distinct agglomeration of AuNps in the APS and is in line with the observation as perceived from the corresponding FESEM image [Fig. 1(a)]. The AFM images of M-APSs soaked in 4-Mpy solution over various STs ranging from 1 to 2 hrs exhibit noticeable differences in the aggregated features of the plasmonic AuNps [Fig. 2(b, B), (c, C) and (d, D)]. With increase in ST, the agglomerated domains of AuNps are distinctively localized showing large surface bumps on specific areas of the M-APSs. These results are again in concordance with the corresponding FESEM images of the substrates [Fig. 1; (*vide supra*)]. However, in this connection it may be worth to mention that the height of the M-APS (1.5) as reflected from its AFM image [Fig. 2(c, C)] is lower than that of M-APS (1) and M-APS (2) [Fig. 2(b, B) and (d, D)]. The rationale behind it may be the fact that the height of the clove like patterns of this plasmonic substrate, as reflected from the corresponding FESEM image [Fig. 1(c)], is much lower than the respective heights of the dense and sprouted aggregated domains of the plasmonic nanoparticles in M-APS (1) and M-APS (2) respectively [Fig. 1 (b) and (d)].

The SERS spectra from the M-APSs so accomplished after soaking in 1.0×10^{-9} M aqueous solution (pH~6.8) of probe 4-MPy for 1 h, 1.5 hrs and 2 hrs are shown in Fig. 3(a), (b) and (c) respectively. All the spectra exhibit enhanced Raman bands at ~711, 1005, 1058, 1092, 1208, 1471, 1582 and 1609 cm^{-1} with appreciable S/N ratio. These vibrational signatures are well recognized and are known to originate from the in-plane bending, ring breathing and stretching modes of the 4-MPy molecule [18,45–47]. The SERS spectral responses of 4-Mpy molecule at nanomolar concentration from three different M-APS substrates thus unarguably demonstrate their efficacies as efficient SERS sensing scaffolds. However, closer inspection of the SERS spectra as shown in Fig. 3 (a)–(c) reveals that the SERS intensity of the 4-MPy molecule upon adsorption on M-APS (1.5) is poorer than that of M-APS (1) and M-APS (2). In general SERS intensities of the probe molecules depend upon the surface morphologies of the SERS active substrates. Surface morphologies of the substrates in turn rely on the size, shape and interparticle distances between the plasmonic nanoparticles. The dimeric, trimeric or higher aggregated plasmonic nanostructured domains are known to promote the generation of hot spots, which are now considered to be responsible for the colossal enhancements of SERS signals [12,48,49]. The FESEM image of the M-APS (1.5) shows clove like aggregated patterns of AuNps [Fig. 1(c)]. This type of aggregated clove like patterns may not support the generation of larger hot spot densities in

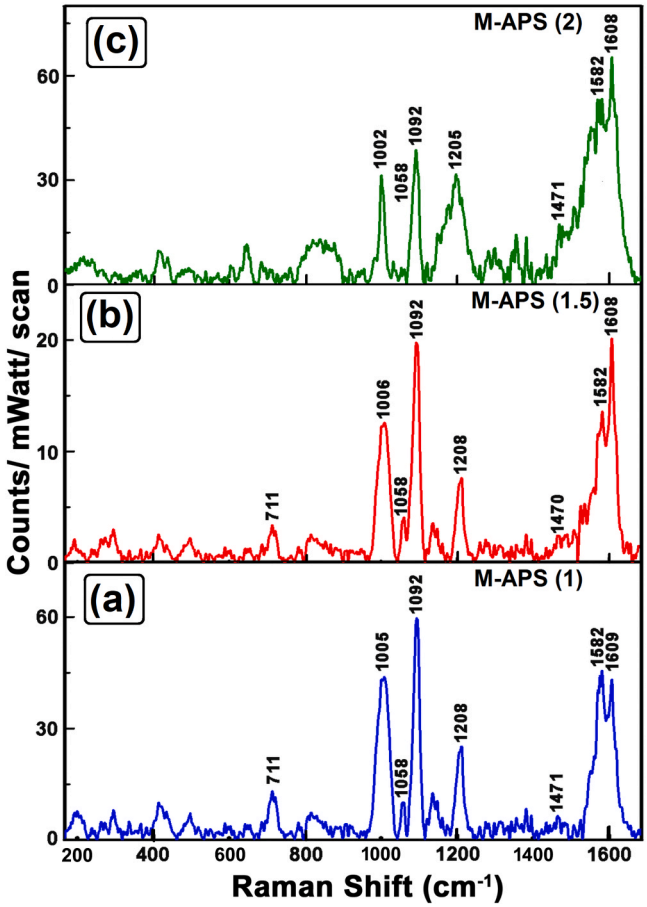

Fig. 3. SERS spectra of 4- MPy molecule (~1.0×10^{-9} M, pH~6.8) as obtained from **(a)** M-APS (1) **(b)** M-APS (1.5) and **(c)** M-APS (2) (λ_{ex} = 632.8 nm).

comparison to those of M-APS (1) and M-APS (2). This may result in poorer SERS intensity of the 4-MPy molecule upon adsorption on M-APS (1.5). Moreover, Fig. 3(c) reveals that the SERS background signal of M-APS (2) is higher than that of M-APS (1) and M-APS (1.5) [Fig. 3(a) and (b)] particularly in ~1300–1685 cm^{-1} wavenumber window. This broad SERS background signal of M-APS (2) is attributed to amorphous carbon and is now well recognized as potential contaminant that results in intense broad background signals ~1300–1685 cm^{-1} wavenumber window of the SERS spectra [50–55]. The amorphous carbon signals in the SERS spectra are known to emanate from surface carbon contamination of the organic molecules on the metal surface [56], or may be generated in situ due to their photodegradation in the vicinity of highly enhanced localized electric fields [51,52,57]. The appearance of this broad background from the SERS signal of 4-MPy molecule upon adsorption on M-APS (2) may be due to amorphous surface contamination or the same may be generated in situ from unwanted photodegradation. The SERS background signal of M-APS (2) is thus accounted for the typical "cathedral peaks" of amorphous carbon which are reported to arise ~1580 and 1350 cm^{-1} in the Raman spectra [50]. This may further infer that in comparison to M-APS (1) and M-APS (1.5), the sprouted aggregated domains of plasmonic nanoparticles M-APS (2) may favor surface carbon contamination of the 4-Mpy molecules on the metal surface or may promote their undesired photodegradation. However, to have deeper understanding on the hidden correlations between the topographical features of the APS and M-APSs with their corresponding SERS responses, the substrates have been analyzed in view of statistical considerations.

3.3. *Understanding the topographical features of APS and M-APSs from statistical considerations*

Topographical features of the SERS active substrates primarily depend on the surface roughnesses and fractal dimensions of the plasmonic nanoparticles [30,31,58–67]. Optimum roughness features and fractal dimensions of the SERS active substrates are intrinsically linked with the SERS signals [15,33,34]. However, SERS signals in general are known to increase with the optimum roughness features of the roughened electrode surfaces mostly of gold and silver [59,62,63] and also on the fractal nature of the colloidal substrates [30,68]. Topographies of the SERS active substrates on the other hand are closely related with the statistical parameters such as lateral correlation length (ζ), the root-mean-square (RMS) roughness or interface width (ω) and the Hurst (roughness) exponent (α) of the substrate. The Hurst exponent (α) in turn is directly related to the local surface fractal dimension (D_f), which can thus be enumerated thereon [33,34].

The AFM images are not limited to understand the morphological features of the substrates qualitatively but they foster wealth of hidden information which can be extracted precisely from the statistical considerations. While the lateral correlation length (ζ) between the surface heights at any two points on the random rough substrates can be estimated from the auto correlation function, the height-height correlation function (HHCF) helps to envisage the root-mean-square (RMS) roughness or interface width (ω) and the Hurst (roughness) exponent (α) of the substrate. The lateral correlation length (ζ) is known to be one of the most important parameters of random substrate and the heights of any two surface points within spatial separation $< \zeta$ are considered to be correlated [69]. However, if they are spatially far apart exceeding the value of ζ, no correlation between the heights of the concerned surface points can be drawn. The lateral correlation length (ζ) has been estimated from the AFM images of the APS and M-APSs with the aid of the auto-correlation function $R(\vec{\rho}_1, \vec{\rho}_2)$, mathematically expressed as [69].

$$R(\vec{\rho}_1, \vec{\rho}_2) = \frac{G(\vec{\rho}_1, \vec{\rho}_2)}{\omega^2} \tag{1}$$

where $\vec{\rho}_1$ and $\vec{\rho}_2$ are the two different surface points on the substrate and $G(\vec{\rho}_1, \vec{\rho}_2)$ is the auto-covariance function of the pre-referred surface points. The auto-covariance function $G(\vec{\rho}_1, \vec{\rho}_2)$ is represented as [69],

$$G(\vec{\rho}_1, \vec{\rho}_2) = E\{h(\vec{\rho}_1)h(\vec{\rho}_2)\} = \int_{-\infty}^{+\infty}\int_{-\infty}^{+\infty} h_1 h_2 p_j(h_1, h_2; \vec{\rho}_1, \vec{\rho}_2) dh_1 dh_2 \tag{2}$$

where h_1 and h_2 are the corresponding surface heights at the locations $\vec{\rho}_1$ and $\vec{\rho}_2$ of the substrate respectively, $p_j(h_1, h_2; \vec{\rho}_1, \vec{\rho}_2)$ is the joint distribution probability density function and ω^2 is the auto-covariance function at zero lag when $\vec{\rho}_1$ and $\vec{\rho}_2$ are superimposed. Thus G(0) is the second order moment or the variance of a surface height and physically represents mean square surface roughness (ω^2) of the substrate concerned. For rough surfaces, the auto-correlation function $R(\vec{\rho}_1, \vec{\rho}_2)$ and the auto-covariance function $G(\vec{\rho}_1, \vec{\rho}_2)$ depend explicitly on the intermediate distance ρ or lag between the two surface points $\vec{\rho}_1$ and $\vec{\rho}_2$. Thus, both these functions can be expressed as

$$G(\vec{\rho}_1, \vec{\rho}_2) = G|\vec{\rho}_1 - \vec{\rho}_2| = G(\rho); \& R(\vec{\rho}_1, \vec{\rho}_2) = R|\vec{\rho}_1 - \vec{\rho}_2| = R(\rho) \tag{3}$$

The variations of the auto-correlation function R(ρ) with lag $|\vec{\rho}_1 - \vec{\rho}_2| = \rho$ have been estimated from the AFM images of the APS and M-APSs and are shown in Fig. 4(a), (b), (c) and (d) respectively. The lateral correlation lengths (ζ) for all the substrates are appraised from the respective values of R(ρ) where it drops to (1/e)th of its value at zero lag (i.e., at $\rho = |\vec{\rho}_1 - \vec{\rho}_2| = 0$). The estimated values of ζ for the APS and M-APSs soaked in 4-Mpy solution for 1, 1.5 and 2 hrs of STs are shown in Fig. 4. No appreciable changes in ζ values for the APS and for the M-APS (1), so attained after 1 h of ST, have been noticed. These results are in line with the small differences in the morphological features of the APS and the M-APS (1), as recorded from their respective FESEM images [Fig. 1(a) and (b)]. Although topographies of the above referred substrates [ca. APS and M-APS (1)] have not much of difference, yet such small difference is clearly reflected in their respective ζ values [~151 nm for APS and ~141 nm for M-APS (1)]. Interestingly, the ζ values for M-APS (1.5) and M-APS (2) are markedly different from those of APS and M-APS (1). Sharp drop in ζ (~125 nm) is observed for M-APS (1.5), whose FESEM image shows clove like aggregated patterns of AuNps. However, much increase in the ζ value (~180 nm) is noted for M-APS (2) whose corresponding FESEM image exhibits profound and sprouted aggregation of plasmonic nanoparticles (*vide ante*).

The above estimations of ζ values for the APS and M-APSs may be linked with their corresponding surface roughnesses, albeit qualitatively. Lower the value of ζ, higher is the surface roughness. From this consideration, the M-APS (1.5) happens to be most rough while the roughness for the M-APS (2) is least. There are not much prominent differences in the roughness features between the APS and M-APS (1), as their respective ζ values [~151 nm for APS and ~141 nm for M-APS (1)] are estimated to be nearly same. As surface roughness plays a pivotal role in the fabrication of SERS active substrates, we believe that estimated ζ values in the range ~125–180 nm for the M-APSs are enough to exhibit good SERS responses, as depicted in Fig. 3.

For precise estimation of the roughness features of the APS and M-APSs, the root-mean-square (RMS) roughness or interface width (ω) and the Hurst (roughness) exponent (α) of the substrates have been determined from height- height correlation function (HHCF) H(r). For self-affine surfaces HHCF is mathematically represented as [69],

$$H(r) = 2\omega^2\left[1 - e^{\left(-\frac{r}{\zeta}\right)^{2\alpha}}\right] = 2\omega^2 f\left(\frac{r}{\zeta}\right) \tag{4}$$

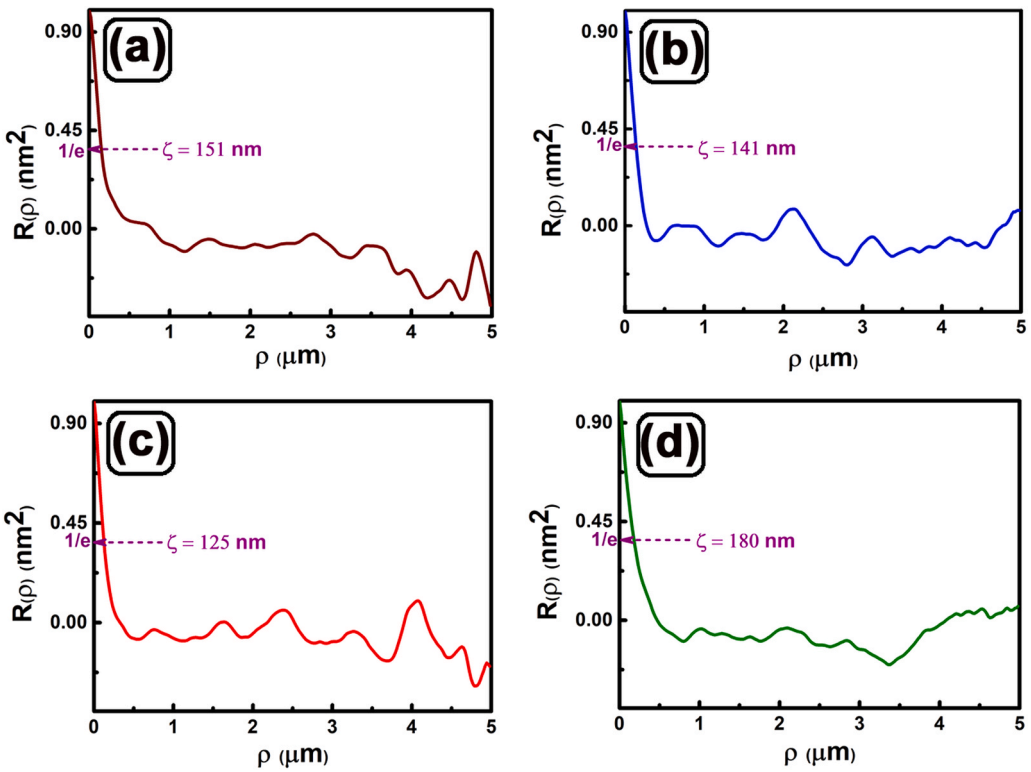

Fig. 4. The auto- correlation function R(ρ) as a function of displacement vector $\vec{\rho}$ for **(a)** APS and **(b)** M-APS (1), **(c)** M-APS (1.5) and **(d)** M-APS (2).

where $\vec{r}$ represents the position vector on the surface, ω^2 and α signify the RMS roughness or interface width and Hurst or roughness exponent respectively, while $(0 \leq \alpha \leq 1)$ and ζ refers to the lateral correlation length. We designate $f(x)$ as the scaling function of $f(x) = f\left(\frac{r}{\zeta}\right)$ with the following properties,

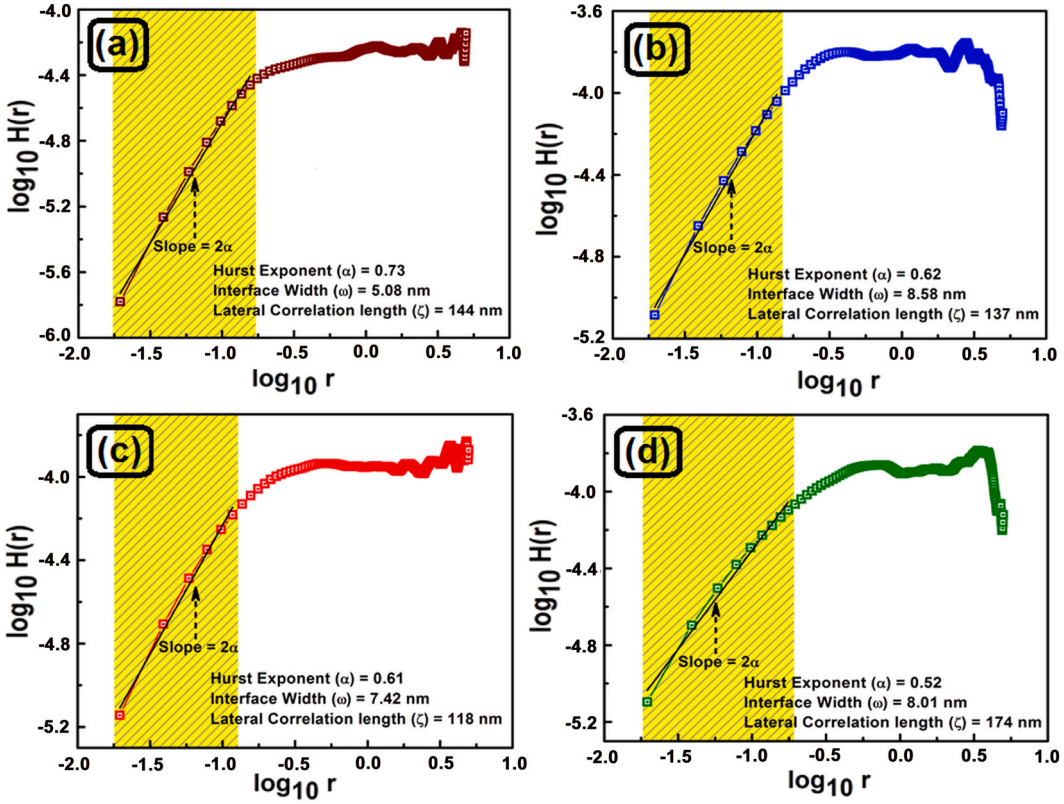

Fig. 5. Variation of $\log_{10}H(r)$ as a function of $\log_{10}r$ for **(a)** APS and **(b)** M-APS (1), **(c)** M-APS (1.5) and **(d)** M-APS (2).

$$f(x) = x^{2\alpha}, \quad \text{for} \quad x \ll 1$$

$$f(x) = 1, \ \text{for} \quad x \gg 1 \tag{5}$$

Within the lateral correlation length ($r \ll \zeta$), H(r) obeys the power law and the Hurst (roughness) exponent (α) determines how much ragged the concerned surface is? However, beyond the correlation length (*i.e* for $r \gg \zeta$), H(r) reaches the asymptotic limit ($\sim 2\omega^2$) in the form of a plateau and allows one to estimate the RMS roughness or interface width (ω) of the substrate. Fig. 5 shows the HHCF plots depicting the variation of $\log_{10}H(r)$ as a function of $\log_{10}r$ plot for the APS and M-APSs. The data for the above referred plots is accomplished from the AFM images of the substrates recorded from five different domains of 5 μm × 5 μm scan area. Interestingly, while the log-log plots for APS as well as for the M-APSs show linear rise obeying the power law at shorter length scales for $r \ll \zeta$, however at larger length scales for $r \gg \zeta$, the HHCF curves attain the saturation limit showing their asymptotic nature. The values of ξ for the APS and M-APS (1), M-APS (1.5) and M-APS (2) have also been estimated from the HHCF plots. The correlation lengths (ξ) for the APS and M-APS (1), M-APS (1.5) and M-APS (2) are noted to be ~144 nm, 137 nm, 118 nm and 174 nm respectively, which are in good agreement with the results as estimated from the auto-correlation function R(ρ).

The Hurst or roughness exponent (α), as determined from the respective HHCF plots, are estimated to be ~0.73 for the APS and ~0.62, 0.61 and 0.52 for the M-APS (1), M-APS (1.5) and M-APS (2) respectively. These results suggest that M-APSs exhibit more jagged local surface morphologies in comparison to the APS. The adsorption of the probe 4-Mpy molecules on the APS substrates thus promote surface roughness which may favor improved plasmonic coupling of AuNps leading to the generation of "hot spots". "Hot spots" are the special locations on the M-APS substrates, wherein the electric fields are strongly localized satisfying the plasmon dispersion relation. Probe molecules snared in these "hot spots" experience huge electric field resulting in colossal enhancements of Raman bands as observed in the SERS spectra of 4-Mpy at nanomolar concentration [Fig. 3 (*vide ante*)].

The Hurst exponents (α) so obtained for the APS and M-APSs are further utilized to enumerate the fractal dimensions (D_f) of the plasmonic AuNps that remain entrapped within the bilayer LB matrix of SA. The Hurst exponent (α) in terms of D_f can be expressed as [69],

$$\alpha = d + 1 - D_f \tag{6}$$

where the dimension of the embedded space is represented by $(d+1)$. Considering the dimension of the embedded space of the substrates to be $(2 + 1)$ [69], the values of D_f are estimated to be 2.27 (± 0.021) for the APS and 2.38 (± 0.025), 2.39 (± 0.022) and 2.48 (± 0.020) for M-APS (1), M-APS (1.5) and M-APS (2) respectively. These results signify that regardless of different surface morphologies, as observed in APS and M-APSs, there is no significant alteration in the D_f values of the plasmonic AuNps. These observations may further invoke us to conclude that for our APS and M-APSs, variation in surface morphologies, correlation lengths or surface roughnesses have limited influence on the overall fractal nature of the substrates. The RMS roughnesses or interface widths (ω) for the substrates have been estimated from the respective HHCF plots and their variations for the APS and M-APS (1), M-APS (1.5) and M- APS (2) are shown in Fig. S3 in the Supplementary Material. The higher values of ω for the M-APSs at various STs with respect to the APS primarily indicate that the former substrates are rougher than the later one. These results are almost in line with their corresponding roughness exponents (α) and the correlation lengths (ξ), as discussed earlier (*vide ante*). Interestingly, the lateral correlation length (ξ) for the M-APS (2), as obtained from R(ρ) (HHCF) is estimated to be 180 nm (174 nm) [Fig. 5(d)]. This value of ξ is higher in comparison with APS and M-APS (1) and M-APS (1.5), albeit its roughness exponent (α) is least and the RMS roughness (ω) is considerably large (*vide ante*). The observed disparity in the apparently interrelated α, ω and ξ values of the M-APS (2) relating its surface roughness features in comparison with the APS, M-APS (1) and M-APS (1.5) may primarily signify the existence of chaotic patterns on the surfaces of the substrates that may remain ingrained within the correlation length.

3.4. Estimation of Lyapunov exponents, phase space trajectories of APS and M-APSs

The chaotic features of the substrates have been estimated from the Lyapunov exponents (λ). The Lyapunov exponents of the substrates are estimated from TISEAN software package applying Rosenstein's method [70,71]. In non-linear dynamics, this parameter provides a measure of exponential divergence or convergence of trajectories in phase space as a function of time. While the magnitude of λ signifies unpredictability of the system dynamics, its positive sign refers a chaotic system involving the divergence of two states with the evolution of time. Here, the time series is replaced by the spatial series and value of λ denotes the rate of loss of predictability of heights of APS and M-APSs over space.

The evolution of trajectories over space due to the variations of the surface heights h(r) for successive iterations is represented as [33,34,72].

$$|\delta_l| \approx |\delta_0| e^{\lambda l} \tag{7}$$

where $\delta_0 = h_n - h_{n'}$,; h_n and $h_{n'}$ are the surface heights of any two points on the substrate located very close to each other at the onset of the iteration step and l denotes the number of steps involving with the space iteration. The height profiles h(r) for the APS and M-APS substrates were extracted along the breadth of the respective AFM images and were subsequently linked together in series. The values of λ for all the prereferred substrates were found to saturate after stitching with five successive lines of the respective AFM images. Fig. 6 shows the plot of < ln (divergence) > as a function of iterations. The positive values of λ, as estimated from the slopes of the different plots associated with APS and M-APSs, indicate the prevalence of chaos with various degrees in all the substrates. The average height profiles h along six typical lines traced over the AFM images of APS and M-APSs as a function of r, are shown in the left column of Fig. 7(a–d). The spatial derivatives h′(r) vs h(r) plots of the respective height profiles are shown in the corresponding right column of the same figure (Fig. 7). Variation of h′(r) as a function of h(r) represents the 2D- phase space diagrams of the substrates. The phase space diagrams, as shown in Fig. 7 for the APS and M-APSs, mark the presence of non-periodic orbits, distinctively disposed on the respective phase spaces. The traces of non-periodic close orbits for APS and M-APS (1) [Fig. 7(A) and (B)] look similar with almost equal densities of low

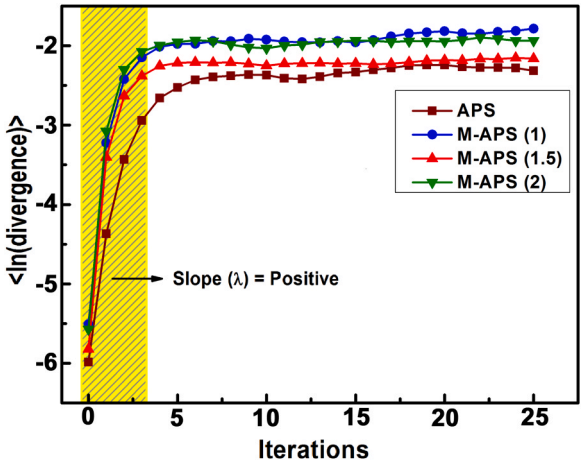

Fig. 6. < ln (divergence) > vs iteration plot for the APS and M-APSs. The shaded portion shows the linear regime of the plot.

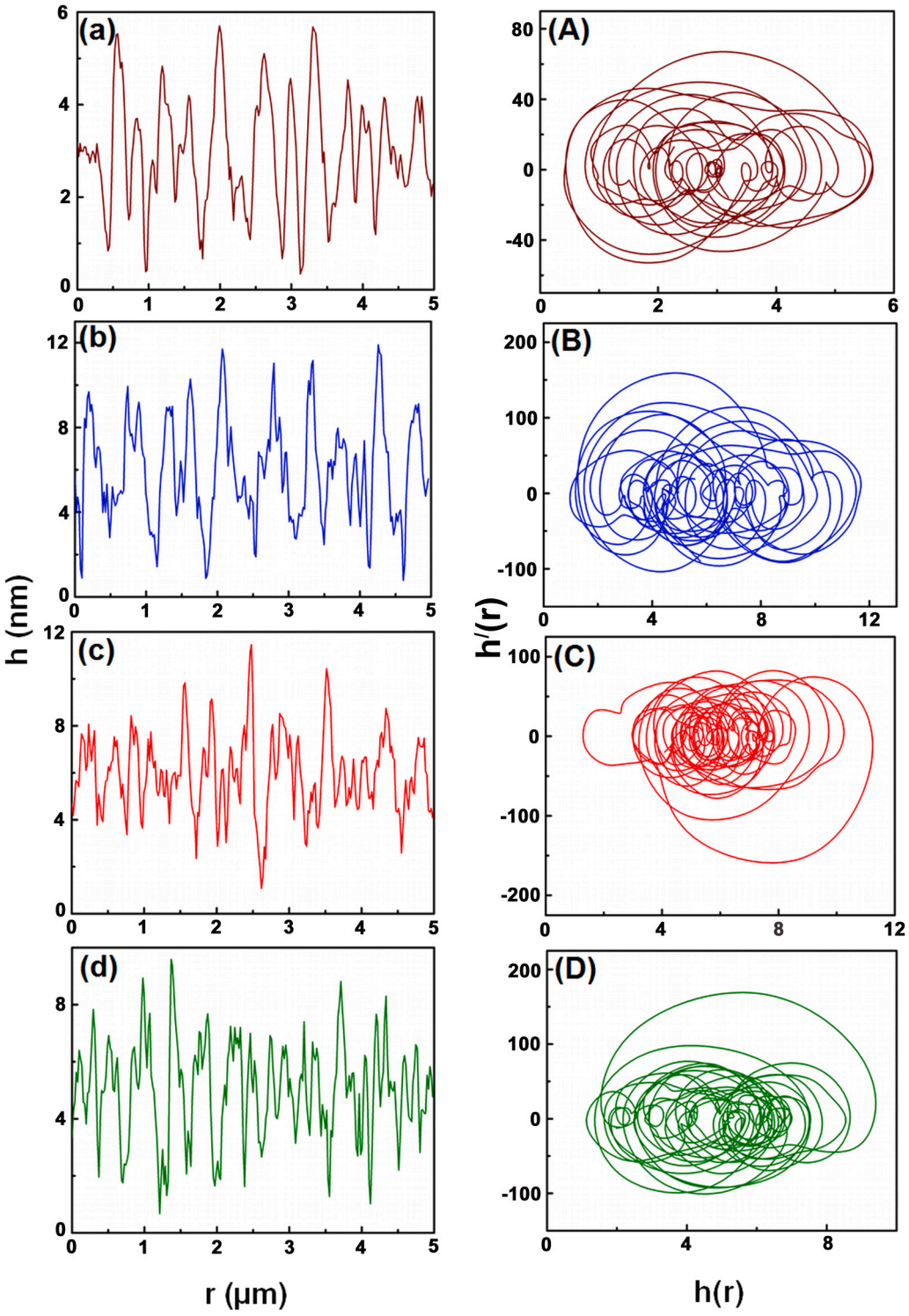

Fig. 7. Left Column: Average height profile [h(r) vs. r plot] along six typical lines drawn from the AFM images of **(a)** APS and **(b)** M-APS (1) **(c)** M-APS (1.5) and **(d)** M-APS (2). Right Column [**(A)**–**(D)**]: Spatial derivatives h′(r) as a function of h(r) of the corresponding height profiles for the above-mentioned substrates.

and large amplitude structures. The phase space diagrams for the APS and M-APSs (1) may be closely linked with their nearly identical morphological features as observed from their FESEM images [Fig. 1(a) and (b), *vide ante*)]. Interestingly, the general features of the phase space trajectories for M-APS (1.5) and M-APS (2) share fair amount of similarities. For both these substrates, large density of low amplitude structures prevails in certain spatial locations of the phase space, while the large amplitude one with low density are seen to surround them. The spatial distribution of the phase space trajectories for M-APS (1.5) and M-APS (2) can again be mapped with the corresponding FESEM images [Fig. 1(c) and (d)], which show clove like and sprouted aggregated patterns of plasmonic gold nanoparticle (*vide ante*). All the above observations collectively suggest that the APS and M-APSs are spatially chaotic of different natures. Reproducible SERS response from all the M-APSs may further accentuate the importance of chaotic substrates towards successful accomplishment of enhanced Raman signals.

4. Conclusions

Detail topographical features of SERS active substrates, fabricated through Langmuir-Blodgett and self-assembly techniques in presence of probe 4-MPy molecules, have been explored for the first time. Earlier studies were devoted to estimate the topographical parameters of bare SERS active substrates in the absence of probe molecules. However, correlating SERS responses with the topographical parameters of bare SERS active substrates may be imprecise, as in real experimental conditions the SERS signals are collected from the probe molecules only upon adsorption on the substrates. The topographical features of the substrates in presence of 4-MPy molecules have been elucidated from the statistical considerations in terms of lateral correlation length (ξ), Hurst or roughness exponents (α), root mean square surface roughnesses (ω) and fractal dimensions (D_f). Correlations between the topographical features of the substrates in presence of the 4-Mpy molecule and their corresponding SERS responses have been mapped. Detail investigations from the FESEM, AFM images and XPS studies reflect noticeable changes in the surface morphologies of the substrates upon the adsorption of probe 4-Mpy molecule. The present study reveals that the lateral correlation length (ζ) in the range ~118–180 nm for the M-APSs is enough to exhibit good SERS responses. Moreover, the Hurst (roughness) exponent (α) and the root-mean-square (RMS) roughness or the interface width (ω) of the as prepared substrates so determined from height-height correlation function (HHCF) H(r) show that the optimum values of α and ω in the range ~0.52–0.62 and 7.42–8.58 nm respectively favor appreciable SERS responses. The local surface fractal dimensions (D_f) of the as prepared substrates are estimated to lie within 2.38 ($\pm$ 0.025) to 2.48 ($\pm$ 0.020). These results further justify the importance of fractal nature of the substrates to foster appreciable SERS signals. The chaotic features of the substrates have also been estimated from the respective Lyapunov exponents and the corresponding 2D phase space trajectories. We believe that the present report will provide the fundamental link that connects the topographical features of more realistic SERS active substrates in presence of probe molecules with their corresponding SERS activities. This in turn will render significant advancement towards successful fabrications of efficient SERS sensing platforms in future endeavors.

CRediT authorship contribution statement

Somsubhra Saha: Data curation, Formal analysis, Investigation, Methodology, Validation, Visualization, Roles/Writing – original draft. **Manash Ghosh:** Resources, Investigation, Visualization. **Subhendu Chandra:** Visualization. **Joydeep Chowdhury:** Conceptualization, Roles/Writing – original draft, Supervision, Writing – review & editing.

Declaration of Competing Interest

The authors declare that they have no known competing financial interests or personal relationships that could have appeared to influence the work reported in this paper.

Acknowledgements

Authors are thankful to the Council of Scientific and Industrial Research (CSIR) and Department of Science & Technology (DST, SERB, Govt. of India) and the Department of Higher Education, Science & Technology and Biotechnology (DHESTB, Govt. of West-Bengal) for the provision of necessary funds via the research projects [Project Sanction No.: 03(1437)/18/EMR-II, EMR/2017/000901 and 202 (Sanc.)/ST/P/S&T/16G-22/2017)]. SS expresses his thank to UGC, Government of India for providing the necessary financial support in the form of NFSC fellowship. Authors would like to thank Mr. Uttam Ghara, IIT Kharagpur for recording the XPS spectra.

Appendix A. Supporting information

Supplementary data associated with this article can be found in the online version at doi:10.1016/j.colsurfa.2021.127319.

References

[1] M. Wang, B.D. Vivo, W. Lu, M. Muniz-Miranda, Sensitive Surface-Enhanced Raman Scattering (SERS) detection of nitroaromatic pollutants in water, Appl. Spectrosc. 68 (2014) 784–788, https://doi.org/10.1366/13-07428.
[2] I. Lopez-Tocon, J.C. Otero, J.F. Arenas, J. Garcia-Ramos, S. Sanchez-Cortes, Multicomponent direct detection of polycyclic aromatic hydrocarbons by surface-enhanced Raman spectroscopy using silver nanoparticles functionalized with the viologen host lucigenin, Anal. Chem. 83 (2011) 2518–2525, https://doi.org/10.1021/ac102771w.
[3] T.A. Saleh, M.M. Al-Shalalfeh, A.T. Onawole, A.A. Al-Saadi, Ultra-trace detection of methimazole by surface-enhanced Raman spectroscopy using gold substrate, Vib. Spectrosc. 90 (2017) 96–103, https://doi.org/10.1016/j.vibspec.2017.03.009.
[4] E. Lopez-Tobar, M. Antalik, D. Jancura, M.V. Canamares, A. Garcia-Leis, D. Fedunova, G. Fabriciova, S. Sanchez-Cortes, Adsorption and detection of amyloid marker thioflavin T on Ag nanoparticles by surface-enhanced Raman scattering, J. Phys. Chem. C 117 (2013) 3996–4005, https://doi.org/10.1021/jp310619c.
[5] Q. Hao, M. Li, J. Wang, X. Fan, J. Jiang, X. Wang, M. Zhu, T. Qiu, L. Ma, P.K. Chu, O.G. Schmidt, Flexible Surface-Enhanced Raman Scattering chip: a universal platform for real-time interfacial molecular analysis with femtomolar sensitivity, ACS Appl. Mater. Interfaces 12 (2020) 54174–54180, https://doi.org/10.1021/acsami.0c16315.
[6] S.K. Das, K. Pal, T.S. Bhattacharya, P. Karmakar, J. Chowdhury, Fabrication of SERS active Langmuir–Blodgett Film substrate for screening human cancer cell lines: experimental observations supported by multivariate data analyses, Sens. Actuators B 299 (2019) 126962–126970, https://doi.org/10.1016/j.snb.2019.126962.
[7] H. Qiu, J. Guo, M. Wang, S. Ji, M. Cao, M.A. Padhiar, A.S. Bhatti, Reduced graphene oxide supporting Ag meso-flowers and phenyl-modified graphitic carbon nitride as self-cleaning flexible SERS membrane for molecular trace-detection, Coll. Surf. A 560 (2019) 9–19, https://doi.org/10.1016/j.colsurfa.2018.09.059.
[8] J. Chowdhury, J. Sarkar, R. De, M. Ghosh, G.B. Talapatra, Adsorption of 2-amino-6-methylbenzothiazole on colloidal silver particles: quantum chemical calculations and surface enhanced Raman scattering study, Chem. Phys. 330 (2006) 172–183, https://doi.org/10.1016/j.chemphys.2006.08.016.
[9] R. Chadha, A. Das, A.K. Debnath, S. Kapoor, N. Maity, 2-thiazoline-2-thiol functionalized gold nanoparticles for detection of heavy metals, Hg (II) and Pb (II) and probing their competitive surface reactivity: a colorimetric, surface enhanced Raman scattering (SERS) and x-ray photoelectron spectroscopic (XPS) study, Coll. Surf. A 615 (2021) 126279–126291, https://doi.org/10.1016/j.colsurfa.2021.126279.
[10] X. Wang, M. Wang, T. Jiang, F. Wang, Y. Qing, S. Bu, J. Zhou, Dual-functional Fe_3O_4@SiO_2@Ag triple core-shell microparticles as an effective SERS platform for adipokines detection, Coll. Surf. A 535 (2017) 24–33, https://doi.org/10.1016/j.colsurfa.2017.09.025.
[11] S.K. Das, T.S. Bhattacharya, M. Ghosh, J. Chowdhury, Probing blood plasma samples for the detection of diabetes using SERS aided by PCA and LDA multivariate data analyses, New J. Chem. 45 (2021) 2670–2682, https://doi.org/10.1039/D0NJ04508J.
[12] S.D. Roy, M. Ghosh, J. Chowdhury, Near-field response on the far-field wavelength-scanned surface-enhanced Raman spectroscopic study of methylene blue adsorbed on gold nanocolloidal particles, J. Phys. Chem. C 122 (2018) 10981–10991, https://doi.org/10.1021/acs.jpcc.8b00315.
[13] E.C. Le Ru, C. Galloway, P.G. Etchegoin, On the connection between optical absorption/extinction and SERS enhancements, Phys. Chem. Chem. Phys. 8 (2006) 3083–3087, https://doi.org/10.1039/B605292D.
[14] S.K. Das, T.S. Bhattacharya, J. Chowdhury, Deciphering the near-field response with the far-field wavelength-scanned SERS spectra of 4-mercaptopyridine adsorbed on gold nanocolloidal particles entrapped in Langmuir Reverse Schaefer film of 5CB liquid crystal molecules, Phys. Chem. Chem. Phys. 22 (2020) 8719–8729, https://doi.org/10.1039/C9CP06925A.
[15] S.K. Das, M. Ghosh, S. Ghosh, J. Chowdhury, SERS active substrates of gold nanoparticles embedded in the pool of 5-CB liquid crystal molecules organized in Langmuir–Reverse Schaefer films: a facile fabrication route to make the topological defects useful, Appl. Surf. Sci. 484 (2019) 1263–1273, https://doi.org/10.1016/j.apsusc.2019.04.178.
[16] Z. Tang, J. Xu, X. Yu, R. Hong, X. Zu, X. Lin, H. Luo, W. Lin, G. Yi, Fabrication of Au nanoparticle arrays on flexible substrate for tunable localized surface plasmon resonance, ACS Appl. Mater. Interfaces 13 (2021) 9281–9288, https://doi.org/10.1021/acsami.0c22785.
[17] O. Volochanskyi, M. Svecova, V. Bartunek, V. Prokopec, Electroless deposition via galvanic displacement as a simple way for the preparation of silver, gold, and copper SERS-active substrates, Coll. Surf. A 616 (2021) 126310–126316, https://doi.org/10.1016/j.colsurfa.2021.126310.
[18] S. Saha, M. Ghosh, J. Chowdhury, Infused self-assembly on Langmuir–Blodgett Film: Fabrication of highly efficient SERS active substrates with controlled plasmonic aggregates, J. Raman Spectrosc. 50 (2019) 330–344, https://doi.org/10.1002/jrs.5529.

[19] S. Saha, M. Ghosh, B. Dutta, J. Chowdhury, Silver coated gold nanocolloids entrapped in organized Langmuir–Blodgett Film of stearic acid: potential evidence of a new SERS active substrate, Appl. Surf. Sci. 362 (2016) 364–373, https://doi.org/10.1016/j.apsusc.2015.11.137.
[20] S. Saha, M. Ghosh, B. Dutta, J. Chowdhury, Self-assembly of silver nanocolloids in the Langmuir–Blodgett Film of stearic acid: evidence of an efficient SERS sensing platform, J. Raman Spectrosc. 47 (2016) 168–176, https://doi.org/10.1002/jrs.4771.
[21] J. Li, H. Yan, X. Tan, Z. Lu, H. Han, Cauliflower-inspired 3D SERS substrate for multiple mycotoxins detection, Anal. Chem. 91 (2019) 3885–3892, https://doi.org/10.1021/acs.analchem.8b04622.
[22] S. Yadav, J. Satija, The current state of the art of plasmonic nanofibrous mats as SERS substrates: design, fabrication and sensor applications, J. Mater. Chem. B 9 (2021) 267–282, https://doi.org/10.1039/D0TB02137G.
[23] M. Sakir, S. Salem, S.T. Sanduvac, E. Sahmetlioglu, G. Sarp, M.S. Onses, E. Yilmaz, Photocatalytic green fabrication of Au nanoparticles on ZnO nanorods modified membrane as flexible and photocatalytic active reusable SERS substrates, Coll. Surf. A 585 (2020) 124088–124098, https://doi.org/10.1016/j.colsurfa.2019.124088.
[24] Y. Yue, C. Chen, W. Li, X. Guo, H. Yang, H. Guan, H. Bai, W. Liu, G. Xi, Highly sensitive W18O49 mesocrystal Raman scattering substrate with large-area signal uniformity, Anal. Chem. 93 (2021) 3138–3145, https://doi.org/10.1021/acs.analchem.0c04516.
[25] Q. Shao, D. Zhang, C. Wang, Z. Tang, M. Zou, X. Yang, H. Gong, Z. Yu, S. Jin, P. Liang, Ag@MIL-101(Cr) film substrate with high SERS enhancement effect and uniformity, J. Phys. Chem. C 125 (2021) 7297–7304, https://doi.org/10.1021/acs.jpcc.1c01757.
[26] A.B. Zrimsek, A.I. Henry, R.P. Van Duyne, Single molecule surface-enhanced Raman spectroscopy without nanogaps, J. Phys. Chem. Lett. 4 (2013) 3206–3210, https://doi.org/10.1021/jz4017574.
[27] T. Wu, Y.W. Lin, Surface-enhanced Raman scattering active gold nanoparticle/nanohole arrays fabricated through electron beam lithography, Appl. Surf. Sci. 435 (2018) 1143–1149, https://doi.org/10.1016/j.apsusc.2017.11.213.
[28] D. Caprara, F. Ripanti, A. Capocefalo, A. Sarra, F. Brasili, C. Petrillo, C. Fasolato, P. Postorino, DNA-functionalized gold nanoparticle assemblies for Surface Enhanced Raman Scattering, Col. Surf. A 589 (2020) 124399–124406, https://doi.org/10.1016/j.colsurfa.2019.124399.
[29] V. Suresh, L. Ding, A.B. Chew, F.L. Yap, Fabrication of large-area flexible SERS substrates by nanoimprint lithography, ACS Appl. Nano Mater. 1 (2018) 886–893, https://doi.org/10.1021/acsanm.7b00295.
[30] M.I. Stockman, V.M. Schalaev, M. Moskovits, R. Botet, T.F. George, Enhanced Raman scattering by fractal clusters: scale-invariant theory, Phys. Rev. B 46 (1992) 2821–2830, https://doi.org/10.1103/PhysRevB.46.2821.
[31] C. Douketis, Z. Wang, T.L. Haslett, M. Moskovits, Fractal character of cold-deposited silver films determined by low-temperature scanning tunneling microscopy, Phys. Rev. B 51 (1995) 11022–11031, https://doi.org/10.1103/PhysRevB.51.11022.
[32] P. Zhang, T.L. Haslett, C. Douketis, M. Moskovits, Mode localization in self-affine fractal interfaces observed by near-field microscopy, Phys. Rev. B 57 (1998) 15513–15518, https://doi.org/10.1103/PhysRevB.57.15513.
[33] S.K. Das, M. Ghosh, J. Chowdhury, Effects of surface topography on SERS response: correlating nanoscopy with spectroscopy, Appl. Surf. Sci. 439 (2018) 1–10, https://doi.org/10.1016/j.apsusc.2017.12.224.
[34] S.K. Das, S. Saha, M. Ghosh, J. Chowdhury, How SERS responses of probe molecules depend on topographies of the substrates? A vis-à-vis exploration, Vib. Spec. 107 (2020) 103031–103038, https://doi.org/10.1016/j.vibspec.2020.103031.
[35] G. Frens, Controlled nucleation for the regulation of the particle size in monodisperse gold suspensions, Nat. Phys. Sci. 241 (1973) 20–22, https://doi.org/10.1038/physci241020a0.
[36] S. Basu, S.K. Ghosh, S. Kundu, S. Panigrahi, S. Praharaj, S. Pande, S. Jana, T. Pal, Biomolecule induced nanoparticle aggregation: effect of particle size on interparticle coupling, J. Colloid Interface Sci. 313 (2007) 724–734, https://doi.org/10.1016/j.jcis.2007.04.069.
[37] K.L. Lee, L.H. Chen, A new method for coarse classification of textures and class weight estimation for texture retrieval, Pattern Recognit. Image Anal. 12 (2002) 400–410.
[38] K. Shimoda, J.-S. Park, T. Hinoki, A. Kohyama, Influence of surface structure of SiC nano-sized powder analyzed by X-ray photoelectron spectroscopy on basic powder characteristics, Appl. Surf. Sci. 253 (2007) 9450–9456, https://doi.org/10.1016/j.apsusc.2007.06.023.
[39] D. Xu, L. Sun, H. Li, L. Zhang, G. Guo, X. Zhao, L. Gui, Hydrolysis and silanization of the hydrosilicon surface of freshly prepared porous silicon by an amine catalytic reaction, New J. Chem. 27 (2003) 300–306, https://doi.org/10.1039/B204359A.
[40] S. Caporali, F. Muniz- Miranda, A. Pedone, M. Muniz-Miranda, SERS, XPS and DFT study of xanthine adsorbed on citrate-stabilized gold nanoparticles, Sensors 19 (2019) 2700–2709, https://doi.org/10.3390/s19122700.
[41] Z. Wang, X. Shen, Y. Yan, T. Qian, J. Wang, Q. Sun, C. Jin, Facile fabrication of a PDMS@ stearic acid-Al(OH)3 coating on lignocellulose composite with super hydrophobicity and flame retardancy, Appl. Surf. Sci. 450 (2018) 387–395, https://doi.org/10.1016/j.apsusc.2018.04.220.
[42] M. Choudhuri, A. Datta, Time-structuring in the evolution of 2D nanopatterns through interactions with substrate, Soft Mat. 12 (2016) 5867–5875, https://doi.org/10.1039/C6SM00814C.
[43] J.N. Israelachvili. Intermolecular and Surface Forces, Academic Press, USA, 2010.
[44] Saha S., Dutta B., Ghosh M., Chowdhury J., Unpublished.
[45] H.S. Jung, K. Kim, M.S. Kim, Raman spectroscopic investigation of the adsorption of 4-mercaptopyridine on a silver-sol surface, J. Mol. Struct. 407 (1997) 139–147, https://doi.org/10.1016/S0022-2860(97)00006-9.
[46] J. Hu, B. Zhao, W. Xu, B. Li, Y. Fan, Surface-enhanced Raman spectroscopy study on the structure changes of 4-mercaptopyridine adsorbed on silver substrates and silver colloids, Spectrochim. Acta Part A 58 (2002) 2827–2834, https://doi.org/10.1016/S1386-1425(02)00074-4.
[47] M. Pradhan, J. Chowdhury, S. Sarkar, A.K. Sinha, T. Pal, Hierarchical gold flower with sharp tips from controlled Galvanic replacement reaction for high Surface Enhanced Raman Scattering activity, J. Phys. Chem. C 116 (2012) 24301–24313, https://doi.org/10.1021/jp306330p.
[48] S.D. Roy, M. Ghosh, J. Chowdhury, Adsorptive parameters and influence of hot geometries on the SER(R) S spectra of methylene blue molecules adsorbed on gold nanocolloidal particles, J. Raman Spectrosc. 46 (2015) 451–461, https://doi.org/10.1002/jrs.4675.
[49] J.P. Camden, J.A. Dieringer, Y. Wang, D.J. Masiello, L.D. Marks, G.C. Schatz, R. P. Van Duyne, Probing the structure of single-molecule Surface-Enhanced Raman Scattering hot spots, J. Am. Chem. Soc. 130 (2008) 12616–12617, https://doi.org/10.1021/ja8051427.
[50] A. Ferrari, J. Robertson, Interpretation of Raman spectra of disordered and amorphous carbon, Phys. Rev. B 61 (2000) 14095–14107, https://doi.org/10.1103/PhysRevB.61.14095.
[51] T. Sang, J.E. Demuth, P.N. Sanda, J.R. Kirtley, Enhanced Raman scattering from carbon layers on silver, Chem. Phys. Lett. 76 (1980) 54–57, https://doi.org/10.1016/0009-2614(80)80603-8.
[52] G.M. Goncher, C.A. Parsons, C.B. Harris, Photochemistry on rough metal surfaces, J. Phys. Chem. 88 (1984) 4200–4209, https://doi.org/10.1021/j150663a003.
[53] J. Chowdhury, M. Ghosh, T.N. Misra, pH-dependent Surface-Enhanced Raman Scattering of 8-hydroxy quinoline adsorbed on silver hydrosol, J. Colloid Interface Sci. 228 (2000) 372–378, https://doi.org/10.1006/jcis.2000.6977.
[54] J. Chowdhury, M. Ghosh, T.N. Misra, Surface enhanced Raman scattering of 2,2/biquinoline adsorbed on colloidal silver particles, Spectrochim. Acta Part A 56 (2000) 2107–2115, https://doi.org/10.1016/S1386-1425(00)00263-8.
[55] J. Chowdhury, M. Ghosh, Adsorption of 3- and 4-benzoylpyridine on colloidal silver particles: a surface-enhanced Raman scattering study, J. Raman Spectrosc. 35 (2004) 1023–1033, https://doi.org/10.1002/jrs.1241.
[56] C.E. Taylor, S.D. Garvey, J.E. Pemberton, Carbon contamination at silver surfaces: surface preparation procedures evaluated by Raman spectroscopy and X-Ray photoelectron spectroscopy, Anal. Chem. 68 (1996) 2401–2408, https://doi.org/10.1021/ac950753h.
[57] J.S. Suh, M. Moskovits, J. Shakhesemampour, Photochemical decomposition at colloid surfaces, J. Phys. Chem. 97 (1993) 1678–1683, https://doi.org/10.1021/j100110a034.
[58] Y. Zhao, X. Liu, D.Y. Lei, Y. Chai, Effects of surface roughness of Ag thin films on surface-enhanced Raman spectroscopy of graphene: spatial nonlocality and physisorption strain, Nanoscale 6 (2014) 1311–1317, https://doi.org/10.1039/C3NR05303B.
[59] S. Kruszewski, Dependence of SERS signal on surface roughness, Surf. Interface Anal. 21 (1994) 830–838, https://doi.org/10.1002/sia.740211203.
[60] G. Macias, M. Alba, L.F. Marsal, A. Mihi, Surface roughness boosts SERS performance of imprinted plasmonic architectures, J. Mater. Chem. C 4 (2016) 3970–3975, https://doi.org/10.1039/C5TC02779A.
[61] C. Lee, C.S. Robertson, A.H. Nguyen, M. Kahraman, S. Wachsmann-Hogiu, Thickness of a metallic film, in addition to its roughness, plays a significant role in SERS activity, Sci. Rep. 5 (2015) 11644–11653, https://doi.org/10.1038/srep11644.
[62] D.D. Tuschel, J.E. Pemberton, J.E. Cook, SERS and SEM of roughened silver electrode surfaces formed by controlled oxidation-reduction in aqueous chloride media, Langmuir 2 (1986) 380–388, https://doi.org/10.1021/la00070a002.
[63] A.G. Brolo, D.E. Irish, G. Szymanski, J. Lipkowski, Relationship between SERS intensity and both surface coverage and morphology for pyrazine adsorbed on a polycrystalline gold electrode, Langmuir 14 (1998) 517–527, https://doi.org/10.1021/la970051i.
[64] C. Douketis, T.L. Haslett, Z. Wang, M. Moskovits, S. Iannotta, Rough silver films studied by surface enhanced Raman spectroscopy and low temperature tunnelling microscopy, Prog. Surf. Sci. 50 (1995) 187–195, https://doi.org/10.1016/0079-6816(95)00053-4.
[65] S.M. Novikov, S. Boroviks, A.B. Evlyukhin, D.E. Tatarkin, A.V. Arsenin, V. S. Volkov, S.I. Bozhevolnyi, Fractal shaped periodic metal nanostructures a top dielectric-metal substrate for SERS applications, ACS Photonics 7 (2020) 1708–1715, https://doi.org/10.1021/acsphotonics.0c00257.
[66] D. Risovic, H. Gebavi, M. Ivanda, Influence of fractal and lacunar characteristic of a nanostructured substrate on SERS enhancement, Appl. Surf. Sci. 537 (2021) 147915–147923, https://doi.org/10.1016/j.apsusc.2020.147915.
[67] G.Q. Wallace, F. Lagugné- Labarthet, Advancements in fractal plasmonics: structures, optical properties, and applications, Analyst 144 (2019) 13–30, https://doi.org/10.1039/C8AN01667D.
[68] J. Zhu, M.J. Liu, J.J. Li, X. Li, J.W. Zhao, Multi-branched gold nanostars with fractal structure for SERS detection of the pesticide thiram, Spectrochim. Acta Part A 189 (2018) 586–593, https://doi.org/10.1016/j.saa.2017.08.074.
[69] Y. Zhao, G.C. Wang, T.M. Lu, Experimental Methods in the Physical Sciences, Academic Press, San Diego, USA, 2001.

[70] R. Hegger, H. Kantza, Practical implementation of nonlinear time series methods: the TISEAN package, Chaos 9 (1999) 413–435, https://doi.org/10.1063/1.166424.

[71] M.T. Rosenstein, J.J. Collins, C.J. De Luca, A practical method for calculating largest Lyapunov exponents from small data sets, Phys. D. 65 (1993) 117–134, https://doi.org/10.1016/0167-2789(93)90009-P.

[72] S.H. Strogatz. Nonlinear Dynamics and Chaos with Applications to Physics, Biology, Chemistry and Engineering, Perseus, Cambridge, UK, 1994.